Thermodynamic and Tunneling Measurements of van der Waals Heterostructures

by

Spencer Louis Tomarken

B.A. Physics
The University of Chicago, 2012

Submitted to the Department of Physics
in partial fulfillment of the requirements for the degree of

Doctor of Philosophy

at the

MASSACHUSETTS INSTITUTE OF TECHNOLOGY

June 2019

Signature redacted

Author .....
Department of Physics
May 23, 2019

Signature redacted

Certified by ...
Raymond C. Ashoori
Professor of Physics
Thesis Supervisor

Signature redacted

Accepted by .....
Nergis Mavalvala
Associate Department Head of Physics

Thermodynamic and Tunneling Measurements of van der Waals Heterostructures

by

Spencer Louis Tomarken

Submitted to the Department of Physics
on May 23, 2019, in partial fulfillment of the
requirements for the degree of
Doctor of Philosophy

Abstract

In certain electronic systems, strong Coulomb interactions between electrons can favor novel electronic phases that are difficult to anticipate theoretically. Accessing fundamental quantities such as the density of states in these platforms is crucial to their analysis. In this thesis, I explore the application of two measurement techniques towards this goal: capacitance measurements that probe the thermodynamic ground state of an electronic system and planar tunneling measurements that access its quasiparticle excitation spectrum. Both techniques were applied to van der Waals materials, a class of crystals composed of layered atomic sheets with weak interplane bonding which permits the isolation of single and few-layer sheets that can be manually assembled into heterostructures.

Capacitance measurements were performed on a material system commonly known as magic-angle twisted bilayer graphene (MATBG). When two monolayers of graphene, a single sheet of graphite, are stacked on top of one another with a relative twist between their crystal axes, the resultant band structure is substantially modified from the cases of both monolayer graphene and Bernal-stacked (non-twisted) bilayer graphene. At certain *magic angles*, the low energy bands become extremely flat, quenching the electronic kinetic energy and allowing strong electron–electron interactions to become relevant. Exotic insulating and superconducting phases have been observed using conventional transport measurements. By accessing the thermodynamic density of states of MATBG, we estimate its low energy bandwidth, Fermi velocity, and interaction-driven energy gaps.

Time-domain planar tunneling was performed on a heterostructure that consisted of monolayer graphene and hexagonal boron nitride (serving as the dielectric and tunnel barrier) sandwiched between a graphite tunneling probe and metal gate. Tunneling currents were induced by applying a sudden voltage pulse across the full parallel plate structure. The lack of in-plane charge motion allowed access to the tunneling density of states even when the heterostructure was electrically insulating in the quantum Hall regime. These measurements represent the first application of time-domain planar tunneling to the van der Waals class of materials, an important step in extending the technique to new material platforms.

Thesis Supervisor: Raymond C. Ashoori
Title: Professor of Physics

Acknowledgments

Over the course of my PhD, I have always found myself surrounded by a constellation of coworkers, friends, and family members who have supported me in a number of different ways. I mean it when I say it: Thank you all! I know that whatever success I've had is not entirely self-made but due in large part to my good fortune in meeting all of you.

I think it's only appropriate to start with my advisor. There are many things I admire about Ray, but chief among them is his sincere, unpretentious love of physics. It's been a joy to work for someone who, despite a long research career, can hardly contain his enthusiasm when discussing fun physics ideas. During my time in the group, Ray has always pushed unique, bold research directions, often through leveraging unconventional measurement techniques. I'm inspired by his sense of individualism and commitment to exploring physics that otherwise may never come to light. Ray impressed upon me the importance of identifying and simplifying the essence of any complex problem with toy models and heuristics—a skill that I have not yet mastered but which is always at the forefront of my mind. I'm not sure if I'll stay in physics for the rest of my career, but I hope to draw on the critical thinking and approach to learning which Ray has helped me hone over the course of my PhD.

I want to thank Pablo for both providing a critical eye on my thesis committee and embodying the true spirit of collegiality throughout our collaboration. At this point our groups have a long history of successful collaboration which I have been very lucky to be a part of. In my experience it's rare to find scientists so willing to share lab space, resources, and credit time and again. One of the main results of this thesis came out of work that was pioneered in Pablo's group, and the project benefited greatly from Pablo's guidance and perspective.

The person who has impacted my productivity the most is without a doubt Yuan Cao. Yuan, I owe you a great deal for not only fabricating the twisted bilayer graphene devices I measured but also for breaking open the whole field of magic angle graphene largely on your own. You independently developed much of the fabrication techniques that enabled successful sample development and led the groundbreaking transport measurements that established magic angle graphene as a remarkable platform. You are a rising tide that has lifted many boats!

Andrea, you were the first person I worked closely with at MIT. As a young student, I didn't appreciate how lucky I was to be paired up with you, cutting my teeth and learning how to measure from one of the best in the business. You guided my early scientific growth, and you taught me through example what it means to devote all of one's energy to research, whether that entails staying up all night to redesign the cryostat grounding scheme or obsessively typing `E` on a gnuplot terminal to plot incoming data.

Neal, you provided a much needed steadying hand at the helm of our group, armed with a remarkably broad and deep background in all things experimental physics. I shudder to think at the state of our dil fridge had you not been around to lead major repairs. Your gentle prodding and seasoned perspective helped me out of a fabrication rut and onto a successful research plan at what may have been the most critical juncture in my PhD.

Over the last three years, Ahmet, you have played many roles in my life: lab mate, collaborator, gym buddy, and most importantly a true friend. It's been a ton of fun getting to know you, remaining indefinitely in the "linear gains regime" at the gym, and discussing capacitance data in our office. If you hadn't been around, not only would my PhD have been much less fruitful, it would have been much less fun.

Javier and Valla, though you have both left Boston already, I know we will remain close friends. You have been fountains of both physics and experimental nuts-and-bolts knowledge. Whenever we talk I am reminded of the importance of being able to ask really smart people really dumb questions. Additionally, I would like to thank both Lisa and Tina for rounding out our social group—dinner and charades on Friday night were a perfect antidote to a grueling work week.

Joel, thank you so much for taking me under your wing when I started working with hBN tunnel barriers. I'm quite sure I would not have managed to make any successful tunneling structures without your fab introduction. Thank you for training me on Raman characterization, allowing me to participate on your projects in small ways, and for cooking some amazing Taiwanese street food!

Although graduating and leaving MIT is bittersweet, I am encouraged by the talented students who will be assuming responsibility. Mo, you are wise beyond your years. You are one of the deepest-thinking and careful physicists I've ever met. I have no doubt you are equipped for whatever challenges lay ahead. Thank you for sharing your knowledge on pulsing, Weinreb amplifiers, and a litany of other topics. Sam, though we have only had a brief period of overlap, I can already tell that you have a maturity and patience that is rare in first-year students. I think you are the perfect candidate to absorb many of the unfinished project goals despite being at such an early stage of your career. Thank you for your hard work and taking on substantial responsibility.

I am blessed to have a very large, supportive, and loving family. Throughout my PhD, and particularly at the beginning, I knew I could always lean on you. You've cheered me on when things were successful, and you've commiserated and lent perspective when things seemed hopeless. Your steady, unconditional love and reassurance have done more than you probably realize. Thank you to my wonderful (step-)parents and sister: Erin and Del, Andy and Laurel, and Norah. Thank you to Jill and John for hosting in New York and Florida. In particular, I am thankful to my amazing extended family in Milwaukee (anchored by my grandparents Curt and Connie) which was frequently a much needed reprieve from labwork in Cambridge.

Additionally I would like to thank Professor Jaffe for providing useful insight on my thesis committee despite a very short lead time. Thanks to Ben Hunt, Kuei-Lin Chiu, and Joonho Jang for creating an inviting and stimulating environment in the Ashoori group. Thanks to our amazing division administrator Monica Wolf who routinely leaves the boundaries of her job description in order to go the extra mile for everyone on the floor. Thanks to Jason Luo, Dani Rodan-Legrain, David MacNeill, Dahlia Klein, Qiong Ma, Yafang Yang, Alex Frenzel, Dan Pilon, Fahad Mahmood, Emre Ergecen, Linda Ye, and many others who have made the second floor of Building-13 a fun, friendly, collaborative space. Thank you Brian Skinner, one of the rare theorists fluent in "experimentalist", for teaching me more about Wigner crystals in five minutes than the rest of my PhD put together. I'd like to thank Rich Helms for mentoring me at the end of high school and

providing crucial "PhD-perspective" that ultimately crystalized my interest in pursuing physics. Moreover, thank you for being a great friend and sounding board for countless side projects over the last decade. Thanks to my local Cambridge friends (Bobby, Ari, Jenny and Eddie, Ben, Paige), my college friends (Dan, Eduardo, Jeff, Zach), and my high school friends (Raynor, Mark, Oliver, Dallas, Clare, Sarah) for providing much needed levity and changes of scenery. Thanks to Peng, Ramy, and Coudé for opening up your apartment for frequent trips to New York, sneaking me into countless airport lounges, and sharing in many wonderful travel adventures.

DiDi, I saved the best for last. Many PhD students have significant others and even more have scientific collaborators, but I think very few can claim to have found both in the same person. You selflessly provided clarity and optimism, even when we were both in short supply. You taught me the majority of my fabrication knowledge and bailed me out on more than one occasion. You have studied for quals with me, proofread manuscript drafts, discussed interesting papers at my request, and listened to what can only be described as an inhumane number of 45-minute practice job talks. Perhaps most importantly, you shared in one of the most rewarding decision of grad school: adopting our two dogs Beans and Izzy, which I would have never mustered the courage to do on my own. Thank you for your patience, generosity, and fearlessness.

Contents

List of Figures

List of Tables

Chapter 1

Introduction

1.1 Motivation

At a basic level, we learn about the world by interacting with the objects around us. For the physicist, interaction takes the form of measurement in which we either gently perturb a system from equilibrium and study its subsequent response, or we excite it to a higher energy in order to understand its possible excitations. In the field of solid state physics, we attempt to understand the myriad ways in which electrons organize themselves inside materials, often through directly accessing their electrical degrees of freedom in the laboratory. This thesis will focus on the application of a few specific electronic measurements towards the goal of revealing the beautiful and sometimes unexpected behavior of the electrons in van der Waals platforms.

1.2 Overview and Organization

To the nonexpert, the term *van der Waals material* may sound esoteric, but the reader is likely already familiar with one important example. Graphite, the substance commonly used in pencils, consists of two-dimensional atomic sheets of carbon stacked on top of

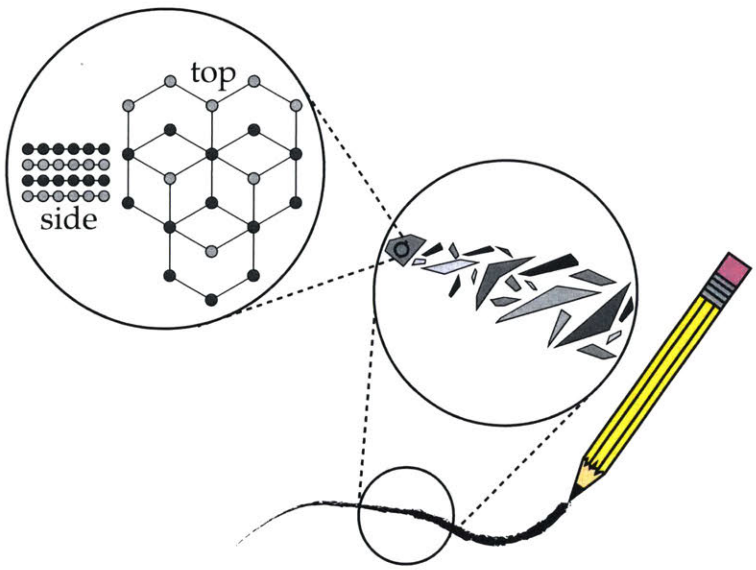

Figure 1-1: **Graphite exfoliation** Graphite is exfoliated from the core of a pencil as it is dragged across a piece of paper. The graphite trail consists of small flakes of exfoliated graphite of varying thickness and lateral size. The atomic structure of graphite consists of a stack of atomic sheets of carbon atoms on a honeycomb lattice. Neighboring layers are staggered.

one another. Within each sheet, the neighboring carbon atoms are chemically bonded very strongly to one another while the interaction between neighboring sheets is weak and mediated by van der Waals molecular forces [1, 2]. Graphite's small interplane coupling allows for isolation of single- and few-layer graphite crystals by mechanically exfoliating the parent compound. In fact, it is this property that makes graphite useful as a writing utensil. When one drags a pencil across a sheet of paper, microscopic crystals of graphite are exfoliated from the larger graphite composite core and deposited onto the paper, leaving behind a legible trail as shown in Figure 1-1. The ability to efficiently isolate single crystalline monolayers is not generic to all crystals and is the hallmark of a van der Waals material. Most crystals are too brittle, with neighboring atomic planes too strongly coupled, to isolate a single sheet. Other material systems require advanced fabrication techniques to access quasi-two-dimensional limits such as molecular beam epitaxy [3] for semiconductors [4] or pulsed laser deposition [5, 6] for complex oxides [7].

So far, I have only mentioned graphite, but it turns out there are dozens of van der

Waals materials with a wide variety of electronic phases ranging from band insulators to superconductors [8]. The ability to isolate atomically thin sheets of such diverse materials enables experimentalists to fabricate van der Waals heterostructures by manually stacking and sandwiching together distinct planar materials [9, 10]. In Chapter 2, I will explore both the two-dimensional physics of common van der Waals materials as well as the modern fabrication techniques that allow the construction of heterostructures with increasingly fine-tuned electronic properties.

The ability to precisely build a stack of van der Waals layers affords us the opportunity to explore the physics of two-dimensional materials with a variety of techniques. One popular technique, electron transport, involves treating the van der Waals heterostructure as a resistor of unknown value. Figure 1-2 shows the measurement scheme with a monolayer of graphite, commonly referred to as *graphene*, and equivalent circuit in panels **a** and **b**, respectively. By sourcing a voltage V and measuring a current I, the material's resistance R can be inferred from Ohm's law $V = IR$. However, electron transport is only capable of measuring electrons that can carry an electrical current through the sample. In other words, transport measurements access extended electronic states which support the movement of charge across the full extent of the sample. One drawback of transport schemes is that spatially localized electrons, which do not efficiently participate in transport, are neglected. Furthermore, it is difficult to extract fundamental equilibrium properties of the material (even qualitatively) due to the non-equilibrium nature of electron transport which necessarily involves a complicated mess of electrons colliding and scattering off of each other, the underlying ionic lattice, and the sample boundaries.

Are there other measurement techniques that might allow us to access the equilibrium properties of van der Waals materials? Taking inspiration from basic circuit elements, we might be inspired to treat the sample not as a resistor as done in transport but as a capacitor. If a metal electrode is separated from the van der Waals material by an insulating dielectric layer (which may itself be a van der Waals material), the electrode–van der Waals

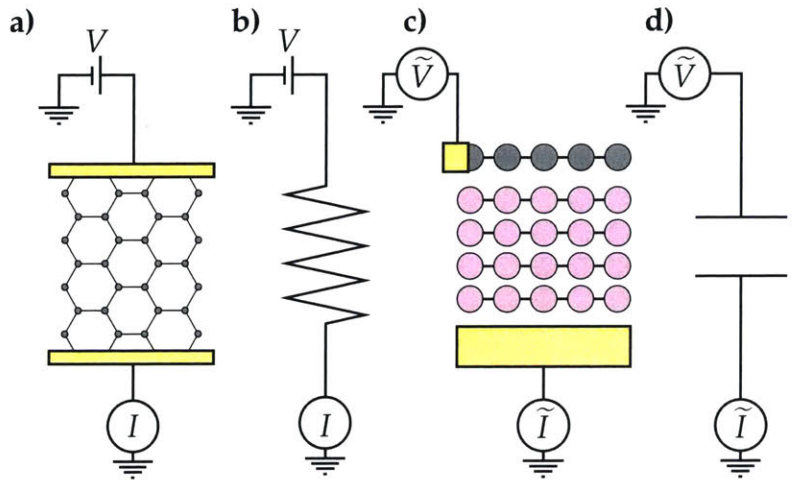

Figure 1-2: **Transport and capacitance schemes a)** A voltage V is sourced across a monolayer graphene device which has been ohmically contacted by a metal as indicated by the yellow regions. Current I is measured. **b)** The equivalent circuit treats the graphene flake as a resistor. **c)** In a capacitance scheme, an AC voltage $\widetilde{V}$ is applied to a graphene flake (gray) which has been contacted ohmically. The inert dielectric (light pink) is also a van der Waals material and separates the graphene from a nearby metal electrode (yellow). The AC current $\widetilde{I}$ is measured. **d)** The equivalent circuit treats the graphene–electrode structure as a capacitor.

system forms an approximately parallel plate capacitor geometry as shown in panels **c** and **d** of Figure 1-2. (There is still a series resistance arising from the sample's in-plane resistivity, however, this is negligible at sufficiently low measurement frequency.) It turns out that measuring the capacitance of such a device is directly related to the material's *electronic compressibility* [11] which in the context of this thesis will be synonymous with the thermodynamic density of states which determines the amount of energy required to add electrons to the material. The thermodynamic density of states is one of the most fundamental quantities of interest because it allows one to anticipate whether a material is insulating or conducting, whether strong electron–electron interactions are likely to be relevant, the role of localization, as well as a plethora of other electronic properties. In Chapter 3, I will explain the relationship between the thermodynamic density of states and capacitance, cryogenic capacitance bridge measurement techniques, as well as how to interpret capacitance data and extract fundamental quantities of interest such as energy

gaps and bandwidths.

In Chapter 4 I will discuss the application of capacitance measurements to a van der Waals heterostructure known as twisted bilayer graphene. When graphite is exfoliated, it often yields double-layer crystals known as bilayer graphene. The most common configuration is Bernal or AB stacking [12, 13], so named for the alignment of the A and B sublattices of each monolayer as shown in Figure 1-3. Bilayer graphene has also been studied in the AA stacking configuration [14, 15] which occurs less frequently. Twisted bilayer graphene, a third allotrope, is rarely formed from exfoliation alone and is typically fabricated by manually stacking two monolayer of graphene which are given an explicit relative rotation as shown in Figure 1-3.

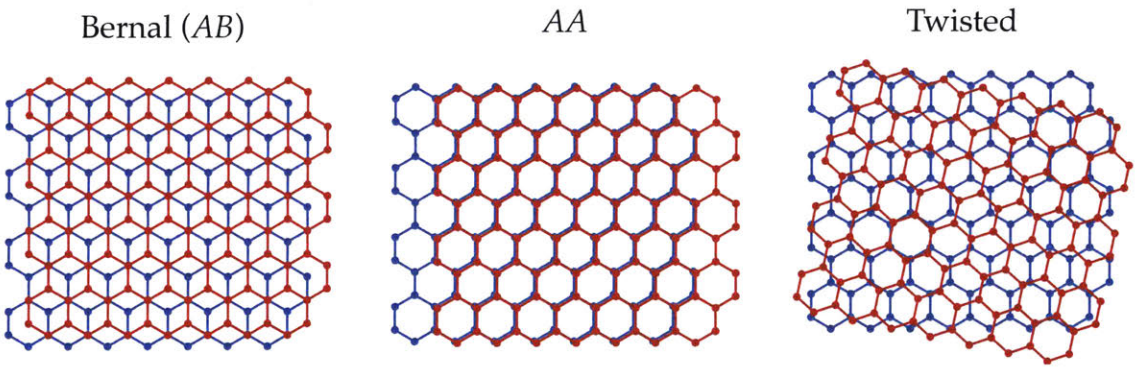

Figure 1-3: **Stacking configurations of bilayer graphene** Bernal (AB) stacking is the most common type because it is the lowest energy ionic configuration. AA stacking is also found frequently with graphite exfoliation. Twisted bilayer graphene occasionally occurs with exfoliation, but typically it is explicitly fabricated in the laboratory with higher yield and fine control over its twist angle.

When we directly stack and rotate two crystals, we induce a long-range spatial variation known as a moiré pattern. The spatial modulation can be thought of as the two-dimensional version of a beat frequency in which two waveforms of slightly different frequencies f_1 and f_2 experience a slow modulation at their difference $\Delta f = |f_1 - f_2|$. For f_i that are close in value, the modulation period T becomes very large, $T = \frac{1}{\Delta f}$, as shown in Figure 1-4.

For two graphene crystals which are slightly misaligned by θ, their spatial period of

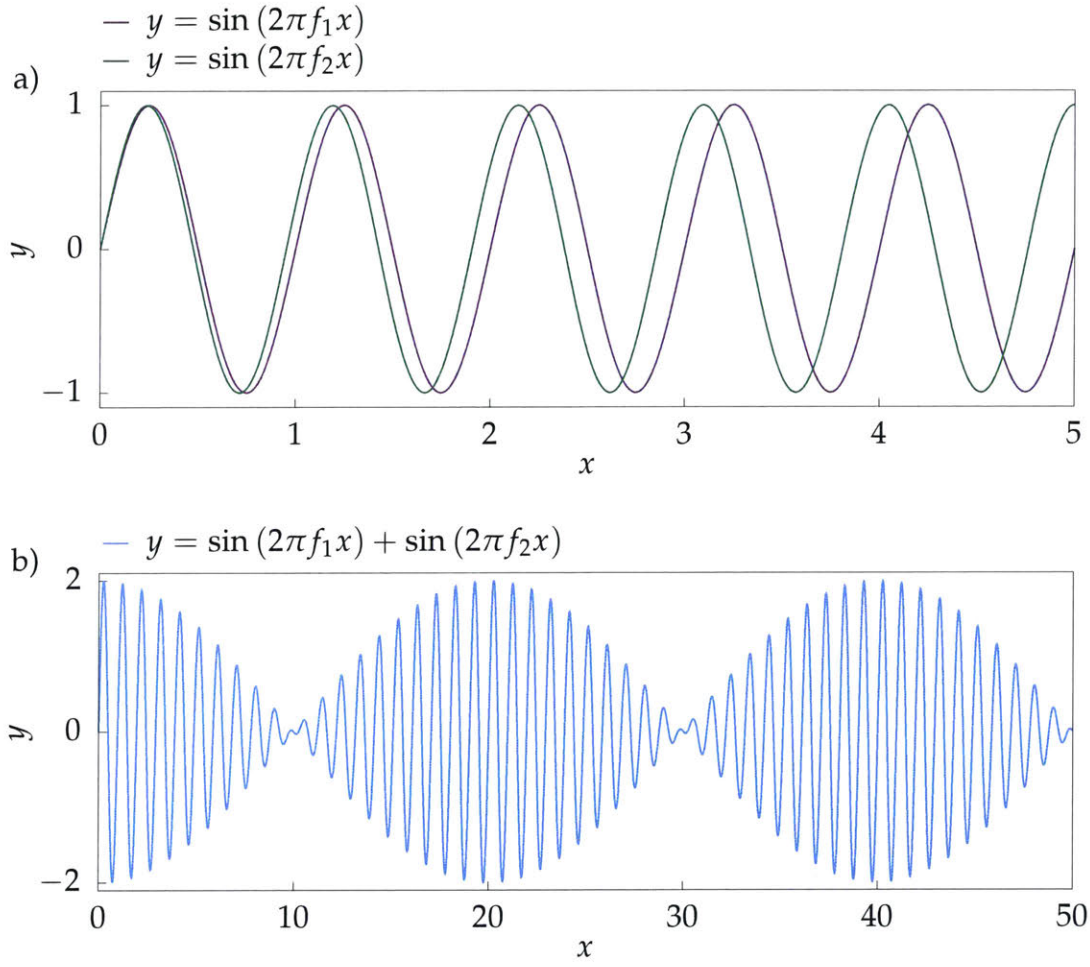

Figure 1-4: **Beating effect in one dimension a)** Two sinusoids with frequencies $f_1 = 1$ and $f_2 = 1.05$ are plotted. **b)** The sum of the two sinusoids creates a beating pattern in which the amplitude is modulated over a period of 20.

modulation λ is given by

$$\lambda = \frac{a/2}{\sin(\theta/2)} \tag{1.1}$$

where $a = 2.46$ Å is the lattice constant of graphene. For small values of θ it is obvious that $\lambda \gg a$, effectively renormalizing the lattice constant and creating a so-called superlattice. For example, Figure 1-5 shows the superlattice formed from two monolayers twisted at an angle of 5°.

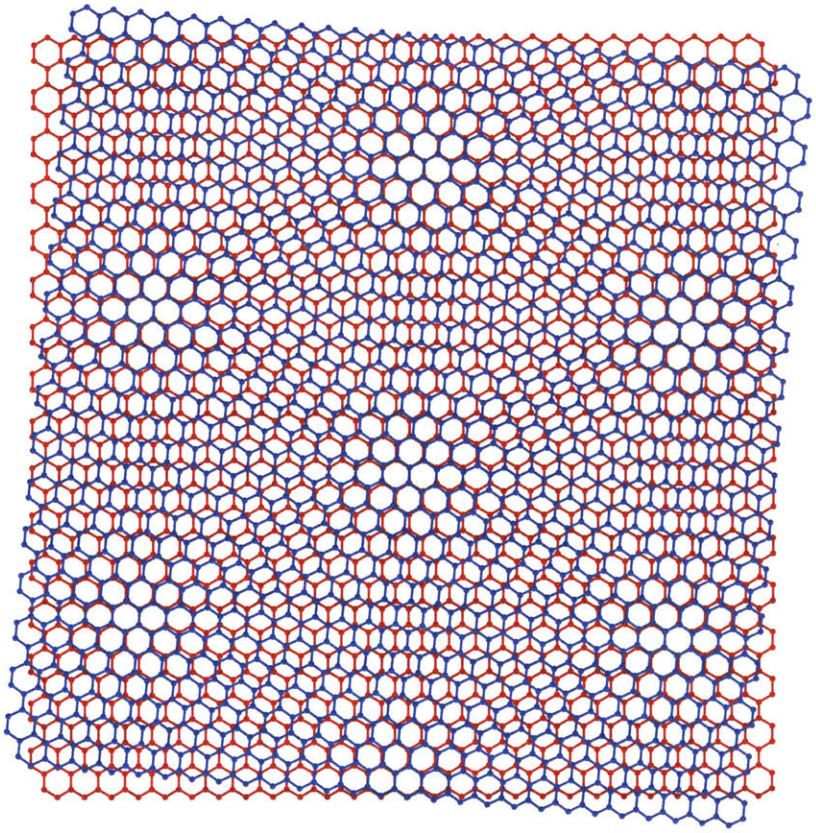

Figure 1-5: **Moiré pattern from twisted bilayer graphene** When two monolayers of graphene are twisted by a small angle, the induced moiré pattern can be much larger than the original lattice constant of graphene. Here, an angle of 5° induces a triangular superlattice whose unit cell includes dozens of constituent graphene unit cells from each layer.

The spatial modulation of the lattice creates an effective potential which interacts with the electrons and influences the allowed energy levels in much the same way that a tradi-

tional atomic potential generates a band structure via Bragg scattering at high symmetry points. The superlattice potential has a strong influence on the behavior of electrons at small twist angles where the relevant electrons of the two layers are close to one another in momentum space, allowing for hybridization. Numerical calculations have shown that at certain small angles known as the magic angles, the electronic band structure becomes incredibly flat [16]. Because the electronic kinetic energy is proportional to the width of the energy bands, the kinetic energy is extremely suppressed in this limit. When the kinetic energy is very weak, this provides an opportunity for potential energy contributions, in the form of Coulomb forces between pairs of electrons, to become relevant. This is an unusual state of affairs: typically, the electron density in most materials is large enough that the Coulomb potential between two electrons at relevant length scales is effectively screened by the presence of the other electrons—much like a Faraday cage. In the limit of strong electron–electron Coulomb repulsion, traditional single-particle band theory fails and exotic electronic phases emerge. Previous measurements have revealed an unexpected insulating state [17] where one would naïvely anticipate a metallic state as well as a possibly unusual form of superconductivity [18]. In Chapter 4 I will explore the application of the measurement techniques discussed in Chapter 3 to two twisted bilayer graphene heterostructures at twist angles close to the first magic angle. By accessing the compressibility, important quantities such as the Fermi velocity, energy bandwidth, and interaction-driven energy gaps can be estimated. Chapter 4 will also provide a comparison to results from other measurement techniques as well as a connection with theory proposals for magic-angle graphene systems.

The thermodynamic measurements described previously access the ground state properties of electronic systems. Instead of gently perturbing an equilibrium system and studying its response, it is possible to excite the electronic system in order to access its allowed higher energy states. Perhaps it is useful to picture an analogy from classical mechanics. Consider a ball sitting in the valley shown in Figure 1-6. The ball is in its ground

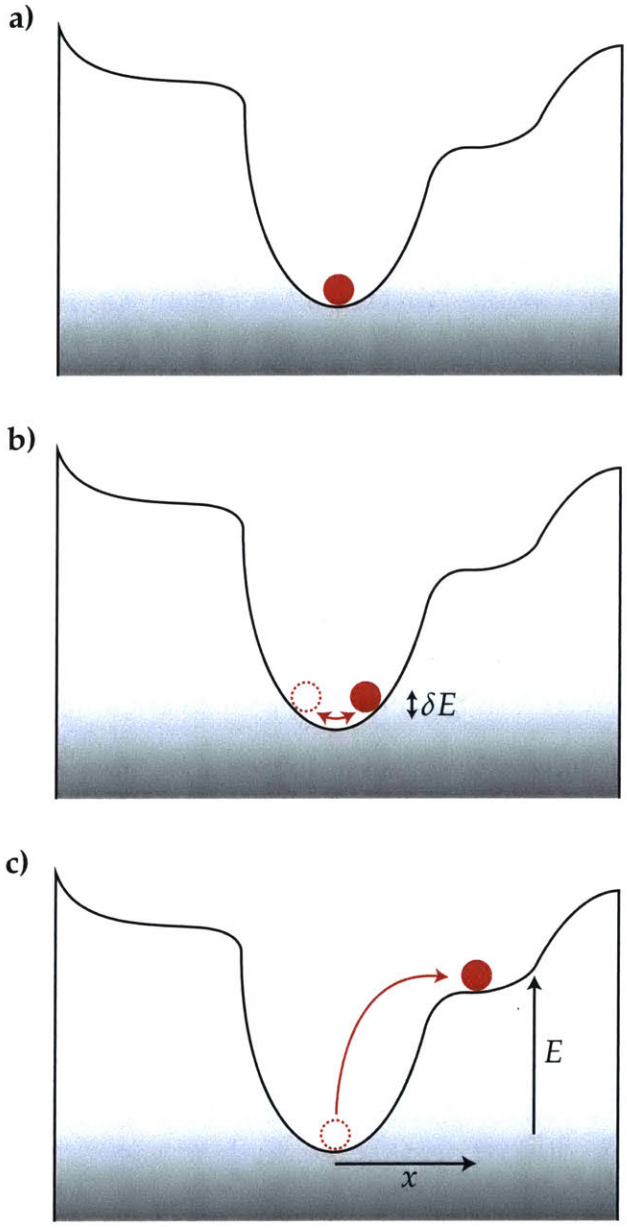

Figure 1-6: **Ball sitting in a potential energy profile a)** The ball is in the ground state at the bottom of the valley where its gravitational potential energy is minimized. At rest, it is in equilibrium. **b)** To probe the properties of the ground state, the ball can be given a small perturbation (a small kick) and its response, which is related to its equilibrium state, is observed. **c)** The potential energy landscape can also be probed by exciting the ball instantaneously out of its ground state and into a higher energy (metastable) state on the shoulder of the hill.

state when at the bottom of the valley as shown in panel **a**. Here, the ball's gravitational potential energy is minimized. In order to learn more about the ground state properties of the system, we might be tempted to give the ball a small perturbation in order to explore the potential energy landscape. If we imagine giving the ball a small kick of energy δE such that δE is much less than the potential energy of the hill at its highest point, then the ball will oscillate back and forth about its minimum as shown in panel **b**. If we could record the frequency of oscillation, this would tell us the local steepness of the minimum. This is conceptually similar to the thermodynamic capacitance measurements described previously in which we apply a small voltage modulation to an electronic system and ask how much charge is modulated in response.

Alternatively, we could try to excite the ball to a much higher energy level by giving it a large kick as shown in panel **c**. The ball would then be able to explore the higher energy landscape. If we could record its maximum displacement x from its ground state position $x = 0$ as a function of the energy of excitation E, then the function $E(x)$ would exactly map out the potential landscape (energy spectrum). After exciting to a higher energy, the ball would then be allowed to roll back and forth, exchanging potential and kinetic energy indefinitely. If we assume some dissipative mechanism like friction ultimately brings the ball back to its ground state energy, then we could also monitor the lifetime τ of each excitation as a function of energy E. The quantity $\tau(E)$ would tell us a great deal about the structure of the potential energy landscape. For example, if we imagine exciting the ball to one of the shoulders on the left or right of the minimum, the ball would experience a small restoring force from the shallow slope and take much longer to fall to equilibrium. However, if we excited the ball to one of the steep slopes immediately adjacent to the minimum, the large restoring force (and friction) would quickly bring the ball back to its ground state. In this way, studying high energy excitations can tell us a great deal about the energy landscape away from the ground state energy.

In this thesis, I will describe a unique type of electron tunneling measurement in which

we attempt to measure the relative ease with which we can suddenly inject electrons into (or out of) an electronic system at various energies. The basic planar tunneling scheme is shown in Figure 1-7. In panel **a** the energy diagram shows a metallic structure (yellow) being biased across an insulating barrier (pink) and injecting electrons into the available energy levels of a system under study (gray). The Fermi level of the material is indicated by the gray dashed line that separates filled energy bands from empty ones. The total current which is tunneled through the potential barrier into the system under study is proportional to the integrated single-particle density of states within the energy bias window [19]. The tunneling scheme can be achieved in van der Waals materials by separating a two-dimensional material under study, say graphene, from a metallic electrode with a thin insulating barrier (typically two to four atomic layers thick) as shown in panel **b**. In this thesis the insulating barrier will always be hexagonal boron nitride (which also serves as the dielectric layers in all devices).

In practice, after electrons are tunneled, they must relax to the Fermi level in order to be pulled out of the planar device through a contact in order to be measured by an amplifier further away. This means that there are two impedances that must be considered: the tunneling resistance and the in-plane resistance as shown in panel **c**. This poses a problem: if the *in-plane* resistance of the material (which is a property of relaxation and scattering at the Fermi level) is much larger than the *tunneling* resistance (which is a property of the single-particle density of states within the excitation window), then the measured tunneling current will be dominated by properties of the Fermi level. In the worst cases, the in-plane resistance will be so large that the extracted current will be too small to be measurable above electrical noise. This issue is particularly egregious in high magnetic field when two-dimensional systems undergo Landau quantization and the in-plane resistance oscillates rapidly as a function of the total carrier density. Chapter 5 will explore this conundrum in more detail, introduce a contactless pulsed tunneling scheme which avoids these issues, and discuss its modifications that were necessary for application to

van der Waals systems. Chapter 6 will demonstrate the application of this contactless time-domain technique to monolayer graphene at high magnetic field in the quantum Hall regime.

Finally, in Chapter 7 I will briefly discuss the status of capacitance and tunneling measurements in the broader quest to understand van der Waals materials. There are many van der Waals systems that have not been studied with capacitance and tunneling techniques. I will discuss a few promising directions which are currently underway.

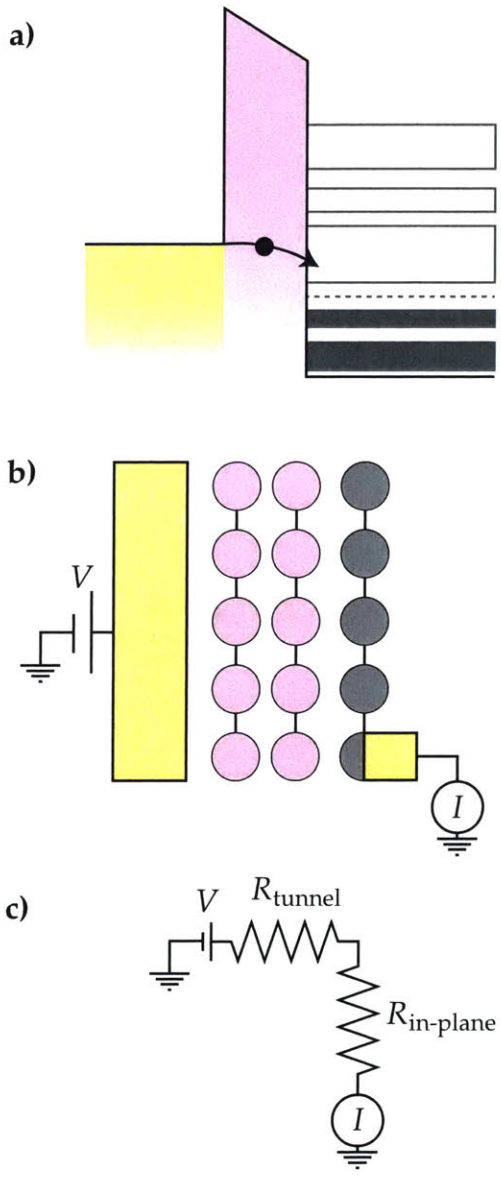

Figure 1-7: **Basic planar tunneling scheme a)** The schematic shows the tunneling electrode (yellow) being biased across an insulating barrier (pink) by a voltage $V < 0$ and injecting electrons into the available energy levels of a material (gray). **b** This tunneling structure can be fabricated from van der Waals materials. For example, graphene can be tunnel-coupled to a metal electrode with few-layer hexagonal boron nitride acting as the insulating barrier. **c** The effective DC circuit shows the contributions from both tunneling and in-plane resistances. It is important to have $R_{\text{tunnel}} \gg R_{\text{in-plane}}$ at all times.

Chapter 2

Van der Waals Materials

2.1 Chemical Bonding in Solids

Solid materials form due to the ability of crystalline order to minimize the electrostatic interactions of the constituent ions and electrons while still obeying Pauli exclusion. If one takes into account the great diversity of crystal structures, it should come as no surprise that the chemical bonding that binds solids together comes in a variety of flavors. Perhaps the most well known bond types are the ionic and covalent bonds which are largely responsible for gluing together the majority of compounds around us with substantial binding energies. Ionic bonding occurs whenever it is energetically favorable for an atom to lose one of its valence electrons so that it may occupy the available orbital of a neighboring atom. Ionic bonding is frequently illustrated with common table salt in which a sodium atom, containing one valence electron in the outer $3s$ valence shell, loses one electron to a nearby chlorine atom which has one available orbital in its outer $3p$ valence shell as shown in panel **a** of Figure 2-1. The positively charged sodium ion and the negatively charged chlorine ion then attract one another via the Coulomb force. The cost to ionize the sodium atom by liberating its single valence electron is more than made up for by both filling chlorine's outer $3p$ shell to a more stable configuration as well as the cohesive

energy gained by the positive and negative ion attracting one another. The end result is that the energy per molecule in a sodium chloride crystal is 6.4 eV less than separated neutral atoms [20]. In contrast to ionic bonding, covalent bonding consists of the sharing of one electron between two atoms or molecules. In the case of molecular hydrogen H_2, two hydrogen atoms with a single $1s$ electron can partially overlap one another in order to experience a full $1s^2$ valence shell over the spatial extent of the bond as shown in panel **b** of Figure 2-1. In many materials covalent bonding can rival the strength of common ionic bonds. For example, the carbon atoms in diamond form a tetragonal structure with a covalent bond energy of 711 kJ mol^{-1} [21] resulting in a binding energy of about 7.4 eV per molecule.

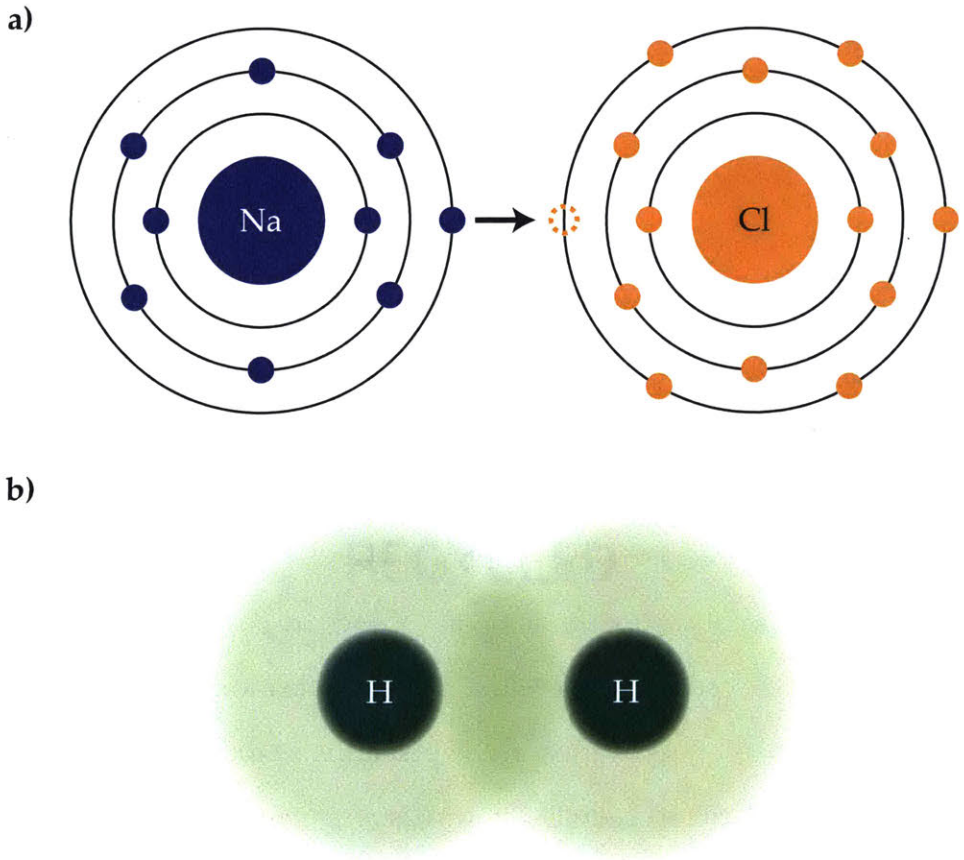

Figure 2-1: **Chemical bonds a)** NaCl forms through an ionic bond in which the outer $3s$ electron in the sodium atom is ionized and fills the empty orbital in the $3p$ shell of chlorine. **b)** A covalent bond forms between hydrogen atoms so that their half-filled $1s$ shells can experience a full $1s^2$ shell over the extent of the bond.

2.1.1 Van der Waals Forces

While ionic and covalent bonding are responsible for tightly gluing together the atoms and molecules that make up solid materials, there exists a set of intermolecular forces which interact with much lower energy scales but, nonetheless, are sufficient to form crystalline phases from electrically neutral atoms without the direct exchange of electrons. Johannes van der Waals famously incorporated these intermolecular forces into his equation of state which improved upon the ideal gas law by considering both the volume of molecules and their weak attractive interactions [22]. Due to his pioneering work, the set of generalized attractive and repulsive intermolecular forces are known as *van der Waals forces*. Although the full range of complex intermolecular interactions is beyond the scope of this thesis, the relevant forces in layered van der Waals solids take the form of dipole–dipole interactions. This may seem counterintuitive because in many van der Waals solids the individual layers are symmetric with respect to reflection across the plane. For example, graphene's relevant π bonds extend perpendicularly away from the honeycomb structure in a symmetric fashion. Hence, each layer is nonpolar in the out-of-plane direction and experiences no permanent dipole moment. However, it turns out that quantum mechanical fluctuations in the positions of the electrons can create instantaneous dipoles through the so-called London dispersion force first described by Fritz London [23–25]. The instantaneous dipole in one layer can in turn induce a dipole in an adjacent layer and form an attractive interaction. Despite these subtleties, the essential idea is captured by considering the basic electrostatics of two interacting atomic dipoles as shown in panels **a**–**c** in Figure 2-2.

In panel **b** of Figure 2-2, the first atom develops spontaneous dipole moment $\boldsymbol{p}_1$. The electric field generated far away from the dipole moment is proportional to $\frac{p_1}{r^3}$. Thus, at the separation R of the two atoms the electric field strength $\boldsymbol{E} \sim \frac{p_1}{R^3}$. The electric field will induce a dipole moment in the second atom, producing panel **c** of Figure 2-2. The second atom will acquire a dipole moment $\boldsymbol{p}_2 = \alpha \boldsymbol{E} \sim \frac{\alpha p_1}{R^3}$ where α is the polarizability of the

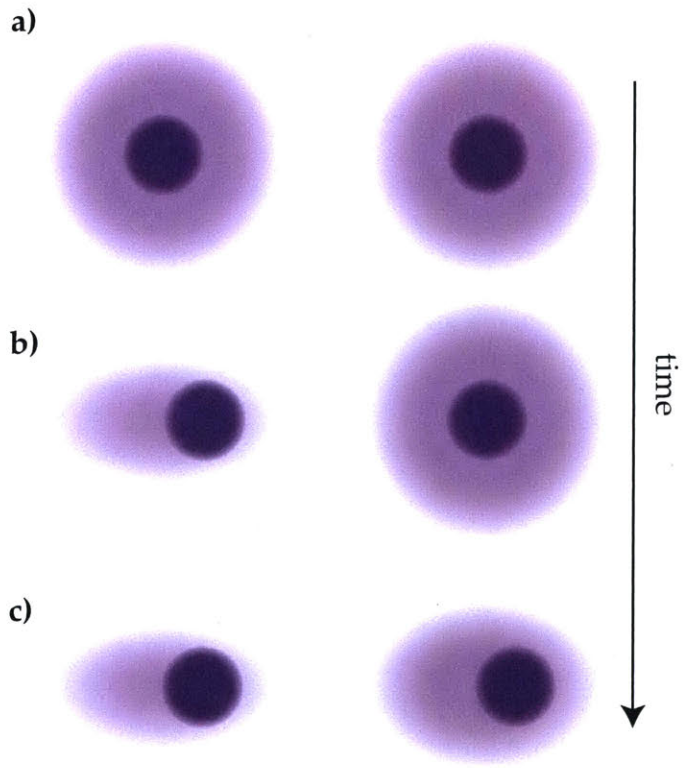

Figure 2-2: **Dipole–dipole interaction a)** Two neutral atoms are adjacent to one another. **b)** Quantum mechanical fluctuations create a spontaneous dipole in the left atom. **c)** The newly created dipole induces a (possibly unequal) dipole in the second atom by encouraging negative charge to migrate close to the nucleus of the first atom.

atom. The two dipoles have an interaction energy U that follows $U \sim \frac{p_1 p_2}{R^3} \sim \frac{\alpha p_1^2}{R^6}$, which demonstrates the important result that the dipole–dipole interaction falls off quickly with separation as $\frac{1}{R^6}$. The rapid decrease in interaction strength with distance is why the van der Waals forces are so weak in comparison to ionic and covalent processes.

The previous calculations would lead one to believe that two dipoles would lower their energy by attracting to one another indefinitely by sending $R \to 0$. At short distance, our treatment of each polarized atom as a perfect dipole would fail, but more importantly, strong repulsion ultimately arising from Pauli exclusion would prevent small separations from being energetically favorable. As two atoms are brought closer together, their spatial overlap forces electrons to occupy empty higher energy orbitals to avoid being in the same quantum state as their neighbor. At short distance this becomes very costly. This type of short-range repulsion is typically modeled with an interaction of the form $\frac{1}{R^{12}}$ or e^{-R} [20]. Taking short-range repulsion into account, the full interatomic energy is described by the Lennard–Jones potential:

$$U(R) = 4\varepsilon \left(\left(\frac{\sigma}{R} \right)^{12} - \left(\frac{\sigma}{R} \right)^{6} \right) \tag{2.1}$$

where $\varepsilon, \sigma > 0$ are material-dependent parameters. This potential has a stable minimum around $r_0 = 2^{1/6}\sigma$ as shown in panel **a** of Figure 2-3.

The details worked out previous apply to atoms and molecules in three dimensions. The situation is quantitatively, but not qualitatively, different for the case of two-dimensional layered sheets. Here, we imagine charge fluctuations on one side of an atomic layer inducing a dipole moment in the adjacent layer. The full calculation which determines the binding energy and equilibrium separation of a layered structure is quite involved and necessitates advanced numerical methods. For two-dimensional sheets it turns out that the induced dipole–dipole interaction falls of as $\frac{1}{R^4}$ instead of $\frac{1}{R^6}$ in the case of three-dimensional atomic dipoles. The equilibrium separation can be faithfully calcu-

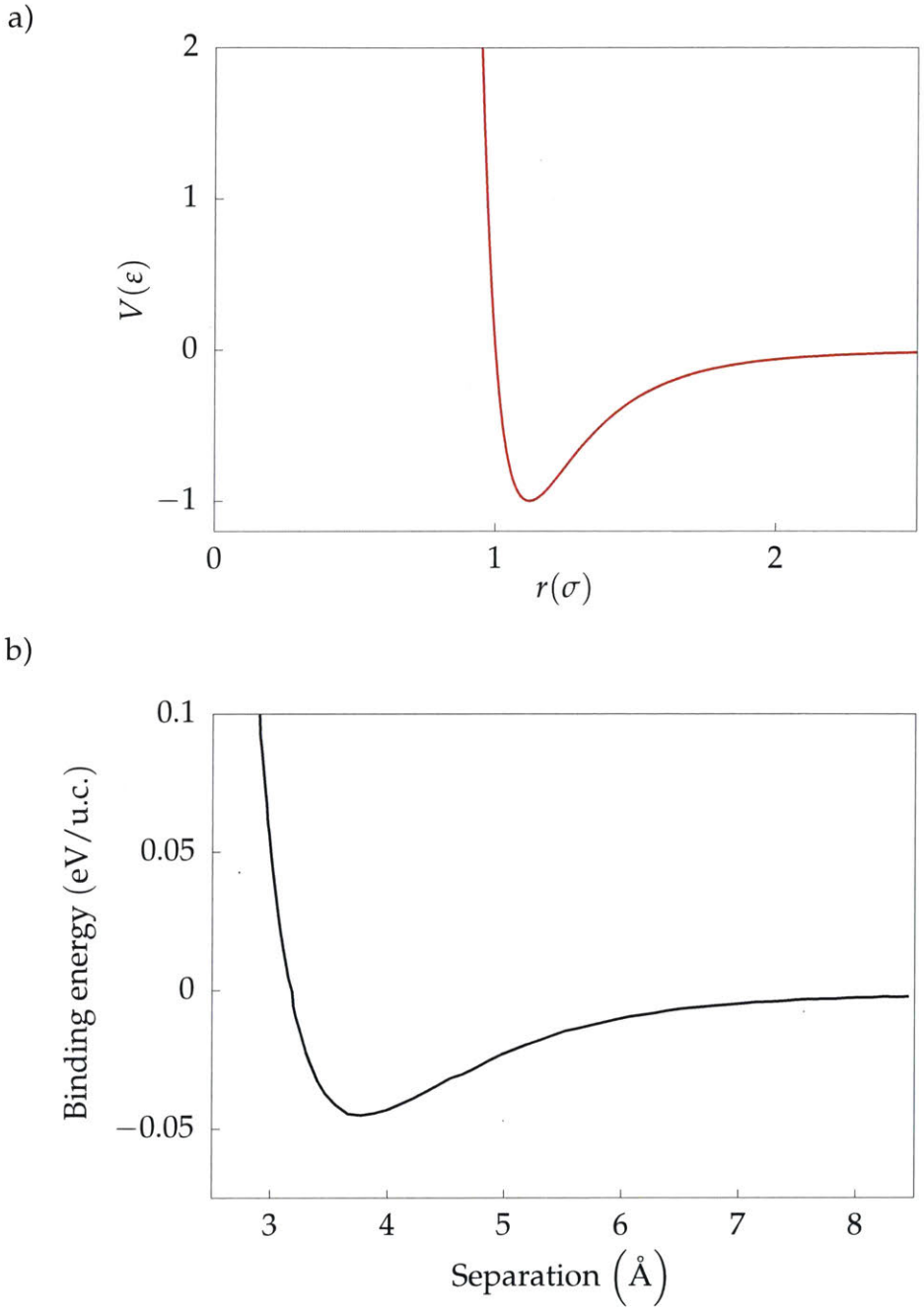

Figure 2-3: **Van der Waals potential strength a)** General Lennard–Jones potential for atomic dipoles showing the stable minimum around $r = 2^{1/6}\sigma$ where σ is the value at which the potential vanishes. **b)** Calculated van der Waals binding energy as a function of layer separation for two layers of graphite (Bernal-stacked bilayer graphene) adapted from reference [2]. For bulk graphite the layer separation was found to be 3.76 Å which agrees well with the experimentally verified value of around 3.35 Å [26].

lated as done in reference [2] and replotted in panel **b** of Figure 2-3 where the authors found a layer separation for bulk Bernal-stacked graphite of 3.76 Å. This analysis agrees nicely with experimentally determined values such as 3.35 Å according to reference [26]. Similar calculations were also successful at modeling additional van der Waals layered materials such as hexagonal boron nitride and molybdenum disulfide [2].

2.2 Monolayer Graphene

2.2.1 Thermodynamic Stability

Graphite was the first van der Waals material to be thinned down and isolated in the monolayer limit in 2004 [27]. Despite theoretical interest as early as 1947 [28], it took many decades for graphene to become a laboratory reality due to the widespread belief that two-dimensional crystals are thermodynamically unstable according to the Mermin–Wagner theorem [29]. The basic notion is that in two dimensions, long-wavelength density fluctuations which grow in magnitude logarithmically with the crystal size will eventually destroy the crystalline order for sufficiently large crystals at finite temperature. In reality, when graphene is prepared in the laboratory, it is either exfoliated onto a substrate, typically SiO_2 [27], which tethers the atoms with van der Waals forces and stabilizes the graphene, or it is suspended over trenches [30] and anharmonic coupling of the in-plane and out-of-plane phonons allows ripples to form and stabilize the long-range order [31].

2.2.2 Crystal Structure

The crystal structure of graphene consists of a two-dimensional plane of carbon atoms in a honeycomb structure. The honeycomb structure itself is not a Bravais lattice, however, it forms a triangular Bravais lattice with a two-atom basis. The bond length between carbon

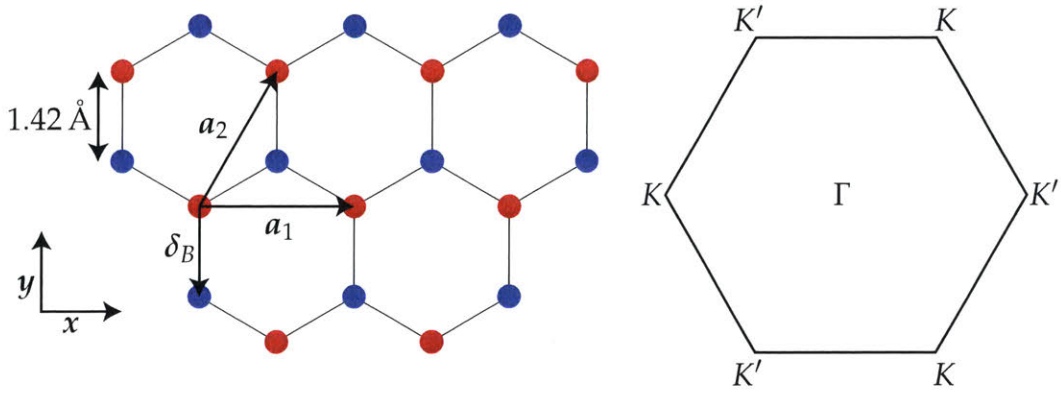

Figure 2-4: **Graphene crystal structure and Brillouin zone** (Left) Graphene forms a honeycomb lattice of carbon atoms with bond length 1.42 Å. Graphene's Bravais lattice is triangular with a two-atom basis. The two sublattices (A and B) of graphene are depicted with blue and red carbon atoms. The triangular basis vectors are given by $\boldsymbol{a}_1$ and $\boldsymbol{a}_2$ and $\boldsymbol{\delta}_B$ gives the displacement from the unit cell origin to the second sublattice. (Right) The reciprocal Brillouin zone is given by a hexagon whose center Γ point is labeled. The low energy physics of graphene is concentrated about the valleys at the crystallographically inequivalent zone vertices labeled K and K'. The K and K' points are generic features of the triangular Bravais lattice and not a consequence of the two-atom basis. The conduction and valence band contact points which occur at K and K' are a result of the sublattice symmetry.

atoms is $a = 1.42$ Å and the triangular lattice is spanned by

$$\boldsymbol{a}_1 = \sqrt{3}a\hat{\boldsymbol{x}} \tag{2.2}$$

$$\boldsymbol{a}_2 = \frac{\sqrt{3}a}{2}\left(\hat{\boldsymbol{x}} + \sqrt{3}\hat{\boldsymbol{y}}\right) \tag{2.3}$$

as shown in Figure 2-4. If we convert to reciprocal space, it turns out that graphene's low energy band structure is concentrated around the so-called *Dirac points* which are located at the valleys on the vertices of the Brillouin zone. These are customarily labeled K and K':

$$\boldsymbol{K}(\boldsymbol{K}') = \mp\frac{4\pi}{3\sqrt{3}a}\hat{\boldsymbol{x}}. \tag{2.4}$$

The other two sets of K and K' values are related to the above positions in momentum space by the addition of a reciprocal lattice vector and are therefore crystallographically equivalent. Each carbon atom has four available valence electrons. Three of these electrons are hybridized sp^2 orbitals which have s, p_x, and p_y character. These electrons participate in the in-plane covalent σ bonding with neighboring carbon atoms and are responsible for the in-plane tensile strength of graphene [32]. The remaining p_z orbitals form π bonds which stick away from the plane of the graphene. It turns out that the energy scale of the π bonds is significantly lower than that of the σ bonds so that the low energy electronic properties are only dependent on the π bonds [32]. This means that we can consider only one electron per atomic site when computing graphene's low-energy band structure [28]. Because there is one orbital per atom, the low energy bands will be exactly half-full when accounting for the spin degeneracy which gives an extra factor of 2 to the total number of allowed electrons within the π bands. Furthermore, because we will only consider one orbital per atom and there are two atoms per unit cell (one each from the two sublattices), there will be two low energy bands. The two previous statements imply that graphene's Fermi level will be exactly between the valence and conduction band derived in the tight-binding model in the absence of extrinsic carrier doping.

2.2.3 Tight-Binding Model

Graphene's low-energy band structure and many of its most interesting properties can be derived from a tight-binding model due to the relatively localized nature of the π orbitals [28]. In a tight-binding model, we consider the local wave function on each atomic site to consist of an atomic carbon orbital modified perturbatively by the *hopping* or wave function overlap with adjacent carbon atoms. Typically, consideration of nearest- and next-nearest-neighbor atoms is sufficient. Here, we will consider just nearest-neighbor hopping in the interest of describing the essential features of graphene's band structure.

The wave function for the two atom basis takes the form

$$\psi_k(\boldsymbol{r}) = a_k \psi_k^{(A)}(\boldsymbol{r}) + b_k \psi_k^{(B)}(\boldsymbol{r}) \tag{2.5}$$

where a_k and b_k represent the complex weight of the wave function on each sublattice. Due to chemical symmetry between the two sublattices, these magnitudes are always equal (at zero magnetic field) but contain nontrivial relative phase. $\psi_k^{(A)}$ and $\psi_k^{(B)}$ are the Bloch functions which sum over all the relevant orbitals:

$$\psi_k^{(j)} = \frac{1}{\sqrt{N}} \sum_{\boldsymbol{R}_l} e^{i\boldsymbol{k}\cdot\boldsymbol{R}_l} \phi^{(j)}(\boldsymbol{r} - \boldsymbol{R}_l - \delta_j). \tag{2.6}$$

The term $\phi^{(j)}(\boldsymbol{r} - \boldsymbol{R}_l - \delta_j)$ is the relevant π orbital on the atom located within the Bravais lattice site $\boldsymbol{R}_l$ at the basis position δ_j. We assume a crystal of N unit cells. We will set our coordinate system so that the A sublattice coincides with $\boldsymbol{R}_l$. Then, $\delta_A = 0$ and the B sublattice atoms are displaced by $\delta_B = -a\hat{\boldsymbol{y}}$. By construction, the atomic orbital ϕ is an eigenstate of an atomic (Schrödinger) Hamiltonian $\mathcal{H}_0$ such that $\mathcal{H}_0\phi = \epsilon_0\phi$ where ϵ_0 is the on-site energy of the orbital on the carbon atom. The full tight-binding Hamiltonian is broken into two components $\mathcal{H} = \mathcal{H}_0 + \delta\mathcal{H}$ where the term $\delta\mathcal{H}$ represents the perturbative hopping interaction from orbitals on adjacent atoms.

The full Hamiltonian $\mathcal{H}$ can be expressed in the sublattice basis:

$$\psi_k^\dagger \mathcal{H} \psi_k = \begin{pmatrix} a_k^* & b_k^* \end{pmatrix} \begin{pmatrix} \psi_k^{(A)*}\mathcal{H}\psi_k^{(A)} & \psi_k^{(A)*}\mathcal{H}\psi_k^{(B)} \\ \psi_k^{(B)*}\mathcal{H}\psi_k^{(A)} & \psi_k^{(B)*}\mathcal{H}\psi_k^{(B)} \end{pmatrix} \begin{pmatrix} a_k \\ b_k \end{pmatrix}. \tag{2.7}$$

Because the two sublattice wave functions $\psi_k^{(A)}$ and $\psi_k^{(B)}$ are not perfectly orthogonal, the

wave function overlap is typically accounted for with an overlap matrix $\mathcal{S}$:

$$\psi_{\boldsymbol{k}}^{\dagger}\mathcal{S}\psi_{\boldsymbol{k}} = \begin{pmatrix} a_{\boldsymbol{k}}^{*} & b_{\boldsymbol{k}}^{*} \end{pmatrix} \begin{pmatrix} \psi_{\boldsymbol{k}}^{(A)*}\psi_{\boldsymbol{k}}^{(A)} & \psi_{\boldsymbol{k}}^{(A)*}\psi_{\boldsymbol{k}}^{(B)} \\ \psi_{\boldsymbol{k}}^{(B)*}\psi_{\boldsymbol{k}}^{(A)} & \psi_{\boldsymbol{k}}^{(B)*}\psi_{\boldsymbol{k}}^{(B)} \end{pmatrix} \begin{pmatrix} a_{\boldsymbol{k}} \\ b_{\boldsymbol{k}} \end{pmatrix}. \tag{2.8}$$

In the case of graphene's tight-binding band structure, the overlap integral is a second-order effect [32] which we will neglect by making the simplification $\mathcal{S} = \mathbb{1}$. Beginning with the non-perturbative portion, we can calculate the matrix elements:

$$\psi_{\boldsymbol{k}}^{(A)*}\mathcal{H}_0\psi_{\boldsymbol{k}}^{(A)} = \frac{1}{N}\int d^2\boldsymbol{r}\sum_m e^{-i\boldsymbol{k}\cdot\boldsymbol{R}_m}\phi^{(A)*}(\boldsymbol{r}-\boldsymbol{R}_m)\mathcal{H}_0 e^{i\boldsymbol{k}\cdot\boldsymbol{R}_l}\phi^{(A)}(\boldsymbol{r}-\boldsymbol{R}_l) \tag{2.9}$$

$$= \frac{1}{N}\sum_{l,m} e^{i\boldsymbol{k}\cdot(\boldsymbol{R}_l-\boldsymbol{R}_m)}\int d^2\boldsymbol{r}\phi^{(A)*}(\boldsymbol{r}-\boldsymbol{R}_m)\mathcal{H}_0\phi^{(A)}(\boldsymbol{r}-\boldsymbol{R}_l). \tag{2.10}$$

Because the atomic orbitals are assumed orthogonal on different atoms, this reduces to

$$\psi_{\boldsymbol{k}}^{(A)*}\mathcal{H}_0\psi_{\boldsymbol{k}}^{(A)} = \frac{1}{N}\sum_l \int d^2\boldsymbol{r}\phi^{(A)*}(\boldsymbol{r}-\boldsymbol{R}_l)\mathcal{H}_0\phi^{(A)}(\boldsymbol{r}-\boldsymbol{R}_l) \tag{2.11}$$

$$= \epsilon_0. \tag{2.12}$$

By sublattice symmetry, $\psi_{\boldsymbol{k}}^{(B)*}\mathcal{H}_0\psi_{\boldsymbol{k}}^{(B)} = \epsilon_0$ as well. We can also easily see that the off-diagonal terms will vanish, since the summations above only survive for terms that consider orbitals on the same atom. The off-diagonal term $\psi_{\boldsymbol{k}}^{(A)*}\mathcal{H}_0\psi_{\boldsymbol{k}}^{(B)}$ and its Hermitian conjugate must vanish because the same atom cannot be found on both the A and B sublattice. Therefore

$$\mathcal{H}_0 = \begin{pmatrix} \epsilon_0 & 0 \\ 0 & \epsilon_0 \end{pmatrix}. \tag{2.13}$$

Due to chemical symmetry of the two sublattices, the on-site energy terms are identical. Because this matrix is simply proportional to the identity $\mathbb{1}$, it simply shifts the to-

tal energy by a constant and can be entirely neglected. Note that this subtraction is *not* possible when one considers the overlap matrix $\mathcal{S}$ with nearest-neighbor terms (which contribute off-diagonal terms that cannot be subtracted). Additionally, if one computes a tight-binding model for other honeycomb structures with distinct chemical species on each sublattice (such as hexagonal boron nitride), the diagonal terms of this matrix will not be equivalent and cannot be ignored.

Next, we can compute the perturbative contribution $\delta\mathcal{H}$ in which we consider only nearest-neighbor hopping. Inspection of the crystal structure in Figure 2-4 reveals that the nearest neighbors of atoms on sublattice A all reside on sublattice B and vice versa. Therefore, it should be intuitive that the diagonal terms such as $\psi_{\boldsymbol{k}}^{(A)*}\delta\mathcal{H}\psi_{\boldsymbol{k}}^{(A)}$ must vanish since the nearest-neighbor hopping is not possible within the same sublattice. Note that the diagonal terms do not vanish if one considers higher order hopping terms in which the diagonal terms acquire a momentum-dependent term $f(\boldsymbol{k})$ arising from next-nearest-neighbor hopping occurring within the same sublattice. Although this term is equivalent for the A and B sublattices, it cannot be subtracted due to its momentum dependence. We have the freedom to subtract a constant value from our Hamiltonian but not a function $f(\boldsymbol{k})$ if we wish to compute the band structure. We compute the off-diagonal terms:

$$\psi_{\boldsymbol{k}}^{(A)*}\delta\mathcal{H}\psi_{\boldsymbol{k}}^{(B)} = \frac{1}{N}\int d^2\boldsymbol{r}\sum_m e^{-i\boldsymbol{k}\cdot\boldsymbol{R}_m}\phi^{(A)*}(\boldsymbol{r}-\boldsymbol{R}_m)\delta\mathcal{H}e^{i\boldsymbol{k}\cdot\boldsymbol{R}_l}\phi^{(B)}(\boldsymbol{r}-\boldsymbol{R}_l-\boldsymbol{\delta}_B) \tag{2.14}$$

$$= \frac{1}{N}\sum_{<l,m>} e^{i\boldsymbol{k}\cdot(\boldsymbol{R}_l-\boldsymbol{R}_m)}\int d^2\boldsymbol{r}\phi^{(A)*}(\boldsymbol{r}-\boldsymbol{R}_m)\delta\mathcal{H}\phi^{(B)}(\boldsymbol{r}-\boldsymbol{R}_l-\boldsymbol{\delta}_B) \tag{2.15}$$

where we explicitly only consider the indices l and m for which the two orbitals are nearest-neighbor pairs. We can now simplify the notation dramatically by defining the nearest-neighbor hopping integral:

$$t \equiv \int d^2\boldsymbol{r}\phi^{(A)*}(\boldsymbol{r})\delta\mathcal{H}\phi^{(B)}(\boldsymbol{r}-\boldsymbol{\delta}_B). \tag{2.16}$$

Referring to Figure 2-4, we can see that this integral considers the hopping between the atom at the origin of sublattice A and its nearest neighbor directly beneath on sublattice B. Of course, the atom at the origin has three nearest neighbors, not just the one directly beneath it. The atom at the origin experiences nearest-neighbor hopping also with the atoms in the B sublattice located at $\boldsymbol{R} = \boldsymbol{a}_2$ and $\boldsymbol{R} = \boldsymbol{a}_2 - \boldsymbol{a}_1$. The value of the integral at each of these locations must be equivalent to the integral at the origin in the definition of t by three-fold rotation symmetry of the lattice. Therefore, for the atom on the A sublattice at $\boldsymbol{R}_m$, we consider the $\boldsymbol{R}_l$ such that $\boldsymbol{R}_l - \boldsymbol{R}_m \in \{\boldsymbol{0}, \boldsymbol{a}_2, \boldsymbol{a}_2 - \boldsymbol{a}_1\}$. We find

$$\psi_{\boldsymbol{k}}^{(A)*} \delta\mathcal{H} \psi_{\boldsymbol{k}}^{(B)} = \frac{1}{N} \sum_{<l,m>} e^{i\boldsymbol{k}\cdot(\boldsymbol{R}_l - \boldsymbol{R}_m)} \int d^2\boldsymbol{r} \phi^{(A)*}(\boldsymbol{r} - \boldsymbol{R}_m) \delta\mathcal{H} \phi^{(B)}(\boldsymbol{r} - \boldsymbol{R}_l - \boldsymbol{\delta}_B) \tag{2.17}$$

$$= t\left(1 + e^{i\boldsymbol{k}\cdot\boldsymbol{a}_2} + e^{i\boldsymbol{k}\cdot(\boldsymbol{a}_2 - \boldsymbol{a}_1)}\right) \tag{2.18}$$

$$= t\gamma_{\boldsymbol{k}} \tag{2.19}$$

where in the last line we have defined the phase factor $\gamma_{\boldsymbol{k}} \equiv 1 + e^{i\boldsymbol{k}\cdot\boldsymbol{a}_2} + e^{i\boldsymbol{k}\cdot(\boldsymbol{a}_2 - \boldsymbol{a}_1)}$. And of course the Hermitian conjugate must be $\psi_{\boldsymbol{k}}^{(B)*} \delta\mathcal{H} \psi_{\boldsymbol{k}}^{(A)} = t\gamma_{\boldsymbol{k}}^*$. Therefore, our complete Hamiltonian (up to a constant shift) is given by

$$\mathcal{H} = \begin{pmatrix} 0 & t\gamma_{\boldsymbol{k}} \\ t\gamma_{\boldsymbol{k}}^* & 0 \end{pmatrix}. \tag{2.20}$$

Solving for the spectrum we find:

$$0 = |\mathcal{H} - E_\lambda \mathbb{1}| = E_\lambda^2 - t^2 |\gamma_k|^2 \tag{2.21}$$

$$\Rightarrow E_\pm = \pm t |\gamma_k| \tag{2.22}$$

$$= \pm t \sqrt{3 + 2\sum_{i=1}^{3} \cos(\boldsymbol{k} \cdot \boldsymbol{a}_i)} \tag{2.23}$$

$$= \pm t \sqrt{3 + 4\cos\left(\frac{\sqrt{3}ak_x}{2}\right)\cos\left(\frac{3ak_y}{2}\right) + 2\cos\left(\sqrt{3}ak_x\right)} \tag{2.24}$$

where we have defined $\boldsymbol{a_3} \equiv \boldsymbol{a}_2 - \boldsymbol{a}_1$. Figure 2-5 shows the full band structure.

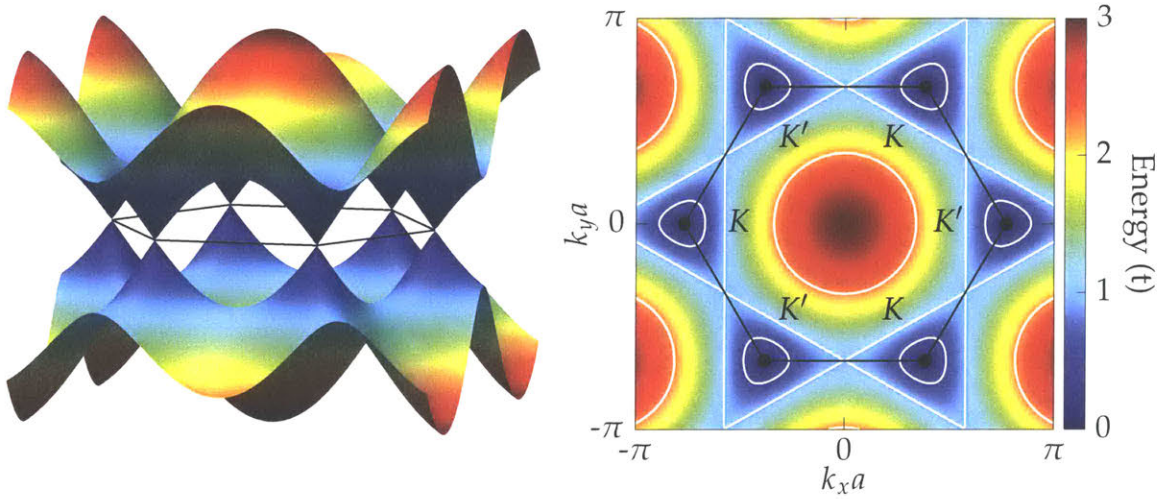

Figure 2-5: **Graphene tight binding band structure** (Left) The conduction and valence π bands are plotted for graphene's nearest-neighbor tight-binding model. The energy is plotted in units of the hopping parameter $t \simeq 3\,\text{meV}$ [33]. (Right) The isoenergy lines are plotted throughout the Brillouin zone. The K and K' points are labeled.

The positive (negative) solution represents the conduction (valence) band. These can be thought of as the crystal-scale equivalent of bonding and antibonding states of the π bonds. Inspection of the band structure reveals that the conduction and valence band meet at sharp points at each of the K and K' vertices on the Brillouin zone boundary.

Continuum Limit

If we zoom into the K point at $-\frac{4\pi}{3\sqrt{3}a}\hat{\boldsymbol{x}}$, we can linearize the spectrum to find

$$E_{\pm} \approx \pm\frac{3ta}{2}\left|\delta\boldsymbol{k}\right|. \tag{2.25}$$

With the Fermi velocity $v_{\mathrm{F}} = \frac{1}{\hbar}\frac{\delta E}{\delta k} = \frac{3ta}{2\hbar}$ we find the important continuum limit for small relative momenta:

$$E_{\pm} \approx \pm\hbar v_{\mathrm{F}}\delta k. \tag{2.26}$$

We can also expand $\gamma_{\boldsymbol{k}}$ around the K point to find: $\gamma_{\boldsymbol{K}+\delta\boldsymbol{k}} \approx \frac{3at}{2}\left(\delta k_x - i\delta k_y\right)$. Therefore, the tight-binding Hamiltonian can be expressed as

$$\mathcal{H} \approx \begin{pmatrix} 0 & \hbar v_{\mathrm{F}}(\delta k_x - i\delta k_y) \\ \hbar v_{\mathrm{F}}(\delta k_x + i\delta k_y) & 0 \end{pmatrix} = \hbar v_{\mathrm{F}}\delta\boldsymbol{k}\cdot\boldsymbol{\sigma} \tag{2.27}$$

where the σ_i are the usual Pauli matrices:

$$\sigma_x = \begin{pmatrix} 0 & 1 \\ 1 & 0 \end{pmatrix} \quad \sigma_y = \begin{pmatrix} 0 & -i \\ i & 0 \end{pmatrix} \quad \sigma_z = \begin{pmatrix} 1 & 0 \\ 0 & -1 \end{pmatrix}. \tag{2.28}$$

If instead we had expanded around the K' point we would have found

$$\mathcal{H} \approx \begin{pmatrix} 0 & -\hbar v_{\mathrm{F}}(\delta k_x + i\delta k_y) \\ -\hbar v_{\mathrm{F}}(\delta k_x - i\delta k_y) & 0 \end{pmatrix} = -\hbar v_{\mathrm{F}}\delta\boldsymbol{k}\cdot\boldsymbol{\sigma}^*. \tag{2.29}$$

If we were to swap the basis order in the K' sector from $\left(\psi^{(A)}_{K'}, \psi^{(B)}_{K'}\right)$ to $\left(\psi^{(B)}_{K'}, \psi^{(A)}_{K'}\right)$ we would have found the more aesthetically pleasing $\mathcal{H} \approx -\hbar v_{\mathrm{F}}\delta\boldsymbol{k}\cdot\boldsymbol{\sigma}$. In fact, if we drop the δ from δk, redefine k to be relative to the K or K' point, and convert from crystal

momentum to kinetic momentum $p = \hbar k$, then the continuum model can be expressed as

$$\mathcal{H}_{K(K')} = \pm v_{\mathrm{F}} \boldsymbol{p} \cdot \boldsymbol{\sigma}. \tag{2.30}$$

Dirac Electrons

The confused reader might ask, "Why go through the trouble of changing basis, dropping δ, and lumping constants?" The goal of this largely aesthetic exercise is to cast the Hamiltonian around the K and K' points in the form of the relativistic Hamiltonian first proposed by Paul Dirac [34]. Additionally, this form makes a firm connection to the concept of chirality which is borrowed from particle physics. The chirality operator η is given by

$$\eta = \hat{\boldsymbol{p}} \cdot \boldsymbol{\sigma}. \tag{2.31}$$

In high energy physics, the Pauli matrices σ_i refer to the physical spin of a particle and η measures its projection onto the direction of the kinetic momentum $\boldsymbol{p}$. Of course, our use of the Pauli matrices applies not to the physical spin of the electrons but to the graphene sublattice basis (A, B). In our continuum expansion, the Pauli matrices appeared in a somewhat sneaky fashion as a convenient way to express the (complex) distribution of crystal momentum on each of the A and B sublattices. In this context, we can think of the chirality operator η as projecting the sublattice amplitude onto a given electron or hole's crystal momentum. The operator η commutes with graphene's tight-binding Hamiltonian in the continuum limit because $\mathcal{H} \sim \eta$, making chirality a good quantum number. Electrons in graphene that are close to the K point are positive eigenstates (right-handed) of the sublattice projection operator η, meaning that their relative phase on the two sublattices acquires a well-defined value which rotates as we wind around the K point. The same is true of the K' point, except the electrons are left-handed with opposite

phase relationship to their cousins across the Brillouin zone at the K point.

Because of the unique properties close to the K and K' points where there is an analogy to relativistic physics, electrons at low energy in graphene are referred to as relativistic or Dirac electrons and the K and K' points are referred to as Dirac points. The existence of two species of electrons which reside at spatially separated locations in the Brillouin zone (which are not related by reciprocal lattice vectors), each described by different good quantum numbers (chirality), means we can simply keep track of the orbital physics associated with one valley and tack on an extra degeneracy factor of 2 (called the valley degree of freedom) in addition to spin when accounting for the density of states. Many of graphene's special properties ultimately relate back to this unique, linear band structure at low energy. For example, the relative suppression of backscattering in graphene (and other carbon electronics) as compared to other metals ultimately relates to the chiral nature of the charge carriers [35]. When we discuss quantum Hall physics later in section 2.5, we will discuss some additional consequences at high magnetic field.

It is important not to lose sight of graphene's larger band structure away from the Dirac points. Only at low energy and momenta close to the Dirac points is chirality a well-defined quantum number. If we could go to higher energy where coupling between K and K' becomes larger, these arguments would break down. However, it turns out that experimentally the accessible range of chemical potential in graphene is on the order of a few hunder meV and the continuum limit is generally considered quite accurate up to about 2 eV when including next-nearest neighbor and overlap corrections [32]. At sufficiently high energy, on the order of $t \simeq 3\,\text{eV}$, the Fermi surface is no longer concentrated about the Dirac points but instead encircles the Γ point, at which point the Dirac nature of our electrons is completely lost.

We have made use of several approximations in this section. We assumed no overlap correction, only nearest neighbor interactions, and a linear expansion about the K and K' points. It is worth asking if the essential features of graphene's Dirac spectrum survive

higher order hopping terms. While the linear approximation and particle-hole symmetry break down upon additional hopping terms and higher order expansions about the Dirac points, the contact point at K and K' are protected by the inversion symmetry of the honeycomb structure. This symmetry can be broken by considering honeycomb-structured materials with different atomic species on each sublattice (like hexagonal boron nitride) or with certain superlattice structures such as aligned monolayer graphene on hexagonal boron nitride or twisted bilayer graphene. The latter case will be discussed in section 2.4 and Chapter 4.

2.3 Bernal-Stacked Bilayer Graphene

Bernal-stacked bilayer graphene is more complicated than monolayer graphene because it has more than one strong hopping term arising from a combination of intra- and interlayer tunnel coupling. In lieu of deriving the full tight-binding Hamiltonian, we will make use the monolayer graphene tight-binding Hamiltonian as a starting point and simply expand the Hamiltonian to account for the increased complexity.

2.3.1 Crystal Structure

Bernal-stacked bilayer graphene consists of two monolayers of graphene on top of one another as shown in Figure 2-6. Their lattices are staggered so that the A sublattice of the top layer is over the B sublattice of the lower layer. This leaves the B sublattice of the top and A sublattice of the bottom sitting in the middle of the honeycomb plaquettes of the other layer. The tight-binding Hamiltonian will require a basis that takes into account the sublattice and layer degrees of freedom. In Figure 2-6 the hopping parameters t_0 and t_1 are shown. The term t_0 is equivalent to the term t used in the monolayer graphene case. It represents intralayer hopping on each of the two layers. The term t_1 represents hopping between the upper A sublattice and lower B sublattice. In principle, there are

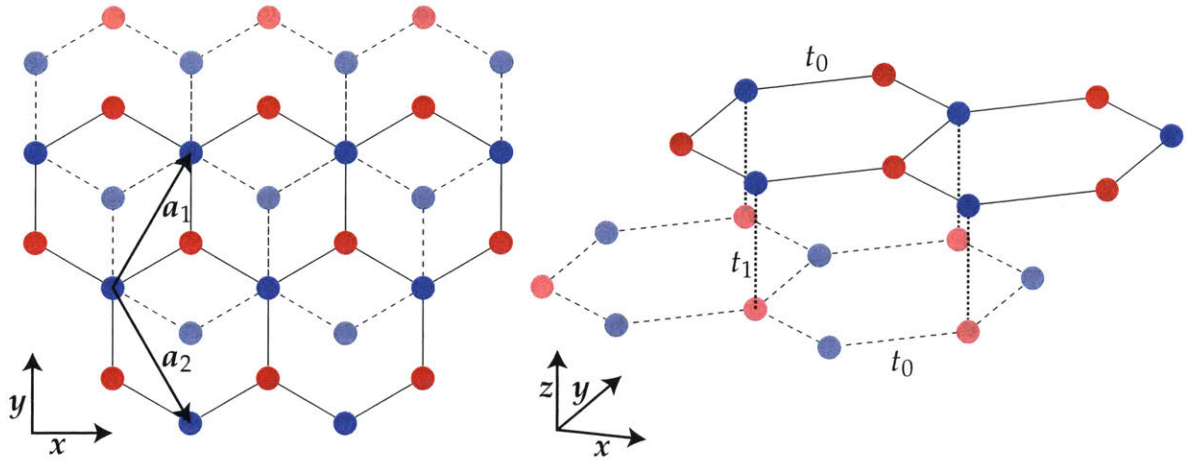

Figure 2-6: **Bernal-stack bilayer graphene crystal structure** (Left) Bernal-stacked bilayer graphene consists of two monolayers of graphene stacked on top of one another and staggered so that the A sublattice of the upper layer (darker colors) is located over the B sublattice of the lower layer (lighter colors). (Right) The hopping term t_0 is equivalent to the hopping t used in monolayer graphene. It represents hopping within the same layer to nearest neighbors. The term t_1 represents hopping between the A sublattice of the top layer and the B sublattice of the bottom layer which are directly on top of one another.

additional terms t_3 and t_4 which represent hopping from the A sublattice of the bottom to the B sublattice of the top and hopping from the $A(B)$ sublattice of the bottom to the $A(B)$ sublattice of the top, respectively. We will ignore these terms because they are small in magnitude and will only affect the band structure at irrelevant energies scales.

2.3.2 Tight-Binding Hamiltonian

Let the bottom and top layers be indexed as 1 and 2, respectively. We use the basis (A_1, B_1, A_2, B_2). The tight-binding Hamiltonian $\mathcal{H}$ takes the form

$$\mathcal{H} = \begin{pmatrix} \frac{\Delta}{2} & t_0\gamma_{\boldsymbol{k}} & 0 & 0 \\ t_0\gamma_{\boldsymbol{k}}^* & \frac{\Delta}{2} & t_1 & 0 \\ 0 & t_1 & -\frac{\Delta}{2} & t_0\gamma_{\boldsymbol{k}} \\ 0 & 0 & t_0\gamma_{\boldsymbol{k}}^* & -\frac{\Delta}{2} \end{pmatrix} \tag{2.32}$$

where Δ represents a layer asymmetry which may be induced by a vertical electric field (or different substrates on either side). Note that the terms $t_0\gamma_k$ are equivalent to the case of monolayer graphene because they only concern nearest neighbors within a layer. The terms t_1 do not have any associated phase because they represent hopping at the same in-plane coordinates. Solving for the spectrum gives four separate bands which resemble the general curvature and scale of monolayer graphene including the important band-touching around the K and K' points as shown in Figure 2-7.

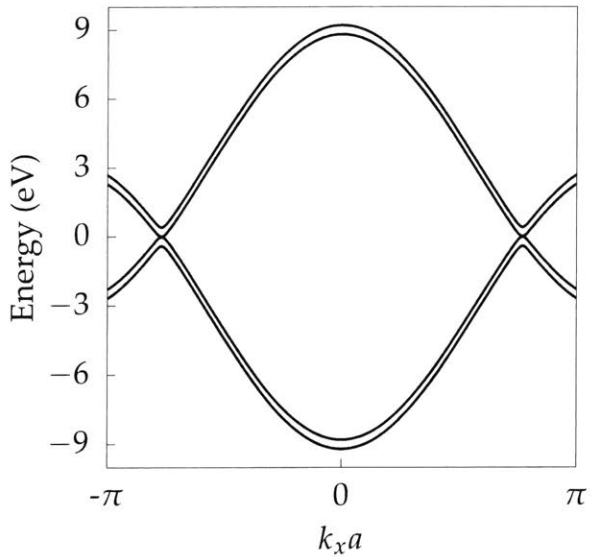

Figure 2-7: **Bilayer graphene spectrum** Plot along k_x of the four bands derived from the bilayer graphene tight-binding Hamiltonian at $k_y = 0$ for $\Delta = 0$, $t_0 = 3\,\text{eV}$, and $t_1 = 0.4\,\text{eV}$ [13]

Continuum Limit

We can linearize the model around the K and K' points as done previously for monolayer graphene. We will use the expansion $t_0\gamma_{k+\delta k} \approx \hbar v_F(\delta k_x - i\delta k_y) = \hbar v_F \delta k e^{-i\theta}$ where $\theta =$

$\tan^{-1}(\delta k_y/\delta k_x)$. The Hamiltonian becomes

$$\mathcal{H}_{\boldsymbol{K}+\delta\boldsymbol{k}} \approx \begin{pmatrix} \frac{\Delta}{2} & \hbar v_{\mathrm{F}}\delta k e^{-i\theta} & 0 & 0 \\ \hbar v_{\mathrm{F}}\delta k e^{i\theta} & \frac{\Delta}{2} & t_1 & 0 \\ 0 & t_1 & -\frac{\Delta}{2} & \hbar v_{\mathrm{F}}\delta k e^{-i\theta} \\ 0 & 0 & \hbar v_{\mathrm{F}}\delta k e^{i\theta} & -\frac{\Delta}{2} \end{pmatrix}. \tag{2.33}$$

If we solve for the eigenvalues we find (switching $\delta k \to k$ for convenience)

$$E_{\pm}^2 = (\hbar v_{\mathrm{F}} k)^2 + \frac{\Delta^2}{4} + \frac{t_1^2}{2} \pm \sqrt{(\hbar v_{\mathrm{F}} k)^2 \left(\Delta^2 + t_1^2\right) + \frac{t_1^4}{4}}. \tag{2.34}$$

Consider the case of no layer asymmetry: $\Delta = 0$. The four bands are plotted in Figure 2-

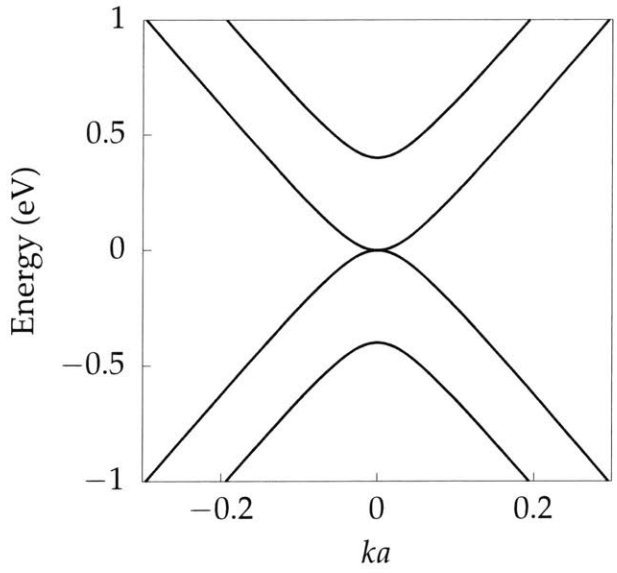

Figure 2-8: **Bilayer graphene in the continuum limit** showing the four bands close to K with no interlayer asymmetry ($\Delta = 0$).

8. At high energies and momenta, the bands acquire the monolayer-graphene-like linear dispersion characterized by v_{F}. They separate into two sets which are displaced by the hopping parameter t_1. The two bands which are split by $2t_1$ at $k = 0$ are associated with the strong vertical tunneling between sites $A2$ and $B1$ which form a dimer with a bonding

and anti-bonding energy branch ($\pm t_1$). The low energy bands that touch at $k = 0$ are associated with a higher order tunneling process between sites $A1$ and $B2$, in which an electron first tunnels from A_1 to B_1 $\left(t_0\gamma_k = \hbar v_F k e^{-i\theta}\right)$, from B_1 to A_2 (t_1), and finally from A_2 to B_2 $\left(t_0\gamma_k^* = \hbar v_F k e^{i\theta}\right)$ so that the energy of interaction $E_{A1-B2} \sim t_1 v_F^2 k^2$ and we get a quadratic dispersions (at small momentum). This is more explicit if we expand near the K point where $\hbar v_F k \ll t_1$ in which:

$$E_\pm^2 \approx (\hbar v_F k)^2 + \frac{t_1^2}{2} \pm \frac{t_1^2}{2}\left(1 + \frac{2}{t_1^2}(\hbar v_F k)^2 - \frac{2}{t_1^4}(\hbar v_F k)^4\right). \tag{2.35}$$

This yields the four equations to lowest order:

$$E_\pm^{(1)}(k) = \pm\frac{(\hbar v_F k)^2}{t_1} \tag{2.36}$$

$$E_\pm^{(2)}(k) = \pm\left(t_1 + \frac{(\hbar v_F k)^2}{t_1}\right) \tag{2.37}$$

which look semiconductor-like with effective mass $\frac{t_1}{2v_F^2}$. A gap in the lowest two energy bands can be opened up with application of an electric field so that $\Delta \neq 0$ which breaks the sublattice symmetry protecting the Dirac point band contact as show in Figure 2-9 with $\Delta = 0.5\,\text{eV}$.

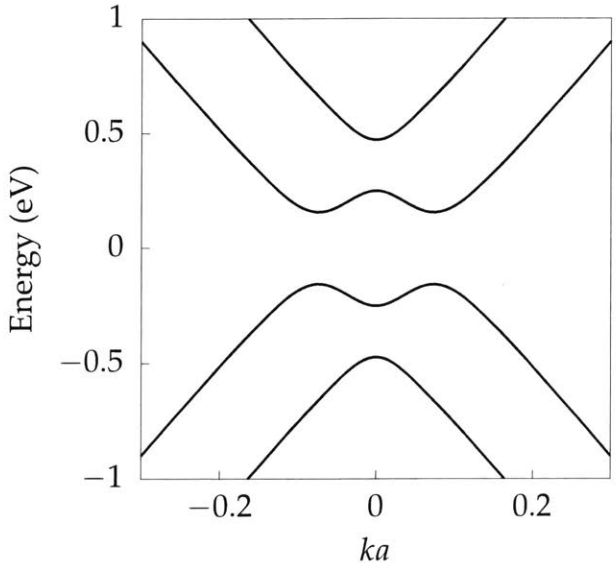

Figure 2-9: **Bilayer graphene gapped** by a layer asymmetry which breaks the sublattice symmetry protection ($\Delta = 0.5\,\text{eV}$).

2.4 Twisted Bilayer Graphene

Twisted bilayer graphene consists of two monolayers of graphene that have been stacked on top of one another and given a relative rotation, or twist, between the crystal axes of each layer. Twisted bilayer graphene can be found by exfoliating bulk graphite, but Bernal-stacked bilayer graphene is much more commonly found due to its more chemically stable arrangement of carbon atoms as well as being the stacking order for bulk graphite. Further, one typically wants a high degree of control over the twist angle as well as the ability to fabricate samples with a reasonable throughput, requiring a more directed approach than exfoliating and characterizing the stacking order of individual flakes. Fortunately, recently developed layer-transfer techniques enable the consistent fabrication of twisted bilayer graphene with $\simeq 0.1^\circ$ precision [36, 37].

2.4.1 Superlattice Structure

When two crystals of similar lattice constant are stacked on top of one another, an additional periodic modulation emerges beyond the periodicity of the individual crystals.

The new spatial modulation is often referred to as a *moiré* pattern.[1] Due the rotational misalignment (or different lattice constants), the local coordination of the atoms between layers varies over a long length scale λ compared to the atomic spacing. Here, we will only discuss the specific case of two monolayer graphene crystals with equal lattice constants rotated with respect to one another. In this case, atoms from both layers smoothly transition from AA sublattice coordination (in phase) in which the carbon atoms from the A sublattice in each layer are directly on top of one another to AB and BA stacking coordination (out of phase) in which the carbon atoms from the A and B sublattices are aligned on each layer. The coordination or the ionic lattices creates an effective electronic potential with the length scale λ. Although this interlayer potential is much weaker than the effect of the ionic potential within each single layer, it is sufficient to cause twisted bilayer graphene to take on markedly different properties from both monolayer and Bernal-stacked bilayer graphene.

Basic geometry reveals that the moiré wavelength is

$$\lambda = \frac{a/2}{\sin(\theta/2)} \tag{2.38}$$

where a is graphene's lattice constant $\simeq$2.46 Å and not the carbon-carbon bond length as used in the tight-binding section. The long wavelength spatial modulation is the two-dimensional analog of a beat frequency resulting from the addition of two sinusoids of different frequencies f_1 and f_2 such that they are close in value $|f_1 - f_2| \ll f_i$ as plotted in Figure 1-4. Figure 2-10 shows the moiré pattern for two monolayer graphene crystals at a variety of twist angles. For the smallest twist angle shown, 4°, the moiré wavelength $\lambda \approx 35$ Å. The twisted layers develop hexagonal plaquettes with unit cells of length λ. These additional periodic features are referred to as a superlattice, in which we can imagine the crystal being renormalized from scale $a \rightarrow \frac{a/2}{\sin(\theta/2)}$. This would be a very

[1] *Moiré* comes from the French term for double-layer silks which have been pressed to form a rippled pattern. The two silk layers have slightly different thread spacing arising from variations in the manufacturing process that produces a rippling effect on a long length scale compared to the thread spacing.

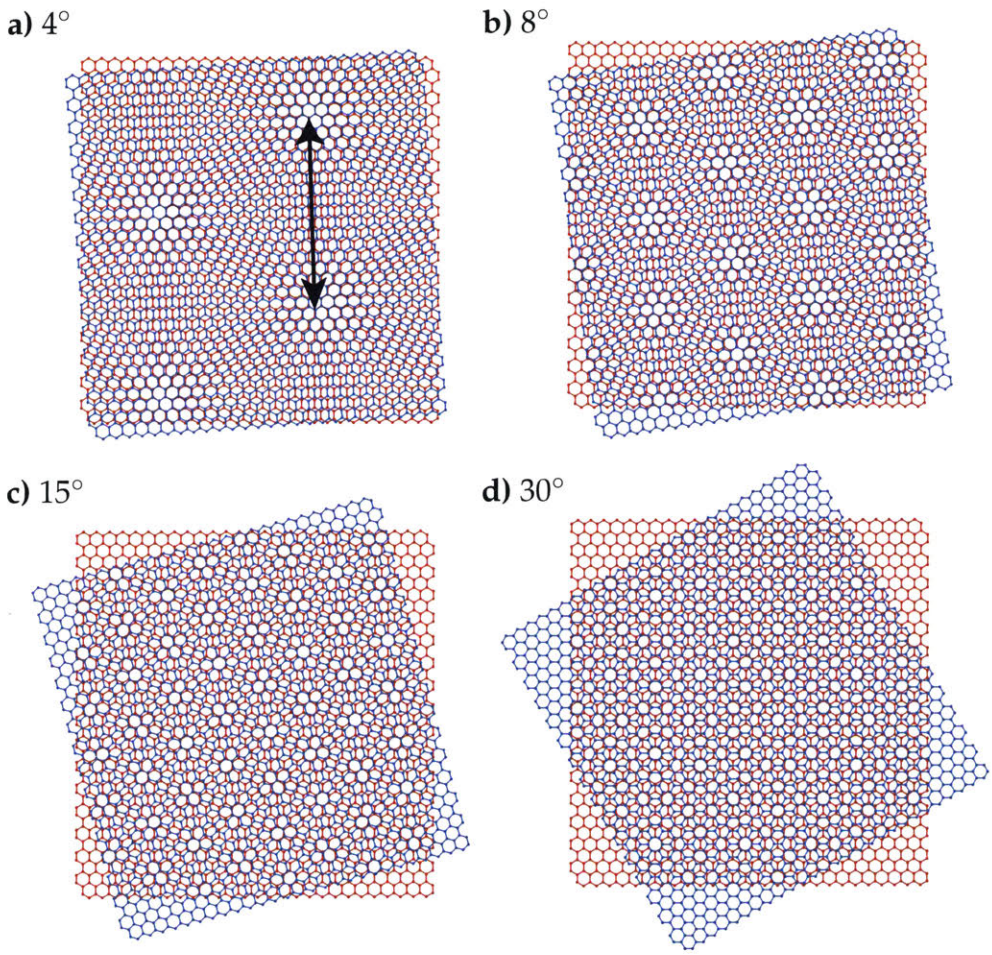

Figure 2-10: **Moiré patterns with different twist angle a)** $\theta = 4°$, the arrow indicates the moiré wavelength λ. **b)** 8° **c)** 15° **d)** 30°

complicated crystal to describe precisely—its unit cell would consist of approximately $(\lambda/a)^2 \sim 200$ graphene unit cells, making the type of analytical tight-binding model we considered previously unfeasible even if we only took into account the simplest nearest-neighbor hopping terms. Fortunately, there are advanced computational packages as well as simplifications that make band structure calculations tractable which will be discussed shortly. For the largest angle shown, 30° in panel **d**, the wavelength $\lambda \approx 5$ Å is on the order of the graphene latice constant. The periodic potential is much less dramatic and encompasses only about four graphene unit cells. In this limit, the superlattice only weakly competes with the monolayer graphene lattices of the constituent layers.

It turns out that not all rotation angles produce precise translational and rotational symmetry [38]. At an arbitrary twist angle we are not guaranteed to find primitive translation vectors that define the allowed symmetries of the superlattice. For these rotations, crystal momentum is not well defined and calculations that rely on Bloch waves become challenging. However, as discussed in subsection 2.4.3, at small twist angle, one can often find a true commensurate crystal at a rotation angle very close to an incommensurate one, allowing many of the essential physical properties of incommensurate crystals to be extrapolated from nearby commensurate orientations. Although the commensuration of the two crystals rapidly varies with arbitrarily small deviations in θ, physical properties should not change if one moves infinitesimally away from a particular commensurate angle. Additionally, at low twist angles one can develop a continuum model to study the low energy properties without regard to the commensuration of the superlattice [16].

2.4.2 Electronic Structure

Because there are two graphene layers, it may seem that Bernal-stacked bilayer graphene is the logical starting point for describing the band structure of twisted bilayer graphene. It turns out that decoupled monolayer graphene is a more useful point of departure for the range of twist angles we will be considering ($\gtrsim 1°$). To see this, consider starting

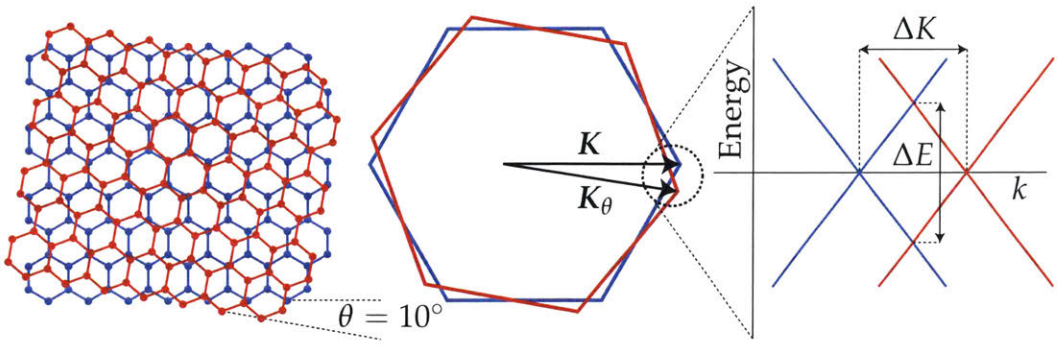

Figure 2-11: **Twisted bilayer experiences degeneracies** at positive and negative energies from each set of adjacent Dirac cones. Two crystals with a twist angle of 10° are shown. Here we consider the Dirac points at $\boldsymbol{K}$ and $\boldsymbol{K}_\theta$. The cones are displaced by ΔK and the degeneracies occur at $E_\pm = \pm\hbar v_\mathrm{F}\Delta K/2$.

with a larger twist angle θ, perhaps around 10° as shown in Figure 2-11. To zeroth order, we can consider the two monolayers to be fully decoupled. The two Brillouin zones of the monolayers will also be rotated by θ relative to each other like the real space lattices. The two Dirac cones near the K points are displaced by $\Delta K = 2K\sin(\theta/2) \simeq K\theta$. The pair of conduction and valence bands will intersect at $\pm\Delta K/2$ at energies given by $E_\pm = \hbar v_\mathrm{F} K\theta/2$ as plotted on the right in Figure 2-11. For the commonly used value of $v_\mathrm{F} \simeq 10^6\,\mathrm{m/s}$ [32] and $K \simeq 10^{10}\,\mathrm{m}^{-1}$, the degeneracy points are separated by $\Delta E \approx 1\,\mathrm{eV}$. This energy difference is extremely large compared to the range of Fermi energy typically accessed in experiments and we are justified in treating the Dirac cones in neighboring layers as decoupled.

At what rotation angle does this break down? The degeneracy at the Dirac points is protected by the inversion symmetry of the monolayer graphene, however, the degeneracies at $E_\pm$ are incidental degeneracies arising from the rotation angle and are not generally protected. Therefore, any interlayer coupling will have a tendency to gap out these degeneracies and modify the band structure in the process. If this interlayer coupling strength is small in comparison to $E_\pm$, then this will only have a weak, perturbative effect on the low energy physics. In Bernal-stacked bilayer graphene we saw that the low

energy bands were displaced by the dimerization hopping energy t_1 which we have previously approximated as $t_1 \simeq 0.4\,\text{meV}$ [13]. Without considering additional complexity, let us use t_1 as the interaction energy scale. By setting the interaction energy scale equal to the degeneracy energy difference ΔE we can solve for the θ at which competition between these energy scales becomes significant:

$$0.4\,\text{meV} \simeq t_1 \sim \Delta E = \hbar v_\text{F} K\theta. \tag{2.39}$$

These energy scales are roughly equal around $\theta \sim 3^\circ$. This crude estimate, which does not consider the specific form of interlayer hopping, agrees well with computational band structure calculations for low-angle twisted bilayer graphene that find an approximately monolayer, Dirac-like spectrum above $\sim 2^\circ$ [16, 39, 40]. Below this cutoff the twisted bilayer graphene spectrum is highly exotic and deviates in significant ways from both Bernal-stacked and large-angle twisted bilayer graphene.

Moiré Potential

At small twist angles, the Dirac cones are separated by small momenta and experience potentially large hybridization. One way of viewing this interlayer coupling is through Bragg scattering off of the superlattice cells. In an atomic lattice (non-superlattice), Bragg reflection of plane wave states occurs at the zone boundaries and high symmetry points of the Brillouin zone [20]. These scattering processes are responsible for generating standing waves at restricted momenta. In one dimension, with an ionic interaction of the form $U(x) = U_0 \cos(2\pi x/a)$, these standing waves produce two solutions $e^{ikx} \pm e^{-ikx}$ which either enhance or diminish the electron density over the positive ion cores, leading to an increase (U_0) or decrease $(-U_0)$ in kinetic energy and a band gap of $2U_0$. In a superlattice, the moiré pattern can be said to produce a *moiré potential* which generates coupling at the renormalized high symmetry points due to the superlattice of the form

$W(\boldsymbol{r}) = \sum_n w_n e^{-iG_n \cdot \boldsymbol{r}}$ which will open up gaps of the form $2w_n$ at high symmetry points of the superlattice where $|\boldsymbol{G}_n| \sim \frac{n}{\lambda}$.

Before discussing more advanced theoretical approaches, we can develop a simple model that accounts for some interlayer hybridization energy scale w related to interlayer tunneling t_1 which we will not specify in detail. In general, if we consider two linear bands which are degenerate at $k = k_0$ and energy E_0, the interaction w will open up an avoided-crossing. If there are no other energy bands nearby (and no symmetries which protect the degeneracy), we can consider the local two-band Hamiltonian in the basis (ψ_1, ψ_2) where ψ_1 and ψ_2 are the Bloch states for the lower and upper bands. Let the lower band ψ_1 have the form $E_1(k) = E_0 - \alpha|k - k_0|$ and the upper band have $E_2(k) = E_0 + \alpha|k - k_0|$. In the absence of interactions the Hamiltonian is simply given by

$$\mathcal{H}_0(k) = \begin{pmatrix} E_0 - \alpha|k - k_0| & 0 \\ 0 & E_0 + \alpha|k - k_0| \end{pmatrix}. \tag{2.40}$$

If we introduce the interaction energy $w \equiv \langle \psi_1 | \delta\mathcal{H} | \psi_2 \rangle$, the off-diagonal matrix elements are modified and the total Hamiltonian $\mathcal{H} = \mathcal{H}_0 + \delta\mathcal{H}$ becomes

$$\mathcal{H}(k) = \begin{pmatrix} E_0 - \alpha|k - k_0| & w \\ w & E_0 + \alpha|k - k_0| \end{pmatrix}. \tag{2.41}$$

We can solve for the new eigenspectrum to find

$$E_\pm(k) = E_0 \pm \sqrt{\alpha^2(k - k_0)^2 + w^2} \tag{2.42}$$

where at $k = k_0$ the two eigenstates are made up of symmetric and antisymmetric combinations of the original Bloch states $\psi_1 \pm \psi_2$. The modified bands close to k_0 are shown in Figure 2-12 (blue traces).

Utilizing this basic model, we can plot the band structure for two Dirac cones with

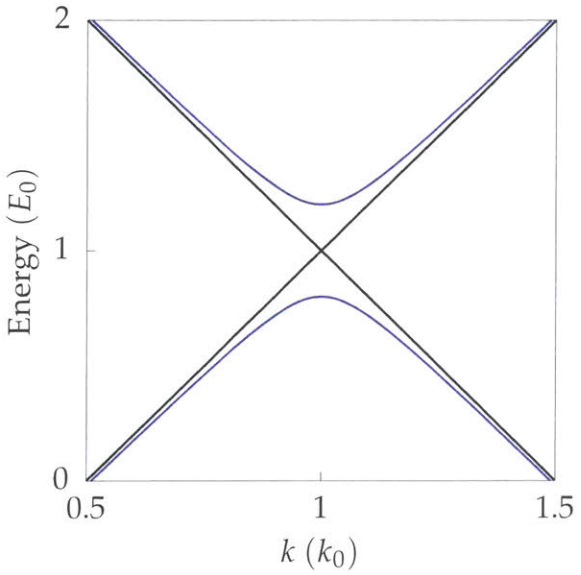

Figure 2-12: **Avoided crossing** resulting from the interaction $w \simeq 0.14\alpha k_0$. The original band structure (black traces) has a degeneracy at $k = k_0$ which is lifted by the interaction w to form an avoided crossing (blue traces).

fixed separation ΔK and vary the interaction strength w to consider its influence. As w becomes large $w \sim \Delta E$, the interlayer hybridization is no longer a simple perturbation and should be accounted for by a proper treatment of the Hamiltonian. Additionally, the Dirac cones become displaced and ultimately merge when $w = \Delta E$ which is not allowed without breaking additional symmetries. Despite these limitations, Figure 2-13 serves to illustrate the role that interlayer coupling w plays in the twisted bilayer band structure. At $w \ll v_F \Delta K$, it perturbatively decreases the dispersion between the two Dirac cones, slightly modifying the Fermi velocity. At $w \sim \Delta E$, the conduction and valence bands between the Dirac cones merge towards one another, strongly suppressing the Fermi velocity.

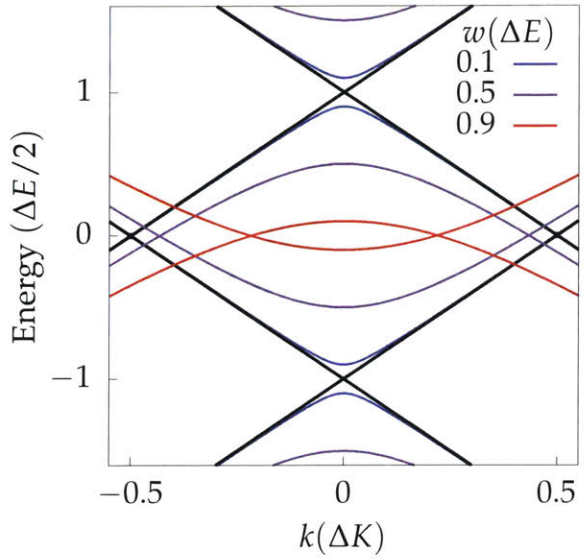

Figure 2-13: **The twisted bilayer dispersion flattens** as w is increased from $0.1\Delta E$ (blue traces) to $0.9\Delta E$ (red traces). The original uncoupled Dirac cones (black traces) are strongly modified even at low energy for sufficiently strong coupling.

2.4.3 Review of Single-Particle Band Structure Calculations

In the previous subsection, we applied very crude estimates and overextended perturbative approaches to gain insight into the qualitative behavior of twisted bilayer graphene. We were limited by both the relative complexity of the twisted bilayer graphene unit cell, containing potentially thousands of carbon atoms at small twist angles, as well as the fact that not all rotation angles result in commensurate superlattice cells with true translational and rotational symmetry, making tight-binding approaches difficult. Here, we will review some of the early computational and analytical work which placed the concepts previously alluded to on firmer footing (e.g. the renormalization of the Fermi velocity and the flattening of the low energy bands). More recent calculations and experiments have revealed significant differences from these early theoretical works and there is presently no widespread theoretical consensus on the correct approach to calculating the band structure. Nonetheless, there is insight to be gained from some of the early models.

Early *ab inito* density functional theory calculations focused on calculating the band structure for a few specific commensurate rotations [41, 42] at relatively large twist an-

glc. At the time of these calculations, unanticipated monolayer-graphene-like behavior in multilayer graphene grown on SiC [43] was not well understood. The observation of rotational misalignment of the top layer and accompanying calculations [41] helped to emphasize the degree to which a twisted sheet of graphene can decouple from its neighboring layers.

A later tight-binding analysis [39] that considered multiple commensurate rotations down to small twist angles of $\sim 3^\circ$ derived a continuum model for large twist angles in the limit of weak interplane coupling that showed a general trend in the renormalization of the Fermi velocity of the form

$$\frac{v^\star}{v_\mathrm{F}} = 1 - 9\left(\frac{t_1/3}{v_\mathrm{F}\Delta K}\right)^2 \propto 1 - \frac{1}{\theta^2}. \tag{2.43}$$

This formula is only applicable at large twist angle $\theta \gtrsim 10^\circ$ where the coupling t_1 can be considered perturbative. The authors of reference [39] were able to reduce the complexity of the calculation by Fourier expanding the interlayer hopping parameter $t(r)$ in units of the reciprocal lattice and considering the dominant terms. In previous calculations we have simply treated t_i as a constant and restricted its application to a particular hopping distance and orientation (intraplane or interplane hopping to neareast neighbors). Here, we allow it to take on a continuous range because the task of computing nearest-neighbor hopping for each atom within the moiré site is not defined by a constant interaction distance. Each atom in general experiences a slightly different nearest interplane neighbor due to the complex registration of atoms between each layer within the moiré cell. An important point is that interlayer tunneling of this form requires traversing a transverse distance $\delta(r)$ as well as the perpendicular interlayer distance (the van der Waals layer separation) $d_\perp \simeq 3.35\,\text{Å}$. Because $d_\perp$ is larger than the typical nearest neighbor transverse distance $\delta(r) \sim 1 - 2\,\text{Å}$, the hopping function $t(r)$, which decays exponentially with the interatomic distance, is dominated by length scales $\lesssim d_\perp$ and

falls off rapidly at larger values. Taking its Fourier expansion, $\widetilde{t}(\boldsymbol{G}) = \int d^2\boldsymbol{r} t(\boldsymbol{r}) e^{-i\boldsymbol{G}\cdot\boldsymbol{r}}$, the dominant components in momentum will have values $G \lesssim \frac{2\pi}{d_\perp} \approx \frac{2.7}{a}$ where a is the carbon-carbon bond length. In particular, the smallest reciprocal lattice vectors have the magnitude $|\boldsymbol{G}| = K = \frac{4\pi}{3\sqrt{3}a} \approx \frac{2.42}{a}$ which satisfy the condition $G \lesssim \frac{2.7}{a}$. Additional reciprocal lattice vectors of larger magnitude, such as $\frac{8\pi}{3\sqrt{3}a} \simeq \frac{4.84}{a}$ will have Fourier coefficients significantly smaller by at least a factor of 5 or more [39]. In contrast, a typical tight binding hopping parameter $t(r)$ for a monolayer crystal with no interplane coupling will have a typical length scale shorter than the atomic spacing a and its Fourier expansion will in turn be more spread out in momentum space than the case of twisted bilayer graphene (in general, greater localization in real space leads to greater extent in momentum space). Its expansion cannot be truncated at the smallest reciprocal lattice vectors unlike the unique case of interlayer tunneling.

In order to visualize the meaning of $\widetilde{t}(\boldsymbol{G})$ being dominated by the smallest reciprocal lattice vectors, we can consider the mini-Brillouin zone. Just as the crystal lattice becomes renormalized $a \rightarrow \frac{a/2}{\sin(\theta/2)} = \lambda$, the Brillouin zone of the atomic lattice is renormalized to a miniature momentum space of order λ^{-1}. The hexagonal mini-Brillouin zone emerges from the corners of the original rotated Dirac cones as shown in Figure 2-14. Momentum coupling $\boldsymbol{q}_1 = \boldsymbol{\Delta K}$ between the $\boldsymbol{K}_\mathrm{s}$ and $\boldsymbol{K}'_\mathrm{s}$ superlattice points hybridizes the two Dirac cones as shown with the green arrow on the right hexagonal zone. Additionally, the reciprocal lattice vectors of the original blue Brillouin zone link the equivalent $\boldsymbol{K}_\mathrm{s}$ points on the other two crystallographically equivalent vertices. Momentum coupling from $\boldsymbol{q}_2$ and $\boldsymbol{q}_3$ of the same magnitude as $\boldsymbol{q}_1$, but with different orientation, also contributes to hybridization. For an electron of momentum $\boldsymbol{k}$ near the $\boldsymbol{K}_\mathrm{s}$ point close to zero energy, hybridization strongly couples it to three electrons of momenta $\boldsymbol{k} + \boldsymbol{q}_i$ near the $\boldsymbol{K}'_\mathrm{s}$ point. These coupled electron are at significantly different energy, $v_\mathrm{F}\Delta K$. This is in stark contrast to the case of Bernal-stacked bilayer graphene which we can imagine as two uncoupled monolayers at a rotation angle of $\theta = 0$. Here, at electron near the $\boldsymbol{K}$ point with momen-

tum k is strongly coupled to another electron with very similar momentum and energy. This strong coupling in Bernal-stacked bilayer graphene is responsible for altering the band structure from linear behavior to quadratic at low momentum. In twisted bilayer, because the coupled electrons are at such different energies, the linear band structure is not strongly modified until small twist angle at which the energy difference between coupled electrons is of the same order as the hybridization strength.

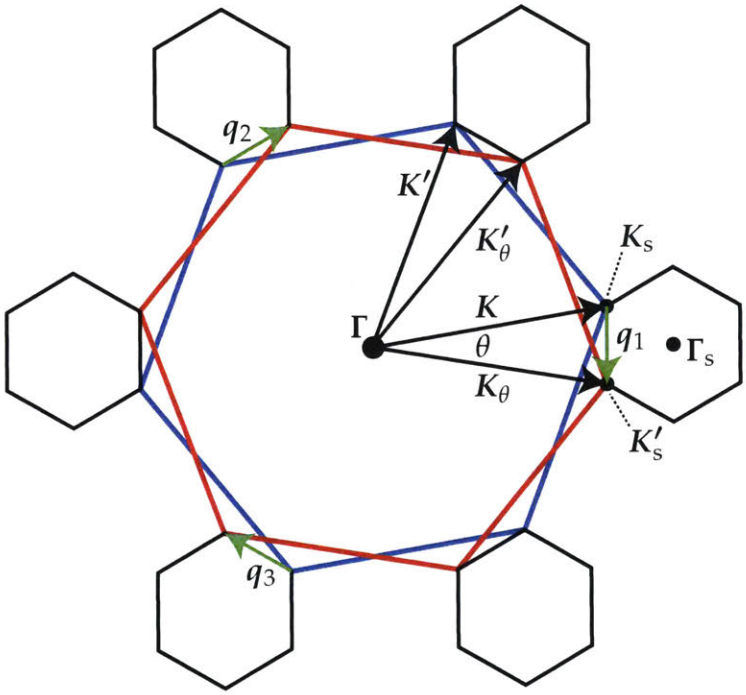

Figure 2-14: **The miniature Brillouin zone of twisted bilayer graphene** is constructed from the vector $\Delta K = K - K_\theta$. The miniature zone contains Dirac points K_s and K'_s. Momentum coupling q_1 between the Dirac points is indicated by the vertical green arrow on the right. By applying the reciprocal lattice vectors of the original blue Dirac cone, additional momentum coupling between the two other equivalent sites is shown with the additional green arrows. In principle, larger reciprocal lattice vectors can couple K_s and K'_s at additional momenta q_i but these additional momenta are found to be negligible [39].

Magic Angles

The main result of reference [39], the reduction of the Fermi velocity as twist angle decreases, stimulated other researchers to develop additional *ab initio* and tight-binding ap-

proaches for commensurate structures. References [44] and [40] both made the key observation that along with a small Fermi velocity, the entire bandwidth of the the valence and conduction band becomes very confined at small twist angle, with reference [44] observing strongly localized wave functions at small twist angle and reference [40] identifying non-monotonic behavior of the bandwidth at low twist angle, in contrast to the monotonic trend of the Fermi velocity at large twist angle from reference [39] $\frac{v^\star}{v_F} = 1 - 9\left(\frac{t_1/3}{v_F \Delta K}\right)^2$. The low energy bandwidth was found to reach a minimum at a critical angle $\theta_c \approx 1.5°$.

These insights set the stage for the more complete continuum model developed in reference [16] that was derived for all twist angles regardless of commensuration below about $10°$ and allowed for a continuous exploration of the band structure as a function of θ. The tight binding model was very similar to the one derived by reference [39] in which only the dominant Fourier components were retained. The key observation is that hopping at small values of momentum is locally periodic, allowing the construction of Bloch waves at all rotation angles. In qualitative agreement with reference [40], reference [16] calculated extremely confined low energy bands ($< 10\,\text{meV}$ separation) for a small twist angle of $1.05°$ where the Fermi velocity reaches exactly zero. Surprisingly, the authors observed that the Fermi velocity also vanishes for a large series of angles beneath the critical angle of $1.05°$ as $\theta \to 0$ as plotted in Figure 2-15. Lacking an analytical way to understand the emergence of this set of special angles, the authors referred to them collectively as the magic angles, a term that has proved enduring and come to signify any twisted bilayer graphene structure at small twist angle around $1.05°$ that exhibits the effects of strong bandwidth confinement. The next few magic angles in reference [16] are $\theta \approx 0.5°, 0.35°, 0.24°$, and $0.2°$. The existence of (approximately) flat bands has been confirmed experimentally for $\theta \sim 1°$ [17, 45], although, there is currently no experimental evidence for the existence of subsequent magic angles below $\sim 1°$.

This will conclude the discussion of the single-particle band structure of twisted bilayer graphene, but it is worth mentioning that recent experiments [17, 18] have indicated

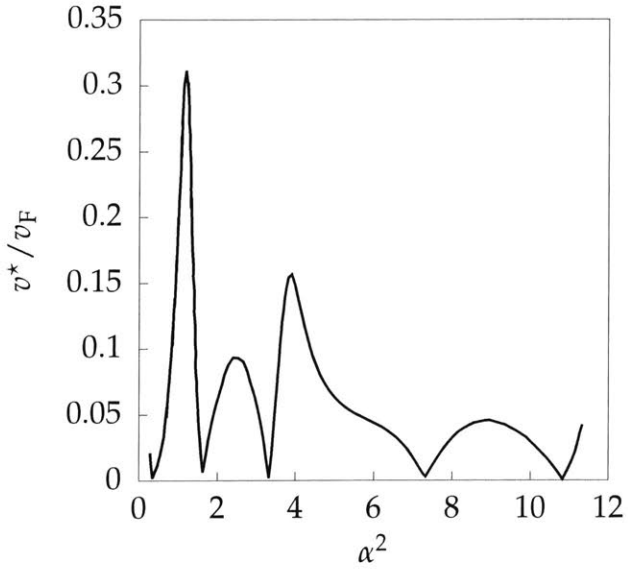

Figure 2-15: **Renormalized Fermi velocity** as a function of twist angle adapted from reference [16]. The angle θ is expressed in terms of $\alpha = w/\hbar v_\mathrm{F}\Delta K$. The renormalized Fermi velocity vanishes at the magic angles $\theta \approx 1.05°, 0.5°, 0.35°, 0.24°$, and $0.2°$.

that twisted bilayer graphene near the magic angle may host very exotic physics (Mott-like insulation and potentially unconventional superconductivity) arising from electron–electron interactions that go beyond the relatively simple single-particle calculations discussed so far. In order to understand these unconventional phases of twisted bilayer graphene, there has been renewed focus on calculating the single-particle band structure. Reference [17] utilized localized Wannier orbitals to calculate the single-particle band structure, however, recent theoretical works (e.g. references [46] and [47] among dozens) have called into question many of the calculations of the low twist angle band structure on the grounds that previous tight-binding and Wannier orbital approaches do not respect basic symmetries of the twisted bilayer graphene electronic system, precluding their accurate use in predicting the low energy physics. Even questions as to the correct tight-binding unit cell remain up for debate. Chapter 4 contains a longer discussion of current experimental results and will present capacitance measurements that shed light on recent theoretical proposals for the band structure as well as the nature of the exotic insulating phases.

2.4.4 Interaction Physics

The previous subsection placed large emphasis on the relative flatness of the low energy bands and the suppression of the Fermi velocity at that superlattice K_s points in the mini-Brillouin zone. The reader may wonder why flat energy bands are worth the numerous calculations and theoretical focus. In many materials such as conventional insulators, metals, or semiconductors away from the band edge, the interactions between electrons are very weak. This may seem counter-intuitive—a metal consists of a huge density of free electrons forming a Fermi sea that permeates the crystal lattice. It would seem that under such high charge densities the electrons would be strongly interacting with one another as compared to a dilute electronic system where electrons are spaced farther apart. The resolution of this puzzle is electronic screening. Just as a metal Faraday cage is capable of shielding its interior from an external electric field, the dense fluid of electrons surrounding any one electron shields it from the strong electric fields of the others further away. The Thomas–Fermi screening length for a metal is given by

$$\frac{1}{k_0} = \sqrt{\frac{2\varepsilon_0 E_F}{3e^2 n}}. \tag{2.44}$$

For a material such as gold with $n \sim 5\,\text{eV}$ and $n \sim 10^{28}\,\text{m}^{-3}$ this gives a screening length of about 1 Å. Thus, the large number of free electrons effectively shields each electron from the electric potential created by all of the other electrons. This means Coulomb repulsion between electrons is a negligible effect.

Strong screening, as in the case of a metal, simplifies band structure calculations considerably because we do not have to keep track of electron–electron interactions for Avogadro's number of electrons. We are able to compute the band structure as if only the electronic kinetic energy mattered, which was done in the tight-binding approach in subsection 2.2.3. In general, we can rephrase this discussion in terms of the competition between kinetic and potential energy. In a parabolic energy band the kinetic energy is

given by

$$T = \frac{\hbar^2 k^2}{2m} \tag{2.45}$$

and the potential energy by

$$V = \frac{e^2}{r} \tag{2.46}$$

we can make the substitution $r \sim \frac{1}{k} \sim n^{-1/3}$ to say that

$$\frac{V}{T} = \frac{e^2}{n^{-1/3}} \frac{2m}{\hbar^2 n^{2/3}} = \frac{2me^2 n^{-1/3}}{\hbar^2}. \tag{2.47}$$

Recall that the band mass for a parabolic system is given by

$$m = \frac{\hbar^2}{\partial^2 E / \partial k^2}. \tag{2.48}$$

If we identify $\partial^2 E / \partial k^2$ as the curvature of the band structure at the Fermi level, then our relationship tells us generically that interactions between electrons are strongest for flat energy bands with small dispersion. In the limit that the energy bands are flat, we expect strongly correlated physics to play a potentially pronounced role in stabilizing the ground state of the electronic system. There are many examples of flat electronic bands hosting strongly interacting physics. The application of a strong magnetic field to a two-dimensional electronic system leads to the formation of Landau levels that are very flat in momentum space. Landau levels are known to host phases such as the fractional quantum Hall effect [48–50], quantum Hall ferromagnetism [51, 52], and Wigner crystals [53, 54]. One advantage of studying interaction physics with twisted bilayer graphene is that the band structure's relative flatness can be tuned by careful stacking and relative rotation, offering a highly controllable platform for novel ground states.

2.5 Graphene in Strong Magnetic Field

2.5.1 Non-Relativistic Electrons

At high magnetic field, the previous tight-binding models no longer apply. The atomic lattice, which was the very starting point for the hopping picture we developed, turns out be negligible for the case of monolayer graphene. This is due to the fact that the typical length scale of the wave functions at high magnetic field scales as $l_{\mathrm{B}} = \sqrt{\frac{\hbar}{eB}} \simeq 26\,\mathrm{nm}/B[\mathrm{T}] \gg a$. Instead of adopting a lattice picture, we can simply solve the Hamiltonian of a free electron in magnetic field. The momentum $\boldsymbol{p}$ which entered the Schrödinger equation $\mathcal{H}_0$ must be modified to its gauge-invariant form $\boldsymbol{p} \to \boldsymbol{\Pi} = \boldsymbol{p} + e\boldsymbol{A}$. For non-relativistic electrons, the Schrödinger equation now reads:

$$\mathcal{H} = \frac{1}{2m}\boldsymbol{\Pi}^2 = \frac{1}{2m}\left(\boldsymbol{p} + e\boldsymbol{A}\right)^2 \tag{2.49}$$

where m is the band mass. If one uses the fact that $[x, p_x] = i\hbar$ and $\boldsymbol{\nabla} \times \boldsymbol{A} = \boldsymbol{B}$, it can be shown that Π_x and Π_y obey:

$$\left[\Pi_x, \Pi_y\right] = -ie\hbar B = -i\frac{\hbar^2}{l_B^2}. \tag{2.50}$$

Due to the fact that the $\frac{l_B}{\sqrt{\hbar}}\Pi_i$ satisfy canonical quantization and appear in quadrature in $\mathcal{H}_0$ like the simple harmonic oscillator, the problem can be solved easily using ladder operators:

$$a = \frac{l_B}{\sqrt{2}\hbar}\left(\Pi_x - i\Pi_y\right) \tag{2.51}$$

$$a^\dagger = \frac{l_B}{\sqrt{2}\hbar}\left(\Pi_x + i\Pi_y\right). \tag{2.52}$$

Therefore

$$\mathcal{H} = \hbar\omega_c \left(a^\dagger a + \frac{1}{2} \right) \tag{2.53}$$

and the spectrum takes the simple form $E_n = \hbar\omega_c \left(n + \frac{1}{2} \right)$. These states are indexed for $n = 0, 1, 2, \ldots$ and disperse linearly with magnetic field B.

2.5.2 Relativistic Electrons

For the case of Dirac electrons, we need the continuum approximation we derived earlier in Equation 2.27. Expanding around the K point we have:

$$\mathcal{H} = \begin{pmatrix} 0 & v_F(p_x - ip_y) \\ v_F(p_x + ip_y) & 0 \end{pmatrix}. \tag{2.54}$$

Using the same substitutions $p_i \to \Pi_i$ we find:

$$\mathcal{H} = \hbar\omega_c \begin{pmatrix} 0 & a \\ a^\dagger & 0 \end{pmatrix} \tag{2.55}$$

where we will redefine $\omega_c \equiv \sqrt{2} v_F / l_B$. Substituting a general eigenstate $\psi_i = \begin{pmatrix} u_i & v_i \end{pmatrix}^T$ and solving for the spectrum yields the equations

$$\hbar\omega_c a v_i = E_i u_i \tag{2.56}$$

$$\hbar\omega_c a^\dagger u_i = E_i v_i \tag{2.57}$$

$$\Rightarrow (\hbar\omega_c)^2 a^\dagger a v_i = E_i^2 v_i. \tag{2.58}$$

Exploiting the fact that oscillator states $|n\rangle$ satisfy $a^\dagger a|n\rangle = n|n\rangle$ we get

$$E_{\pm n} = \pm\hbar\omega_c\sqrt{|n|}. \tag{2.59}$$

We thus have states indexed for $n = 0, \pm1, \pm2, \ldots$ which disperse with $\sqrt{B}$ in contrast to the non-relativistic case. Plots of the spectra for the non-relativistic and relativistic cases are shown in Figure 2-16.

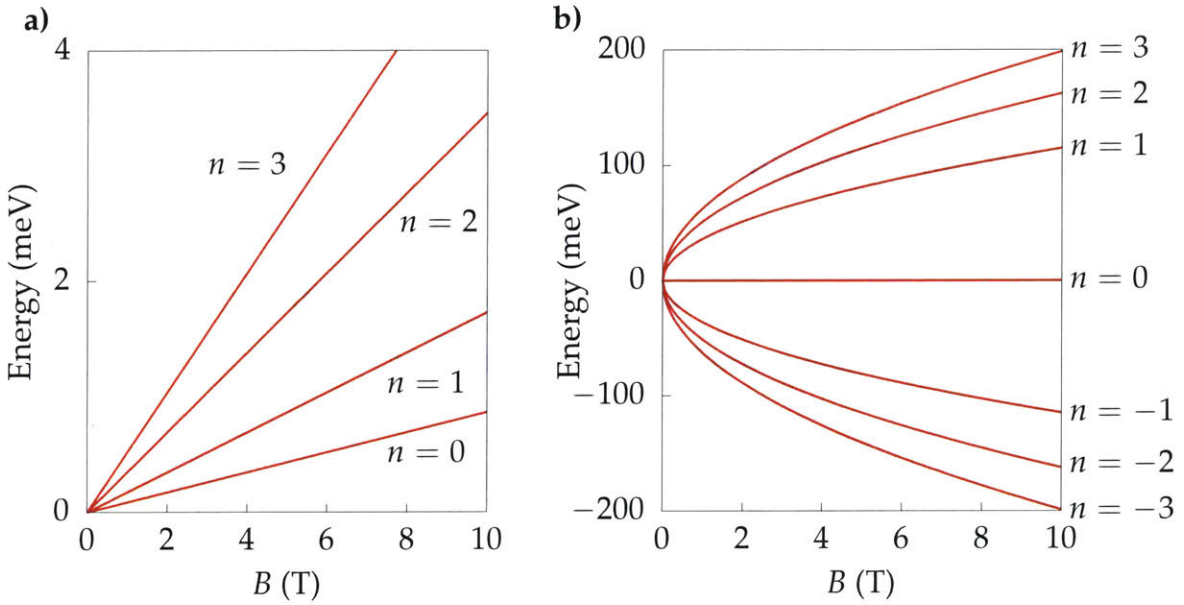

Figure 2-16: **The Landau level spectrum** is plotted for **a)** non-relativistic electrons using the conduction band mass of GaAs $0.067m_e$ [20] and **b)** relativistic electrons using the Fermi velocity $10^6\,\mathrm{m\,s^{-1}}$ [32].

2.5.3 Landau Fan Diagrams

For measurement techniques such as transport or capacitance, the Landau level spectrum is not directly accessed in excitation energy as displayed in Figure 2-16, but rather, properties of the Fermi level are monitored as either charge density is modulated or magnetic field modulates the Landau quantization energy. Despite naïvely expecting features which disperse with $\sqrt{B}$ for graphene, quantum Hall features take on linear trajectories

in magnetic field–gate voltage sweeps.[2] This is due to the fact that the movement of the chemical potential is sensitive to the carrier capacity of each Landau level which supports a universal number of orbital states independent of the host material. We can derive this result by considering the dependence of various integer filling factors (gapped phases) ν on the gate voltage and magnetic field. The filling factor is defined as the ratio of the number of electrons to the number of flux quanta:

$$\nu = \frac{N_{\text{el}}}{N_{\phi_0}} = \frac{nA}{BA/\phi_0} = \frac{\phi_0 n}{B} \tag{2.60}$$

and it is clear that ν depends linearly on the ratio $\frac{B}{n}$. We can convert to gate voltage via:

$$n = \int_0^V \frac{C_{\text{T}}}{Ae} dV' \tag{2.61}$$

where we integrate the total capacitance (including the quantum capacitance, see Chapter 3) across the gate voltage V which corresponds to the carrier density n. In the limit that C_{T} can be approximated by the geometric capacitance $C_{\text{T}} \approx C_{\text{geo}}$, we find

$$n \approx \frac{C_{\text{geo}} V}{Ae}. \tag{2.62}$$

Then we can say

$$\nu = \frac{\phi_0 C_{\text{geo}}}{Ae} \frac{V}{B}. \tag{2.63}$$

Therefore, as we add carriers to the system by changing V, the magnetic field at which the chemical potential lies in a gap at integer filling ν changes an amount proportional to the change in V. The final result is that the incompressible gapped phases of the quantum

[2]There are small deviations from linearity due to quantum capacitance contributions which reduce the rate at which charge enters the sample as a result of gating (see Chapter 3), however, most samples are dominated by the geometric capacitance to the nearby metallic gate. Then, quantum capacitance contributions can be safely ignored, resulting in essentially linear trajectories. Additionally, converting from gate voltage to carrier density results in exactly linear dependence in magnetic field–carrier density.

Hall regime take on linear trajectories labeled by integer ν. This result is independent of the host material due to the fact that all Landau levels hold a universal charge density. Although, it is worth mentioning that the specific integers ν at which cyclotron gaps occur depend on the non-orbital degeneracy factors like spin and valley. In graphene without additional symmetry-breaking terms (e.g. exchange gaps, see Chapter 4), the four-fold degeneracy of spin and valley generates cyclotron gaps at $\nu = \pm 2, \pm 6, \pm 10, \ldots$ whereas in GaAs the cyclotron gaps occur at $\nu = 2, 4, 6, \ldots$ due to the two-fold spin degeneracy. While the presence of the zero-energy Landau level in graphene (between $\nu = \pm 2$) is a unique property of the linear band dispersion close to $E = 0$, it is worth mentioning that GaAs (and other semiconductors) host similar hole-type Landau levels with cyclotron gaps corresponding to $\nu = -2, -4, -6, \ldots$ associated with the valence band. Unlike graphene, in which these two sets of Landau levels are accessible with an experimentally realizable range of gating, the two sets of Landau levels in GaAs are not typically accessible simultaneously due to the large band gap separating them which would require a prohibitively large gate voltage. Even if both sets of Landau levels were accessible, GaAs would lack a Landau level at $E = 0$ like graphene despite cyclotron gaps occurring between at $\nu = \pm 2$ in both systems.

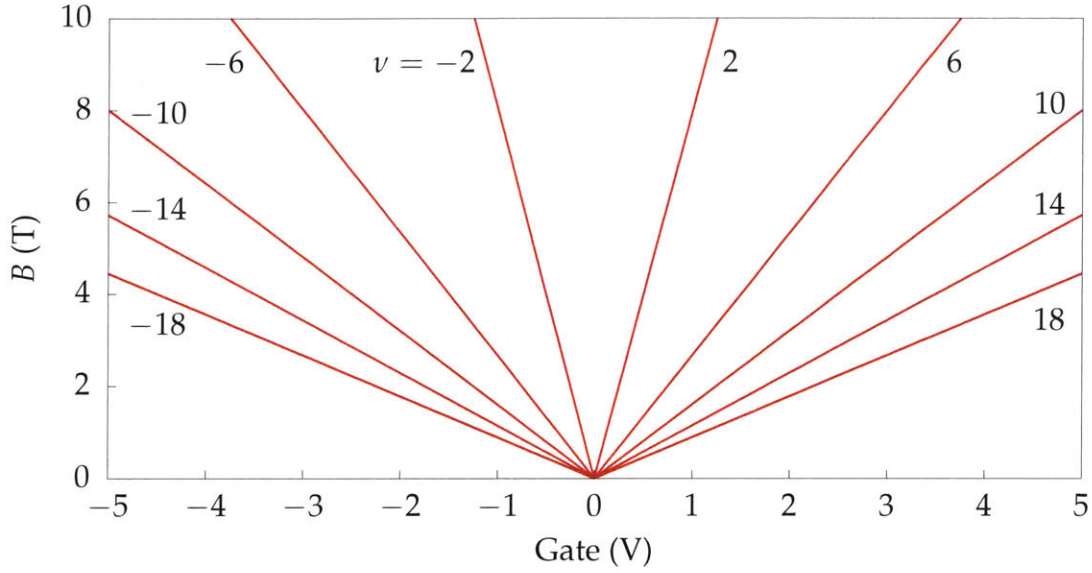

Figure 2-17: **Schematic showing monolayer graphene Landau fan** as a function of magnetic field B and gate voltage V under the approximation that the gate voltage is linearly proportional to carrier density. Trajectories of the cyclotron gaps at $\nu = \pm 2, \pm 6, \pm 10, \ldots$ are shown in red.

Chapter 3

Compressibility and Capacitance Measurements

3.1 Thermodynamic Relations

The field of thermodynamics is concerned with measuring equilibrium properties of large ensembles of particles. Here, we will be concerned with measuring the ground state of a large number of electrons by accessing their compressibility, a fundamental thermodynamic quantity which can be related directly to the free energy of the electronic system. Before discussing the electronic compressibility, it is useful to describe the more familiar *mechanical* compressibility

$$\kappa = -\frac{1}{V}\left(\frac{\partial V}{\partial p}\right)_{T,N} \tag{3.1}$$

which measures the relative change of an object's volume V in response to an applied pressure p while the temperature T and particle number N are fixed. (Here, V is used for full generality but may be replaced by the area for a two-dimensional system). An object which is easily deformed, such as a rubber ball, is characterized by a large compressibility whereas a rigid object, such as a tungsten rod, has a very small compressibility as shown

in the cartoon in Figure 3-1. The mechanical compressibility can be converted into an electronic compressibility with a few thermodynamic relationships. The Gibbs–Duhem equation constrains changes in the intensive variables μ, T, and p:

$$Nd\mu = Vdp - SdT. \tag{3.2}$$

For constant temperature we can say

$$\left(\frac{\partial\mu}{\partial p}\right)_T = \frac{V}{N} \Rightarrow \left(\frac{\partial\mu}{\partial(V/N)}\right)_T = \frac{V}{N}\left(\frac{\partial p}{\partial(V/N)}\right)_T. \tag{3.3}$$

Each side of the equation involves a derivative with respect to the reduced volume V/N. We are free to differentiate with either N or V held constant without affecting the relationship in Equation 3.3 [55]. We choose to hold V constant on the left to find

$$\left(\frac{\partial\mu}{\partial(V/N)}\right)_{T,V} = \left(\frac{\partial\mu}{\partial N}\right)_{T,V}\left(\frac{\partial N}{\partial(V/N)}\right)_{T,V} = -\frac{N^2}{V}\left(\frac{\partial\mu}{\partial N}\right)_{T,V}. \tag{3.4}$$

For the derivative on the right of Equation 3.3, we hold N constant to find

$$\frac{V}{N}\left(\frac{\partial p}{\partial(V/N)}\right)_{T,N} = \frac{V}{N}\left(\frac{\partial p}{\partial V}\right)_{T,N}\left(\frac{\partial V}{\partial(V/N)}\right)_{T,N} = V\left(\frac{\partial p}{\partial V}\right)_{T,N}. \tag{3.5}$$

Putting everything together yields

$$\frac{1}{\kappa} = -V\left(\frac{\partial p}{\partial V}\right)_{T,N} = \frac{N^2}{V}\left(\frac{\partial\mu}{\partial N}\right)_{T,V}. \tag{3.6}$$

In contrast to measuring relative changes in volume with respect to pressure, the electronic compressibility considers changes in the total particle number in response to changes in the chemical potential as shown in panels **c** and **d** of Figure 3-1. For an electronic system, this often amounts to asking the question: "How much charge enters a system if we increase its Fermi level slightly?"

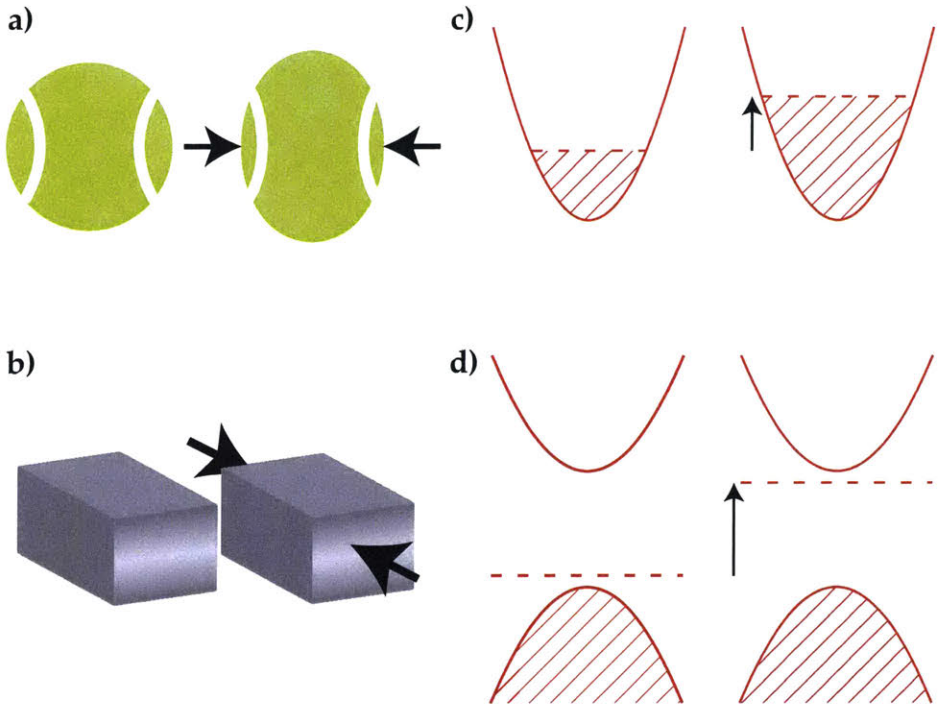

Figure 3-1: **Comparison of mechanical and electronic compressibility a)** A rubber tennis ball is highly mechanically compressible, deforming readily with a relatively small applied pressure. **b)** A rod of tungsten has low mechanical compressibility. **c)** When the chemical potential is in the middle of an energy band, raising the chemical potential $\delta\mu$ admits a relatively large number of additional carriers δn. It is highly electronically compressible. **d)** When the chemical potential is in a gap, raising the chemical potential $\delta\mu$ admits no additional electrons $\delta n = 0$. It has low electronic compressibility (highly incompressible).

It is worth emphasizing that κ, like heat capacity or magnetization, is considered a thermodynamic quantity because it can be related to a derivative of a thermodynamic potential. In this case, the Helmholtz free energy F is the appropriate potential for a constant temperature and volume:

$$F = U - TS \tag{3.7}$$

$$\Rightarrow dF = TdS - pdV + \mu dN - TdS - SdT \tag{3.8}$$

$$= -SdT - pdV + \mu dN \tag{3.9}$$

where we have used the first law of thermodynamics $dU = TdS - pdV + \mu dN$. We can identify the chemical potential with

$$\mu = \left(\frac{\partial F}{\partial N}\right)_{T,V} \tag{3.10}$$

which implies

$$\frac{1}{\kappa} = \frac{N^2}{V}\left(\frac{\partial^2 F}{\partial N^2}\right)_{T,V}. \tag{3.11}$$

In the context of solid state physics, κ is more conveniently expressed in terms of μ and electron density $n = \frac{N}{V}$:

$$\kappa = \frac{1}{n^2}\left(\frac{\partial n}{\partial \mu}\right)_{T,V}. \tag{3.12}$$

Moreover, the prefactor is often dropped and the compressibility becomes synonymous with the thermodynamic density of states:

$$\kappa \propto \frac{\partial n}{\partial \mu}. \tag{3.13}$$

We will frequently refer directly to $\frac{\partial n}{\partial \mu}$ as the compressibility and often we will use the

terms *compressible* or *incompressible* to signify an electronic phase which has a relatively large or small thermodynamic density of states, respectively.

3.2 Thermodynamic Density of States

Along with the band structure, the thermodynamic density of states is one of the most fundamental quantities describing an electronic system. For example, the existence of gaps in the density of states and their relation to the chemical potential determine if a material is electrically insulating or conducting. The thermodynamic density of states measures the shift in the chemical potential upon adding additional electrons. If electron–electron interactions can be ignored, this quantity is intuitively related to the number of available electronic states at the Fermi level. As we add charge, Pauli exclusion forces us to add electrons only to the unoccupied states immediately above the Fermi level. If the system has a large degeneracy at the Fermi level, perhaps in a metal or the middle of a Landau level, then electrons can occupy states which are very close in energy to μ. Then, the change $\delta\mu$ upon adding δn electrons is very small making the compressibility $\kappa \propto \partial n/\partial\mu$ very large. On the other hand, if the Fermi energy is in the middle of a band gap, such as in the case of a band insulator, the Fermi level is forced to rise rapidly in order to access available states. In this situation the shift $\delta\mu$ after adding δn electrons is large and $\kappa \propto \partial n/\partial\mu$ is very small.

3.2.1 Comparison to Single-Particle Density of States

The thermodynamic density of states must be contrasted with the *single-particle* density of states. The thermodynamic density of states asks: "How much energy $\delta\mu$ does it cost to add δn electrons *after* waiting for the system to relax and return to equilibrium?" The key point is that the electrons are being added in the adiabatic limit, permitting the rest of the electrons already present to rearrange in order to find a new ground state. The single-

particle density of states asks: "If I suddenly add an electron of energy $\Delta E = E - E_F$ away from the Fermi level, how many available electronic states exist at ΔE?" The system is *not* allowed to relax. The capacitance measurements in Chapter 4 will relate to the slow, equilibrium charging of electronic systems characterized by the thermodynamic density of states. The electron tunneling measurements in Chapter 6 will describe the sudden electron addition related to the single-particle density of states.

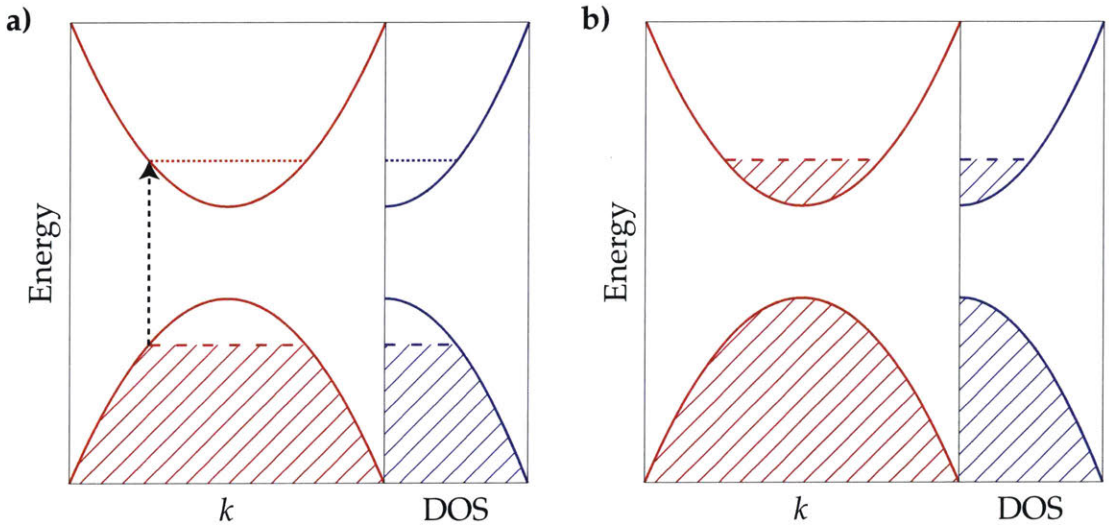

Figure 3-2: **Density of states without electron–electron interactions** In the absence of interactions, **a)** placing the Fermi level at E_0 and measuring the spectral (single-particle) density of states at $E_0 + E_1$ is equivalent to **b)** measuring the thermodynamic density of states while the Fermi level is at $E_0 + E_1$.

In the absence of electron–electron interactions, the two quantities can be easily related to one another. Imagine we perform a tunneling measurement where we fix the Fermi level at E_0 and tunnel up in energy to the unoccupied states at $E = E_0 + E_1$, measuring the density of states $g(E_0 + E_1)$ as shown in panel **a** of Figure 3-2. If we were to then move the chemical potential from $E_0 \rightarrow E_0 + E_1$, and measure the thermodynamic density of states $\partial n / \partial \mu$ as shown in panel **b**, the two quantities would be equivalent. The equivalence is made possible by the assumption that the band structure remains constant as we tune the electron density.

When electron–electron interactions are present, the situation is more complicated. As discussed in subsection 2.4.4, Coulomb interactions between electrons are often highly dependent on the electron density and curvature $\frac{\partial^2 E}{\partial k^2}$ of the band structure. As a result, the relative importance of electron–electron interactions may change as one tunes the carrier density. We no longer have a static band structure which can simply be filled or depleted of electrons. The band structure becomes dynamic and electron–electron interactions can strongly modify both the Fermi level physics and to a lesser extent, the physics of the excitation spectrum at energies far from the Fermi level. Here, it is not possible to equate $\partial n/\partial \mu$ with the number of available energy levels. In this situation of course, $\partial n/\partial \mu$ still rigorously defines the energy cost of adding charge, but its connection to the single-particle density of states breaks down. Figure 3-3 demonstrates this effect schematically by considering a spectral measurement that accesses an electron at an energy away from the Fermi level which lies in a band gap in panel **a**. Generally, electron–electron interactions are negligible if a band is completely empty, as there is no charge available to experience a Coulomb force. And if we consider a fully occupied band as behaving like a completely empty hole energy band, then the same analysis applies. When energy bands are partially filled, if non-orbital degrees of freedom are available such as spin or valley, the orbital degrees of freedom may find it energetically favorable to rearrange their energy hierarchy in order to minimize Coulomb repulsion, as in the case of a quantum Hall ferromagnet. This situation is generically shown in panel **b** where a gap at the Fermi level opens up when at partial-filling of the conduction band. This gap differs from the band gap, which arises from electron–ion interaction and is a single-particle effect.

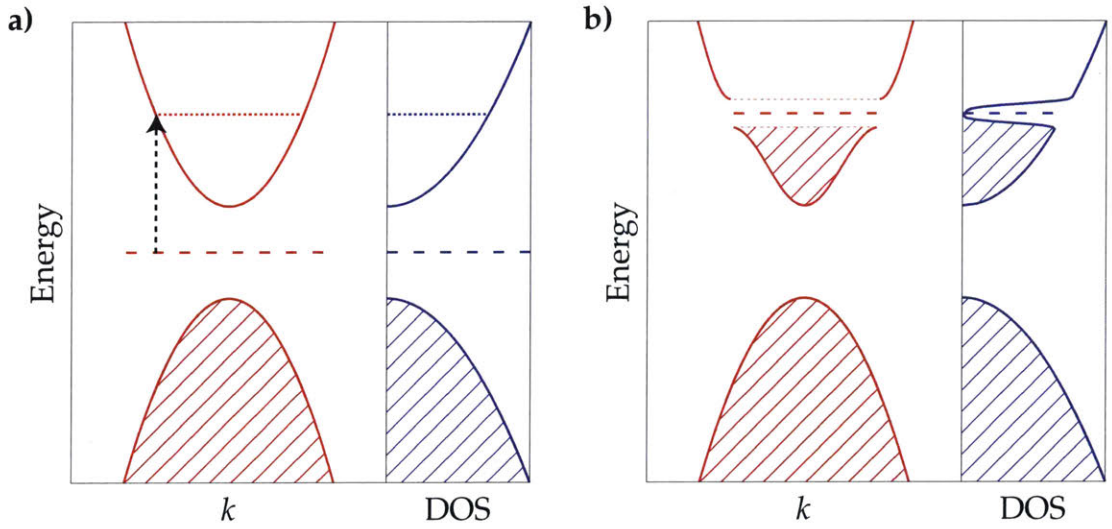

Figure 3-3: **Density of states with electron–electron interactions** Electron–electron interactions modify the band structure as the chemical potential shifts. In **a)**, placing the Fermi level within a band gap and exciting to the middle of the empty conduction band reveals a predictable parabolic dispersion. In **b)**, a many-body energy gap may be opened up around the Fermi level while it is at a particular location due to density-dependent interactions. The thermodynamic density is significantly reduced due to the presence of an energy gap at the Fermi level.

3.3 Capacitance

3.3.1 Metallic Electrodes

It turns out that the capacitance between a two-dimensional material and a nearby metallic electrode is intimately related to the electronic compressibility. Before discussing the capacitance between objects with finite density of states, this subsection will review the capacitance between two pieces of metal.

Any two pieces of metal have a mutual capacitance which defines their propensity to accumulate charge in response to an applied voltage difference $Q = CV$ where Q, taken to be positive, is the net excess accumulated charge on one of the capacitor plates, V is the voltage applied across the structure, and C is the mutual capacitance coefficient. The linear charge–voltage relationship ultimately relates back to superposition. If building up charge Q_0 induces a voltage V_0 between two metal objects, then by doubling the charge density to $2Q_0$, we must also find $2V_0$ in response. The capacitance is entirely determined by the geometric distribution and orientation of the two pieces of metal as well as the dielectric environment. The geometric dependence arises from the inverse-square Coulomb force and the ability of metals to create a perfect equipotential on their surface due to the large density of mobile charge. Free electrons on the surface of a metal will easily spread out to null any voltage difference which builds up along the tangential direction of the surface. After reaching equilibrium, it will turn out that sharp and highly confined regions attract a higher proportion of the total charge density due to the spatial confinement from the rest of the electron sea that these regions confer. These confined regions build up a larger, costly electric field density as a result, causing the geometry to play the key role in determining the ultimate charge capacity.

It is worth stressing that the internal electronic structure of the metal is irrelevant. When capacitors are described in classical electrostatics, the particular metallic material—gold, brass, aluminum, etc. are not typically specified. This (very good) approximation,

is due to the fact that the densities of states of metals are effectively infinite. What does *effectively* mean here? Consider two pieces of gold forming a parallel plate capacitor in vacuum

$$C = \frac{\epsilon A}{d} \tag{3.14}$$

where ϵ is the vacuum permittivity, A the lateral area, and d the plate separation. As we apply a voltage δV across the capacitor, the charge $\delta Q = C\delta V$ accumulates. The charge accumulates across the lateral area as well as a depth of approximately a few Fermi wavelengths $\lambda \sim n^{-1/3}$ where n is the total electron density. For gold (a few) $\lambda \sim 1\,\text{nm}$. The induced carrier density is then

$$\delta n = \frac{\delta Q}{e\lambda A} = \frac{C\delta V}{e\lambda A} = \frac{\epsilon \delta V/d}{e\lambda}. \tag{3.15}$$

The density of states can be approximate by

$$\frac{\partial n}{\partial \mu} \sim \frac{n}{E_\text{F}} \sim 10^{28}\,\text{eV}^{-1}\,\text{m}^{-3} \tag{3.16}$$

where E_F is the Fermi energy of gold. We are free to vary the separation d. We can consider an extreme limit by letting $d = 1\,\text{nm}$, then this yields

$$\frac{\delta \mu}{e\delta V} = \frac{\partial \mu}{\partial n}\frac{\delta n}{e\delta V} = \frac{\partial \mu}{\partial n}\frac{\epsilon/d}{e^2\lambda} \sim 5 \times 10^{-3}. \tag{3.17}$$

For every volt we apply across the capacitor, the chemical potential only rises by a few meV which constitutes a change of a few parts in a thousand of the Fermi energy of gold. This is a negligible change, and importantly, the value of the compressibility in gold will be virtually unchanged as the chemical potential moves by minuscule amounts, ensuring that any shift in the expected charging rate of the capacitor due to chemical

potential drift is constant over any reasonably accessible voltage range. Furthermore, the value of $d = 1\,\text{nm}$ is unphysical for most situations—electron tunneling and then vacuum breakdown would occur at relatively small voltage ranges (<1 V), effectively shunting the capacitor. If we had used a more reasonable 10 nm the effects described above would have been proportionally weaker.

3.3.2 Quantum Capacitance

The preceding analysis suggests a useful way of thinking about capacitance. Whenever a voltage is applied across a capacitor, it supplies a certain amount of energy which can do work on the system. The voltage can transfer charge density in order to set up an electric field, but in so doing, it must spend some of its energy allotment on changing the Fermi level in the plates. For materials such as metals which have a very large density of states, the quantum mechanical cost to increase or decrease the Fermi level is very small in comparison to the purely electrostatic cost of charging. However, in many materials, the density of states can be quite small in relation to the ease of charging, making the chemical potential shift significant upon applying voltage. Even if the shift in chemical potential remains a small perturbation on the roughly linear charging rate, the chemical potential shift will be strongly dependent on the gate and magnetic field, making observation of relative changes in the compressibility viable. As will be clear below, this chemical potential shift manifests as a contribution to the capacitance signal which can be measured and related to the compressibility of the electronic system.

Let us take a parallel plate capacitor with one ideal metallic plate with an infinite density of states and the other plate made from monolayer graphene as shown in panel **a** of Figure 3-4, however, it could be any other electronic system with finite density of states. We ground the graphene through an ohmic contact at the boundary and apply a voltage δV to the metal plate which creates a total electrochemical difference of $e\delta V$ across the capacitor as shown in panel **c**. If we imagine taking a test charge $-e$ and moving it from

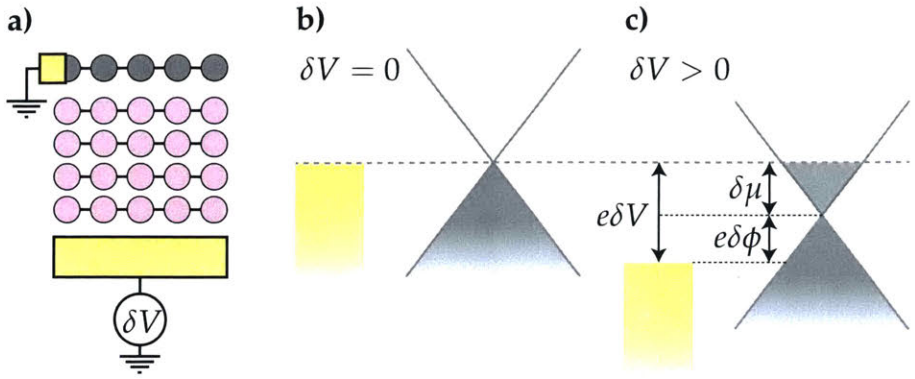

Figure 3-4: **Quantum capacitance schematic a)** A layer of monolayer graphene (gray) is separated by and insulator (pink) from a metal gate (gold). A voltage δV is applied between the gate and an ohmic contact to the graphene. **b)** If $\delta V = 0$, the gate and graphene are in electrochemical equilibrium (we assume no work function difference). **c)** If $\delta V > 0$, the gate and graphene acquire an electrochemical difference of δV. The gate is brought below a ground reference by an amount $e\delta V$. This is composed of two contributions: the electrostatic potential $e\phi$ and the change in chemical potential $\delta\mu$ where μ is referenced from the charge neutrality point.

ground through the voltage source, across the geometric capacitance, raise the chemical potential of the material by $\delta\mu$, and exit back to ground through the ohmic contact, we will have completed a full loop with no net work. Recording the energy at each section we find

$$0 = -e\delta V + e\delta\phi + \delta\mu \tag{3.18}$$

where $\delta\phi$ is the change to the electrostatic potential of the graphene due to its accumulated charge and geometric capacitance $\frac{\delta Q}{C_{\text{geo}}}$. We can think of this equation as describing the energy cost associated with charging the graphene with δQ. We must pay the potential energy cost $e\delta\phi$ as well as the quantum kinetic energy cost within the material $\delta\mu$. We can reorganize this to show

$$\frac{\partial\mu}{\partial V} = e\left(1 - \frac{1}{C_{\text{geo}}}\frac{\partial Q}{\partial V}\right). \tag{3.19}$$

Previously we have defined capacitance in terms of the ratio of charge to voltage $C = \frac{Q}{V}$, however, for our purposes it makes sense to define a differential capacitance $C_T = \frac{\partial Q}{\partial V}$ in terms of the total charge modulated as a function of the voltage V. We can expand this

$$C_T = \frac{\partial Q}{\partial V} = \frac{\partial Q}{\partial \mu}\frac{\partial \mu}{\partial V}. \tag{3.20}$$

In an effort to connect with the compressibility $\frac{\partial n}{\partial \mu}$ we can convert from charge units to density: $\delta Q = eA\delta n$ where A is the lateral area of the capacitor. With the help of Equation 3.19 the total capacitance can be expressed as

$$C_T = e^2 A \frac{\partial n}{\partial \mu}\left(1 - \frac{C_T}{C_{geo}}\right). \tag{3.21}$$

We can solve for C_T to find

$$\frac{1}{C_T} = \frac{1}{C_{geo}} + \frac{1}{Ae^2\partial n/\partial \mu} \tag{3.22}$$

$$\equiv \frac{1}{C_{geo}} + \frac{1}{C_q} \tag{3.23}$$

where we have defined the term directly proportional to the compressibility $Ae^2\partial n/\partial \mu$ as the *quantum capacitance* [11]. Although this term has been expressed as a capacitance, it is important to remember that it arises merely from conservation of energy and the closed equipotential paths of the circuit. The fact that the geometric and quantum capacitances add in reciprocal tells us that the quantum capacitance acts like a fictitious capacitance that is in series with an ideal geometric capacitance. This term obviously plays a large role in any direct measurement of the total capacitance of a system with finite density of states, however, it is always present whenever a two-dimensional system is gated. Even in transport measurements where the capacitance is not measured, the charge density of a two-dimensional structure is modulated by the field effect, and the quantum capacitance affects the rate at which an applied gate voltage adds charge to the system. Typically

experimentalists make the approximation $eA\Delta n = C_{\text{geo}}\Delta V$ which is only ever approximately true. Whenever a parallel-plate capacitor is gated, the relationship

$$\frac{1}{C_{\text{T}}} = \frac{\partial V}{\partial Q} = \frac{1}{C_{\text{geo}}} + \frac{1}{Ae^2\partial n/\partial\mu} = \frac{1}{C_{\text{geo}}} + \frac{1}{C_{\text{q}}} \tag{3.24}$$

holds. In the example above, we considered a metal gate and graphene where $\partial n/\partial\mu$ referred to graphene's thermodynamic density of states in order to emphasize the role of quantum capacitance in a material with small density of states. However, this relationship is entirely general and we could have swapped out the graphene for another metal. In this situation, $\partial n/\partial\mu \gg C_{\text{geo}}/Ae^2$ for typical values of C_{geo} so that

$$\frac{1}{C_{\text{T}}} \approx \frac{1}{C_{\text{geo}}}. \tag{3.25}$$

Lurking beneath many of these approximations and assumptions about the size of the compressibility of metals is the implicit assumption that the typical area-normalized geometric capacitance $C_{\text{geo}}/A \ll e^2C_{\text{q}}$. Whether or not a two-dimensional system will have a large (irrelevant) quantum capacitance is only defined in relation to the other capacitance scale in the system, C_{geo}. It is easy to construct a metal–graphene parallel plate capacitor so that the ratio $\frac{C_{\text{geo}}}{C_{\text{T}}}$ is arbitrarily close to 1 by adjusting the ratio ϵ/d. We can explicitly calculate the ratio for parallel plate capacitance:

$$\frac{C_{\text{geo}}}{C_{\text{T}}} = 1 + \frac{C_{\text{geo}}}{C_{\text{q}}} = 1 + \frac{\epsilon}{de^2\partial n/\partial\mu}. \tag{3.26}$$

The area has dropped out since it is both proportional to the geometric capacitance as well as the total charge which is brought into the material as a result of $eA\,(\partial n/\partial\mu)\,\delta\mu$. However, the length scale d plays a large role through the ratio ϵ/d. If we increase the geometric capacitance through adjusting ϵ or d, then eventually $C_{\text{geo}} \sim C_{\text{q}}$ and both will be strong contributions to C_{T} as shown in Figure 3-5.

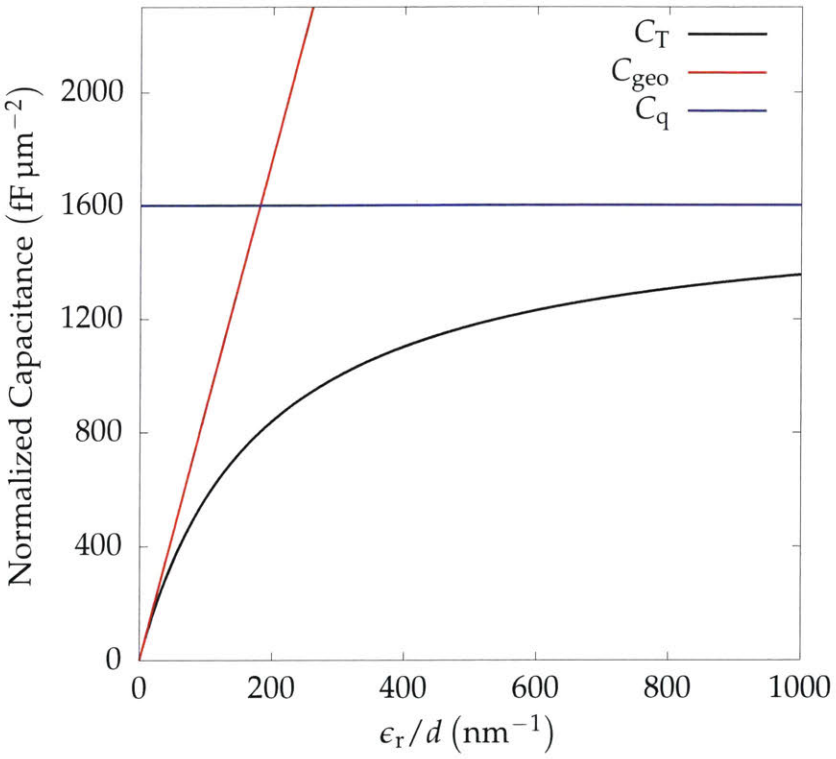

Figure 3-5: **The relative importance of the quantum capacitance** scales with the geometric parameters ϵ_r/d. Here, the area-normalized quantum capacitance of gold $\sim$1600 fF µm^{-2} is plotted along with the area-normalized geometric and total capacitances as a function of ϵ_r/d, the ratio of the relative permittivity and dielectric thickness in inverse nanometers.

Circuit Perspective of Quantum Capacitance

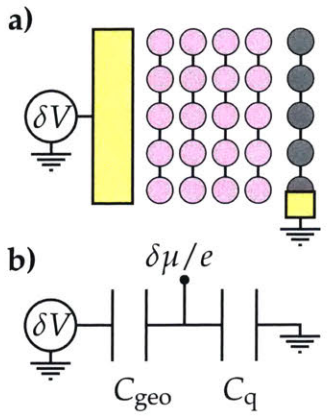

Figure 3-6: **Representation of quantum capacitance in a circuit a)** A piece of metal (gold) separated from graphene (gray) by a dielectric (pink) creates a parallel-plate capacitor. **b)** The parallel-plate geometry can be decomposed into two contributions: the geometric capacitance and the quantum capacitance. The chemical potential chang $\delta\mu$ can be represented as a voltage $\delta\mu/e$ between the geometric and quantum capacitances.

Equation 3.22 encourages treating the quantum capacitance as a genuine circuit element. We can think of any single parallel plate structure as consisting of a geometric and quantum capacitance contribution as shown in Figure 3-6. The task of computing the chemical potential change in response to an applied voltage reduces to solving a basic capacitive voltage divider:

$$\frac{\delta\mu/e}{\delta V} = \frac{C_{geo}}{C_{geo}+C_q} \tag{3.27}$$

$$= 1 - \frac{C_T}{C_{geo}}. \tag{3.28}$$

If $C_q \to \infty$ (as in a perfect metal), $\delta\mu \to 0$ as expected. Equation 3.28 is particularly useful. The gate-dependent (and possibly complicated) quantum capacitance does not need to be measured directly in order to compute changes in the chemical potential.

The (Electro)-Chemical Potential: A Tedious Digression

In subsection 3.3.2 we have used the term μ to define the chemical potential of the electronic system. In the fields of condensed matter physics, semiconductor physics, and electrochemistry there are several different definitions of chemical potential. In this thesis, we will always refer to μ as the energy of the highest occupied electron (or appropriate location within an energy gap so that μ is the 50% electron occupation probability according to the Fermi–Dirac distribution) which is frequently defined with respect to a band minimum (in the case of a semiconductor) or charge neutrality point (in Dirac-like systems). It will not mean the electrochemical potential which will be specified by $\mu_{\text{e-ch}}$ to avoid confusion. At zero temperature, μ is equivalent to the Fermi level E_{F} relative to the band minimum or charge neutrality point. Because the measurements described in Chapter 4 occur at low temperature, we will interchangeably use μ and E_{F}.

In section 3.1 we discussed the concept of electronic compressibility from a careful set of thermodynamic relationship. In an effort to avoid any confusion, care should be taken to distinguish the thermodynamic equilibrium of the full capacitor system which yielded $e\delta V = e\delta\phi + \delta\mu$ and the sense in which $\partial n/\partial\mu$ is an equilibrium thermodynamic property. The proper choice of chemical potential for the full capacitor structure which satisfies the first law of thermodynamics, $dF = \mu dN$ at constant temperature and volume, is the electrochemical potential $\mu_{\text{e-ch}}$. If the circuit were not at electrochemical equilibrium, then the voltage source and potentials would redistribute electrons to make it so. In the previous treatment, the difference of the electrochemical potential of the metal and graphene was given by the external voltage $\delta\mu_{\text{e-ch, graphene}} - \delta\mu_{\text{e-ch, metal}} = e\delta V = e\delta\phi + \delta\mu$. We assume that the electrochemical potential of the metal is fixed at ground. Then, $\partial n/\partial\mu_{\text{e-ch, graphene}} \propto \partial n/\partial V \propto C_{\text{T}}$ which is *not* equivalent to the compressibility $\partial n/\partial\mu$ which is defined with respect to the chemical potential. The resolution lies in realizing that the definition of the compressibility $\partial n/\partial\mu$ as a thermodynamic quantity assumes the electronic system is isolated from any external potentials. In this case $\mu = \mu_{\text{e-ch}}$

is the the amount the internal energy is raised by adding one electron. We can use a capacitor structure that is in electrochemical equilibrium with an external voltage source to access the compressibility $\partial n/\partial \mu$ which is a thermodynamic quantity of the isolated two-dimensional system.

3.4 Measurements Scheme

The task of accessing the compressibility can be boiled down to measuring the capacitance C_T and using the established relationships to extract C_q which is defined by the compressibility. It turns out that measuring the capacitance to the resolution required in this thesis is no simple task. Fortunately, there are a set of established techniques for measuring high-resolution capacitance signals at cryogenic temperatures [56] which we will now review.

3.4.1 Limitations of Basic Transport-Style Scheme

The simplest approach to measuring a device with an unknown impedance Z is to simply source a voltage across it and measure the current I running through it as done in typical electron transport. Using Ohm's law $V = IZ$, the impedance can be simply related. First, let us imagine $Z \approx R$ (any capacitive or inductive terms are small). If we decide to place the device in a cryostat, we will need some long cabling which will add line resistance. Additionally, there may be significant contact resistance where ohmic contacts connect with van der Waals or semiconductor materials at low temperature. These parasitic resistances can be lumped together as a term R_{par} for each line. We assume the measurements are carried out at DC or very slow AC excitations V so that rotations arising from the capacitance of the measurement lines to ground can be neglected. The total impedance

inferred from a two-terminal measurement will be

$$Z = R + 2R_{\text{par}}. \tag{3.29}$$

Typically the $2R_{\text{par}}$ term is a simple additive contribution which shifts the baseline. Importantly, the parasitic elements add to the sample impedance in series, often only slightly modifying the signal which is measured at room temperature in a two-probe geometry. If precision is required, such as measuring the zero-resistance state of a superconductor, a four-probe geometry can be employed in which the current is sourced along two lines which incur a voltage drop from the contact resistance, and the voltage difference across the sample can be probed with separate contacts. In the laboratory, this only costs the experimenter an additional voltmeter at room temperature. The cryogenic portion of the circuit can remain identical with the exception of requiring four ohmic contacts instead of two.

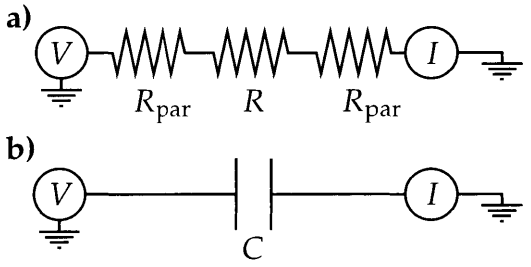

Figure 3-7: **Transport-style measurement scheme a)** An impedance $Z = R$ is sourced with voltage V and its current is measured with an ammeter. Parasitic resistances arising from the lines and contacts R_{par} are easy to deal with in a laboratory setting. **b)** The equivalent measurement scheme for a capacitor is challenging due to the inability of most ammeters to operator above about 10 kHz, limiting currents to about 1 pA for a sample on the order of 1 pF or less.

The situation is very different if $Z \approx \frac{1}{i\omega C}$. For starters, Z is infinite in the DC limit, requiring the use of an AC technique. In the same vein, the frequency of the measurement ought to be reasonably high or else the current output $I \propto \omega$ will be prohibitively small in comparison to noise. However, most current amplifiers experience significant input

impedance above about 10 kHz, limiting measurable currents to the picoampere range for a 1 mV source voltage and samples on the order of 1 pF or less.

3.4.2 Capacitance Bridge

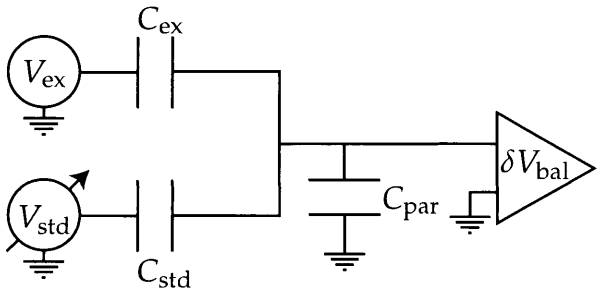

Figure 3-8: **The basic capacitance bridge scheme** uses two voltage sources to balance an unknown experimental capacitance C_{ex} against a known standard C_{std}. The voltage V_{ex} is fixed to some excitation amplitude and frequency appropriate for the sample. The standard excitation is 180° out of phase and adjusted in amplitude only (though if there is resistive impedance present the phase must also be adjusted slightly). The output signal δV_{bal} is measured at the balance point of the bridge with a shunting capacitance C_{par} arising from cabling, bond pads, wire bonds, etc.

A major improvement is to employ a capacitance bridge which allows two voltage sources to balance an unknown capacitance against a known reference capacitor. When the output voltage at the balance point is nulled, the relationship between the sources and capacitances can be used to extract a value for C_{ex}. We will first describe a very basic version which only balances two ideal capacitances. We will then add the complication of resistive impedance. The basic scheme is depicted in Figure 3-8. The voltage source V_{ex} is fixed at a given frequency and amplitude and applied to C_{ex}, the experimental capacitance which is unknown. A separate voltage V_{std} which has variable amplitude and phase is applied to C_{std}, a standard capacitor of known value. V_{std} is approximately 180° out of phase with V_{ex} when balanced. In the basic scheme considered here, because we are balancing two pure capacitance, we never need to adjust the phase away from 180° but the phase degree of freedom will be used when we consider an experimental impedance

Z_{ex} which includes a resistive component. In practice, the two voltage sources are set to some initial value, the output of the bridge δV_{bal} is measured at the balance point, and V_{std} is adjusted until $\delta V_{bal} = 0$. The shunt capacitance arising from cabling reduces the signal output and limits the resolution of the bridge. The output at the balance is computed by superposition of two capacitive voltage dividers:

$$\delta V_{bal} = V_{ex}\frac{C_{ex}}{C_{ex} + C_{std} + C_{par}} + V_{std}\frac{C_{std}}{C_{ex} + C_{std} + C_{par}} \tag{3.30}$$

$$= \frac{V_{ex}C_{ex} + V_{std}C_{std}}{C_{\Sigma}} \tag{3.31}$$

where $C_{\Sigma} = C_{ex} + C_{std} + C_{par}$. Balance is achieved when

$$\frac{C_{ex}}{C_{std}} = -\frac{V_{std}}{V_{ex}}. \tag{3.32}$$

The ratio of the source voltages $-\frac{V_{std}}{V_{ex}}$ gives the experimental capacitance in units of the standard capacitance. This formula makes it clear that the size of δV_{bal} is divided by the total capacitance $C_{\Sigma} \approx C_{par}$ for large parasitic capacitance. For sufficiently large parasitics, it may be difficult to find an accurate bridge balance because even when relatively far from optimally balanced, the charge imbalance term $V_{ex}C_{ex} + V_{std}C_{std}$ will be suppressed by C_{Σ}, and the balance will not be sensitive above noise.

In typical measurements, finding an ideal balance at each point in phase space is time-consuming. If changes in the total capacitance remain small, we typically perform an initial balance to remove a large background capacitance and then measure off balance to detect small relative changes in C_{ex} which arise from gating, changing magnetic field, etc. If we find an ideal balance, we can then ask: What voltage accumulates at the balance point if $C_{ex} \to C_{ex} + \delta C$? To leading order

$$\delta V_{bal} \approx \frac{\delta C V_{ex}}{C_{\Sigma}}. \tag{3.33}$$

Here, again, the shunting capacitance divides the signal. Thus, good capacitance sensing is synonymous with reducing the shunt capacitance C_{par} in front of the amplifier. For standard coaxial cabling, the capacitance per unit length from core to shield (ground) is $30\,\mathrm{pF\,ft^{-1}}$. For a cryogenic measurement, long cables must reach all the way into the frige and then back out for measurement at room temperature. The cabling between balance point and measurement will be on the order of $10 - 20\,\mathrm{ft}$ creating around $500\,\mathrm{pF}$ of shunt. In the best case scenario, the signal will experience no noise beyond the intrinsic noise floor of the lock-in amplifier $\delta V_n \sim 5\,\mathrm{nV}/\sqrt{\mathrm{Hz}}$. With a $1\,\mathrm{mV}$ source we are limited to a capacitance sensitivity of about

$$\delta C_n \sim \frac{\delta V_n C_\Sigma}{V_{ex}} \sim 1\,\mathrm{fF}/\sqrt{\mathrm{Hz}}. \tag{3.34}$$

Typical noise floors experienced with cryogenic bridge circuits are more like $50\,\mathrm{nV}/\sqrt{\mathrm{Hz}}$ at the input of the lock-in, and below $\lesssim 10\,\mathrm{kHz}$ the noise is typically much worse arising from $1/f$–noise in the cryogenic amplifiers. $1\,\mathrm{fF}/\sqrt{\mathrm{Hz}}$ is a pretty disappointing figure. For comparison, the total capacitance C_T after background subtraction of the devices measured in Chapter 4 are around $20\,\mathrm{fF}$ and the most important features in the data correspond to a capacitance changes of about $50\,\mathrm{aF}$. In principle, long averaging times can overcome some of these issues, as done in one study on carbon nanotubes for a limited range of carrier density at zero magnetic field [57]. But if one attempts to sweep two parameters such as carrier density as well as magnetic field and take fine point-spacing, long averaging times become unfeasible, particularly in the low frequency limit where $1/f$–noise is worse. Furthermore, very low-frequency noise and DC drift may be difficult to average away, even with very long averaging times.

The major limitation of capacitance sensing in a cryogenic environment is the need for long cabling. It is difficult to get around this limitation whenever the primary stage of the measurement circuit is placed at room temperature since the capacitance balance point

must begin inside an isolated cryogenic space on one plate of the nanoscale capacitor. The obvious solution is to place the first stage amplifier in the cryogenic space as close to the sample capacitor as possible. This effectively decouples the balance point from the rest of the measurement line downstream by presenting a large impedance. The idea can be traced back to the work of Ashoori et al. [56] who first utilized a high electron mobility transistor (HEMT) as a first stage "bridge on chip" amplifier at low temperature as shown in Figure 3-9. The HEMT transistor is often set to an operating point with unit or even subunit voltage gain. The HEMT's small loss at this operating point is more than made up for by acting as an impedance bridge which can reduce the shunt capacitance by a factor of around 1000 from $\sim$500 pF to less than 1 pF. This reduction in the shunt capacitance increases our capacitance sensitivity to around $\delta C_n \sim 1\,\mathrm{aF}/\sqrt{\mathrm{Hz}}$ under ideal noise conditions. Additionally, two new circuit elements appear in the schematic. The resistor R_{bias} and the DC voltage V_{bias} are used to set the DC operating point of the HEMT. R_{drain} and V_{dd} set the HEMT drain-source voltage and current. Modulation in the gate voltage manifests as a change in the voltage across the HEMT which can be inferred at room temperature. Because the HEMT has a low $\sim$500 Ω output impedance, the large capacitive cabling going to room temperature presents no issue.

Further details of the cryogenic bridge amplifiers scheme can be found in Appendix B. For the rest of this section, we will assume we have some low-temperature bridge similar to Figure 3-9 which is capable of measuring capacitance with high resolution. We will not specify the exact value of the shunt or the amplification downstream of the balance point as these do not affect the interpretation of the measurement signal, only the ability to measure. In the following subsections, we will discuss the output of the bridge and its relationship to the capacitive and resistive impedances of real capacitance devices. At the end of the chapter, we will relate the bridge output signal to real physical quantities of interest such as compressibility, chemical potential, in-plane conductivity, and carrier density as well as discuss data processing techniques.

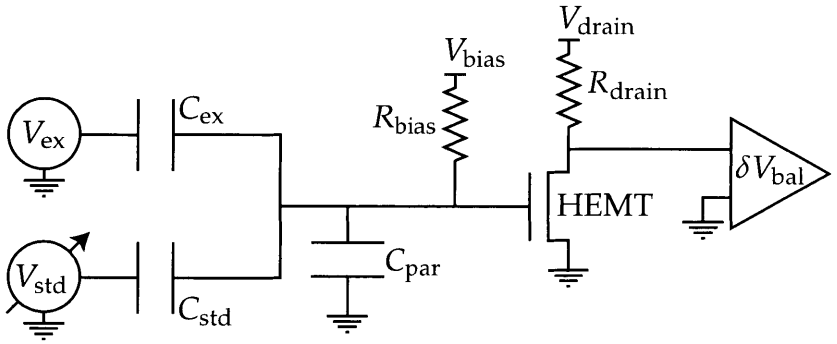

Figure 3-9: **The capacitance bridge with HEMT amplifier** is very similar to the original bridge but the room temperature measurement has been preempted by a low temperature high electron mobility transistor (HEMT) which isolates the balance point from the long cabling going to room temperature. The new value of $C_{par} < 1\,pF$.

3.4.3 In- and Out-of-Phase Signals

Impedance of van der Waals Capacitors

In the previous derivations, we have made use of the approximation that $Z_{ex} \approx \frac{1}{i\omega C_{ex}}$, allowing us to more easily compute the balance condition without phase rotations because both sides of the bridge only presented reactive impedances. However, in typical van der Waals systems at low temperature and high magnetic field, the in-plane resistance can be significant. In fact, interpretation of capacitance data in terms of compressibility rests crucially on the ability to measure effectively low in-plane resistance in relation to the size of the capacitive impedance. We need a realistic, but hopefully simple, model for the impedance of ohmically contacted van der Waals capacitors (with one plate made of metal). To leading order, this can be well captured by a resistance R in series with the capacitance C_T (which includes both the geometric and quantum capacitances). Additionally, there is a stray background capacitance C_{back} which arises from capacitive coupling between the bond pads, wire bonds, and additional metal connected to ether side of the capacitance structure. This manifests as a constant addition to the total capacitance in measurement $C_{meas} = C_T + C_{back}$ and is effectively removed at the initial balance point. However, it is important to accurately subtract this contribution when quantita-

tively analyzing capacitance data. Accurate background subtraction will be discussed in subsection 3.4.5.

Before proceeding with a circuit analysis, we should mention some alternative models for the sample impedance. In reality, the in-plane resistance and capacitance form a distributed RC network instead of the lumped element model we have adopted. The distributed model changes the quantitative shape of some of the frequency response curves discussed below, but the qualitative behavior is no different. In particular, at low frequency both models converge. (See Appendix E of Gary Steele's thesis for details [58].) Additionally, we could worry about a leakage resistance $R_{\text{dielectric}}$ which would manifest as a parallel resistance to the sample capacitance C_T, but in practice this is so large that it is effectively infinite and ignored.

Balanced Measurements

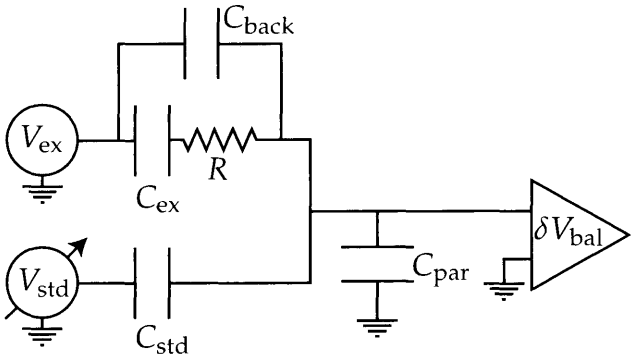

Figure 3-10: **An effective model for the sample impedance** consists of an in-plane resistance R in series with the total capacitance C_T. Additionally, stray capacitance C_{back} from coupling between bond pads, wire bonds, etc. adds a constant background on the measurement signal.

Figure 3-10 shows the effective measurement circuit we wish to analyze. First, we will find the balance condition and then calculate the off-balance signal to leading order in response to small changes in C_T and R. The total sample impedance Z_{ex} is given by

summing the three impedances:

$$Z_{ex} = \frac{1 + i\omega R C_T}{i\omega(C_{back} + C_T) - \omega^2 C_{back} C_T R}. \tag{3.35}$$

Similarly, the impedances of the standard capacitor and parasitic capacitance are

$$Z_{std} = \frac{1}{i\omega C_{std}} \tag{3.36}$$

and

$$Z_{par} = \frac{1}{i\omega C_{par}}. \tag{3.37}$$

If the amplifier at the balance point has a total amplification G, then the output voltage is given by superposition:

$$V_{bal} = G V_{ex} \frac{Z_{std} Z_{par}/(Z_{std} + Z_{par})}{Z_{ex} + Z_{std} Z_{par}/(Z_{std} + Z_{par})} + G V_{std} \frac{Z_{ex} Z_{par}/(Z_{ex} + Z_{par})}{Z_{std} + Z_{ex} Z_{par}/(Z_{ex} + Z_{par})} \tag{3.38}$$

$$= \frac{G Z_{par}(V_{ex} Z_{std} + V_{std} Z_{ex})}{Z_{par}(Z_{ex} + Z_{std}) + Z_{ex} Z_{std}}. \tag{3.39}$$

The balance condition is achieved when

$$0 = V_{bal} \Rightarrow \frac{Z_{std}}{Z_{ex}} = -\frac{V_{std}}{V_{ex}}. \tag{3.40}$$

In the limit $C_{back} \to 0$ and $R \to 0$ this reduces to Equation 3.32. Because Z_{ex} contains both reactive and resistive impedances, the voltage V_{std} must acquire a nonzero phase. We can solve for the real and imaginary parts of V_{std}/V_{ex} which we will label X and Y,

respectively:

$$X = -\frac{(C_T + C_{back})/C_{std}}{1 + (\omega R C_T)^2} - \frac{C_{back}(\omega C_T R)^2/C_{std}}{1 + (\omega R C_T)^2} \tag{3.41}$$

$$Y = \frac{C_T^2 R\omega/C_{std}}{1 + (\omega R C_T)^2}. \tag{3.42}$$

Let us consider the low frequency limit defined by $\omega R C_T \ll 1$. We can expand to leading order in powers of $\omega\tau$ where $\tau = RC_T$:

$$X = -\frac{C_T + C_{back}}{C_{std}}\left(1 - (\omega\tau)^2\right) + \mathcal{O}\left(\omega\tau\right)^3 \tag{3.43}$$

$$Y = \frac{C_T \omega\tau}{C_{std}}\left(1 - (\omega\tau)^2\right) + \mathcal{O}(\omega\tau)^4 \tag{3.44}$$

The physical interpretation of these expressions is quite clear. At low frequency, the resistance R does not compete with the impedance $\frac{1}{i\omega C_T}$ and so it is negligible. The in-phase component is simply the total capacitive term in Z_{ex} in units of the standard capacitor. It may be counter-intuitive that the in-phase signal mostly describes the capacitive impedance. This true because in the low frequency limit (where R is negligible) the balance point forms a capacitive voltage divider, resulting in no net phase shift with respect to the excitation. Additionally, if we were to use a resistive impedance as Z_{std}, then this would effectively change the "units" with which we measure impedance and would cause the capacitance to manifest in the out-of-phase component. Importantly, if we imagine varying C_T we can see that the background capacitance simply manifests as a constant additive term. The out-of-phase component is slightly more complicated as it contains both reactive and resistive components. It is directly proportional to the in-plane resistance of the sample, so it effectively tracks the bulk transport behavior of the sample (though in units and a geometry that generally do not allow direct access to any well-defined resistivity elements such as ρ_{xx} or ρ_{xy}). After discussing the high frequency limit, we will return to the out-of-phase component to discuss its physical interpretation

as well as its crucial role in capacitance experiments.

Now let us consider the high frequency limit. At high frequency $\omega R C_T \gg 1$ and

$$X \approx -\frac{C_{back}}{C_{std}} - \frac{(C_T + C_{back})/C_{std}}{(\omega R C_T)^2} \tag{3.45}$$

$$Y \approx \frac{1}{C_{std} R \omega}. \tag{3.46}$$

The capacitance of the sample needs a time of several $\tau = RC_T$ in order to completely charge. In the high frequency limit, the sample fails to charge completely and the sample's series resistance and capacitance are shunted by the background capacitance C_{back}. Turning to the out-of-phase component, there are no additional resistive components which are not suppressed at high frequency by the failure of the sample to charge. As a result, Y falls off uniformly as $\frac{1}{\omega R C_T}$, which can be viewed as the bulk conductivity $\frac{1}{R}$ measured in units of ωC_{std}.

At intermediate frequencies, we can interpolate the two limits. The behavior of $-X$ is fairly straightforward. The contribution to the charging signal at the balance from the sample is slowly killed by the sample failing to charge as frequency increases. It monotonically decreases from a value of $C_T + C_{back}$ to C_{back} in units of the standard. The full expression for Y in Equation 3.44 is not simply intuited; a possibly useful heuristic is that Y represents the unitless *competition* between resistive and reactive impedances. Competition is high whenever the two impedances are comparable and suppressed whenever one dominates. At extremely low frequency, the impedance of the capacitance is much larger and dominates. $Y \approx 0$ and increases linearly with $\omega\tau$. At very high frequencies, the resistive component dominates and $Y \approx 0$ due to the sample's failure to charge and falls off as $\frac{1}{\omega\tau}$. At some intermediate regime, the out-of-phase signal peaks when $R \sim \frac{1}{\omega C_T}$.

The out-of-phase signal can be cast in more illuminating form by taking the ratio of Y to $-X$ (after removing the background term in X). By doing so, the denominators in Equations 3.41–3.42 vanish. It turns out that the background subtracted ratio is equal

to the loss tangent $\tan(\delta)$ of the sample, which is defined as the ratio of the resistive to reactive impedances

$$\tan(\delta) = \text{loss tangent} = \frac{Z_{\text{res}}}{Z_{\text{react}}}. \tag{3.47}$$

The loss tangent is a quantity that is typically used to describe a capacitor's deviation from an ideal capacitance. All capacitances present a series resistance arising from parasitic resistances and lossy relaxation of the dielectric. The numerator of the loss tangent is equivalent to a capacitor's effective series resistance (commonly ESR in data sheets). In order to calculate this quantity for the sample Z_{ex} we must first background subtract the C_{back} contribution. One way of doing this is to measure $-X$ at both the low and high frequency limit. Their difference is $C_{\text{T}}/C_{\text{std}}$. This is not always possible. Sometimes the rolloff frequency is so high that it is impossible to reach the high frequency limit. Another approach is discussed in subsection 3.4.5. Let $X' = X - X_{\text{back}}$ be the background subtracted in-phase component ($X_{\text{back}} = \lim_{\omega\to\infty} X$). The loss tangent is given by:

$$\text{loss tangent} = \frac{Y}{-X'} = \omega R C_{\text{T}}. \tag{3.48}$$

For moderately incompressible phases, often the value of the capacitance does not change as dramatically as the resistance. In such cases, changes in the loss tangent correspond to changes in the bulk resistance of the sample. However, strongly incompressible phases will send $C_{\text{T}} \to 0$ and the loss tangent will vanish.

The values of $-X$, Y, and the loss tangent are plotted on on a logarithmic frequency scale in Figure 3-11. The in-phase component (red) is proportional to C_{T} at low frequency and shows a clear drop at the rolloff frequency $f = 2\pi R C_{\text{T}}$. The out-of-phase component (blue) shows a clear peak at the rolloff frequency. The loss tangent (black, dashed) increases linearly with frequency. In the low frequency limit, $Y \approx$ loss tangent.

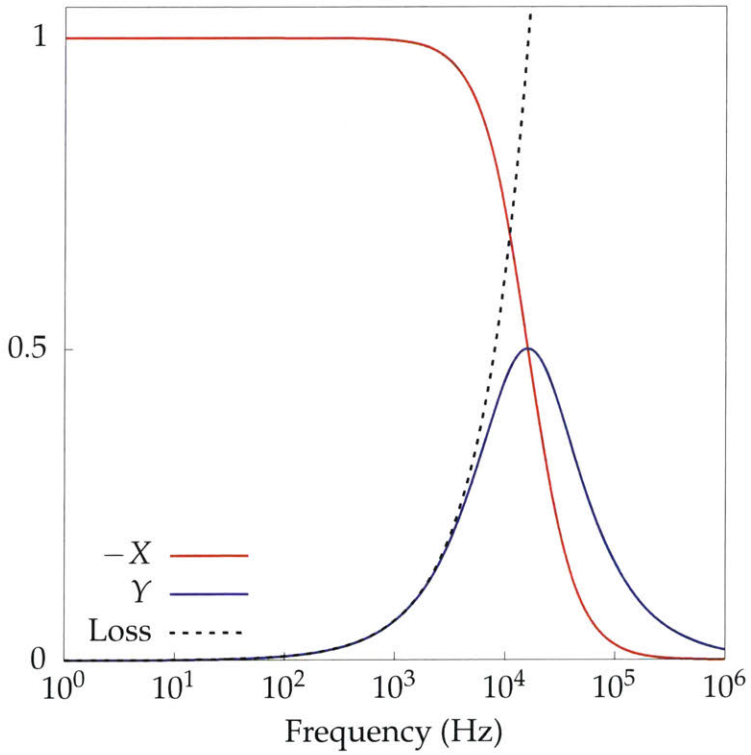

Figure 3-11: **In-phase, out-of-phase, and loss tangent** are plotted as a function of frequency. The background capacitance has been set to zero. $C_T = C_{std} = 100\,\text{pF}$ and $R = 100\,\text{k}\Omega$. The in-phase component (red) falls to 0 monotonically. The out-of-phase component (blue) displays a peak when the resistive and reactive components are comparable. The loss tangent (black, dashed) is linearly increasing in frequency.

Off-Balance Measurements

In order to measure capacitances with a bridge scheme, feedback software can tune the magnitude and phase of V_{std} in order to find the condition $V_{\text{bal}} = 0$. Using the in- and out-of-phase components of V_{std}, the ratio $\frac{V_{\text{std}}}{V_{\text{ex}}}$ gave Equations 3.41–3.42. However, the bridge must be rebalanced at at each gate voltage, magnetic field, or other independent parameter. This leads to long measurement times when, often, the total changes to the capacitance that we are interested in are quite small. In this regime, it is possible to use a linearized off-balance signal to back out the relative changes δX and δY.

We can find an initial balance for some arrangement of independent variables such as carrier density and magnetic field using Equation 3.39. Then, we can ask: What voltage accumulates at the balance point in response to changes $C_{\text{T}} \to C_{\text{T}} + \delta C$ and $R \to R + \delta R$ from sweeping one of the independent parameters? Let our amplifier have a total gain of G. Take V_{std}^0 to be the original balance voltage for $\delta C = 0$ and $\delta R = 0$. Expanding Equation 3.39 to linear order in δC and δR we get:

$$\delta V = \frac{G V_{\text{ex}} (\delta C - i \delta R \omega C_{\text{T}}^2)}{(1 + i\omega\tau)(C_\Sigma + i(C_\Sigma - C_{\text{T}})\omega\tau)}. \tag{3.49}$$

Here, $C_\Sigma = C_{\text{T}} + C_{\text{back}} + C_{\text{std}} + C_{\text{par}}$. This expression can be cleaned up significantly with one other measurement. While the bridge is balanced, $\delta C = 0$ and $\delta R = 0$, we can intentionally put the bridge out of balance by letting $V_{\text{std}}^0 \to V_{\text{std}}^0 + \delta V_{\text{std}}$. The output of the bridge will be

$$\alpha \equiv \frac{\delta V_{\text{bal}}}{\delta V_{\text{std}}} = \frac{G C_{\text{std}} (1 + i\omega\tau)}{C_\Sigma + i(C_\Sigma - C_{\text{T}})\omega\tau} \tag{3.50}$$

where we have defined the bridge response function α. If we multiply Equation 3.49 by $\frac{1}{\alpha}$

then we find

$$\frac{\delta V}{\alpha V_{ex}} = \frac{\delta C - i\delta R C_T^2 \omega}{C_{std}(1 - i\omega\tau)^2}. \tag{3.51}$$

Isolating the in- and out-of-phase components we get in the low-frequency limit:

$$\left(\frac{\delta V}{\alpha V_{ex}}\right)_X = \frac{\delta C}{C_{std}} \tag{3.52}$$

$$\left(\frac{\delta V}{\alpha V_{ex}}\right)_Y = -\frac{\left(\frac{\delta R}{R} C_T + 2\delta C\right)\omega\tau}{C_{std}}. \tag{3.53}$$

The first expression matches $-X$ in the balanced case with $C_{ex} \to \delta C$ and no background capacitance. The second expression matches $-Y$ with $R \to \delta R$ in the limit that the first term in the numerator proportional to δR dominates. Note that the ratio between the two expressions is proportional to the fractional change: $(\delta R/R)/(\delta C/C_T)$. Typically decreases in capacitance are associated with increases in the resistance. The change in total capacitance is typically the smaller of the two due to the fact that the total capacitance is typically dominated by the geometric term. The decrease in the total capacitance may also be relatively weak if there is a large number of localized states within a gap which prevent the quantum capacitance from decreasing to zero. The resistance, however, is very sensitive to the number of available extended states and will potentially increase much more dramatically whenever a gap is entered. In either case, the role of the Y-component is never quantitative but only to verify that changes in the X-component are associated with legitimate changes in the quantum capacitance δC_q and not with increases in R associated with the denominator of Equation 3.51. The X-component, which is often used quantitatively, remains well approximated as purely capacitive in the low-frequency limit.

The issue of whether the capacitance is a genuine measure of the density of states in light of the potential importance of the in-plane conductivity was first addressed in

reference [59]. Though the authors deserve credit for realizing the role of transport in their data, they arrive at the incorrect conclusion that the extraction of density of state is generally impossible due to the intermixing of transport features. In their particular Corbino geometry, they were able to exactly access the conductivity tensor σ_{ij} to study the in-plane transport. The authors failed to consider that the loss tangent is a good indicator of the relative importance of the in-plane transport. If we restrict to the low frequency limit, as verified on the Y channel, the in-phase component is purely capacitive allowing access to the quantum capacitance and thermodynamic density of states.

In practice, the value of R is never known exactly and so the low frequency limit is taken to be whenever the off-balance Y term remains zero or changes only very slightly while a substantial change in X occurs. In this situation, the modulation of X may be attributed to the quantum capacitance (density of states). If Y changes substantially, which typically occurs in substantial band gaps and at high magnetic field in the quantum Hall regime where the in-plane conductivity can become very low in cyclotron or exchange gaps, then it is difficult if not impossible to be quantitative about the changes in compressibility. However, this does not preclude the X component from being an effective *qualitative* tool for exploring compressibility. For example, in the quantum Hall regime, the emergence of exchange gaps at high magnetic field may be clearly seen in both the X and Y channels. Although the magnitude of the gap will be impossible to disentangle from the intertwined transport contribution to the signal, the presence and trajectory of the exchange gap are potentially important observations. The only danger with this type of qualitative analysis is the possibility that resistance increases are associated with localized states and not a true density of states reduction, which is why this type of analysis should be limited to well-understood incompressible phases such as those in the quantum Hall regime.

In this way, capacitance can be separated into roughly two limits. At low frequency, changes in X are attributed to changes in $C_q \propto \partial n/\partial \mu$. At high frequency, X is no longer

directly proportional to the compressibility. In this limit, both the X and Y channel are dominated by transport features. In many situations, this apparent bug can be a feature by measuring transport with a modality that is potentially more sensitive than traditional transport measurement schemes. In a bridge measurement, a large background impedance is subtracted away, allowing very minute changes to be observed. Furthermore, the resistance which is sensed is true bulk spreading resistance. This can be an important quantity to measure in the quantum Hall regime, where traditional two- and four-probe geometries fail to measure the bulk conductivity because they are shorted out by the extended edge states. For example, the observation of insulating bulk with capacitance sensing allowed reference [60] to claim a quantum-spin-Hall-like phase at high magnetic field in monolayer graphene.

3.4.4 Fixed Frequency

The previous calculations were very important to establish the frequency response of the capacitance circuit. At the end of the day, we want to measure impedances and because the frequency plays a natural role in the impedance of a capacitor, it is essential to understanding the bridge response. However, in typical operation, the capacitance bridge is fixed to a working measurement frequency f_0 and independent variables such as density (gate voltage) or magnetic field are modulated in order to sense relative changes in the total capacitance and loss tangent. It is worth thinking about what happens to the signal in the event that a change in gate voltage alters C_T and R. Imagine that at zero gate voltage $V = 0$ the total capacitance is 10 pF and the resistance is 100 kΩ. Then as we change the voltage to $V = 1$ V the capacitance enters the edge of a band gap. The total capacitance decreases to 9 pF and the resistance increases to 500 kΩ. At $V = 2$ V, the sample enters the band gap completely and the total capacitance further reduces to 8 pF while the resistance blows up the 50 GΩ. These changes cause the rolloff frequency to decrease as depicted in panels **a**–**c** in Figure 3-12. Note that C_T is the total capacitance and

not the quantum capacitance. Even in the band gap in panel **c**, the sample's density of states may be substantial due to localized states which cause $C_q \neq 0$. Therefore, the total capacitance may only deviate slightly from the geometric value C_{geo}, particularly in the limit $C_{geo} \ll C_q$. The in-plane resistance, however, is highly sensitive to the absence of extended electronic states. Because R changes much more dramatically than C_T typically, it pulls the rolloff frequency to the left more than the decrease in C_T pulls it to the right. If we were to plot the values of $X(V)$ and $Y(V)$, we would see a steady drop in X as well as a single peak in Y.

These three panels show the importance the choice of measurement frequency f_0 plays. The lowest frequency $f = 5\,\text{Hz}$ is close to the low frequency limit because at all values of V, the change in Y is small in comparison to the changes in X. The middle frequency $f = 1\,\text{kHz}$ is not in the low frequency limit. The change in X which is measured is not truly associated with pure capacitance change. Y will show a double-peak structure if the gate voltage pushes through the band gap and enters another highly compressible band. The highest measurement frequency $f = 500\,\text{kHz}$ is close to the high-frequency limit. The value of the capacitance is not properly measured at any gate voltage V and Y shows a dip as the band gap is entered.

This can be more clear by plotting some artificial resistance and capacitance data as a function of voltage. Then, we can plot the X and Y phase for various measurement frequencies. Panel **a** of Figure 3-13 plots representative capacitance (black) and resistance (red) traces for the series RC model discussed in this section. Panel **b** plots the in-phase and out-of-phase components for a variety of measurement frequencies spanning 1 Hz to 1 GHz. The range of possible in-phase behavior underscores the need to carefully characterize the frequency response. If one were to use the $f = 1\,\text{GHz}$ curve (red), it would appear that the compressibility gap spanned 20 V and approached zero. The low frequency regime begins between 100 Hz (purple) and 1 kHz (blue) as evidence by the saturation of the in-phase component at lower frequencies as well as the small out-of-phase compo-

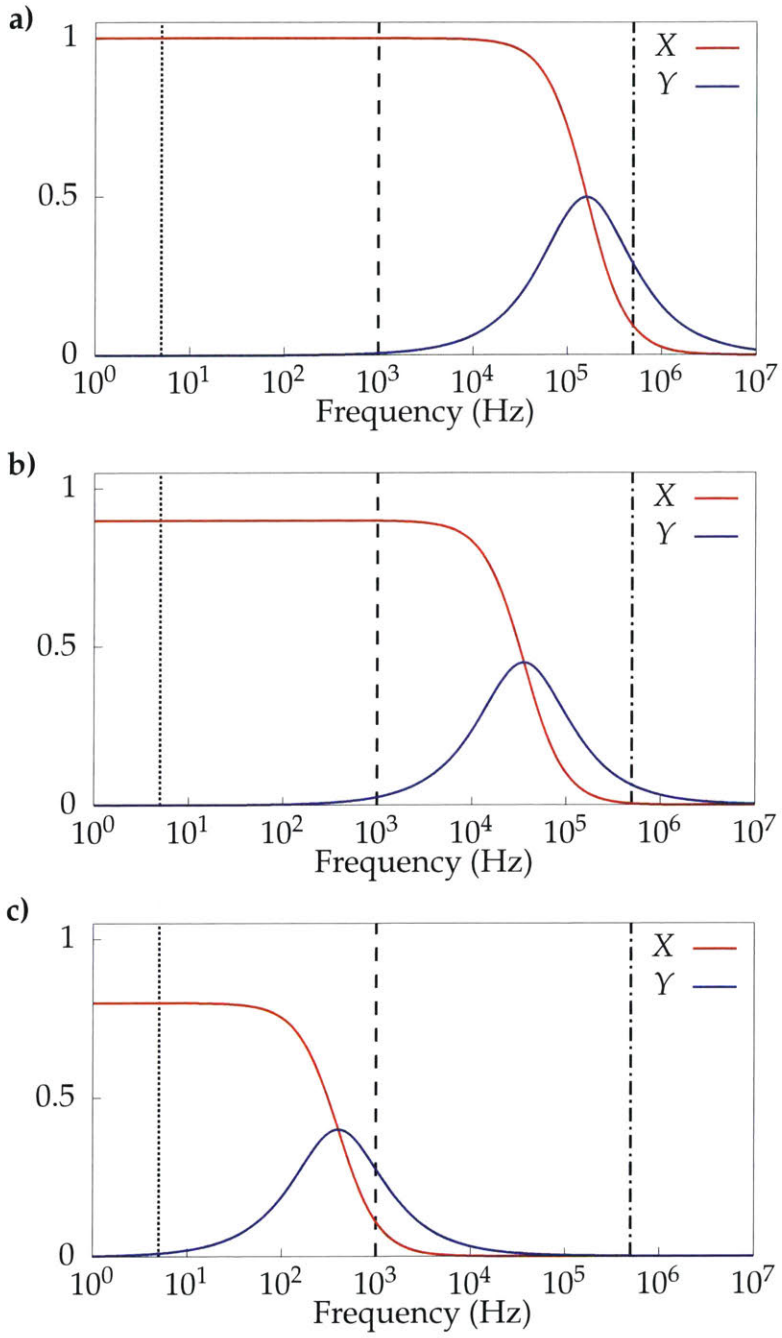

Figure 3-12: **The in-phase and out-of-phase curves shift** as the sample becomes increasingly resistive. The measurement takes place at any one of the black dotted/dashed traces. **a)** At $V = 0$ the sample has $C_T = 10\,\text{pF}$ and $R = 100\,\text{k}\Omega$. **b)** At $V = 1\,\text{V}$ the sample is at the edge of a band gap. $C_T = 9\,\text{pF}$ and $R = 500\,\text{k}\Omega$. **c)** At $V = 2\,\text{V}$ the sample enters a full band gap. $C_T = 8\,\text{pF}$ and $R = 50\,\text{G}\Omega$. The frequency 5 Hz (dotted trace) is near the low-frequency limit whereas the frequency 500 kHz (dot-dashed trace) is near the high-frequency limit. The frequency 1 kHz (dashed trace) is intermediate.

nent below 1 kHz at all gate voltages. This agrees with the minimum rolloff frequency we can calculate from panel **a** where the maximum RC charging time occurs at $V = 0$ and is around 8 kHz.

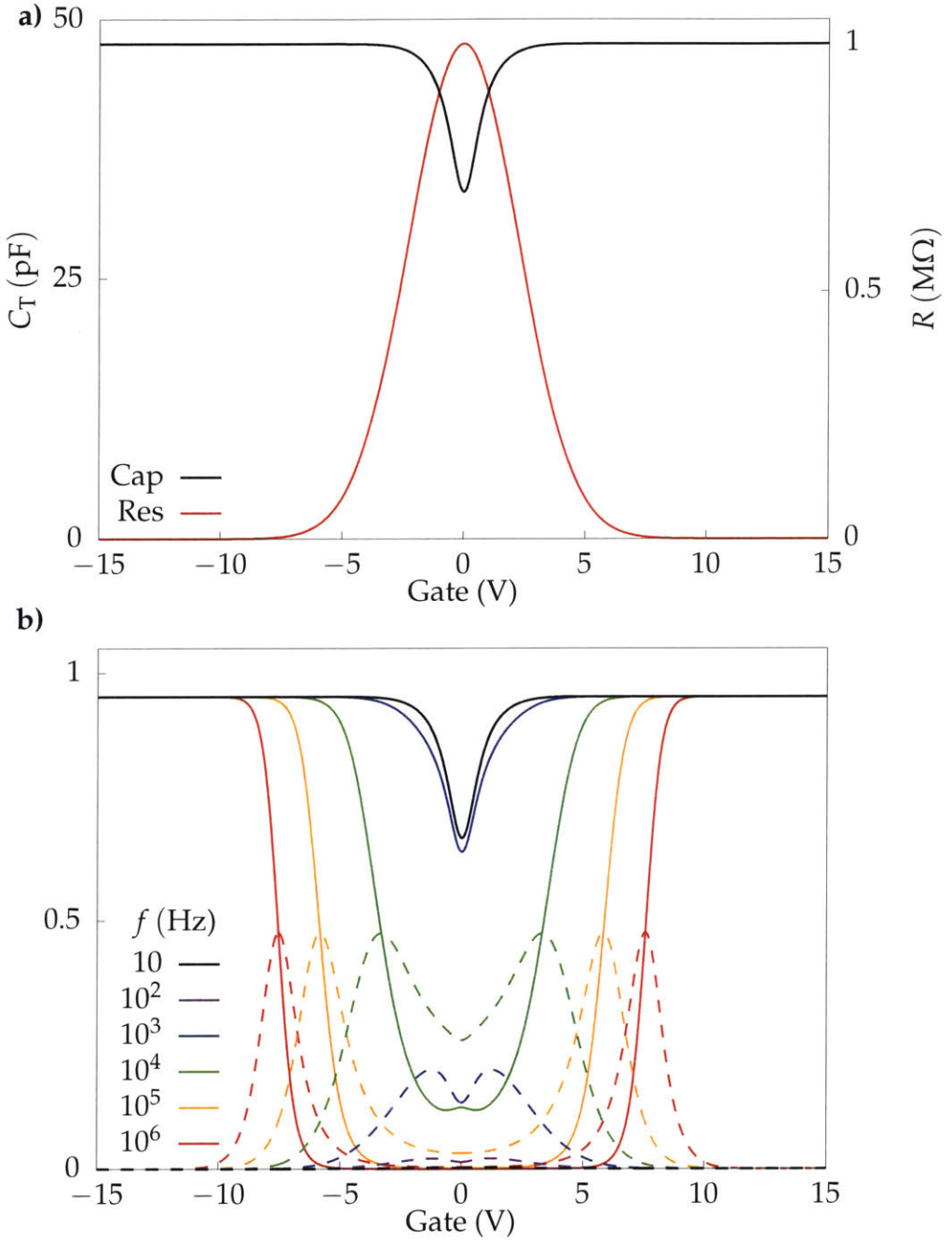

Figure 3-13: **The capacitance bridge output is a sensitive function of frequency a)** Sample capacitance (black) and resistance (red) as a function of gate voltage. **b)** The in-phase component (solid) and out-of-phase component (dashed) are plotted against gate voltage for a series of frequencies spanning $10 - 10^6$ Hz.

3.4.5 Calibrations

Background Subtraction

As mentioned earlier, it is important to be able to subtract the background capacitance from the measured signal at low frequency. One method to solve this is to measure in both the low and high frequency limits. At high frequency the in phase component is $X \approx -C_{back}/C_{std}$ and at low frequency it is $X \approx -(C_T + C_{back})/C_{std}$. Taking the difference removes the background.

This is not possible for all samples. In particular, for small samples $\lesssim$100 fF of moderate in-plane resistance $\lesssim$1 MΩ the rolloff frequency will be in the MHz regime which may or may not be accessible depending on the measurement lines used. An alternative approach exists for samples which have a measurable quantum Hall effect regime which has low in-plane resistance. In the quantum Hall regime, regardless of the host material, the orbital degeneracy of each Landau level is given by

$$\frac{\phi}{\phi_0} = \frac{BAe}{h} \tag{3.54}$$

where ϕ is the total flux at field B through sample of lateral area A and ϕ_0 is the flux quantum. There may be additional degeneracy arising from spin, valley, etc. which we will label g. Therefore, the total number of states within each Landau level is $gBAe/h$. If we integrate the total capacitance (in-phase signal) at low frequency between two Landau level minima, we can extract the appropriate $C_0 = C_{back}$ to subtract off by enforcing:

$$\frac{gBAe^2}{h} = \int_{\Delta V} (C_T(V) - C_0) dV \tag{3.55}$$

where ΔV is a voltage range determined from the field and gate dependence of the capacitance data. This method will be discussed more in Chapter 4.

Carrier Density

Typically, capacitance data are measured with respect to gate voltage as the "fast" independent variable. Gate voltage and carrier density have an approximately linear relationship for samples that are dominated by the geometric capacitance. However, with capacitance data it is possible to integrate the total capacitance to get the density exactly:

$$n = \int_{V_0}^{V} \frac{C_T(V') - C_{back}}{eA} dV' \tag{3.56}$$

where V_0 is the voltage which corresponds with charge neutrality (or depletion).

Geometric Capacitance

The geometric capacitance is a quantity which is difficult to extract in measurements and often must be approximated. In general, there is no relationship which allow one to perfectly extract C_{geo} from C_T because the two are intertwined with C_q which is never known *a priori*. Chapter 4 will discuss an approach to estimating C_{geo} which relies of fitting the zero-magnetic field capacitance data and using finite magnetic field capacitance data to estimate an error range based on the value of the capacitance within highly compressible Landau levels.

Chemical Potential

With an estimate for C_{geo} and C_T background subtracted and expressed in terms of density, one can back out the change in the chemical potential μ:

$$\frac{1}{C_T} = \frac{1}{C_{geo}} + \frac{1}{C_q} \tag{3.57}$$

$$\Rightarrow \frac{\partial \mu}{\partial n} = Ae^2 \left(\frac{1}{C_T} - \frac{1}{C_{geo}} \right). \tag{3.58}$$

Integrating with respect to density we can get

$$\Delta\mu(n) = \int_{n_0}^{n} Ae^2 \left(\frac{1}{C_T} - \frac{1}{C_{geo}} \right) dn. \tag{3.59}$$

By observing the shift in chemical potential, thermodynamic gaps and the bandwidth of energy bands can be extracted provided the entire out-of-phase component is sufficiently small within the entire range of carrier density. Chapter 4 will provide an example.

Chapter 4

Electronic Compressibility of Magic Angle Graphene

4.1 Introduction

In most metals, interactions between electrons are sufficiently weak compared with electronic kinetic energy that they can be considered as a perturbation when calculating band structure. Because the kinetic energy of an electronic system is proportional to the bandwidth of its low energy bands, one route to finding materials with effectively strong electron–electron interactions is to study systems with flat energy dispersions. One well-studied route to generating flat energy bands is the application of a large magnetic field to a two-dimensional electron system. At large magnetic field, the electrons undergo Landau quantization and form flat bands in momentum space. Landau levels are known to host a variety of strongly correlated physics such as fractional quantum Hall phases [48–50], Wigner crystals [53], and quantum Hall ferromagnets [51, 52]. Recent experimental efforts [17, 37] have shown that stacking and rotating two monolayers of graphene by a controllable angle between the two layers can tune the resulting low-energy band structure through a large range of energy dispersion due to the sensitivity of the interlayer

coupling with twist angle [16, 40, 44]. At certain small twist angles, known as *magic angles*, the interlayer hybridization energy concentrates the low-energy density of states within about 10 meV according to calculations [16, 40], providing a highly tunable test bed for strongly correlated physics.

4.1.1 Previous Experimental Work

When twisted at low twist angle, the electronic structure of the two monolayers of graphene become hybridized due to electrons hopping and Bragg scattering off of the emergent superlattice as discussed in section 2.4. The hybridization of the two neighboring Dirac cones enabled by the moiré potential opens up avoided crossings at the degeneracy points at positive and negative energies. This creates an effective mini-band structure driven by the superlattice. At angles close to 1°, the energy scales conspire to suppress the conduction and valence bandwidths to very narrow energies, creating flat bands.

In any tight-binding picture, the total number of eigenstates in the newly diagonalized basis that incorporates hopping must be equivalent to the original number of atomic orbitals used in the tight-binding Hamiltonian. As a result, the inevitable consequence of confining band structure to small ranges of energy is the enhancement of the density of states $\sim\frac{n}{\Delta E}$ because n is constant and ΔE becomes small. The first experimental evidence of a large density of states enhancement in twisted bilayer graphene came from scanning tunneling spectroscopy measurements. Van Hove singularities (logarithmic divergences of the density of states) were observed in the low-energy moiré bands for low twist angle samples. More importantly, these density of states peaks narrowed as the twist angle was reduced down to 1.16°, the smallest twist angle considered [45], demonstrating the ability of rotation angle to be a sensitive tuning parameter.

Advances in laboratory capabilities to precisely control the rotation angle of van der Waals heterostructures [36, 37] enabled the fabrication of a new generation of twisted

bilayer graphene devices at low twist angle with high throughput. Observation of activation gaps of ~30 meV corresponding to the avoided crossings generated by the moiré potential were observed [37, 61]. These single-particle band gaps were observed at electron densities $n = \pm n_s$ where $n_s = \frac{4}{A_m}$ in terms of A_m, the moiré superlattice unit cell area. A_m is given by $\sqrt{3}\lambda^2/2$ where the moiré wavelength $\lambda = \frac{a/2}{\sin(\theta/2)}$ is defined in terms of the twist angle θ and lattice constant of graphene a. The condition $n = \frac{4}{A_m}$ corresponds to filling each moiré cell with 4 electrons as a result of spin (2) and moiré valley (2) degeneracies.

While the existence of superlattice band gaps was entirely expected based on single-particle calculations [16, 40, 44], the discovery of anomalous insulating behavior in twisted bilayer graphene around *half*-filling of the moiré bands, $n = \pm n_s/2$, signaled the presence of strong electron–electron interactions [17] as plotted in Figure 4-1. At half-filling of the conduction or valence band, absent strong Coulomb interactions, the Fermi level is surrounded by a large number of available charge carriers similar to common metals. The observation of insulating behavior is only consistent with a scenario in which the electrons are strongly correlated and formed a many-body insulating state. In fact, the observation of anomalous insulation at half-band-filling is the hallmark of a class of materials known as Mott insulators. The theory of Mott physics was first developed to explain the unexpected insulation of the transition metal oxides at half-filling [62].

The basic idea behind a Mott insulator can be intuited from considering an extension of tight-binding approaches. In Chapter 2 we considered tight-binding models for different materials in which the electron hopping term described by t characterized the strength of the electronic kinetic energy. If we imagine the electrons being roughly localized on each atomic site, such as at half-filling where there is one electron per ion, an electron can lower its confinement energy by delocalizing. This is achieved by hopping back and forth from neighboring atomic sites. Of course, this treatment only considers the kinetic energy. Whenever an electron hops onto its neighbor's site, two electrons are

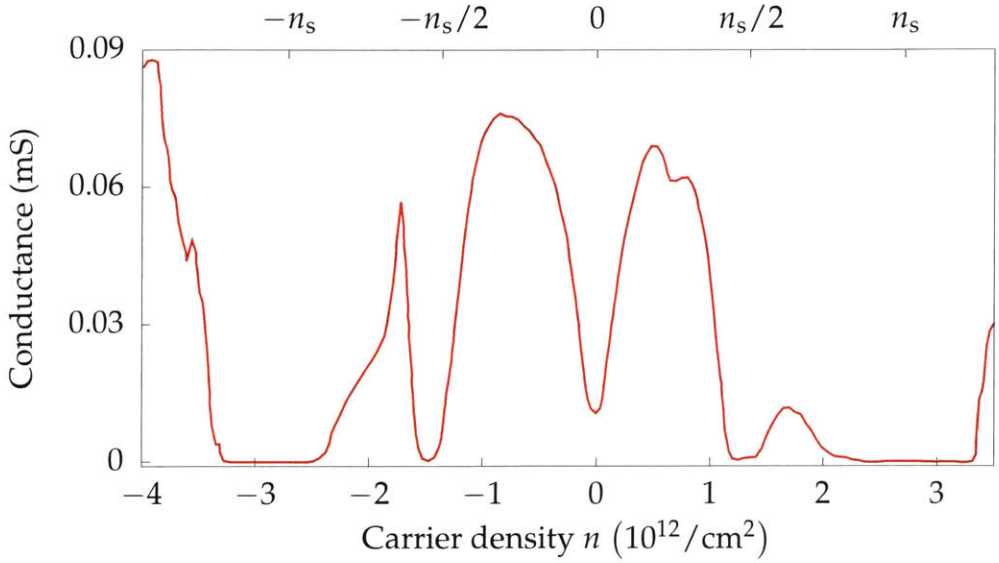

Figure 4-1: **Anomalous insulating behavior in magic angle graphene** The two-terminal conductance is plotted as a function of carrier density (adapted from reference [17]). Broad insulating features occur near $n = \pm 2.7 \times 10^{12}/\mathrm{cm}^2$ which correspond to $\pm n_s$. Additional insulating states are seen at $n = \pm n_s/2$.

cohabiting the same ion. This extreme proximity costs a sizable on-site Coulomb repulsion energy which is commonly labeled U. Because the electron's kinetic energy wants to spread out the electron wave function but its potential energy wants it to stay confined, the two energy scales are in competition with one another. In typical metals and semiconductors $t \gg U$. However, in the limit that $U \gtrsim t$, the electrons find it favorable to localize. If we imagine injecting an additional electron into the system, it must double-occupy one atomic site which will cost energy U. This opens a gap to charged excitations of order U at the Fermi level as depicted in Figure 4-2. Away from half-filling, incommensurate electron number allows for hopping to dominate by freeing up atomic sites for electron (or hole) delocalization without double-occupancy.

Though the condition $n = \pm n_s/2$ corresponds to two electrons (holes) per moiré site, the half-filled condition bears strong resemblance to a Mott-like insulator [17], though there are currently many theoretical proposals for various strongly correlated phases [46, 63–75]. To make the story even more interesting, superconductivity was also ob-

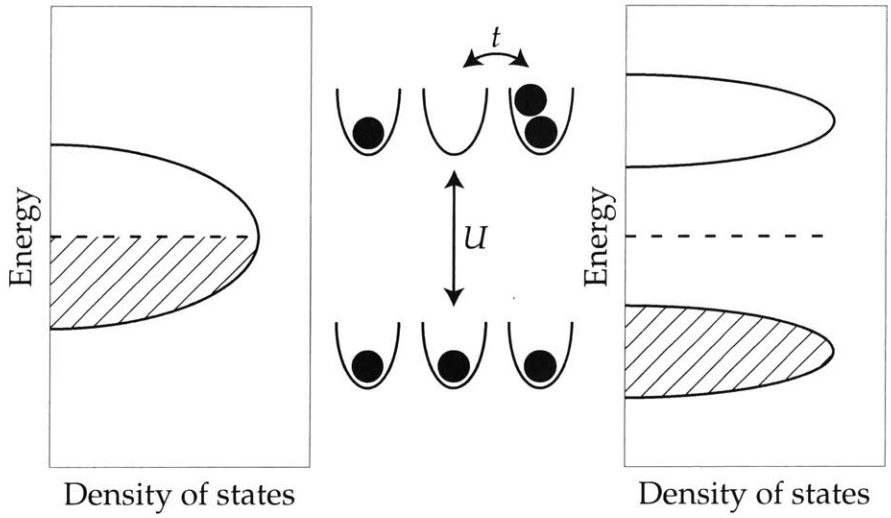

Figure 4-2: **Charge gap of Mott insulator** (Left) The band structure is metallic at half-filling when $t \gg U$. (Right) A charge gap opens due to on-site Coulomb repulsion U.

served around $n = -n_s/2$ (two holes per supercell) with density-dependent critical temperatures up to 1.7 K [18]. Although the observed T_c is low compared to many well-studied superconductors, the ratio of the critical temperature to the Fermi temperature T_c/T_F is similar to or higher than well studied high temperature superconductors [18].

4.2 Capacitance Measurement Scheme

In order to probe the thermodynamic ground state of magic angle graphene, we use a low-temperature capacitance bridge to access the electronic compressibility of the two devices originally characterized with transport in reference [18]. By measuring the compressibility as a function of carrier density, we study the thermodynamic evolution of the interaction-driven phases at fractional filling, offering new insights into the nature of the magic-angle graphene ground state that complement previous transport [17, 18, 76–79] and tunneling efforts [80, 81]. Additionally, we can extract the thermodynamic bandwidth of the low energy bands, enabling us to evaluate their relative flatness and compare to electronic structure calculations. Figure 4-3 shows the device geometry and measure-

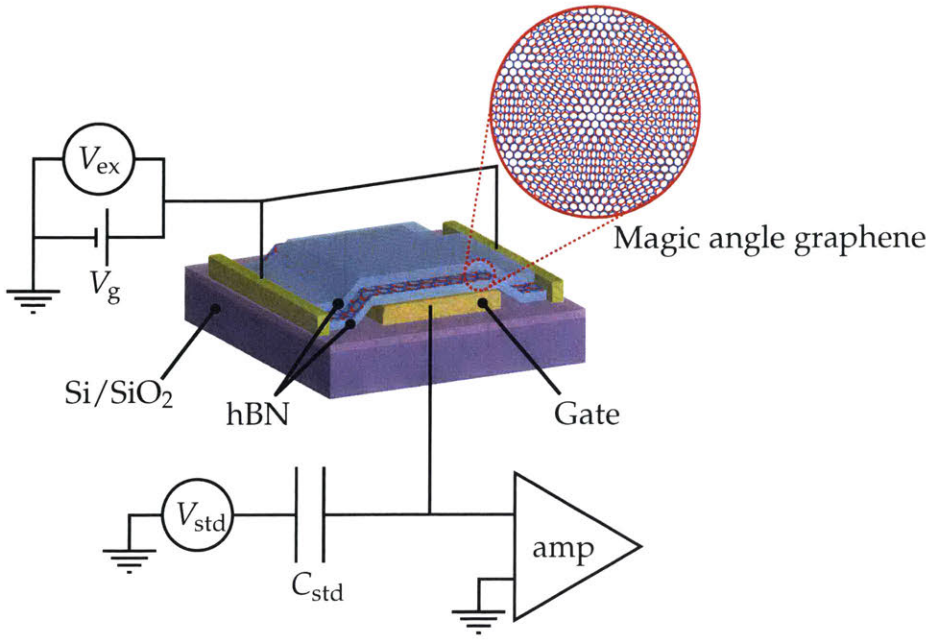

Figure 4-3: **Schematic of magic-angle capacitance devices** Devices from reference [18] were originally measured in a Hall geometry for transport measurements. Here, we tie together all electrical leads to reduce the in-plane spreading resistance. Devices are measured on a cryogenic capacitance bridge in either a helium-3 or dilution cryostat.

ment schematic. Magic angle graphene samples were fabricated using a "tear and stack" technique described previously [36, 37]. The twisted bilayer graphene is encapsulated between two layers of hexagonal boron nitride (hBN) and placed on top of a local, metal back gate. The structures were etched into a Hall geometry for initial transport measurements in reference [18]. However, in our capacitance measurements, we electrically short all contacts together to reduce the *RC* charging time of the devices, allowing the measurements to take place at higher frequency where the signal-to-noise ratio is improved.

We apply an AC excitation to the magic-angle graphene contacts and a balancing AC excitation of variable phase and amplitude to a ~45 fF reference capacitor connected to the back gate in a bridge configuration as shown in Figure 4-3. We measure small changes in the sample impedance by monitoring off-balance voltage accumulation at the balance point, and we model the total capacitance C_T of the magic-angle graphene structure as consisting of two contributions: $C_T^{-1} = C_{geo}^{-1} + C_q^{-1}$. C_{geo} is the geometric capacitance

arising from the parallel plate geometry of the magic angle graphene and local back gate while $C_q = Ae^2\partial n/\partial\mu$ is the quantum capacitance [11] which is directly proportional to the thermodynamic compressibility $\partial n/\partial\mu$ (A is the lateral device area and e is the elementary charge). By measuring modulation of the capacitance as a function of gate voltage and magnetic field, we detect the presence of gaps in the thermodynamic density of states. Importantly, we restrict our measurements to sufficiently low frequencies to ensure that modulation of the measured signal arises entirely from changes of the electronic compressibility and does not result from charging-rate effects from slow in-plane transport noted in previous measurements [59] and discussed in Chapter 3. At high magnetic field in the quantum Hall regime, where the in-plane resistance becomes appreciable, we restrict ourselves to a qualitative discussion of the field-induced gaps.

4.3 Zero-Field Capacitance Data

Panels **a** and **b** of Figure 4-4 show capacitance (red traces) and loss tangent (blue traces) measurements at zero magnetic field for the two devices (M2 and M1) that previously showed unexpected insulating and superconducting phases in reference [18]. Devices M2 and M1 were found previously to have twist angles of 1.05° and 1.16°, respectively [18]. In both samples we observe a Dirac-like feature at charge neutrality accompanied by broad, incompressible regions around $\pm 3 \times 10^{12}\,\mathrm{cm}^{-2}$ that correspond to either four electrons ($+n_s$) or four holes ($-n_s$) per moiré cell. We observe incompressible phases around $n_s/2$ (two electron per moiré cell) in both devices and a smaller feature around $-n_s/2$ in device M2. These incompressible features correspond to the previously reported insulating phases observed around $\pm n_s/2$ in reference [18], however, in our measurement we find that the hole-doped state is significantly less incompressible despite comparable conductance values reported previously. Our results are consistent with more recent transport measurements in which resistive phases in the electron-doped regime are gen-

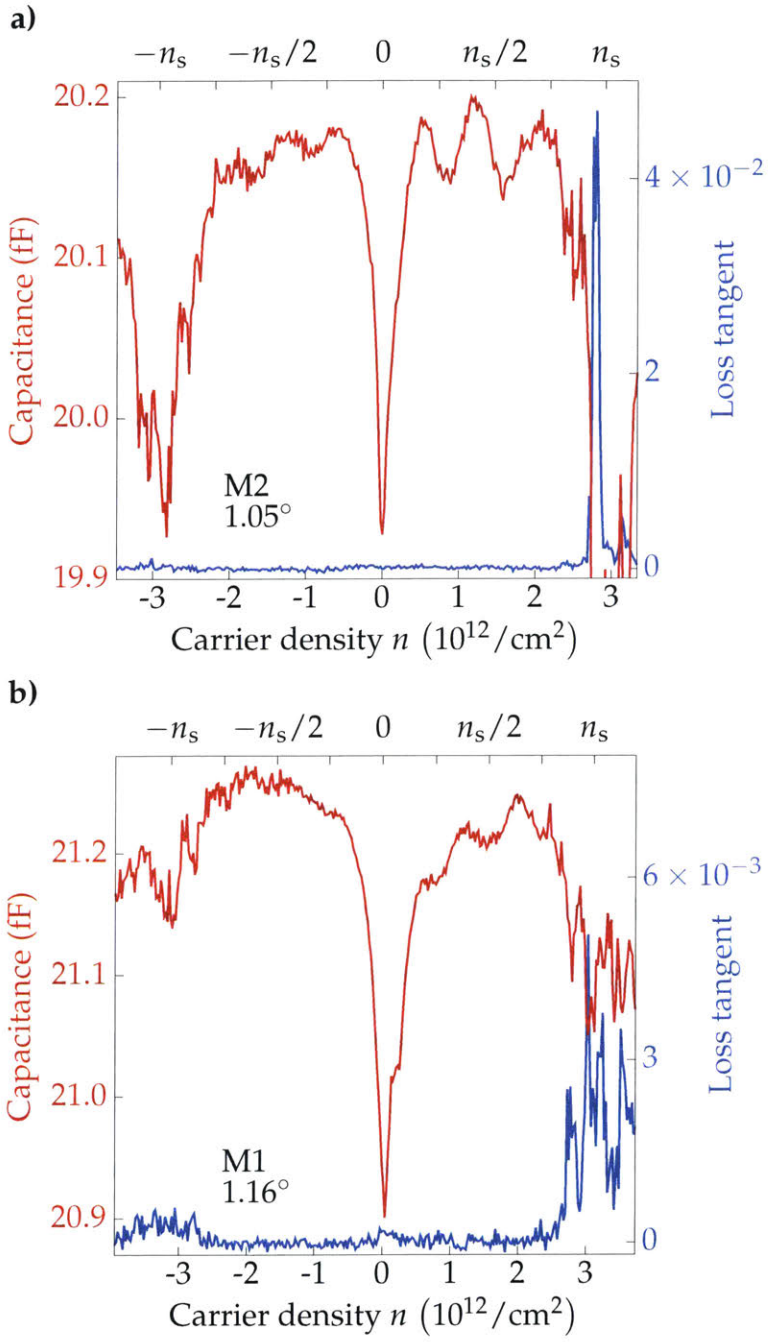

Figure 4-4: **Capacitance and loss tangent of magic angle graphene at zero magnetic field** for **a)** device M2 with angle 1.05° and **b)** device M1 with angle 1.16°. In both devices strongly incompressible phases are seen at $\pm n_s$ corresponding to the superlattice gaps. Additional incommensurate phases are seen at $n_s/4$ and $n_s/2$. Device M2 also shows weak incompressible features at $-n_s/2$ and $-n_s/4$. M2 and M1 were measured in a helium-3 cryostat at 280 mK and dilution cryostat at 225 mK, respectively. Measurements were performed with a 1 mV RMS excitation at 150 kHz.

erally stronger than their hole-doped counterparts [76–79].

In both devices we find incompressible phases at $n_s/4$ and weak incompressible features at $-n_s/4$ in device M2. Importantly, the magnitude of the incompressible features at $n_s/4$ and $n_s/2$ are comparable in magnitude despite a lack of insulating temperature-dependence at $n_s/4$ reported previously [18, 76, 78]. In device M2, raising the temperature to 5 K, the highest temperature accessed, produced virtually no change in the capacitance features at commensurate filling (see subsection 4.3.2). We see no strong compressibility features around $\pm 3n_s/4$ in contrast to recent transport studies [18, 76–79], although, we observe a gradual decrease in capacitance around $\pm 3n_s/4$ as the system enters the superlattice band gaps which makes observation of incompressible features difficult to distinguish in this region.

4.3.1 Reduced Fermi Velocity

After subtracting a constant background capacitance C_{back} arising from the substrate and bond pads (see details at the end of the chapter), the relationship

$$C_T^{-1} = C_{\text{geo}}^{-1} + \left(Ae^2 \partial n/\partial \mu\right)^{-1} \tag{4.1}$$

can be used to extract properties related to the compressibility $\partial n/\partial \mu$. At low temperatures, where thermal smearing from the Fermi–Dirac distribution is negligible, the compressibility can be approximated well by the zero-temperature density of states. Although the electronic structure of magic angle graphene is far from the monolayer graphene limit that holds for larger twist angles, we can still estimate the reduction of the Fermi velocity $v_F = \partial E/\partial(\hbar k)$ at $k = K_s$ using a monolayer-like model with the appropriate degeneracy factor. At low energy the monolayer graphene dispersion is given by

$$E_F = \hbar v_F k \tag{4.2}$$

and in two dimensions the number of k-states available is given by

$$N = g\frac{A}{(2\pi)^2}\pi k_F^2 \tag{4.3}$$

in terms of the lateral area A and the degeneracy factor g. Taking the derivative and substituting in terms of the energy we find

$$\frac{\partial n}{\partial \mu} = \frac{1}{A}\frac{\partial N}{\partial k_F}\frac{\partial k_F}{\partial E_F} = \frac{g k_F}{2\pi}\frac{1}{\hbar v_F} = \frac{\sqrt{g}}{\sqrt{\pi}\hbar v_F}\sqrt{|n|}. \tag{4.4}$$

For a Dirac-like system with eight-fold degeneracy arising from spin, valley, and layer degrees of freedom, $g = 8$. Additionally, because we are spatially averaging the density of states over the lateral area A of the sample, there will be some broadening of the density of states that creates a non-vanishing density of states at charge neutrality. This can be captured phenomenologically by convolving the density of states $\partial n/\partial \mu$ with a Gaussian $g(n) = e^{-n^2/2\Gamma^2}/\left(\sqrt{2\pi}\Gamma\right)$ where Γ characterizes the scales of the charge density broadening. The disorder-broadened density of states is then given by:

$$\frac{\partial n}{\partial \mu} * g(n). \tag{4.5}$$

We fit our capacitance data using Equations 4.1 and 4.5 and determine v_F, Γ, and the geometric capacitance C_{geo} from a best-fitting procedure. Although there is some mutual dependence on the values of C_{geo} and v_F, we do not expect the essential order of magnitude of the reduced Fermi velocity to change if we allow C_{geo} to vary over a reasonable range of uncertainty determined by the high magnetic field Landau level capacitance peaks (discussed at the end of the chapter). We estimate the area A from the lithographic dimensions of the magic-angle graphene heterostructure that lies over the back gate. The capacitance data from sample M2 are best fit by $v_F = 0.116 \times 10^6$ m/s and $\Gamma = 4.0 \times 10^{10}/\text{cm}^2$, both of similar magnitude to the values extracted previously with

a different sample (1.08°) [17]. Figure 4-5 shows the capacitance data from M2 overlaid with the model evaluated at various values of v_F.

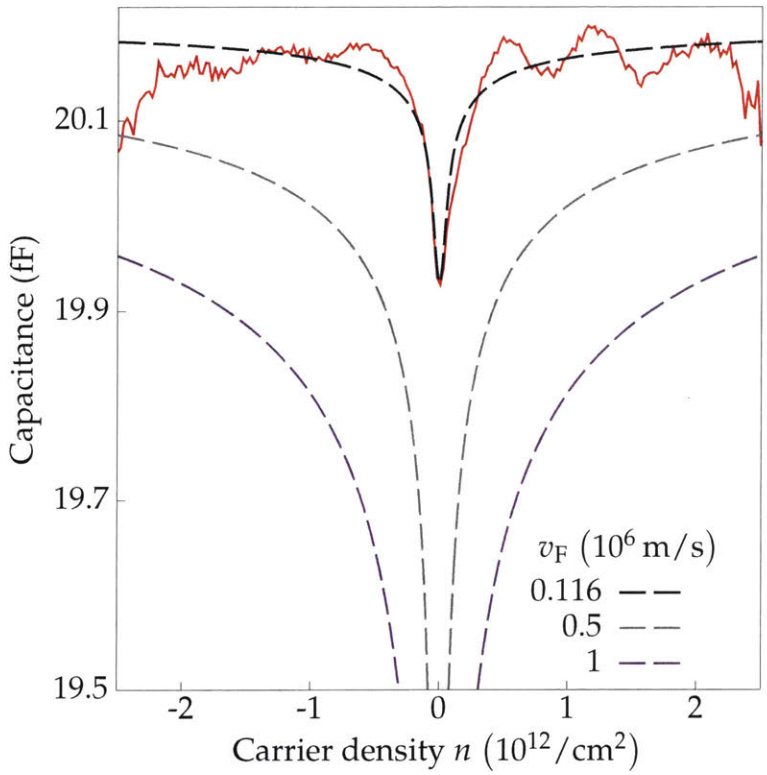

Figure 4-5: **Extraction of Fermi velocity for device M2** The Dirac point is best fit by $v_F = 0.116 \times 10^6\,\mathrm{m/s}$. The bare Fermi velocity $10^6\,\mathrm{m/s}$ (purple trace) and $0.5 \times 10^6\,\mathrm{m/s}$ (gray trace) are plotted for comparison.

4.3.2 Capacitance at Higher Temperature

Upon warming to 5 K the capacitance of sample M2 shows essentially no change near the commensurate filling gaps on the electron side at zero magnetic field as shown in Figure 4-6. The purple (orange) trace shows the capacitance at zero magnetic field and 280 mK (5 K). The lack of temperature evolution implies that the energy gaps at commensurate filling are well in excess of 5 K, consistent with our gap estimation in Figure 4-7. This rules out thermal broadening as an explanation for the relatively wide dips in capacitance at commensurate filling. The lack of sharp features is likely due to inhomogeneity in the twist angle throughout the device, causing the condition $n = n_s/2$ to occur at

slightly different carrier densities throughout the sample. At $B = 9\,\mathrm{T}$ the capacitance minima are suppressed upon warming from 280 mK (blue) to 5 K (red). At high magnetic field our measurements are no longer in the low frequency limit due to the large in-plane resistivity of the sample while in a quantum Hall gap. The capacitance minima at base temperature are exaggerated by the failure of the sample to charge completely on each excitation cycle. Upon warming to 5 K the in-plane conductivity increases, leading to a reduction in the capacitance features. This evolution at high magnetic field with temperature is likely not related to a change in the thermodynamic density of states, but rather in-plane transport features.

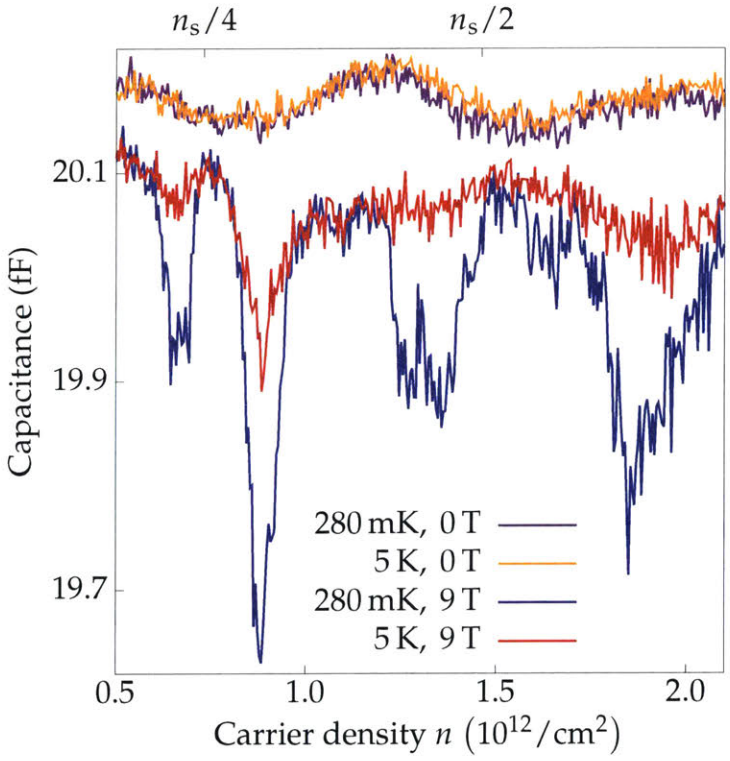

Figure 4-6: **High temperature capacitance of device M2** Plot of the temperature dependence of the capacitance on the electron side near commensurate fillings. The purple (orange) trace shows the zero-field capacitance at 280 mK (5 K) while the blue (red) trace shows the capacitance at $B = 9\,\mathrm{T}$ at 280 mK (5 K). The 9 T data has been shifted down for clarity. The capacitance was measured with a 2.8 mV RMS excitation at 30 kHz.

4.4 Chemical Potential Shift

One of the most important quantities accessible in our measurement is the chemical potential μ. The shift of the chemical potential as carriers are added to the device can be extracted by integrating the inverse quantum capacitance

$$\Delta\mu = \int \frac{\partial\mu}{\partial n} dn = \int Ae^2 \left(C_{\mathrm{T}}^{-1} - C_{\mathrm{geo}}^{-1}\right) dn. \tag{4.6}$$

Panel **a** of Figure 4-7 shows the calculated chemical potential as a function of carrier

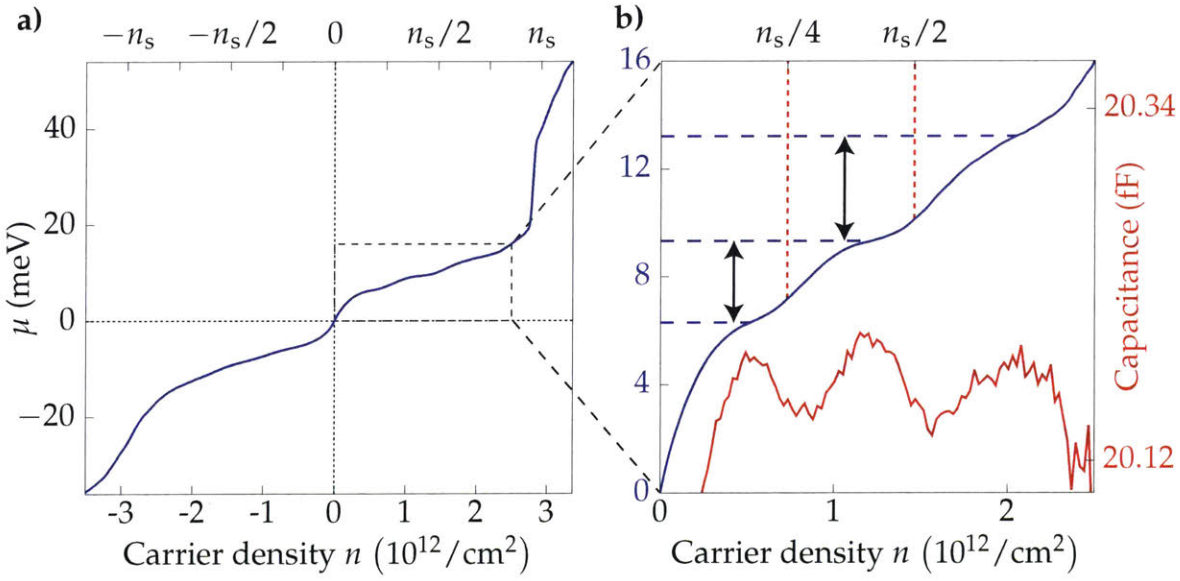

Figure 4-7: **Shift of chemical potential in device M2 as a function of carrier density a)** The shift in μ was extracted by integrating the inverse quantum capacitance. **b)** Zoom-in to boxed region of **a**. The increase in the chemical potential between the density of states maxima at both $n_s/4$ and $n_s/2$ is shown on the left axis with capacitance data from panel **a** of Figure 4-4 replotted on the right axis. The horizontal dashed lines indicate the range of the density of states maxima around the dips at $n_s/4$ and $n_s/2$. We find $\Delta_{n_s/4} = (3.0 \pm 1.0)$ meV and $\Delta_{n_s/2} = (3.9 \pm 1.2)$ meV.

density for device M2. Portions of the trace with relatively flat slopes correspond to compressible phases where the chemical potential shifts relatively little as carriers are added to the system. Conversely, steeper regions correspond to reductions in the density of states. The superlattice band gaps around $\pm n_s$ manifest as the steep slopes near

$n = \pm 3 \times 10^{12}\,\mathrm{cm}^{-2}$. On the electron side, where the size of the capacitance dips is appreciable, the thermodynamic gap between the density of states peaks can be calculated for both $n_s/4$ and $n_s/2$ as shown in panel **b** of Figure 4-7. We find $\Delta_{n_s/4} = (3.0 \pm 1.0)\,\mathrm{meV}$ and $\Delta_{n_s/2} = (3.9 \pm 1.2)\,\mathrm{meV}$ where the error associated with the gap estimation arises from a systematic error in the determination of C_{geo}. In these calculations we use the value of C_{geo} which is determined by the best fit of the capacitance data to the model in Equation 4.1. In order to account for the possibility that the geometric capacitance may deviate from this fit-derived value, we determine a range of uncertainty by inspection of highly compressible Landau levels. The error estimation and its propagation in the thermodynamic gap measurements is discussed at the end of the chapter. The gap at $n_s/4$ was either not observed previously [17, 18, 80, 81], found to have non-activated temperature dependence [76, 78], or the resistive feature was not discussed in detail [77]. A recent transport study reported simply-activated temperature dependence at quarter-filling with a gap value of 0.14 meV [79], though the presence of a gap at charge neutrality in reference [79] may indicate that the twisted bilayer graphene is aligned with the underlying hBN substrate as possibly indicated by the presence of a gap at charge neutrality in contrast to what we observe in our devices. Our estimate of $\Delta_{n_s/2}$ is significantly larger than the previously reported values of 0.31 meV in reference [17], $\sim$1.5 meV in reference [76], and 0.37 meV in reference [79].

We expect the gap extracted from thermodynamic compressibility to be larger than the activation gap measured through the temperature dependence of the resistivity. As temperature is increased, the electron–electron correlations that create the many-body gap may weaken, causing the gap to decrease as a function of temperature and leading to an underestimation in activation measurements. By measuring at a fixed, low temperature, the gap derived from compressibility is potentially larger. Additionally, there may be a large density of charge carriers that can be thermally excited across the many-body gap at energies that are closer to the Fermi level than the density of states maxima, leading

to a smaller activation gap. If we measure the shift in chemical potential just around the steepest portions of trace in panel **b** of Figure 4-7, we find values of approximately 2 meV and 2.5 meV for the $n_s/4$ and $n_s/2$ states, respectively. These values may compare more directly to activation measurements.

We can also make a comparison to recent scanning tunneling spectroscopy (STS) measurements in which splittings of the van Hove singularity at $n_s/2$ of roughly 7.5 meV [80] and $4-8$ meV [81] have been measured. Because the scanning tunneling microscope tip is placed over a clean, atomically resolved region of the sample, the effects of disorder averaging are avoided, leading to a potentially larger observed spectroscopic gap. We note that the van Hove singularity separation when the Fermi level lies at half-filling as seen in STS measurements differs qualitatively from the chemical potential separation observed in compressibility. In the latter case, the carrier density and the band structure itself vary as the Fermi level is raised due to density-dependent electron–electron interactions as discussed in subsection 3.2.1. Additionally, STS measures the single particle density of states which is a different quantity from the thermodynamic density of states $\partial n/\partial \mu$ accessed in our measurements.

4.5 Compressibility at Zero Magnetic Field

We plot the compressibility $\partial n/\partial \mu = \frac{1}{Ae^2}\left(C_T^{-1} - C_{geo}^{-1}\right)^{-1}$ as shown in Figure 4-8. The vertical scale of the compressibility is very sensitive to the precise value of C_{geo}, particularly the highly compressible phases in which $C_T \approx C_{geo}$. Nonetheless, the horizontal axis is much less sensitive to variation in C_{geo}, and we can estimate the bandwidth of the two low-energy moiré bands as 35 meV. If we vary the precise value of C_{geo} over an estimated uncertainty, the bandwidth varies from as small as 25 meV to as large as 45 meV. This range of values is much larger than initial calculations for a rotation angle of 1.05° [16, 17, 40, 44], but it is consistent with the 41 meV separation of the valence and conduc-

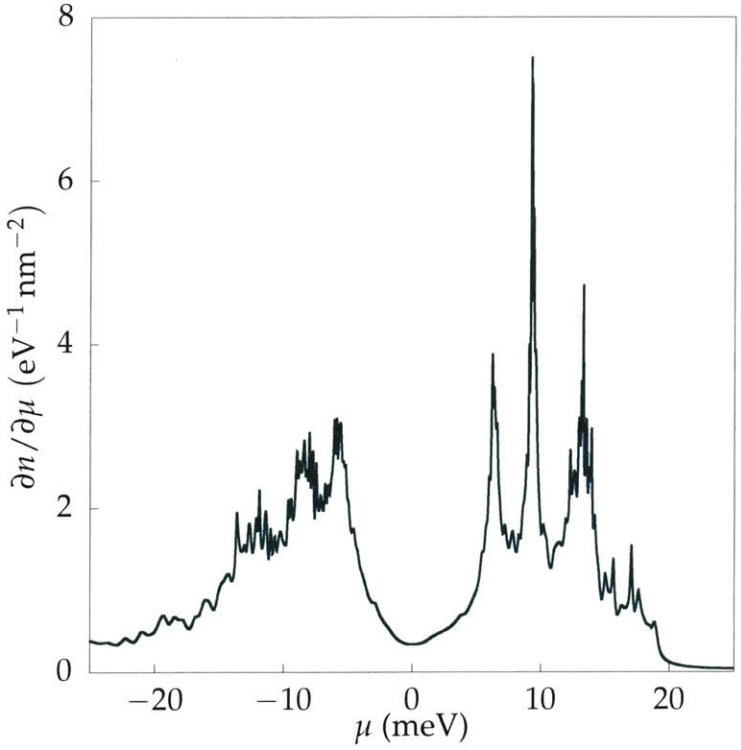

Figure 4-8: **The compressibility of device M2** is plotted as a function of chemical potential μ. The approximate bandwidth is 35 meV.

tion band van Hove singularities predicted by recent tight-binding calculations and the accompanying 55 meV separation observed by STS for a slightly larger rotation angle of 1.10° [80].

In order to explore the dependence of $\partial n/\partial \mu$ on the value of the geometric capacitance, we plot the compressibility for our best estimate of C_{geo} as well as the upper and lower bounds of our uncertainty estimate $C_{geo} \pm \delta c$ for $\delta c = 0.014\,\mathrm{fF}$ in Figure 4-9. The bandwidth range is roughly $25 - 45\,\mathrm{meV}$. The vertical axis is very sensitive to the specific choice of C_{geo} whenever $C_T \approx C_{geo}$ which is why the highly compressible peaks reach such different values of $\partial n/\partial \mu$. The lower compressibility features (e.g. charge neutrality, commensurate filling on the electron side) show much less variation. The plot in panel **c** has been cut off above $15\,\mathrm{eV^{-1}\,nm^{-2}}$, where the central density of states maximum rises to about $55\,\mathrm{eV^{-1}\,nm^{-2}}$, in order to more easily compare the low compressibility features between panels.

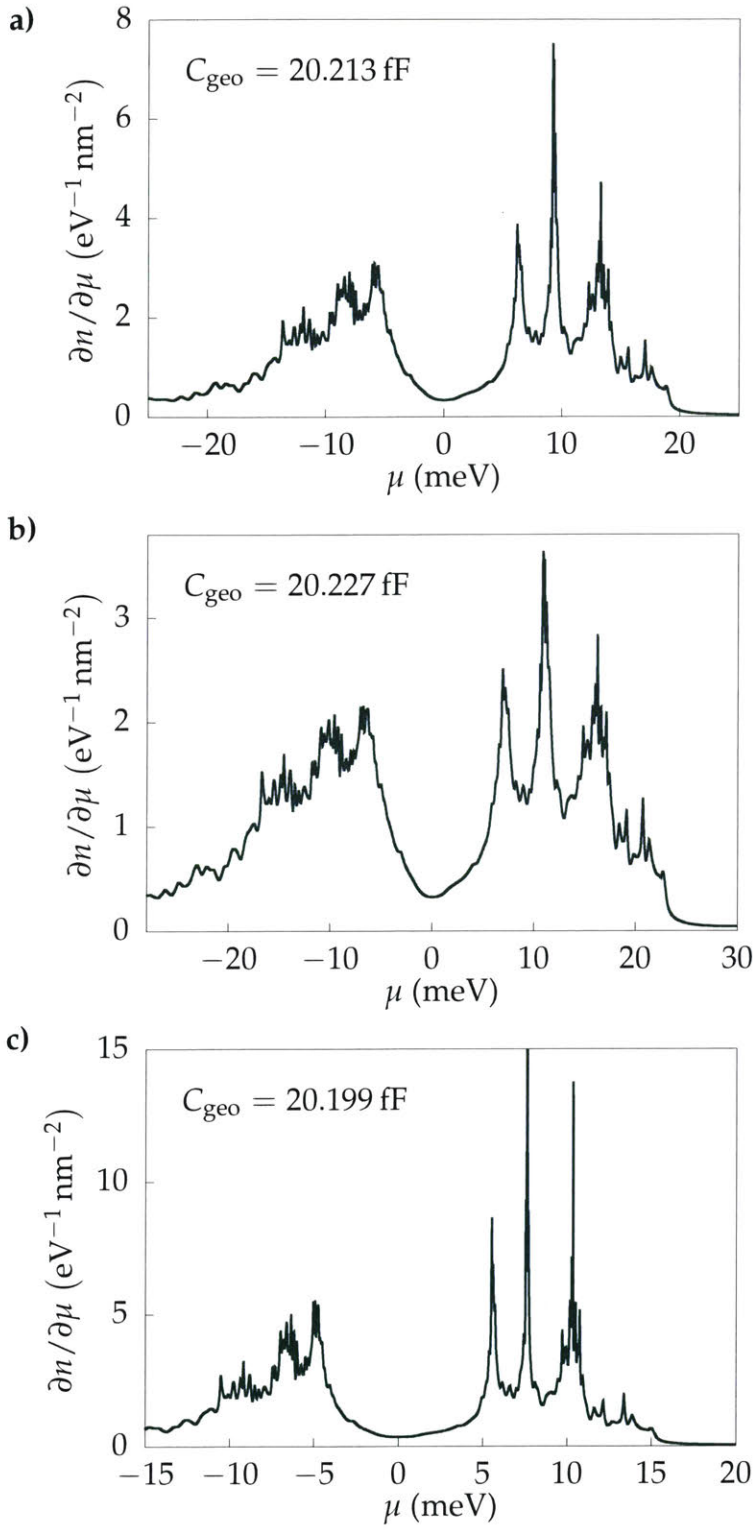

Figure 4-9: **Comparison of the compressibility for M2 with different C_{geo} a)** The best estimate 20.213 fF is used. **b)** The largest value in the uncertainty range 20.227 fF is used. **c)** The smallest value in the uncertainty range 20.199 fF is used.

4.6 Magnetic Field Dependence

We also measure the evolution of the compressibility with magnetic field up to the quantum Hall regime. In panel **a** of Figure 4-10 we plot the capacitance as a function of gate voltage and magnetic field. The incompressible phases at commensurate filling of the mini-band do not appear to change with perpendicular magnetic field up to about 3 T after which field-induced gaps arise and coexist, making it difficult to track the relatively broader features associated with the zero-field incompressible phases. The most prominent feature in panel **a** of Figure 4-10 is the four-fold degenerate Landau fan that emerges from charge neutrality. Despite anticipating an eight-fold degenerate zero-energy Landau level arising from spin, valley, and layer degrees of freedom, our system never develops a compressible phase at charge neutrality, indicating that layer or valley symmetry breaking is present even at zero magnetic field. Four-fold degeneracy may be evidence of C_3 rotational symmetry breaking as recently proposed [82]. At larger magnetic fields, we observe incompressible phases at filling factors within the lowest Landau level octet. These additional incompressible phases presumably arise from exchange-driven gaps as reported in monolayer and bilayer graphene [52, 83–87]. In addition, Landau levels emerging from the superlattice gaps of device M2 are apparent in panel **a** of Figure 4-10 as well as from device M1 (see Figure 4-13).

Additionally, we see a set of gaps emerging from high magnetic field whose intercepts terminate near the fractional filling densities as indicated by the red traces in panel **b** of Figure 4-10. These gaps appear to form as a result of "Hofstadter" fractal mini-bands [88, 89]. In panel **a** of Figure 4-10 some of the gaps which approach commensurate filling appear doubled, suggesting there may be multiple regions within the device with slightly different twist angle. The number of flux quanta per moiré unit cell is plotted on the right vertical axes in Figure 4-10. The incompressible phases shown in red intersect at $\phi/\phi_0 = 1$ which occurs at $B = 29.64\,\mathrm{T}$ for $\theta = 1.05°$. The Wannier diagram in Figure 4-11 displays some of the possible trajectories of the incompressible phases (gray tracs) while the black

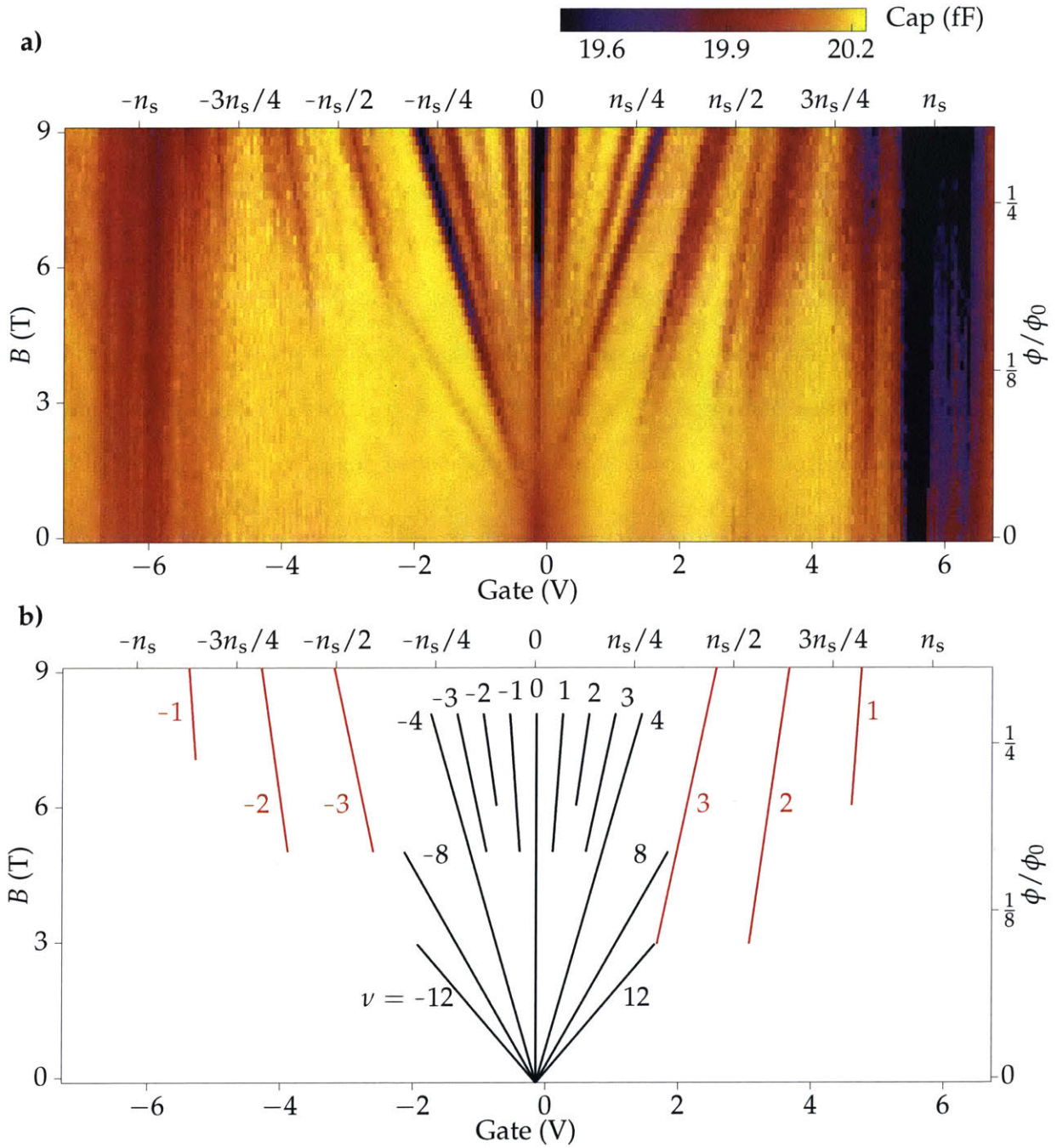

Figure 4-10: **The field-dependence of the capacitance of device M2 a)** The capacitance up to the quantum Hall regime is plotted as a function of gate voltage and magnetic field. The color scale has been suppressed below 19.5 fF in order to show more detail. **b)** A map of observed gaps in magnetic field measurement in **a** is plotted. Black traces indicate cyclotron and exchange gaps arising from charge neutrality with the filling factor labeled. Red traces indicate gaps emanating from high magnetic field due to "Hofstadter" replica mini-bands at commensurate filling and magnetic field.

and red traces are colored to match the features in Figure 4-10. Similar features have been observed extensively in aligned graphene–hBN structures [87, 90, 91] as well as twisted bilayer graphene devices [37, 61].

Unlike reference [76], where no Landau fan was observed emanating from $-n_s/4$, we observe an incompressible phase emerge from high magnetic field whose intercept terminates at $-n_s/4$. Additionally, we observe an incompressible phase emanating from $n_s/4$ corresponding to $\nu = 3$ and not $\nu = 1$ as seen previously [76]. The presence of strong quantum oscillations at low magnetic field close to commensurate filling in transport [18, 76, 79] indicates the formation of an emergent Fermi surface and its quantization in magnetic field. Oscillations in transport measurements reflect the field-dependence of both the scattering time τ as well as the density of available charge carriers. Because low-frequency capacitance measurements are insensitive to changes in the scattering rate, strong features are not expected when Landau quantization is weak which may explain the lack of low-field capacitance oscillations in our data in contrast with transport [18, 76].

In Figure 4-12 we plot the loss tangent of device M2 as a function of carrier density and magnetic field in order to reveal additional information about the in-plane conductivity of the sample. The loss tangent is given by $\omega R_{\text{in-plane}} C_T$. Increases in the loss tangent correspond to increases in the in-plane resistance (which tend to dominate any changes in C_T at high magnetic field for this device) as a resistive state is entered and serve as a qualitative measure of the in-plane bulk transport. The bright features emanating from charge neutrality are the cyclotron and exchange gaps arising from the quantum Hall regime whereas the bright features that emanate from high magnetic field and terminate near the commensurate fillings arise from fractal "Hofstadter" mini-bands due to the interaction of the magnetic field and superlattice potential. Importantly, the half-filling state on the electron-doped regime shows faint vertical features which appear to terminate around 3 T, though they becomes partially obscured due to the coexistence of the fractal mini-band feature. This indicates that the resistive features survive to at least 3 T. There are

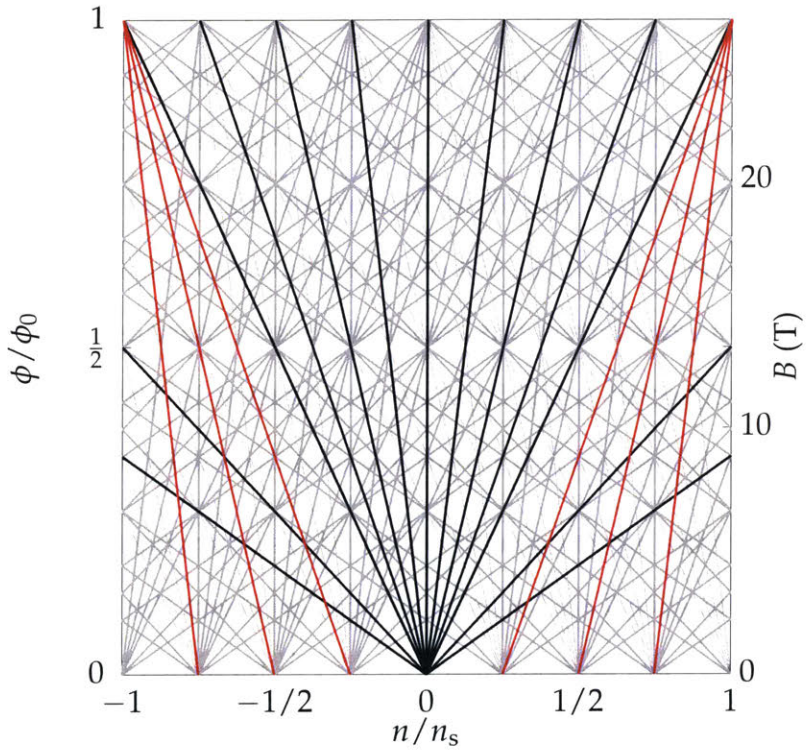

Figure 4-11: **Wannier diagram** showing the possible trajectories of incompressible phases due to a combination of magnetic field and superlattice potential. The black and red traces are colored to match the incompressible phases indicated in panel **b** of Figure 4-10.

multiple closely spaced resistive features which are grouped around the half-filling location, indicating possible inhomogeneity in the rotation angle across the lateral extent of the sample. Importantly, we do not see doubling of the central Landau fan indicating that the charge density across the sample remains uniform. We do not see noticeable resistive features associated with either the hole states or the quarter-filled electronic state.

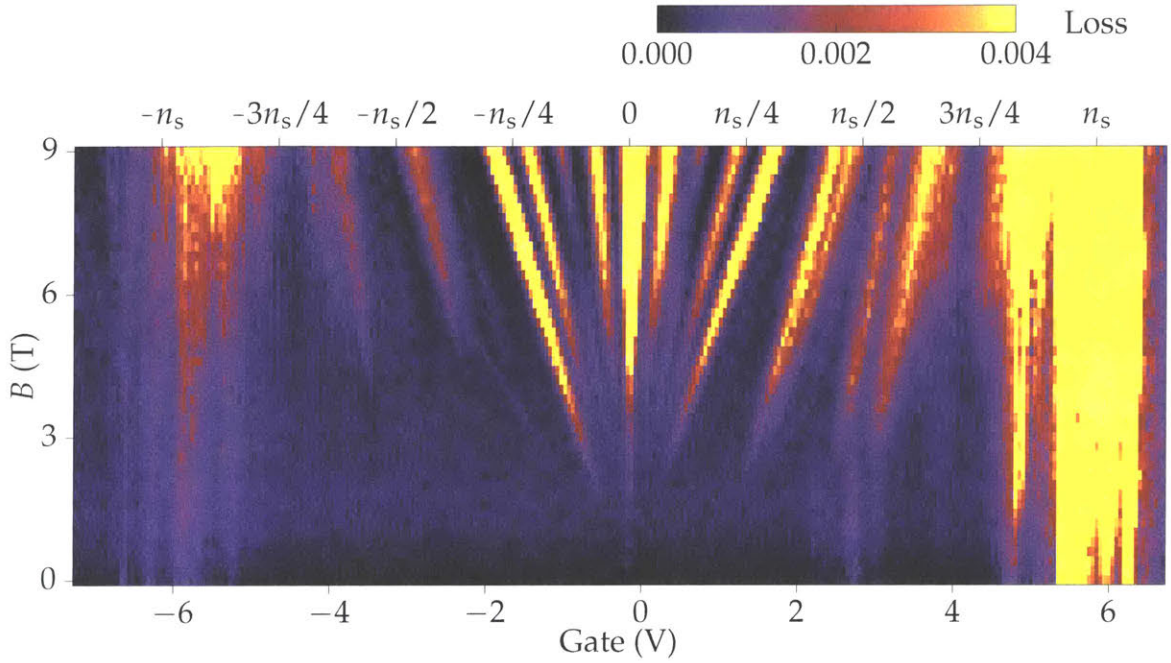

Figure 4-12: **The loss tangent of device M2** is plotted with respect to magnetic field and carrier density. Weak resistive features around $n_s/2$ are visible and track vertically with magnetic field until being obscured by the fractal mini-band gaps around 3 T. Multiple vertical features adjacent to one another indicate that the twist angle may be inhomogeneous through the entire sample. The color scale has been suppressed above 0.004 in order to reveal weaker features at low magnetic field.

In panel **a** of Figure 4-13 we plot the magnetic field dependence of device M1. Adjacent to the main Landau fan is a second, weaker fan emanating from a displaced Dirac point, indicating that the sample experiences a second region which is at a slightly different doping. This may be associated with a region of the device adjacent to one of the ohmic contacts away from the central portion of the etched Hall bar geometry. Similar to device M2, incompressible phases (red lines in panel **b** of Figure 4-13) emerge from high magnetic field on the electron-doped side and tend towards commensurate filling loca-

tions on the abscissa. Here, the gaps emanating from high field do not appear doubled (as in device M2), indicating improved homogeneity in the rotation angle.

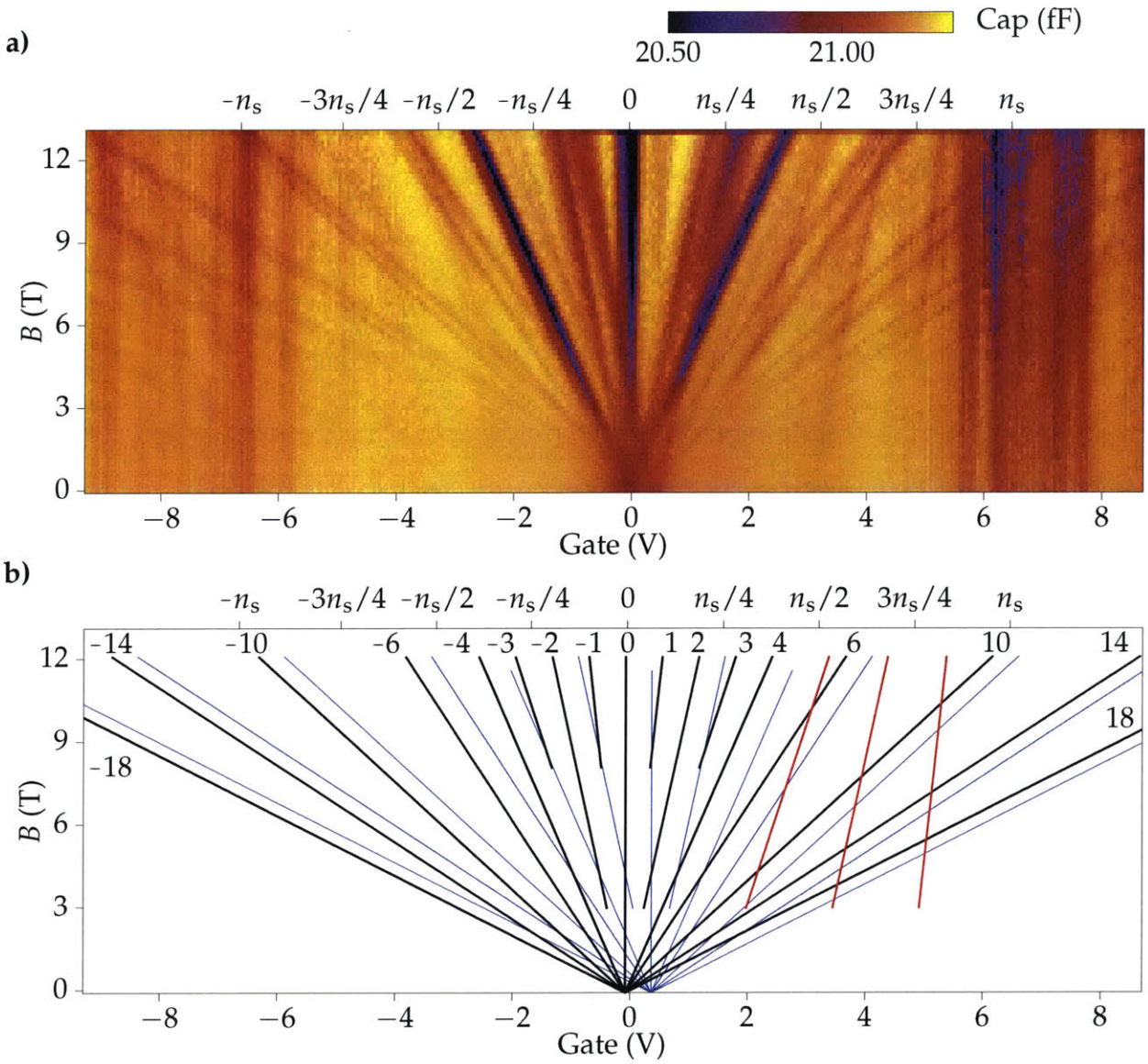

Figure 4-13: **The field dependence of device M1 a)** The capacitance up to the quantum Hall regime is plotted as a function of gate voltage and magnetic field. The color scale has been suppressed below 20.5 fF. **(b)** Schematic showing some of the important incompressible phases of device M1. The black lines indicate cyclotron or exchange gaps arising from the central Landau fan. The blue lines indicate the gaps arising from an additional, weaker Landau fan, indicating device M1 has a region of density inhomogeneity. Filling factors are labeled. The red lines indicate field-induced gaps which terminate at the commensurate filling associated with fractal mini-band gaps. In contrast to device M2, the fractal mini-band gaps do not appear doubled, indicating improved twist angle uniformity.

4.7 Discussion

4.7.1 Incompressible Phases

Although there is no consensus on the nature of the commensurate insulating phases, our results allow us to comment on a few recent proposals. One effort posits that the correlated insulating phase at half-filling is not a Mott-like insulator, but rather a Wigner crystal in which the electrons freeze into an emergent lattice as a result of long-range Coulomb repulsion [64, 74]. Although a Wigner crystal is electrically insulating due to pinning of the electron lattice by disorder, domains, or the moiré lattice itself, the compressibility of the Wigner crystal is expected to be large and negative due to long-range Coulomb interactions [92]. Unlike DC transport, compressibility is one of the few techniques which is capable of providing positive evidence of Wigner crystallization. In our measurements, the compressibility decreases at commensurate filling while remaining positive and non-diverging, implying the likely formation of an energy gap and not a highly (negatively) compressible phase expected for an ideal Wigner crystal. However, unlike the conventional case, if the moiré potential strongly pins the electron lattice, it may be possible to form a thermodynamic energy gap [93]. We also cannot rule out the possibility of such a Wigner crystal and another gapped phase coexisting via phase separation as has been speculated to occur in GaAs bilayers [94]. Additionally, it may be possible to interpret the multiple density of states peaks as arising from differential strain between the two twisted bilayer graphene layers [95].

4.7.2 Bandwidth

Although initial band structure calculations predicted narrow low energy bands between 5 and 10 meV [16, 17, 40, 44, 70], recent focus on lattice relaxation effects have brought estimates closer to experiment ($\sim$20 meV) [96, 97], however, at least one other lattice relaxation model predicts a narrowing of the bandwidth as compared to unrelaxed calcu-

lations [98]. Our data support a bandwidth in the range of 25 to 45 meV, suggesting that the non-interacting band structure is not as narrow as anticipated by theory, leading to larger values of kinetic energy. This suggests that, in the creation of the correlated insulating states, the kinetic energy may play a more substantive role than many single-particle calculations imply. Moreover, as recently proposed [75], it is possible that the interaction effects are also strongly enhanced by a power-law diverging van Hove singularity.

4.8 Conclusions

In summary, we used compressibility measurements to access the shift of the chemical potential as the low-energy band structure is filled. We report a reduced Fermi velocity, a wide $\sim$35 meV bandwidth compared with many electronic structure calculations, and measure the gap widths at $n_s/4$ and $n_s/2$. The incompressible features at commensurate filling show essentially no field-evolution up to 3 T before becoming obscured by other field-induced gaps. We do not observe strong Landau quantization at low magnetic field around commensurate filling, but at larger magnetic field we detect "Hofstadter" gaps that differ from previous transport studies [17, 76, 79].

Reference	**Technique**	θ	$\Delta_{n_s/2}$ (meV)	$\Delta_{n_s/4}$ (meV)	**Bandwidth** (meV)
This work	Compressibility	1.05°	3.9 ± 1.2	3.0 ± 1.0	35 ± 10
[17]	Transport	1.08°	0.31		
[76]	Transport	1.10°	$\sim$1.5		
[80]	STS	1.10°	$\sim$7.5		55
[81]	STS	1.04°	$4 - 8$		$\sim$50
[79]	Transport	1.10°	0.37	0.14	

Table 4.1: **Comparison of gaps and bandwidths** from recent transport and tunneling reports and the results contained in this thesis.

4.9 Additional Details

4.9.1 Sample Preparation

The samples were fabricated using a dry transfer technique modified with a rotation stage described previously [17, 18, 37]. The devices were originally measured in reference [18]. Monolayer graphene and hBN crystals of 10–30 nm thickness were exfoliated onto clean Si/SiO_2 substrates, identified optically, and characterized with atomic force microscopy. The twisted bilayer graphene was constructed by "tearing and stacking" a clean monolayer with a precise rotational misalignment. A poly(bisphenol A carbonate) (PC)/polydimethylsiloxane (PDMS) stack on a glass slide was used to first pick up a piece of hBN at 90 °C after which the van der Waals forces between hBN and graphene were used to tear a graphene flake close to room temperature. The separated graphene pieces were rotated manually by a twist angle around 1.2–1.3° and stacked on top of one another. The stack was encapsulated by a piece of hBN on the bottom and released at 160 °C onto a Cr/PdAu metal back gate on top of a highly resistive Si/SiO_2 substrate. The samples were not annealed to prevent the twisted bilayer graphene from relaxing back to Bernal-stacked bilayer graphene. The device geometry was defined using standard electron-beam lithography techniques and reactive ion etching with fluoroform and O_2 plasmas. Electrical contact was made to the twisted bilayer graphene with Cr/Au edge-contacted leads [99].

4.9.2 Measurement Circuit

Sample M2 was measured in a helium-3 cryostat at 280 mK, and sample M1 was measured in a dilution refrigerator at a temperature of 225 mK with the exception of the high temperature measurements of M2. Capacitance and loss tangent measurements were carried out on homemade cryogenic capacitance bridges on the same chip carriers as the samples. Figure 4-14 shows the full circuit schematic. The sample is modeled as a series

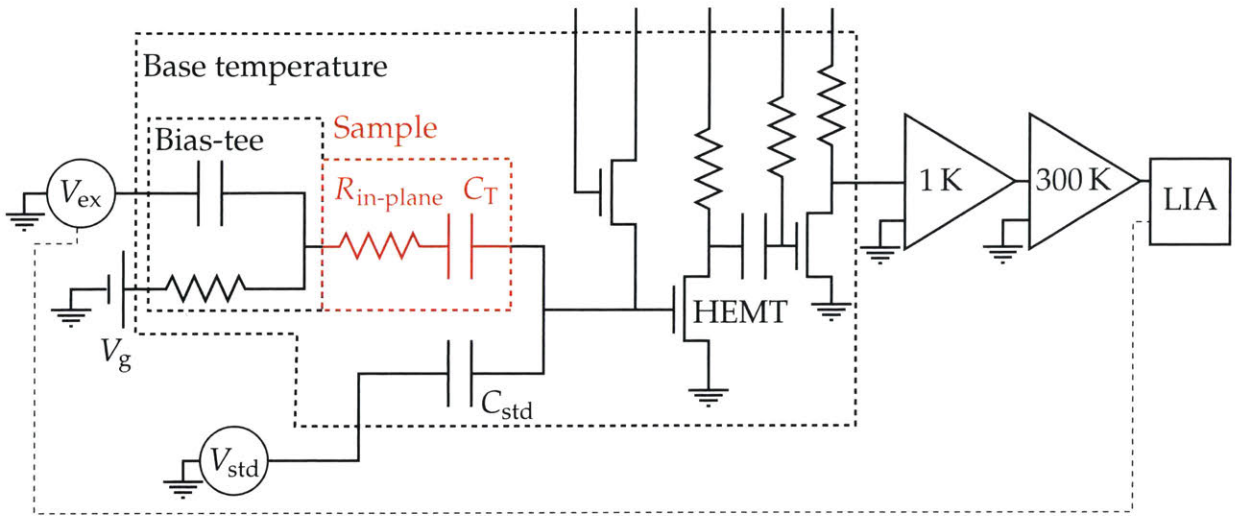

Figure 4-14: **The cryogenic impedance bridge** used to measure the capacitance and loss tangent contains a double-stage amplifier at base temperature. The signal is driven to the lock-in amplifier by additional amplification stages at the 1 K pot and at room temperature.

resistor and capacitor in red. AC and DC voltages are applied to the sample through a cryogenic bias-tee adjacent to the sample. An AC signal of variable phase and amplitude is applied to a fixed ~45 fF reference capacitor to balance the sample capacitance at the bridge balance point. After an initial balance is achieved, changes in the sample capacitance are inferred from the off-balance voltage that accumulates at the balance point. The size of the reference capacitor is determined on a subsequent cooldown with a known 2 pF capacitor. Three Fujitsu FHX35X high electron mobility transistors (HEMTs) are used in a double-amplifier configuration. The main amplification stage occurs at the gate of the labeled HEMT which has been cleaved in half to minimize its stray capacitance. A second HEMT (also cleaved) is used as a variable resistor (typically set to about 100 MΩ) to pinch off the measurement HEMT's channel to about 100 kΩ. A third follower HEMT which is uncleaved drives the signal to a homemade wide-bandwidth amplifier located at the 1 K pot of the fridge followed by a similar amplification stage at room temperature before being measured on a lock-in amplifier (Signal Recovery SR7280). See Appendix B for the full circuit layouts of the cryogenic amplifiers. An excitation voltage of 2.8 mV RMS was

applied at 150 kHz for all measurements unless otherwise indicated.

4.9.3 Capacitance Corrections

Due to slight mismatches in the cabling of the reference and sample lines due to different attenuators as well as slight offsets in the relative phase of the excitation and reference voltages sources, our measurements show a constant offset in the out-of-phase component (which for small values of Y is approximately equal to the loss tangent) that is not attributed to the sample. In order to correct for this small phase shift we find the values of the in-phase and out-of-phase components of our signal near a highly compressible state that should have minimal in-plane resistance and an extremely small out-of-phase component. We apply a rotation matrix $M(\theta)$ (typically the rotation angle $\theta \approx 1°$) to our in- and out-of-phase signal measurements to correct this artifact. This leaves the in-phase component virtually unchanged and shifts the out-of-phase signal to the correct baseline.

Our samples have a substantial stray capacitance of around 50 fF that manifests in our measurement as a constant background in parallel with the sample $C_{raw} = C_{back} + C_T = C_{back} + \left(C_{geo}^{-1} + C_q^{-1}\right)^{-1}$. In order to accurately subtract this constant background, we utilize the field-dependent capacitance measurements where we can accurately determine the minima of the cyclotron gaps of the Landau fan emerging from charge neutrality (see Figure 4-10). Regardless of the underlying band structure, all Landau levels can be characterized by a field-dependent orbital degeneracy $\phi/\phi_0 = BAe/h$ where ϕ is the total magnetic flux through the sample, ϕ_0 is the flux quantum, B is the magnetic field, A the sample area, e is the elementary charge, and h is Planck's constant. This orbital degeneracy is augmented by a factor of 8 arising from the spin, valley, and layer degrees of freedom. Therefore, between the filling factor $\nu = \pm 4$, we know the total charge accumulated in the sample is given by $8BAe^2/h$. The total charge accumulated in the sample is also given by integrating the total capacitance: $Q = \int_{\Delta V} C_T dV$ where the limits of integration are determined by the gate voltages in Figure 4-10. Therefore, the appropriate

value of C_{back} is found by enforcing

$$8BAe^2/h = Q = \int_{\Delta V} (C_{raw} - C_{back})\, dV. \tag{4.7}$$

In this analysis we assume that the strongest gaps emerging from charge neutrality correspond to $\nu = \pm 4$ as expected for a twisted bilayer graphene system. This is confirmed by calculating the slope of the gaps in Figure 4-10 and using the relationship

$$\nu = \frac{nA}{\phi/\phi_0} = \frac{n\phi_0}{B} = \frac{(\overline{C_T}/A)\,\Delta V \phi_0}{eB} \tag{4.8}$$

where $\overline{C_T}$ is the average total capacitance between the Landau level minima. Because $\overline{C_T}$ is roughly equal to the geometric value of the capacitance which is well approximated by a parallel plate model, we can say $\overline{C_T}/A \approx \epsilon\epsilon_0/d$ where ϵ is the relative dielectric of the hBN ($\sim$4.5) and d is the thickness of the dielectric ($\sim$30 nm) determined from atomic force microscopy and ϵ_0 is the vacuum permittivity, yielding:

$$\nu \approx \frac{\epsilon\epsilon_0 \Delta V \phi_0}{deB}. \tag{4.9}$$

After extracting the slope of the gap in Figure 4-10 and equating it to $\frac{B}{\Delta V}$ and using estimated values for ϵ and d, we can verify that $\nu = \pm 4$. Additionally this allows us to verify that our background subtraction is reasonable by confirming $\overline{C_T} \approx C_{raw} - C_{back}$.

4.9.4 Converting to Carrier Density

Unlike transport measurements, our capacitance technique allows us to convert gate voltage to carrier density exactly. Typically, in transport the gating capacitance is taken as a constant $\overline{C_T}$ (usually extracted from Landau fans or modeled with parallel plate geometries) and is often described as purely geometric but in reality is an average value of the *total* capacitance that includes contributions from the quantum capacitance that vary as a

function of density. In most samples $C_q \gg C_{geo}$ so that $C_T \approx C_{geo}$, allowing this approximation to hold. For our measurements we can simply integrate the total capacitance with respect to gate voltage to directly calculate the induced charge density:

$$n(V) = \frac{1}{Ae} \int_{V_{Dirac}}^{V} C_T(V')dV' \tag{4.10}$$

where we have set the carrier density at the gate voltage associated with the Dirac point to 0. For our samples the quantum capacitance C_q is always much larger than the geometric capacitance inside the superlattice gaps. Therefore, the relationship between carrier density and gate voltage is roughly proportional, but there are subtle nonlinearities near locations of relatively small quantum capacitance (e.g. near charge neutrality) that are captured in this conversion.

4.9.5 Determining the Geometric Capacitance

Our quantitative analysis relies on estimating the value of the geometric capacitance C_{geo}. In order to estimate C_{geo} we use the model $\mathcal{C}(n)$ for the total capacitance:

$$\mathcal{C}(n) = \left(\frac{1}{C_{geo}} + \frac{1}{Ae^2 \partial n / \partial \mu(n)} \right)^{-1}. \tag{4.11}$$

For a bilayer graphene system with eight-fold degeneracy the density of states is given by

$$\frac{\partial n}{\partial \mu} = \frac{2\sqrt{2}}{\sqrt{\pi}\hbar v_F} \sqrt{|n|} \tag{4.12}$$

where E_F is the Fermi energy, v_F the Fermi velocity, and $\hbar$ is Planck's reduced constant. We convolve $\partial n / \partial \mu$ with a Gaussian $g(n) = e^{-n^2/2\Gamma} / \left(\sqrt{2\pi}\Gamma \right)$ to take into account disorder-broadening. We fit this model to our data to determine the best fit values of v_F, Γ, and C_{geo}. The value of C_{geo} extracted from best-fitting agrees nicely with the peaks in the

highly compressible Landau levels that we expect to be very close to the geometric capacitance and possibly in excess if negative compressibility is present [100, 101]. See Figure 4-15 for plots of C_{geo} overlaid with the field-dependent capacitance data. In order to account for the fact that our fit-derived value may deviate from the true value of the geometric capacitance, we estimate an uncertain $\delta c = 0.014\,\text{fF}$ in C_{geo} based on a visual analysis of the compressible Landau level peaks. The lower bound of our uncertainty corresponds to assuming that the density of states maxima in the zero-field capacitance data are nearly perfectly compressible. This is a reasonable lower bound assuming that the density of states peaks do not exhibit negative compressibility. This is justifiable if we compare these maxima to the highly compressible Landau levels between $\nu = -12$ and $\nu = -4$ at $B = 3\,\text{T}$, a large enough field for good Landau quantization but low enough that the exchange gaps and "Hofstadter" features at high magnetic field do not overlap. The capacitance signal forms clear plateaus with no sign of negative compressibility and remains larger in value than the zero-field data at all densities. See **b** of Figure 4-15 where the blue trace saturates close to the fit-derived value of C_{geo} between about $n = -1$ and $-0.5 \times 10^{12}\,\text{cm}^{-2}$ and remains larger than all capacitance values in the red trace. The upper bound of C_{geo} is placed near the highest capacitance values recorded at high magnetic field where we expect the capacitance peaks to be highly compressible and possibly enhanced beyond the geometric value if negative compressibility is present. The role of the geometric capacitance uncertainty and its propagation in the thermodynamic gap and bandwidth calculations are detailed below.

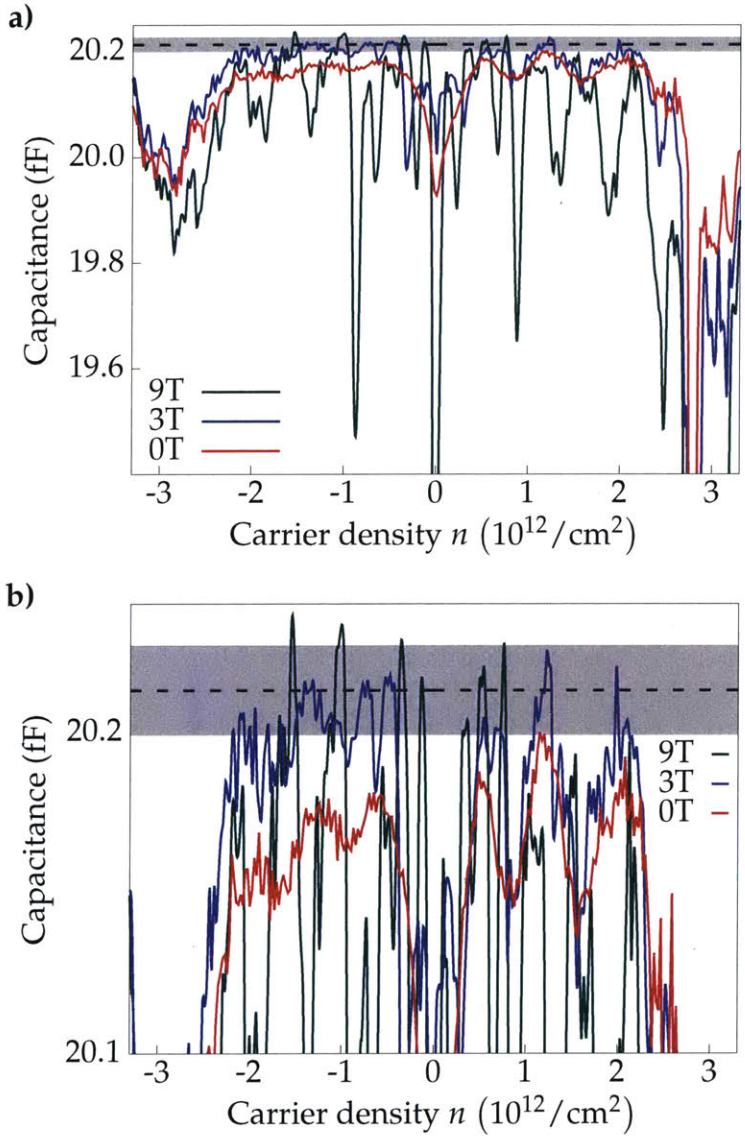

Figure 4-15: **a)** Plot of capacitance traces at $B = 0$ (red), 3 T (blue), and 9 T (green) as well as the estimate for C_{geo} (black dashed trace). The gray region represents the estimated uncertainty in C_{geo}. **b)** Zoom-in of **a**.

4.9.6 Uncertainty in Thermodynamic Gaps and Bandwidth

The inverse compressibility is integrated to extract the chemical potential μ as a function of carrier density n. A small error (compared to the magnitude of C_{geo}) in the geometric capacitance causes a spurious linear background in the overall slope of $\mu(n)$. If we take the true geometric capacitance to be C_{geo} and δc a small error we compute

$$\frac{1}{C_{\text{T}}} - \frac{1}{C_{\text{geo}} + \delta c} \approx \frac{1}{C_{\text{T}}} - \frac{1}{C_{\text{geo}}} + \frac{\delta c}{C_{\text{geo}}^2}. \tag{4.13}$$

Multiplying through by Ae^2 we can cast this in terms of the inverse compressibility and an associated deviation:

$$Ae^2\left(\frac{1}{C_{\text{T}}} - \frac{1}{C_{\text{geo}} + \delta c}\right) \approx \frac{\partial \mu}{\partial n} + \frac{Ae^2 \delta c}{C_{\text{geo}}^2}. \tag{4.14}$$

The change in computed chemical potential across a range of density Δn is therefore

$$\int_{\Delta n} Ae^2\left(\frac{1}{C_{\text{T}}} - \frac{1}{C_{\text{geo}} + \delta c}\right) dn = \Delta\mu + \frac{Ae^2 \delta c}{C_{\text{geo}}^2}\Delta n \tag{4.15}$$

where $\Delta\mu$ represents the true change in chemical potential and $\frac{Ae^2\delta c}{C_{\text{geo}}^2}\Delta n$ the associated systematic error. If we use the value $\delta c = 0.014\,\text{fF}$ based on our fit-derived estimate of C_{geo} and a visual analysis of the field-dependent data, the errors associated with the gaps at $n_{\text{s}}/4$ and $n_{\text{s}}/2$ are found to be $\delta\left(\Delta_{n_{\text{s}}/4}\right) = 1.0\,\text{meV}$ and $\delta\left(\Delta_{n_{\text{s}}/2}\right) = 1.2\,\text{meV}$, respectively. The larger error for $\Delta_{n_{\text{s}}/2}$ is due to its slightly larger span in carrier density Δn.

In a similar vein, when plotting the compressibility in Figure 4-8 uncertainty in the precise value of C_{geo} can contribute an uncertainty in the movement of the chemical potential with density. As detailed previously in Equations 4.13–4.15, the uncertainty in the shift of the chemical potential $\delta(\Delta\mu)$ can be related to the uncertainty in the geometric

capacitance δc through

$$\delta(\Delta\mu) = \frac{Ae^2\delta c}{C_{\text{geo}}^2}\Delta n. \tag{4.16}$$

Because our total bandwidth spans a density approximately given by $\Delta n = 6 \times 10^{12}\,\text{cm}^{-2}$, the associated error in bandwidth is given by $\delta(\Delta\mu) \approx 10\,\text{meV}$. In Figure 4-8 we find a bandwidth of approximately 35 meV. Incorporating our estimated uncertainty, the bandwidth has a range that spans approximately $25 - 45\,\text{meV}$ which matches the range of bandwidths plotted in Figure 4-9.

Chapter 5

Planar Tunneling Measurements

In Chapter 3 we discussed the electronic compressibility $\partial n/\partial \mu$ of two-dimensional systems. Because the compressibility depends explicitly on the chemical potential μ, it describes the quantum mechanical ground state of the electronic system. We cannot use the compressibility to study the excitation spectrum of the system. In order to access its fundamental excitations, we must use a spectroscopic technique. In this chapter, we describe one such tool, electron tunneling.

5.1 Basics of Planar Tunneling

In an electron tunneling measurement, a thin insulating barrier separates two electronic systems. Although the potential energy barrier prevents strong coupling between wave functions on either side, it is thin enough that the exponentially suppressed wave functions within the classically forbidden insulating region have significant overlap. Application of a potential difference across the barrier stimulates electrons to equilibrate by tunneling from the higher Fermi level to the available lower energy states in the neighboring system. This transfer of charge can be related to the densities of state for each electronic system. We will review some of the basic concepts below.

5.1.1 Transmission Through a Barrier

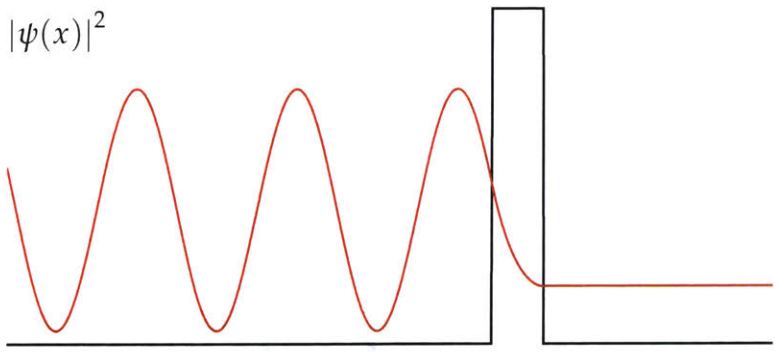

Figure 5-1: **An electron incident on a rectangular potential barrier** with energy E less than the potential barrier height V_0. The wave-like solution on the left gives way to an exponential decay within the classically forbidden region. The probability amplitude is small but nonzero on the right of the potential barrier where another plane wave state is allowed.

If we imagine a one dimensional potential barrier such that it has height V_0 whenever $|x| < a$ and 0 elsewhere, we can calculate the quantum mechanical transmission probability of an electron impinging from the left with energy $E < V_0$. By enforcing continuity of the wave function and its derivative at $x = \pm a$, the transmission coefficient can be calculated [19]:

$$T = \frac{1}{1 + \frac{V_0^2}{4E(V_0 - E)} \sinh^2\left(\frac{2a}{\hbar}\sqrt{2m(V_0 - E)}\right)} \tag{5.1}$$

which demonstrates the permeability of the barrier even for $E < V_0$. Typically we will be interested in energies such that $E \ll V_0$ so that

$$T \simeq \frac{16E}{V_0} e^{-4a\sqrt{2mV_0}/\hbar} \tag{5.2}$$

which is dominated by the exponential term. For our purposes, we will typically be concerned with tunneling in a very narrow range of energy from μ to $\mu + \delta E$ where $\delta E \ll \mu, V_0$ so that $T(E)$ is approximately constant.

5.1.2 Metal–Insulator–Metal Tunneling

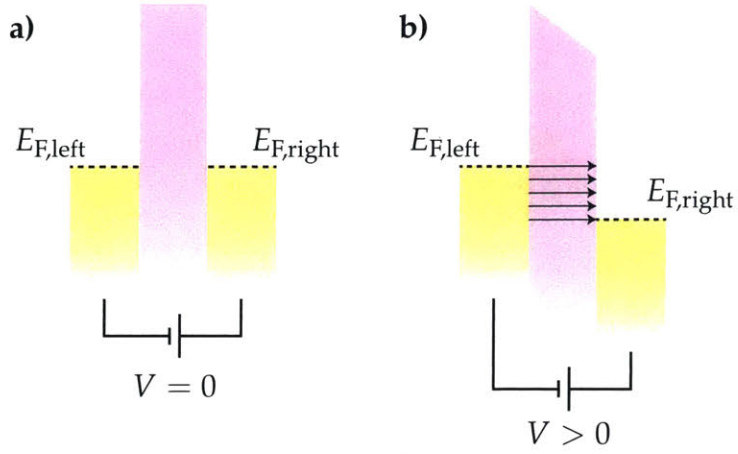

Figure 5-2: **Two metals separated by a thin insulating barrier a)** At $V = 0$, the two metals are in equilibrium and there is no charge transfer. **b)** At $V > 0$ the right electrode is pulled beneath the Fermi level of the left electrode. A net charge current from the left electrode flows into the right electrode.

The tunneling current between two identical metals separated by a thin insulating barrier is perhaps the simplest tunneling scenario we can calculate. If we apply a voltage V across the tunnel junction shown in Figure 5-2, we can use Fermi's golden rule to calculate the current. Let the left electrode be ground and the right electrode be lowered in energy by $-eV$ for $V > 0$. An electron traveling from a state k in the left electrode to a state l in the right electrode tunnels at rate

$$w_{kl} = \frac{2\pi}{\hbar}|T_{kl}|^2\delta(E_k + E_{F,left} - (E_l + E_{F,right})) \tag{5.3}$$

$$= \frac{2\pi}{\hbar}|T_{kl}|^2\delta(E_k - E_l + eV). \tag{5.4}$$

We can integrate over all such states l on the right electrode to find the total rate of transfer from state k on the left to the states on the right:

$$w_k = \frac{2\pi}{\hbar}\int_{-\infty}^{\infty} dE_l \rho_R(E_l)|T_{kl}|^2\delta(E_k - E_l + eV) \tag{5.5}$$

where $\rho_R(E)$ is the density of states of the right electrode. Assuming $T_{kl} \simeq T$ is approximately constant we get

$$w_k = \frac{2\pi}{\hbar}|T|^2\rho_R(E_k + eV). \tag{5.6}$$

We can integrate this total rate from left to right over all states k on the left. We will weight by the Fermi–Dirac distribution $f(E_k)$ to characterize the occupation probability of the states on the left electrode and $1 - f(E_k + eV)$ to characterize the availability for tunneling on the right:

$$\Gamma_{L\to R} = \frac{2\pi}{\hbar}|T|^2 \int_{-\infty}^{\infty} dE_k \rho_L(E_k)\rho_R(E_k + eV)f(E_k)(1 - f(E_k + eV)) \tag{5.7}$$

We can calculate a similar rate from right to left by switching the sign of the voltage:

$$\Gamma_{R\to L} = \frac{2\pi}{\hbar}|T|^2 \int_{-\infty}^{\infty} dE_k \rho_L(E_k)\rho_R(E_k - eV)f(E_k)(1 - f(E_k - eV)) \tag{5.8}$$

$$= \frac{2\pi}{\hbar}|T|^2 \int_{-\infty}^{\infty} dE_k \rho_L(E_k + eV)\rho_R(E_k)f(E_k + eV)(1 - f(E_k)). \tag{5.9}$$

Further, let us assume that the metals have roughly featureless densities of states so that $\rho_i(E) \simeq \rho_i(E + eV)$ over the small range of voltage applied. Then, the net flow of charge is proportional to the difference of the two rates: $I = e(\Gamma_{L\to R} - \Gamma_{R\to L})$. This leads to

$$I(V) = \frac{2\pi e}{\hbar}|T|^2\rho_L(E_F)\rho_R(E_F) \int_{-\infty}^{\infty} dE_k (f(E_k) - f(E_k + eV)). \tag{5.10}$$

The final integral is exactly eV regardless of temperature, leading to

$$I(V) = \frac{2\pi e^2}{\hbar}|T|^2\rho_L(E_F)\rho_R(E_F)V \tag{5.11}$$

which resembles Ohm's law with

$$R_{\text{tun}} = \frac{\hbar}{2\pi e^2 |T|^2 \rho_{\text{L}}(E_{\text{F}}) \rho_{\text{R}}(E_{\text{F}})}. \tag{5.12}$$

5.1.3 Tunneling into Something Interesting

Measuring ohmic conductance between two metals is not that interesting. Typically, we make one electrode a featureless metal and the other an interesting system with nontrivial density of states $\rho(E)$ over the bias range considered. If we return to our previous expression for $\Gamma_{\text{L}\to\text{R}}$ we can let the left electrode be metallic such that $\rho_{\text{L}}(E) \simeq \rho_{\text{L}}(E + eV)$. Then we get

$$\Gamma_{\text{L}\to\text{R}} = \frac{2\pi}{\hbar} |T|^2 \rho_{\text{L}}(E_{\text{F}}) \int_{-\infty}^{\infty} dE_k \rho_{\text{R}}(E_k + eV) f(E_k)(1 - f(E_k + eV)). \tag{5.13}$$

If we take the zero-temperature limit, the product $f(E_k)(1 - f(E_k + eV))$ becomes the product of two step functions. Physically this corresponds to the situation in which no states above $E_{\text{F,left}}$ are occupied on the left and no states above $E_{\text{F,right}}$ are occupied on the right. The only states which are available for tunneling are the ones within eV above $E_{\text{F,right}}$. Therefore

$$\Gamma_{\text{L}\to\text{R}} = \frac{2\pi}{\hbar} |T|^2 \rho_{\text{L}}(E_{\text{F}}) \int_{0}^{eV} dE_k \rho_{\text{R}}(E_k). \tag{5.14}$$

By a similar logic, in the zero-temperature limit there can be no tunneling from right to left, $\Gamma_{\text{R}\to\text{L}} = 0$, due to the fact that all states below $E_{\text{F,right}}$ on the right are also occupied on the left. Then the tunneling current is given by

$$I = e\Gamma_{\text{L}\to\text{R}} = \frac{2\pi e}{\hbar} |T|^2 \rho_{\text{L}}(E_{\text{F}}) \int_{0}^{eV} dE_k \rho_{\text{R}}(E_k). \tag{5.15}$$

By taking a derivative with respect to the voltage V, the conductance is proportional to the density of states on the right at excitation eV:

$$\frac{\partial I}{\partial V}(V) = \frac{2\pi e^2}{\hbar}|T|^2\rho_{\mathrm{L}}(E_{\mathrm{F}})\rho_{\mathrm{R}}(eV) \tag{5.16}$$

Provided the tunneling matrix element T and the metallic density of states $\rho_{\mathrm{L}}(E_{\mathrm{F}})$ remain constant as voltage is applied, $\partial I/\partial V \propto \rho_{\mathrm{R}}(eV)$ at all values of V.

5.1.4 Tunneling Impedances

Planar electron tunneling schemes generally work well for materials which have very high in-plane conductivity. For example, some of the essential features of the Bardeen–Cooper–Schrieffer theory of superconductivity, such as the size of the energy gap, were first verified by electron tunneling measurements [102]. Underlying such results is the (valid) assumption that the in-plane resistance of a metal–insulator–superconductor tunneling junction is very low in comparison to the tunneling resistance. At low temperatures, the in-plane resistance of pure metals is extremely low due to the large density of states and suppression of available phonons. Similarly, the in-plane resistance is exactly zero for DC voltages across superconductors. The high-temperature tunneling resistances in the samples measured in reference [102] were only around $100\,\Omega$, but the extremely small in-plane resistance implied that the tunneling current was dominated by the tunneling impedance.

It is useful to think of the tunneling event as being associated with some *spectral* impedance R_{tun} which describes the availability of charge states at an energy E away from the Fermi level. After the charge has entered the material via tunneling at a high energy, the newly created quasiparticle must relax through scattering with other electrons, phonons, etc. in order to lose excess energy and equilibrate with the Fermi level below. Once at the Fermi level, in-plane voltages must drag the charge through the sample's lat-

eral extent ($R_{\text{in-plane}}$) into an ohmic contact in order to be measured by a current amplifier. The chain of events is depicted in Figure 5-3. Whenever $R_{\text{tun}} \lesssim R_{\text{in-plane}}$, the tunneling current can no longer be faithfully attributed to the tunneling density of states. This competition between R_{tun} and $R_{\text{in-plane}}$ is particularly relevant when studying the tunneling density of states in quantum Hall system where the in-plane resistance oscillates rapidly as a function of the carrier density and magnetic field.

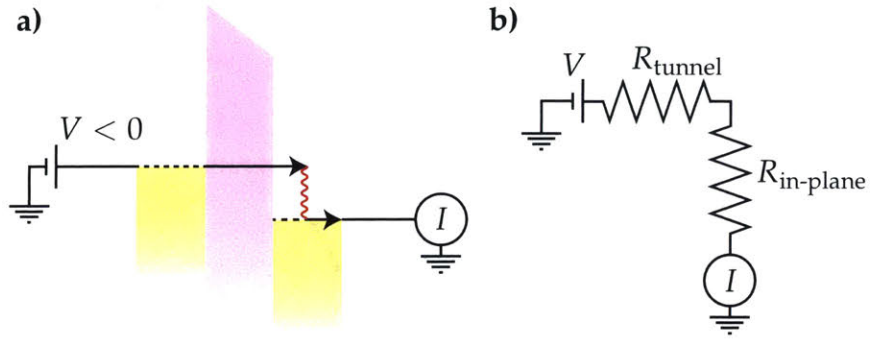

Figure 5-3: **Illustration of tunneling, relaxation, and in-plane transport a)** An electron tunnels from the left electrode to the right at energy eV (black arrow). It must then relax to the Fermi level (red) before being pulled out through the plane of the right electrode (black arrow) to an ammeter located far away. **b)** An approximation of the tunneling measurement treats the tunneling event and its subsequent in-plane transport as separate impedances R_{tun} and $R_{\text{in-plane}}$.

In general, whenever the Fermi level lies in an energy gap, $R_{\text{in-plane}}$ is potentially large and prevents the study of highly degenerate excited states with relatively small R_{tun}. Additionally, we can picture an interacting electronic system which has strong density-dependence. Take the example of a Mott insulator as depicted in Figure 4-2. In order to verify that an interacting energy gap emerges at half-filling of the conduction band, it is essential to show that the energy gap in the conduction band only occurs at half-filling. It may be useful to place the Fermi level in the band gap where there should be no relevant electron–electron interactions. By tunneling up to the half-filling state, the lack of a gap in the tunneling density of states, coupled with the evidence of a gap at the Fermi level while at half-filling of the conduction band, would constitute strong evidence for a

Mott insulator phase. Such measurements are exceedingly difficult due to the in-plane resistivity of gapped phases.

5.2 Contactless Pulsed Tunneling Spectroscopy

In an effort to sidestep the limitations of traditional planar tunneling, an alternative approach utilizing a capacitive sample geometry has been developed (described below). The technique is known as time-domain capacitance spectroscopy, or TDCS, and has been described extensively in the theses of Ho Bun Chan [103], who initiated the technique, and especially Oliver Dial [104], who developed the majority of the software and hardware that are essential for making the technique feasible. For a more thorough introduction to TDCS and its application to semiconductor quantum wells, references [103] and [104] are excellent resources. Recently, there has been interest in studying exfoliable transition metal dichalcogenides, high-T_c superconductors, ferromagnets, and other air-sensitive layered materials for applications such as miniaturizing the field-effect transistor and realizing Majorana zero modes for quantum braiding applications. One common challenge to studying these materials is making reliable ohmic contact before the material oxidizes and degrades (which can happen within minutes under ambient conditions). In an effort to emphasize the contactless nature of TDCS, it has recently been rebranded as *contactless pulsed tunneling spectroscopy*, or CPTS. Both terms can be used interchangeably and we will use the term CPTS in the remainder of this thesis.

5.2.1 CPTS Geometry

The previous discussion highlighted the challenges that in-plane charge motion poses to measurements of the tunneling impedance, effectively convolving the excited state spectrum with Fermi-level properties. The obvious solution is to remove the in-plane charge motion by isolating the two-dimensional electron system between metal plates without

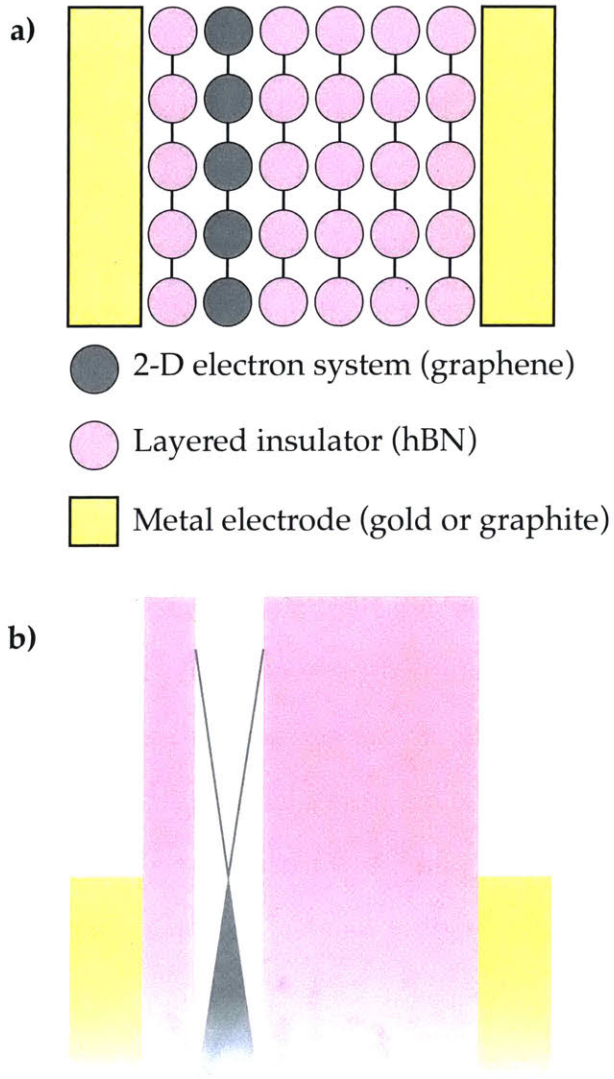

Figure 5-4: **Diagram of CPTS sample geometry a)** A two-dimensional electron system (gray) is isolated from a nearby metal tunneling electrode (gold) by a thin insulating barrier (pink). The two-dimensional system is also isolated from a far metal gate (gold) by a thick blocking barrier (pink). In this example, hexagonal boron nitride (hBN) is both the tunneling barrier and dielectric blocking barrier. We consider the case of monolayer graphene as the two-dimensional system under study. **b)** At zero voltage across the tunnel structure, the graphene is in equilibrium with the tunnel electrode.

an ohmic contact. One metal plate serves as a tunneling electrode, which is separated by a thin insulating barrier that is typically hexagonal boron nitride, but in principle could be any van der Waals insulator such as molybdenum disulfide. For hexagonal boron nitride, typical thicknesses are $\sim$1 nm. Although the system is isolated from direct contact with the metal electrodes, it remains tunnel-coupled. The tunneling barrier is characterized by an associated RC charging time. At times $t \gg RC$, the electrode and two-dimensional electron system reach equilibrium. In this way, a voltage across the outer metal electrodes can induce charge to enter or exit the two-dimensional system.

5.2.2 Measurement Scheme

The basic measurement scheme consists of applying a sudden voltage pulse across the outer metal electrodes and monitoring the voltage induced by the tunneling charge. At $t = 0$ after application of the voltage difference across the metallic plates, the electrode and two-dimensional electron system are suddenly disequilibrated as shown in panel **a** of Figure 5-5. At $t > 0$, charge enters (or exits) the two-dimensional electron system in order to equilibrate as shown in panel **b**. Finally, as $t \to \infty$ in panel **c**, the two systems reach equilibrium across the tunneling barrier, effectively increasing the charge density in the two-dimensional electron system.

In practice, we cannot access the tunneling charge directly since the sample is isolated on either side. Instead, as the sample charges up, we monitor the image charge that accumulates on the opposite metal plate as a result of the displacement current through the capacitor. At $t = 0$, consider a voltage pulse of size V_0 applied across the metal electrodes. Although there is no tuneling current, there is an instantaneous charge which develops on the far electrode as a result of the geometric capacitance of the tunneling capacitor. Over a long time $t \gg RC$, charge tunneling equilibrates the near metal electrode and two-dimensional electron system, causing a proportional rise in the image charge induced on the far electrode. In order to subtract the constant background charge arising

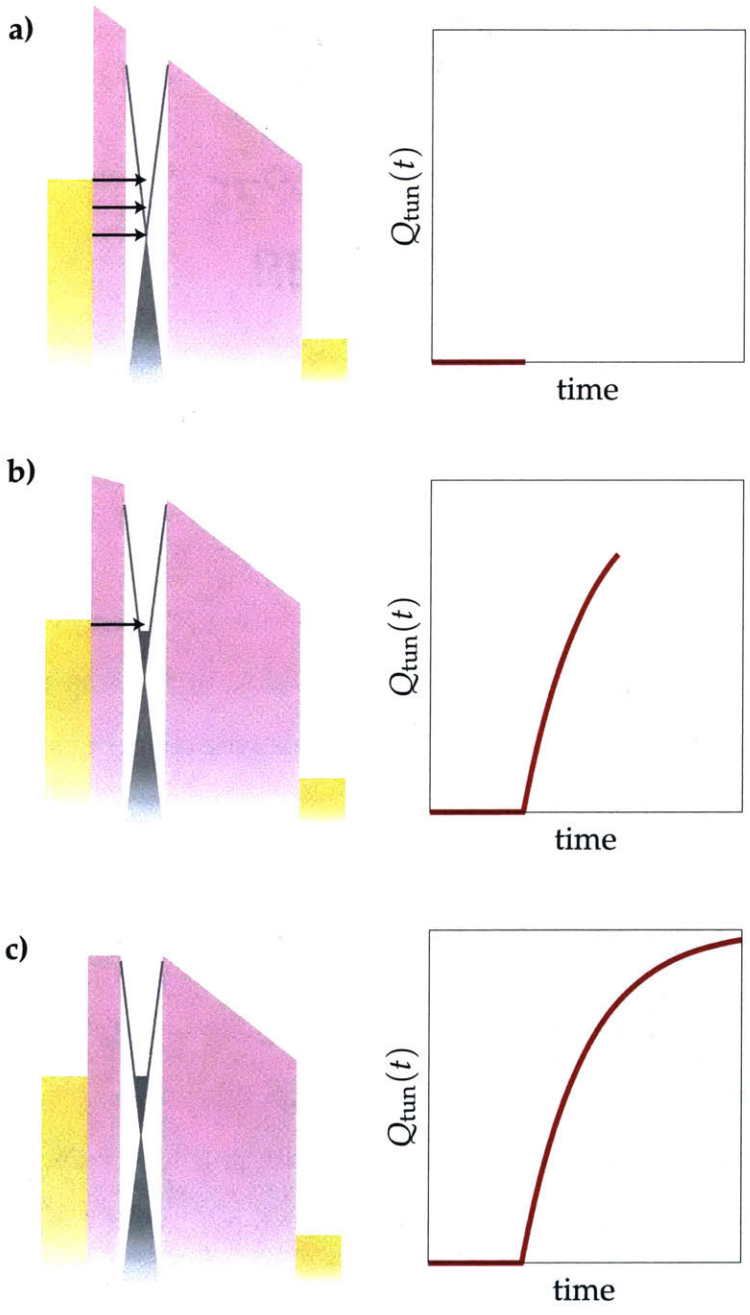

Figure 5-5: **A voltage applied across the CPTS structure induces charge to tunnel a)** At $t = 0$, the full structure is disequilibrated by the sudden voltage pulse. Charge $Q_{tun}(t)$ begins to tunnel into the available states in the graphene layer. **b)** After some time $t \simeq RC$ has passed, an appreciable amount of charge has entered the graphene layer. **c)** After $t \gg RC$, the tunnel electrode and graphene are in equilibrium and the graphene has been charged to a new carrier density.

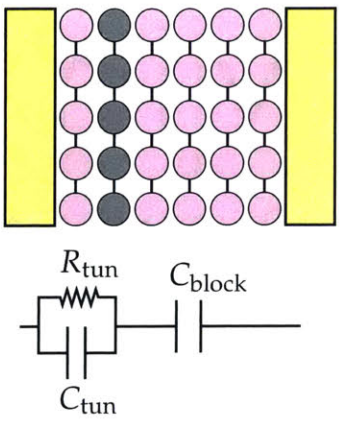

Figure 5-6: **Schematic of CPTS sample geometry** showing the tunnel barrier as forming a parallel RC structure characterized by R_{tun} and C_{tun} as well as the blocking structure forming a capacitor C_{block}.

from the geometric capacitance, a voltage pulse of the opposite polarity is applied to a reference capacitor in a bridge configuration in the same basic scheme as described in Chapter 3 for capacitance measurements. This allows the charging signal to be measured with improved dynamic range.

Converting from Charge to Tunneling Density of States

After measuring a charging pulse, taking a time-derivative of $Q(t)$ gives a quantity proportional to the tunneling current $I_{\text{tun}}(t)$. Although this entire curve at all times is proportional to the tunneling density of states, it is difficult to utilize the portions beyond the $t \to 0$ limit. As the two-dimensional electron system fills with charge, both the carrier density as well as the tunneling energy change in a complicated, mutually-dependent fashion. Thus, only the very initial portion of the charging curve $Q(t)$ is used for extraction of tunneling current. This initial portion of the $Q(t)$ curve represents the tunneling current of the first electrons which enter the two-dimensional electron system at equilibrium. If we measure $Q(t)$ for one voltage pulse of height V_0, then after differentiating with respect to time we get $I(V_0)$. We can repeat this at various pulse heights V to map out an $I(V)$ curve. Taking another derivative, this time with respect to voltage, allows

extraction of the tunneling density of states $\partial I/\partial V$.

5.3 Application to van der Waals Materials

In previous implementations, CPTS was utilized to study semiconductor quantum wells in GaAs/AlAs heterostructures. The fabrication of quantum wells by molecular beam epitaxy easily achieves uniform, defect-free tunnel barriers on lateral length scales of 100 μm. This allows the ultimate lateral area of the device to be on the order of 20 000 μm^2. The situation is much less forgiving with van der Waals heterostructures. Although many research groups can achieve heterostructures on the order of $10 - 100\,\mu m$, the use of hexagonal boron nitride tunneling barriers severely limits the ultimate device size. Typically, hexagonal boron nitride flakes of tunneling-thickness ($3 - 5$ layers) that have been isolated with mechanical exfoliation tend to be much smaller in lateral extent compared to thicker flakes (such as those used for the dielectric blocking layer). Additionally, when forming heterostructures, thin hexagonal boron nitride tends to wrinkle and tear, reducing the effective device size after isolation of an ultraclean section with no mechanical stacking defects. The CPTS devices described in the next chapter are on the order of a few square microns in lateral area, representing a reduction in the tunneling current of about 10000 as compared to GaAs quantum wells. However, the measurement is not quite as dire as these numbers would lead one to believe. While the total tunneling current decreases dramatically, so does the size of the shunt capacitance, meaning that the voltage induced on the blocking electrode is not reduced by the same factor of 10000. For van der Waals heterostructures, the shunting capacitance is on the order of 100 fF as compared to 20 pF for semiconductor devices, leading to an ultimate reduction in the measurement signal of roughly 50. Utilizing low-temperature amplifiers with reduced input shunt capacitance as well as long averaging times can make measurement of small, micron-scale devices feasible.

Chapter 6

Tunneling Spectroscopy of Monolayer Graphene in the Quantum Hall Regime

In this chapter, we will discuss the application of the contactless pulsed tunneling spectroscopy (CPTS) described in Chapter 5 to monolayer graphene. The tunneling geometry consists of the CPTS capacitor structure described previously. A graphite tunneling probe is tunnel-coupled to monolayer graphene by a thin hexagonal boron nitride barrier. An isolated metallic gate (Cr/Au) is separated from the monolayer graphene by a thick hexagonal boron nitride blocking dielectric. The fabrication process will be briefly reviewed below in section 6.1.

6.1 Fabrication

6.1.1 Hexagonal Boron Nitride

Tunneling techniques are only as good as their tunneling barriers. The relative importance of the barrier lies in the exponential sensitivity of tunneling to both barrier height and width. In Chapter 5 we saw that the transmission of an incident electron of energy E on a rectangular barrier of width $2a$ and height V_0 was proportional to $e^{-4a\sqrt{2m(V_0-E)/\hbar^2}}$.

If the barrier thickness $2a$ is too wide or the barrier height V_0 too large, then the tunnel-coupling will be so weak that any tunneling current will be immeasurably small. In the extreme limit, the insulator forms a mere dielectric layer. On the other hand, if the barrier is too transparent, the tunnel-coupling will lead to hybridization of the two electronic systems, strongly perturbing the innate properties of each system in isolation. Moreover, even after an ideal barrier height and width have been chosen, care must be taken to ensure that the tunneling transmission probability is uniform across the lateral extent of the barrier. If there are *pinholes* or other sources of inhomogeneity that either weaken the barrier height or decrease its effective width, the tunneling behavior will be exponentially dominated by such low resistance pathways and effectively shunt the remainder of the tunneling barrier. Finally, the interface between the tunneling barrier and two-dimensional electron system (2DES) must preserve the pristine nature of the 2DES. Interfacial roughness due to strain, dislocations, etc. may reduce the quality of the 2DES to a prohibitive limit. These restrictions severely limit the availability of appropriate materials for tunneling.

Just as GaAs quantum wells can be well lattice-matched to AlAs-based tunneling barriers [105], graphene creates an exceptionally clean interface with hexagonal boron nitride (hBN) which was first identified as a superb dielectric and encapsulation material for monolayer graphene in 2010 [9]. hBN is structurally equivalent to monolayer graphene but has alternating boron and nitrogen atoms on the A and B sublattices. hBN satisfies many of the previously mentioned requirements for a good tunnel barrier. It tends to very chemically stable with few dangling bonds at room temperature and under ambient conditions, leading to reduced charge traps and surface roughness as compared to SiO_2 substrates [106, 107]. In 2011, hBN was identified as a promising van der Waals tunneling barrier based on conductive atomic force microscopy [108, 109] and planar tunneling measurements [109]. The π bands of hbN are associated with a band gap around $5.2 - 5.9\,\mathrm{eV}$ [110–112]. The valence band is offset from the Dirac point of graphene to create a tunnel

barrier of about 1.5 eV [109, 113]. Because hBN is also an excellent dielectric, we build our tunneling structures from both thin hBN in the $3-5$ layer range as well as $\sim$5 nm thick hBN for the dielectric layer.

6.1.2 Graphite Tunnel Probes

In the devices discussed in this chapter, we have utilized graphite flakes that are roughly $5-15$ nm thick. Graphite, as opposed to an evaporated metal such as gold, was chosen due to its ability to make atomically flat, precise heterostructures. Additionally, it has no work function mismatch with monolayer graphene, making the two materials well suited to one another. One drawback of graphite is that during fabrication the graphene is not explicitly aligned with the graphite crystal axes (which are typically not known from basic optical and atomic force microscope techniques) when forming the tunneling heterostructure. At low tunneling energy, this means that the Fermi surface of graphite (centered around similar K and K' points like monolayer or bilayer graphene) may be displaced by approximately $K\theta$ where $K = \frac{4\pi}{3\sqrt{3}a}$ where a is the carbon–carbon bond length of graphene and θ is rotation angle between the crystal axes of the monolayer graphene and graphite tunnel probe. If planar momentum is conserved during the tunneling event, the separation of the Fermi surfaces may suppress tunneling at low energies and carrier densities. An alternative approach would be to use evaporated metals which form thin polycrystalline films. Although not as atomically flat as graphite, the large number of randomly oriented metal nanocrystals effectively averages over all crystal momenta, eliminating momentum conservation as a limitation.

6.2 Tunneling Capacitance

In the CPTS sample geometry, a slow AC excitation relative to the rolloff frequency of the tunnel capacitor RC_{tun} allows the graphite tunnel probe and graphene to remain in

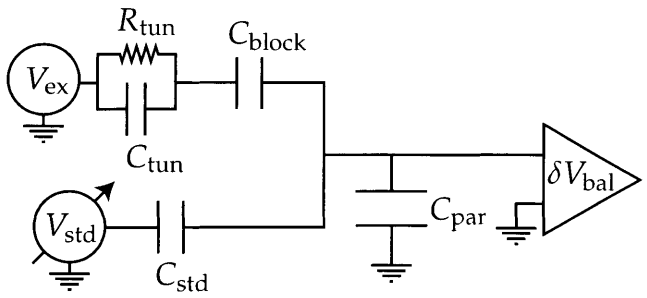

Figure 6-1: **Tunneling capacitance schematic** Using the CPTS geometry, an AC excitation V_{ex} at a frequency $f \ll RC_{tun}$ where RC_{tun} describes the typical rolloff frequency of the tunnel capacitor causes the tunnel probe and two-dimensional electron system to be in equilibrium. This allows the capacitance to be measured in the thermodynamic limit by zero-bias tunneling. In this geometry, there is no in-plane charge motion.

equilibrium throughout each cycle of the excitation V_{ex}. At low frequencies, the capacitance can be measured in a similar fashion to the laterally contacted devices discussed in Chapter 3 and Chapter 4. Here, however, the impedance of the sample is no longer a series resistor and capacitor. It consists of the blocking capacitor C_{block} in series with the parallel R_{tun} and C_{tun} associated with the tunneling barrier as shown in Figure 6-1. In this configuration, the out-of-phase channel of the capacitance bridge involves the tunneling resistance which is proportional to the single-particle density of states at zero bias. Because there is no in-plane charge motion, the out-of-phase component no longer describes transport features.

The tunneling capacitance for the device named "Pulsing3" is shown in Figure 6-2. The carrier density is varied on the horizontal axis with electrons (holes) being added at positive (negative) gate voltages. Charge neutrality is around $V_{gate} = 0.25\,\mathrm{V}$. A Landau fan emerges from charge neutrality as magnetic field is increased. Oscillations in the capacitance near $\nu = \pm 2$ are resolved at fields below 1 T, indicating the high quality of the device. At higher magnetic fields, Landau levels up to $N = \pm 7$ are clearly visible before blurring together due to broadening at high carrier density. Figure 6-3 shows line cuts from Figure 6-2 at constant magnetic field. The zero-field data display a characteristic depression in the total capacitance around charge neutrality due to the vanishing of the

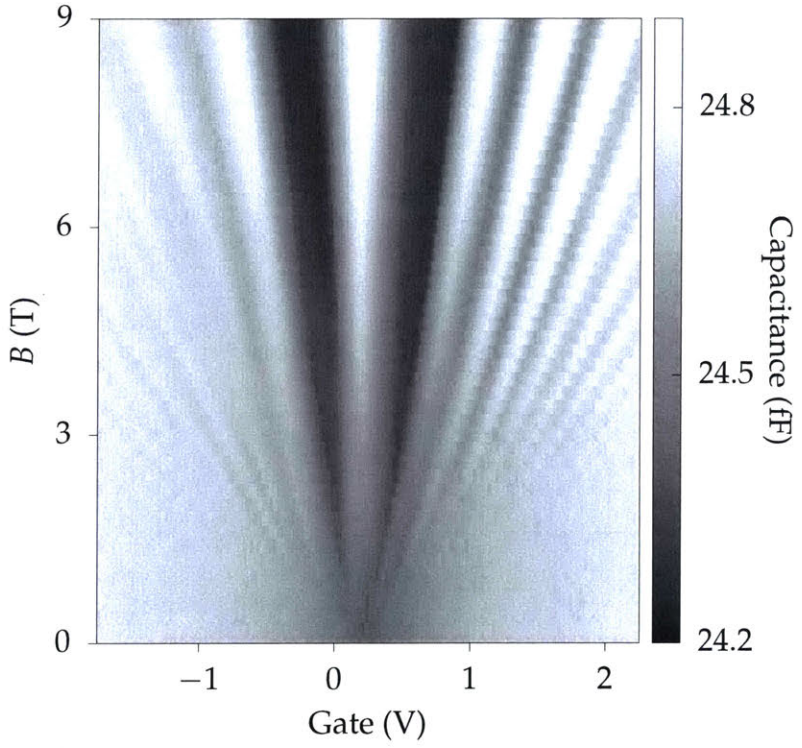

Figure 6-2: **Tunneling capacitance of device Pulsing3** is plotted against gate voltage and magnetic field. A characteristic Landau fan for monolayer graphene emerges from a Dirac-like dip in the capacitance at zero field. The electrons (holes) are added at positive (negative) gate voltages. Landau levels ranging from $N = -7$ to $N = 7$ are clearly resolved. There are no signs of broken symmetry states arising from exchange gaps, perhaps due to the close proximity of the tunnel probe which may screen electron–electron interactions. A 9 mV excitation was used at 3 kHz in a helium-3 cryostat at 280 mK.

Fermi surface at the Dirac point. Landau quantization is evident at higher magnetic field.

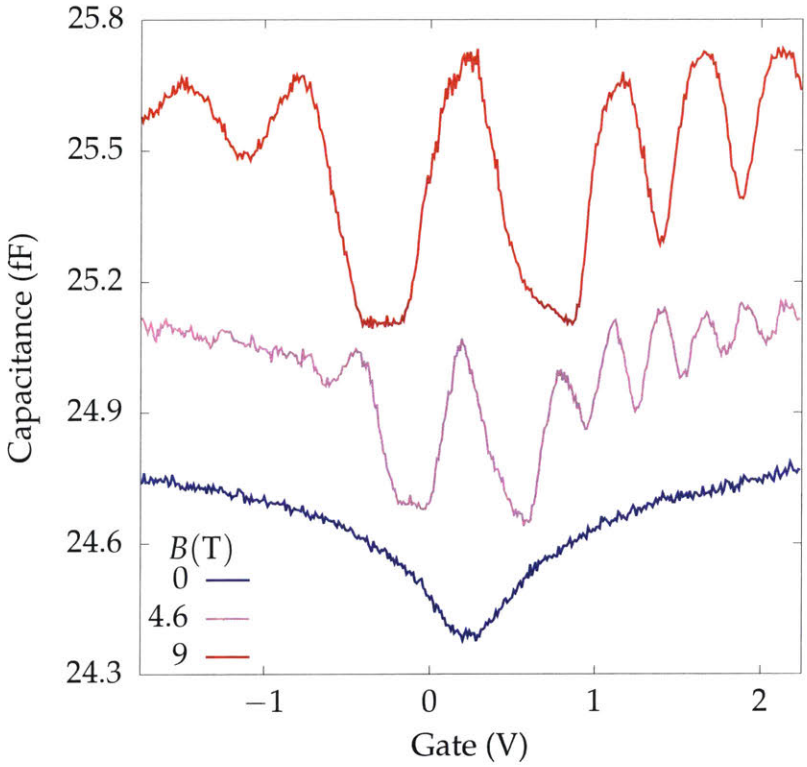

Figure 6-3: **Tunneling capacitance line cuts** at constant magnetic field are plotted for $B = 0, 4.6, 9\,\mathrm{T}$. The curves have been shifted vertically for clarity. The zero-field data shows a clear Dirac-like cusp in the capacitance related to the strong reduction in the thermodynamic density of states around charge neutrality. At higher magnetic field quantum oscillations related to Landau quantization are visible.

6.3 CPTS in Monolayer Graphene

In Figure 6-4 we probe the tunneling spectrum of monolayer graphene in the quantum Hall regime at 7 T and 280 mK. The gate voltage is varied on the horizontal axis, with electron-doping associated with positive gate voltage (to the right). The vertical axis plots the tunneling energy away from the Fermi level. Tunneling upwards in energy away from $E = 0$ represents tunneling an electron into empty excited states. Likewise, tunneling downwards in energy represents tunneling an electron out of the graphene into an available state in the tunneling electrode. To the left of the plot, a sharp, bright fea-

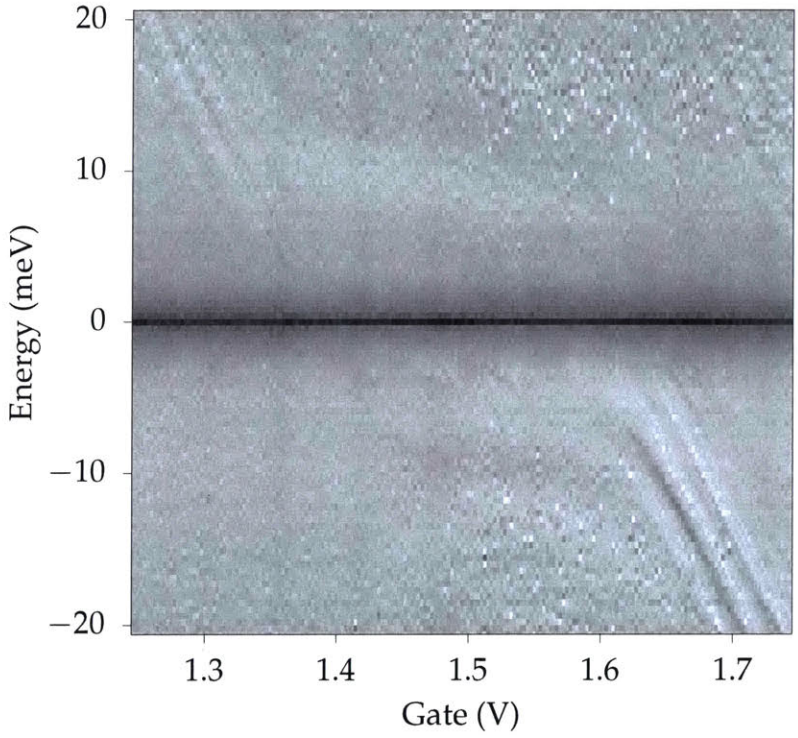

Figure 6-4: **Tunneling spectrum of monolayer graphene at 7 T**. Tunneling energies up to about 20 meV are probed over a range of gate voltage corresponding to the $N = 2$ Landau level approaching the Fermi level. The Landau level is pulled down in energy at low gate voltage and pinned to the Fermi level as it fills. After completely filling, it is pulled beneath the Fermi level as the $N = 3$ level is pulled down. The Landau level experiences several sharp, unexpected splittings whenever it is away from the Fermi level. While pinned to the Fermi level, it blurs due to decreased quasiparticle lifetime.

ture (representing large tunneling density of states) is seen moving downward in energy towards the Fermi level as electrons are added to the system. This bright feature is the empty $N = 2$ Landau level of graphene. Around 1.7 V the Landau level becomes pinned around the Fermi level while its massive degeneracy is filled with electrons. After completely filling, the Landau level is then pulled beneath the Fermi level as the next $N = 3$ Landau level approaches the Fermi level from above.

Perhaps the most visually striking feature of the plot is the sharp density of states suppression around the Fermi level. Although a tunneling gap around the Fermi level is expected from Coulomb repulsion in high magnetic field [114] and has been observed extensively in similar tunneling experiments [104, 115], the tunneling gap typically shows strong dependence on the carrier density and magnetic field. In contrast, we observe a similar gap at all carrier densities and magnetic fields. Density-independent tunneling gaps of order 50 meV have been observed in some scanning tunneling microscopy studies on graphene [116], however, the tunneling gap observed here is much smaller, corresponding to ~4 meV full width at half max. Warming the sample to as little as 5 K strongly suppresses the gap as shown in the temperature dependence in Figure 6-5.

One of the most unusual features of the $N = 2$ Landau level in Figure 6-4 is the sharp splittings which occur when the Landau level is away from the Fermi level at positive and negative energies. Although Landau levels in graphene are expected to form exchange gaps which polarize the spin and valley degrees of freedom [52], the energy scale for such effects is around $e^2/\epsilon l_B \sim 30$ meV which is outside the range of our bias window and much larger than the ~4 meV splitting observed. Furthermore, the splitting due to exchange is expected only to play a role when Landau levels are pinned to the Fermi level because here, the partial filling of the Landau level encourages polarization of the non-orbital degrees of freedom in order to minimize spatial overlap of the wave function. When the Landau level is either completely empty or completely full, there is no freedom to rearrange the non-orbital degrees of freedom and no exchange gap forms. It is unclear

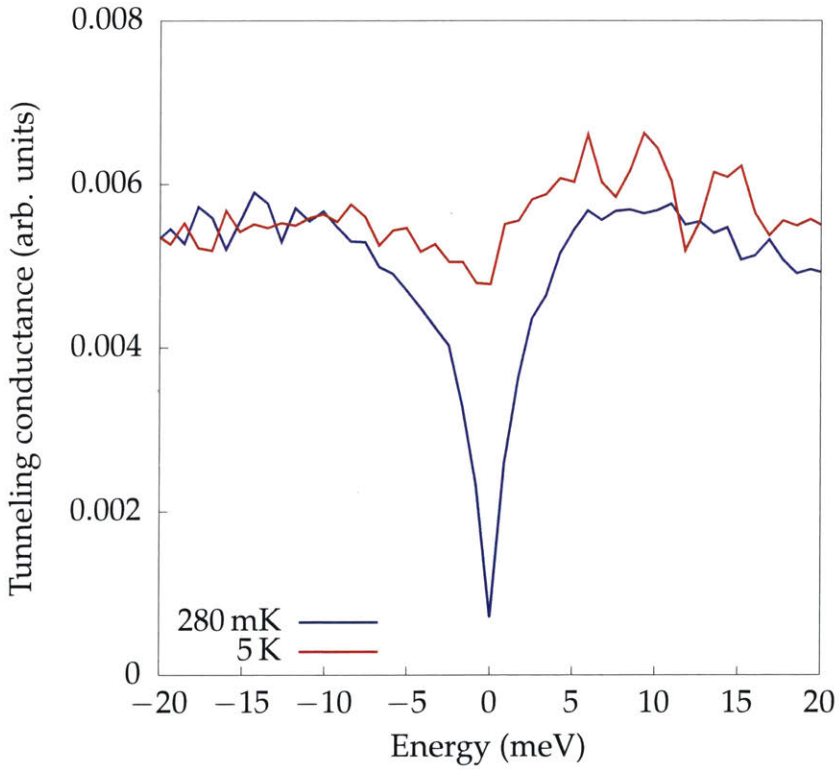

Figure 6-5: **The tunneling gap in graphite–graphene tunneling** shows strong temperature dependence. Upon warming from base temperature to 5 K, the tunneling gap of around 4 meV is strongly suppressed.

what causes the splittings observed in our data. The Zeeman energy scale $g\mu_B B$ is around 0.8 meV for a bare electron g factor at 7 T which is too small to account for the size of the observed splitting. Even more intriguing is the field-evolution of the splitting (and the behavior of the Landau level at the Fermi level). Upon changing magnetic field by as little as 0.25 T, the spectrum rapidly evolves as shown in Figure 6-6. Splittings in the Landau level away from the Fermi level appear to merge and separate upon changing the magnetic field.

The field-dependence of the $N = 2$ Landau level is more clearly depicted by fixing the gate voltage and varying the magnetic field. In panel **a** of Figure 6-7 multiple Landau levels are seen at high energy and brought down to the Fermi level as the magnetic field decreases. Near the Fermi level, several Landau levels split and merge. In panel **b**, the splitting of the $N = 2$ Landau level beneath the Fermi level rapidly changes as magnetic field increases.

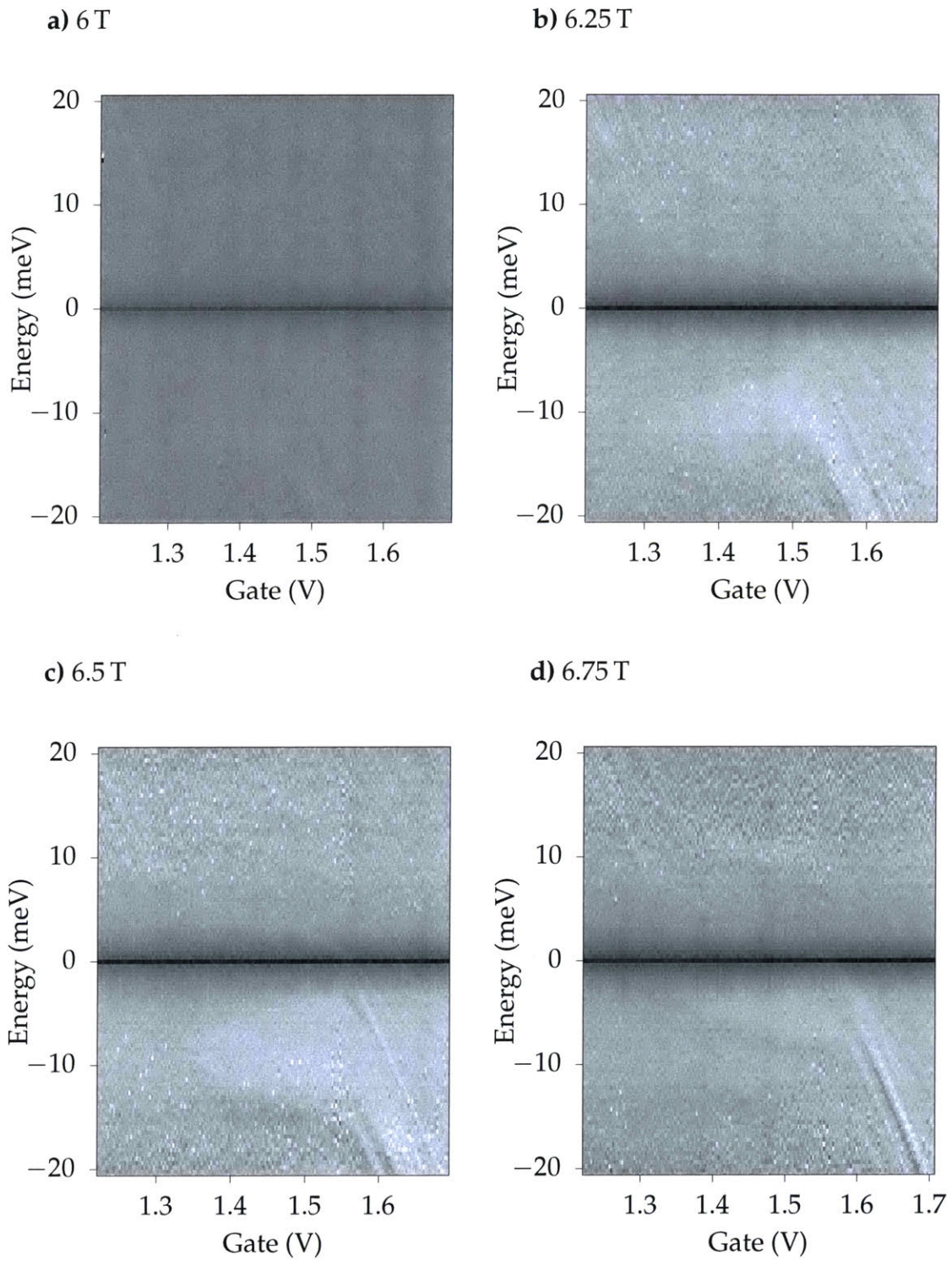

Figure 6-6: **The $N = 2$ Landau level changes rapidly with magnetic field a)** 6 T **b)** 6.25 T **c)** 6.5 T **d)** 6.75 T

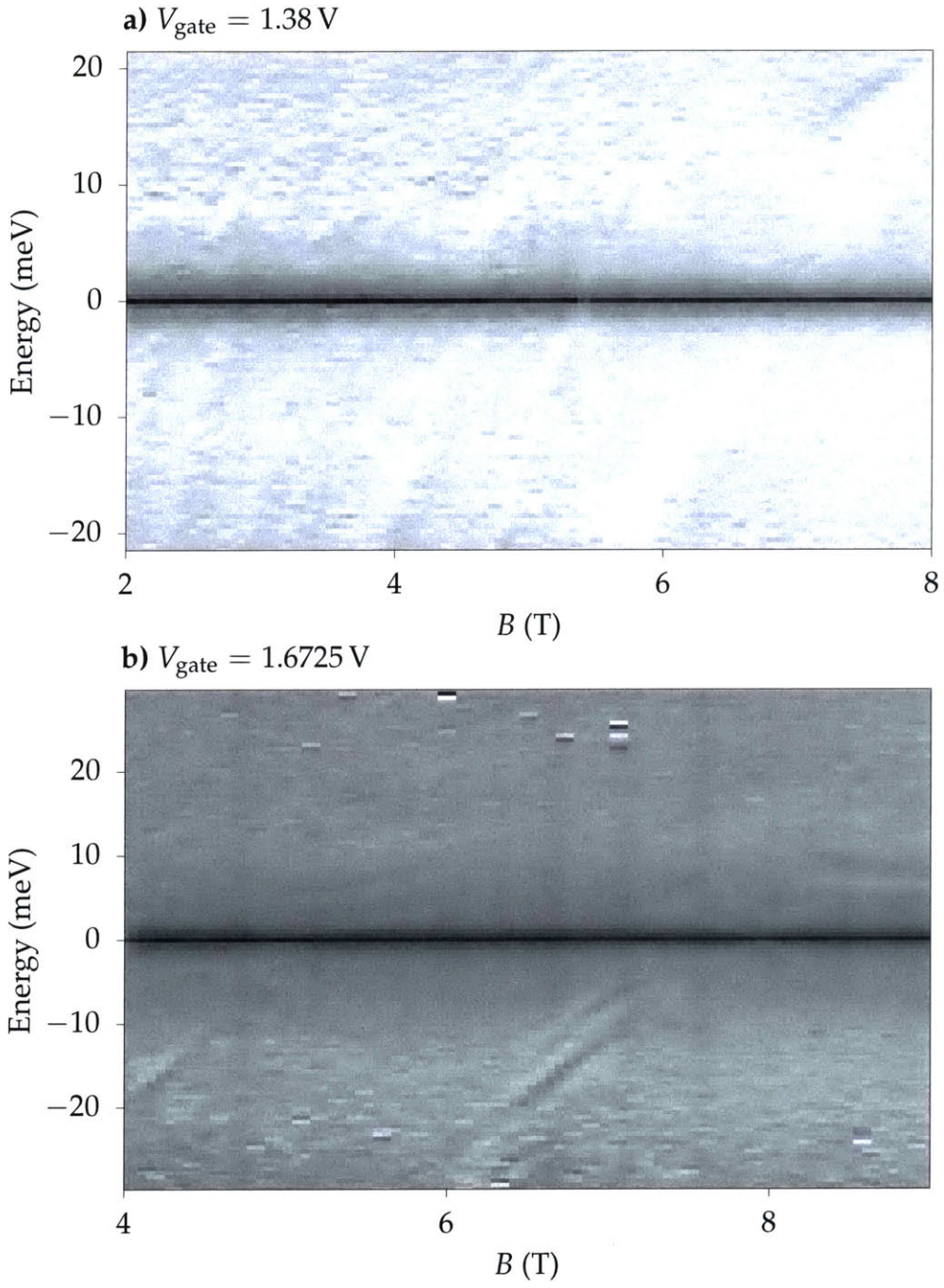

Figure 6-7: **Multiple Landau levels are visible as field is swept a)** As magnetic field decreases, multiple Landau levels are brought down in energy, cross through the Fermi level, and split. **b)** The splitting in the $N = 2$ Landau level beneath the Fermi level rapidly changes with magnetic field.

Chapter 7

Outlook

In this thesis, we have discussed two measurement techniques to study van der Waals systems: capacitance sensing in Chapter 3 and contactless time-domain tunneling in Chapter 5. The ability to access the electronic compressibility of magic-angle graphene superlattices allowed us to measure thermodynamic quantities associated with strongly correlated phases at zero magnetic field in addition to exploring the magnetic field dependence up to the quantum Hall regime in Chapter 4. In Chapter 6 we saw the first application of contactless pulsed tunneling into a van der Waals system where the quantum Hall regime was studied in monolayer graphene without any in-plane transport and with an energy resolution which has not been possible with conventional techniques like scanning tunneling spectroscopy.

There are many promising directions for both techniques to explore in the near future. In addition to magic-angle twisted bilayer graphene, there has been a general explosion of research efforts on *twistronics*, or the explicit fabrication of twisted van der Waals heterostructures. There are indications of superconductivity and correlated insulating phases in twisted Bernal-stacked bilayer graphene (two Bernal bilayers twisted together) [117–119] as well as strong displacement-field tunability in dual-gated twisted bilayer (two monolayers) graphene [76, 77]. Additionally, similar flat band physics with

displacement-field tunable correlated insulation has been seen in aligned ABC trilayer graphene on hexagonal boron nitride [120]. Although there has been less reproducibility in the ABC trilayer system, it is a promising avenue towards flat band physics due to its more mechanically stable arrangement. Because twisted bilayer graphene at low twist angles is extremely close to Bernal stacking, annealing magic-angle twisted bilayer samples frequently causes the two monolayers of graphene to rotate back to zero rotation in order to minimize the ionic potential energy. In the case of ABC trilayer graphene, because it is not lattice-matched to the underlying hexagonal boron nitride, it does not require a relative rotation to form a moiré potential, allowing it to be annealed at higher temperature and potentially offering a cleaner platform. All of these systems have been characterized by electron transport measurements but lack thermodynamic probes. Understanding the evolution of compressibility with displacement field and in a variety of rotated structures is likely to be a worthwhile effort. Furthermore, additional transport measurements on twisted bilayer graphene at low twist angle, but away from the magic angle, have revealed strong electron–phonon coupling over a range of low twist angle [78]. This points to the necessity of performing measurements on twist angles away from the magic angles in order to reveal the physics that is generic to small rotation and which features are unique to the magic angles [16]. Contactless planar tunneling measurements would also be invaluable in this effort. The ability to study the evolution of the insulating phases at fractional filling as they are tuned into the superconducting regime would be a powerful probe of the interaction physics driving the emergence of exotic phases.

Additionally, there are other classes of materials which would be fascinating to study with compressibility and tunneling. Recently, few-layer bismuth strontium calcium copper oxide was isolated with high quality crystals, opening up the field of van der Waals materials to traditional high-T_c platforms [121]. Studying the carrier-density and temperature dependence of two-dimensional superconductors would be a worthwhile venture. Though it is well understood that superconductors form energy gaps in the tunneling

density of states, it is less clear what should happen to the thermodynamic density of states, particularly in the two-dimensional limit. Compressibility could illuminate this interesting topic and tunneling would provide a useful guidepost by allowing direct comparison of the compressibility to the single-particle density of states.

Appendix A

Fabrication

A.1 Exfoliation and Optical Identification

The van der Waals materials used in this work were isolated by manually exfoliating macroscopic crystals of graphite or hexagonal boron nitride with blue semiconductor dicing tape (Ultron Systems 1009R). The tape was subsequently placed into firm contact with a clean Si/SiO_2 substrate. Substrates were prepared by sonicating diced chips first in acetone, then in isopropanol, and finally blow-drying with dry nitrogen gas. Solvent-cleaned chips were then annealed in an approximate vacuum environment at 500 °C for about 10 min in a rapid thermal annealer in order to passivate the surface.

Candidate flakes were manually identified with optical microscopy by color contrast of the van der Waals flakes against the silicon oxide background as shown in Figure A-1. Candiate hexagonal boron nitride and graphite flakes were thermally annealed in vacuum at 500 °C for about 10 min. Graphene was not annealed to prevent flakes from delaminating and rolling up. Candidate graphite, graphene, and hexagonal boron nitride flakes were examined with atomic force microscope to verify that there were no crystal defects or adsorbed contamination.

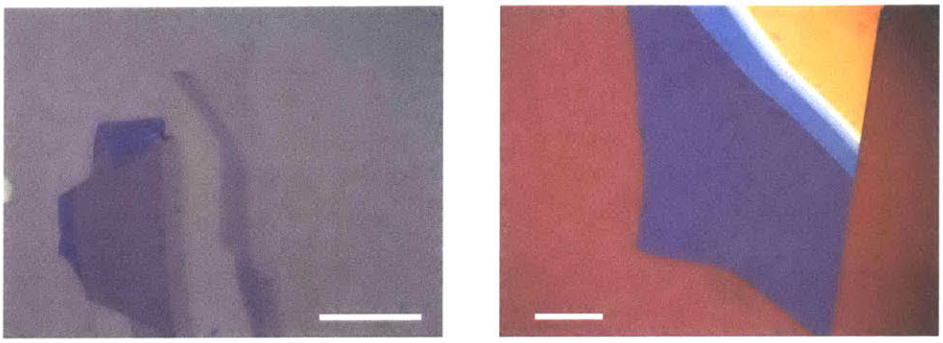

Figure A-1: **Examples of exfoliated van der Waals Materials** (Left) Exfoliated graphite shows a terraced structure. The region with the weakest color contrast is monolayer graphene. (Right) Exfoliated hexagonal boron nitride also shows a terraced structure. The purple region is the thinnest (about 12 nm). The white scale bar in both images is 20 μm.

A.2 Dry Transfer Technique

Suitable flakes were manually stacked to form heterostructures using a polymer-based transfer technique [10]. A polymer film is first made by dissolving poly(bisphenol A carbonate) (PC) crystals in chloroform (6% by weight) and spreading a droplet between two clean glass slides to create a thin coating. After curing in air for a few minutes, the PC polymer may be cut with a sharp blade and transferred onto a suitable surface. The PC film was placed on top of a polydimethylsiloxane (PDMS) "stamp" situated on the end of a glass slide. The polymer stack is controlled by a micro-manipulator at an optical microscope with a long working distance lens. Van der Waals flakes can be picked up by first lowering the polymer stack onto the silicon wafer to make contact away from the flake of interest. Applying heat to the silicon chip causes the PDMS to expand, allowing the waveform of the PC film to slowly approach the desired flake. Once the PC film covers the flake, the chip is cooled down, and the polymer stack is retracted with the van der Waals flake attached as illustrated in Figure A-2.

Once a suitable flake is picked up by the polymer film (typically hexagonal boron nitride), additional flakes can be picked up by using the attractive van der Waals forces between any two flakes in contact as shown in Figure A-3. Many layers can eventually be

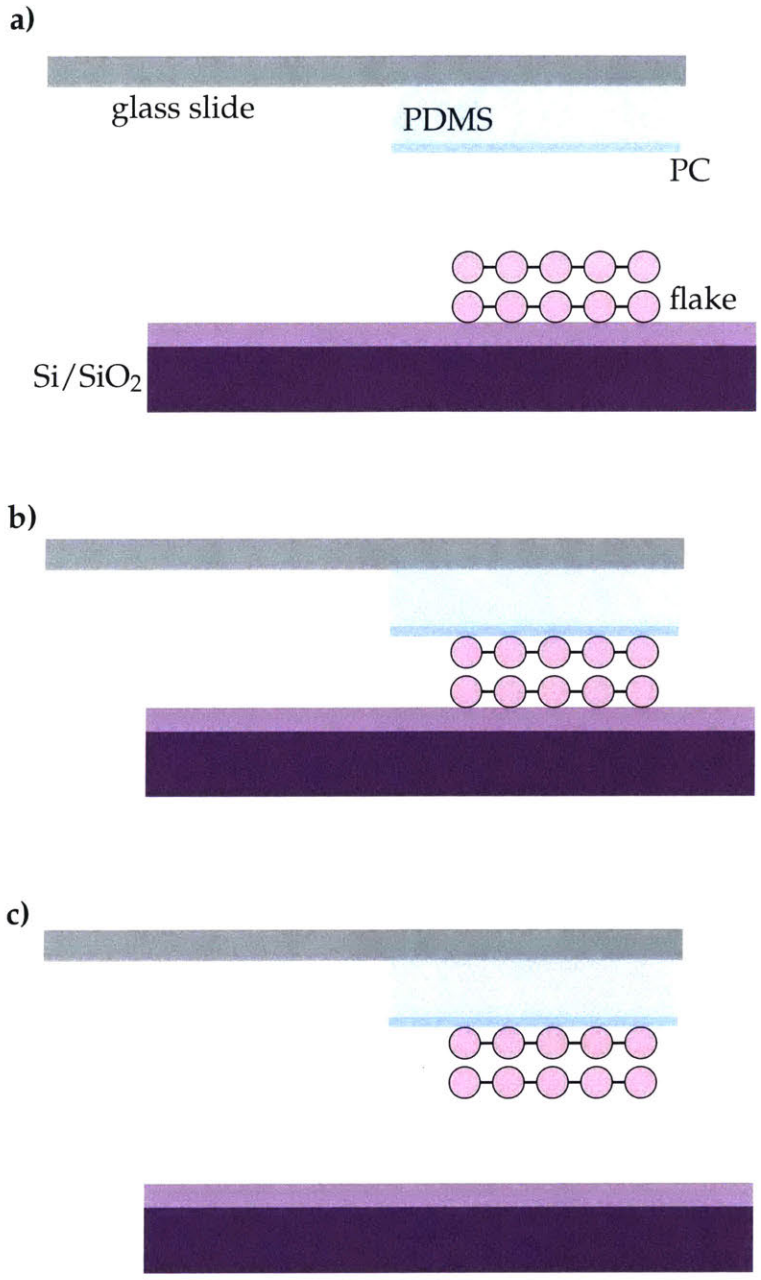

Figure A-2: **Illustration of dry polymer transfer technique a)** The van der Waals flake is approached by the polymer stack. **b)** Heating the chip causes the PDMS to expand and slowly cover the flake. **c)** After cooling, the polymer stack is retracted with the flake firmly attached to the underlying polymer film.

built. Afterwards, the stack is released onto a final flake (perhaps graphite), local metal gate, or silicon oxide substrate. This final step is achieved by placing the polymer stack in firm contact with the destination surface, heating to the melting point of PC (about 150 °C), and retracting the glass slide. The PC film then delaminates from the PDMS. The PC film can then be dissolved in chloroform or other solvents, leaving behind the van der Waals heterostructure. The final stack can then be thermally annealed and characterized with atomic force microscopy.

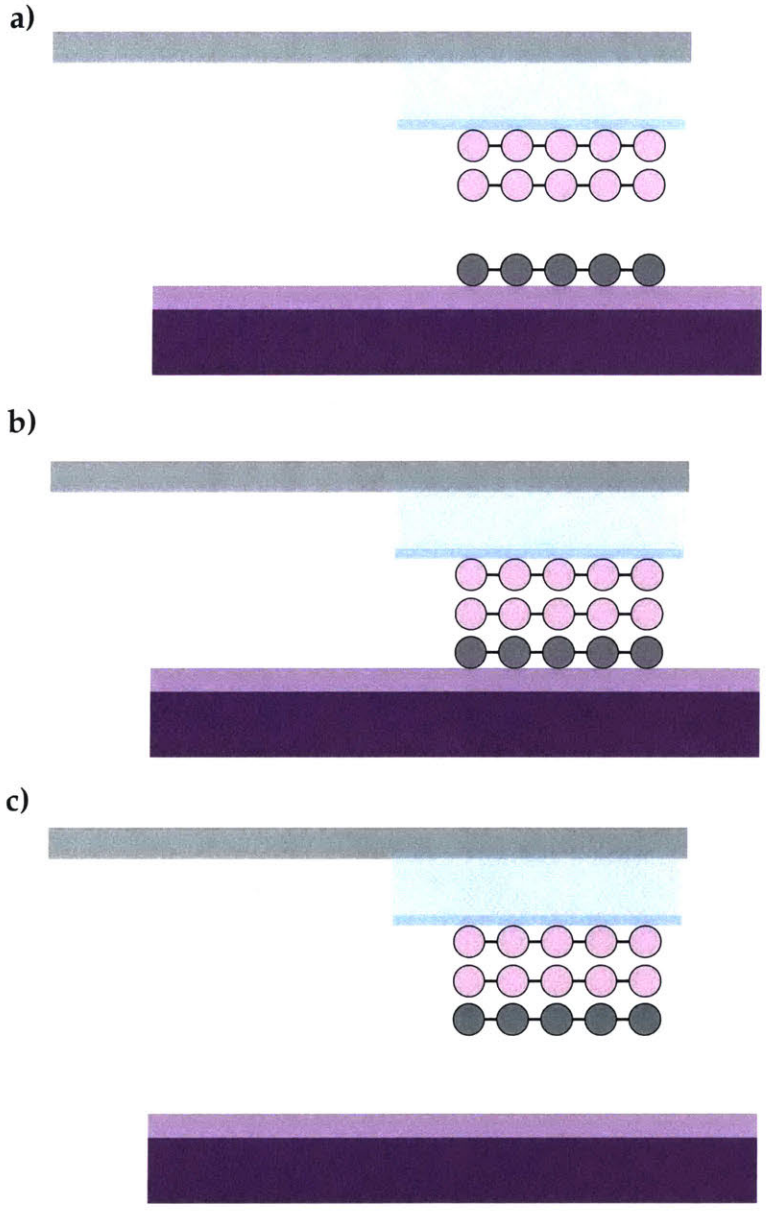

Figure A-3: **An additional flake can be picked up using the van der Waals forces between the two flakes a)** The substrate flake (pink) on the polymer film approaches the flake to be picked up (gray). **b)** Van der Waals forces between the flakes bond them together strongly. **c)** Picking up the transer slide results in a stack of two flakes.

A.3 Electron-Beam Lithography

In order to etch the resulting heterostructures and make electrical contact, electron-beam lithography is utilized to create masks for etching and metallization. Typically, exposure was carried out on an Elionix ELS-7000 with a 100 keV accelerating voltage. The following recipe utilizing a poly(methyl methacrylate) (PMMA) resist was used extensively.

A.3.1 PMMA Resist Recipe

1. Spin PMMA 950 A4 at 4000 rpm for 1 min.
2. Bake chip at 180 °C for 10 min.
3. Expose pattern using Elionix.
4. Development:
   (a) Prepare 3 to 1 deionized water to isopropanol by weight in a clean glass beaker.
   (b) Place beaker with solution in an ice bath for at least 10 min.
   (c) While holding chip in tweezers, agitate gently in the cold solution for 2 min.
   (d) Immediately blow-dry with dry nitrogen gas.

A.4 Reactive Ion Etching

In order to remove unwanted portions of the layer-transferred heterostructure, electron-beam lithography was first utilized to create a metallization mask from PMMA. A Cr/Au top gate was then defined using thermal evaporation. The gold top gate then served as the etch mask. Etching through graphite and graphene was achieved with an O_2 plasma while etching through hexagonal boron nitride required a fluoroform plasma. For devices with an underlying graphite back gate, the device outline was defined with a substantial

fluoroform etch to remove all encapsulating hexagonal boron nitride (as well as monolayer graphene) outside the top gate. The graphite was not significantly affected because fluoroform etches carbon-based materials very slowly. Any unwanted graphite was removed with a final O_2 etch with a double-layer PMMA etch mask. Conventional metallic contact was then made to the graphite while one-dimensional edge-contacts were made to the encapsulated graphene (see below).

A.5 Metallization

Graphite back gates were contacted with a Cr/Au layered thermal evaporation. This was typically performed at normal incidence. Typically, the chromium sticking layer was about 5 nm thick while the gold was around 50 nm thick. For contact to encapsulated graphene-based devices, one-dimensional edge-contacts were utilized [99]. A fresh interface was formed with reactive ion etching. The sample was then quickly loaded into a thermal evaporator equipped with a rotation stage at an angle of about 10° relative to horizontal. Roughly 5 nm of chromium and 50 nm of gold were evaporated while continuously rotating.

A.6 Rotational Alignment

The sample measured in Chapter 4 were fabricated using a "tear and stack" transfer technique [17, 18, 37]. The goal is to rip one flake of graphene into two in order to create two separate crystals of graphene with known lattice orientation. By picking up one flake, applying a precise rotation to the silicon chip with the remaining flake, and then picking up the second flake, twisted bilayer graphene can be created with extremely precise control. This sequence is illustrated in Figure A-4.

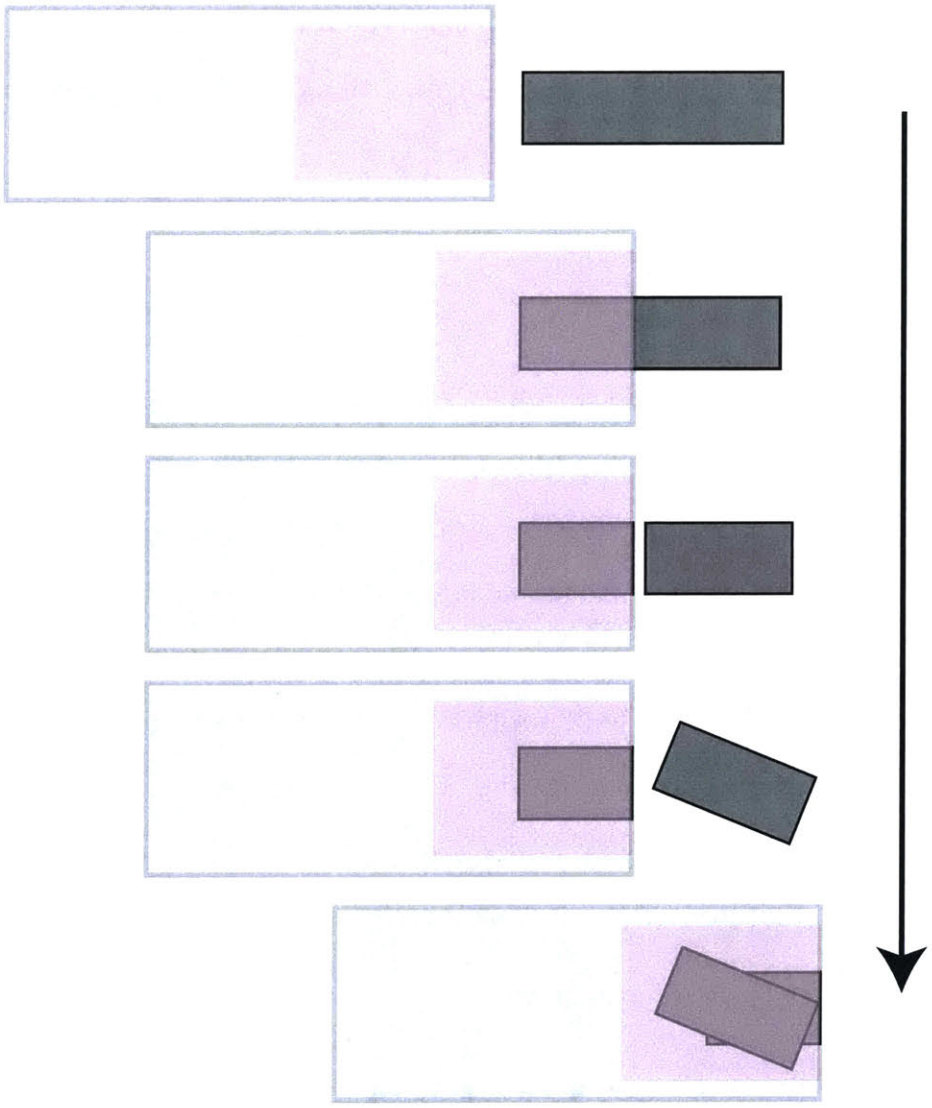

Figure A-4: **One flake of graphene is "torn and stacked" to crate twisted bilayer graphene** A piece of hexagonal boron nitride (pink) is suspended from the polymer attached to a glass slide (light gray). Half of the flake of graphene (dark gray) is contacted by the hexagonal boron nitride. Slowly raising the transfer slide causes the graphene flake to rip into two. A precise rotation of the substrate allows the second piece of graphene to be picked up immediately after the first.

Appendix B

Cryogenic HEMT Amplifiers

The measurements performed in this thesis utilized cryogenic amplification stages placed on the same chip carrier as the sample. In Chapter 3, we discussed the importance of reducing the input parasitic capacitance in impedance bridge configurations. To reduce the input shunt capacitance we utilize the Fujitsu FHX35X, an unpackaged high electron mobility transistor (HEMT), as a versatile low temperature amplifier as first implemented in reference [56]. Though it is often operated with unity or sub-unity voltage gain, it bridges the large impedance difference presented across the balance point and signal line going to room temperature, offering substantial power gain. It effectively isolates everything downstream of the balance point, greatly simplifying the task of measurement.

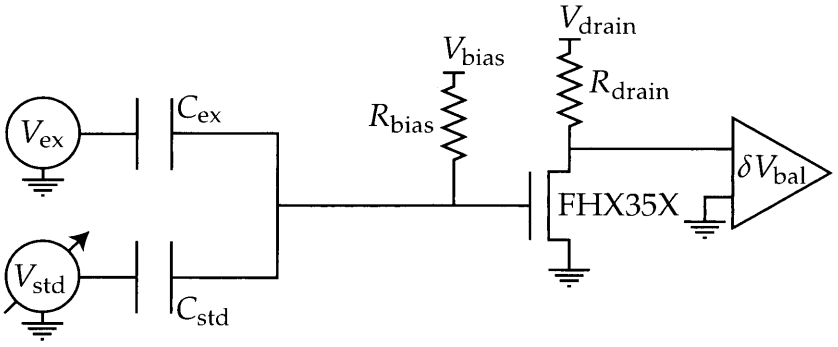

Figure B-1: **The single-stage HEMT amplifier** utilizes a Fujitsu FHX35X HEMT in a common-source configuration. Typically, $R_{drain} \sim 1\,k\Omega$ and $R_{bias} \sim 100\,M\Omega$.

B.1 Single-Stage Design

The basic HEMT amplifier utilizes a single HEMT in a common-source configuration as shown in Figure B-1. The balance point is formed at the gate of the HEMT. In addition to the AC excitation that is capacitively coupled to the balance point, a DC voltage is applied through the resistor R_{bias}. This DC voltage serves two purposes. First, it allows us to pinch off the channel of the HEMT so that its operational point is most sensitive. Second, by defining the DC voltage at the balance point, we can apply DC gate voltages across our capacitance device, allowing us to tune the carrier density. The bias resistor R_{bias} as well as the total capacitance at the balance $C_\Sigma = C_{\text{ex}} + C_{\text{std}} + C_{\text{par}}$ define the low-frequency cutoff for the measurement circuit. At measurement frequencies below $R_{\text{bias}}C_\Sigma$, the accumulated charge on the balance point (which is synchronous with the excitation) is shunted to ground through R_{bias} before it can be amplified and carrier to room temperature. For van der Waals devices, $C_\Sigma \sim 1\,\text{pF}$ so we typically set $R_{\text{bias}} \sim 100\,\text{M}\Omega$ in order to ensure the rolloff frequency $f \sim 1\,\text{kHz}$. This ensures that we are able to measure successfully in the $10 - 100\,\text{kHz}$ range. Low frequencies are necessary to ensure that the sample charges on each cycle of the excitation in order to access the compressibility as opposed to in-plane conductivity (see Chapter 3 for details). The drain resistance is chosen so that the output impedance of the HEMT is sufficiently low to drive the signal to room temperature along the substantial capacitance from the cryostat's coaxial cabling which is of order 0.5 nF. The HEMT resistance must satisfy $R \lesssim 1/2\pi(100\,\text{kHz})(0.5\,\text{nF}) \sim 1\,\text{k}\Omega$ for a measurement frequency in the 100 kHz range.

B.2 Double-Stage Design

In order to reduce the input shunt capacitance, the FHX35X can be cleaved in half and a double-stage cryogenic amplifier can be implemented as first described in Misha Brodsky's thesis [122]. The full double-stage circuit is shown in Figure B-2. The cleaved tran-

sistor has lower input capacitance and can pinched off significantly more than a single-stage amplifier in order to increase its gain. We also utilize a cleaved transistor in place of the bias resistor in order to further reduce the shunt capacitance because the cleaved transistor has less stray capacitance ($\sim$150 fF) than a typical thin film resistor ($\sim$1 pF). The second stage of the amplifier is simply a conventional single-stage HEMT amplifier utilizing an uncleaved HEMT as described previously. Because the first stage amplifier is driving a small load (only the components leading up to the uncleaved transistor over a short wire bond length), it may be pinched off significantly more than the output stage. This affords additional gain without the effects of output loading discussed previously. Typically, the value of R_1 is chosen around 100 kΩ. R_3 is around 1 kΩ in similarity to the single-stage amplifier. R_2 is about 100 MΩ and typically a thin film gold meander because its stray capacitance is not an issue, unlike at the input of the first stage transistor. The coupling capacitor C_1 is around 100 pF. The cleaved transistor cH_2 which biases the gate of the cleaved measurement transistor cH_1 is typically pinched off to around $10 - 100$ MΩ. The cleaved transistor which forms the biasing resistor for the first-stage amplifier tends to be the most susceptible to broadcasting noise into the experiment due to the extreme sensitivity of the DC operation point. Placing cold cryogenic low-pass RC filters made from conventional surface mount components in-line with both the DC line going to the gate of the biasing transistor as well as the DC line going to its drain significantly decreases the noise broadcast into the input of the amplifier in the relevant audio range.

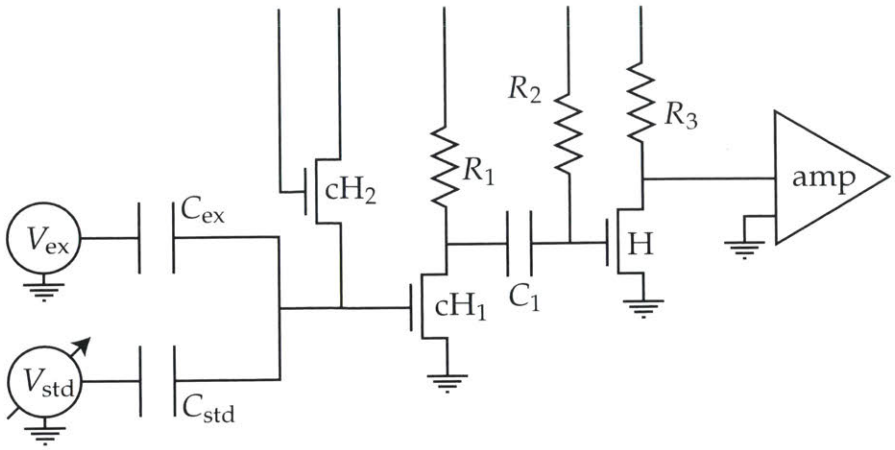

Figure B-2: **The double-stage HEMT amplifier** utilizes a first stage composed on a cleaved measurement transistor (cH_1) which is pinched off by an additional cleaved transistor (cH_2) in order to reduce the input shunt capacitance as much as possible. The second stage consists of an uncleaved transistor (H) which drives the signal to the next amplification stage along a large capacitive cable load.

B.2.1 Cleaving Transistors

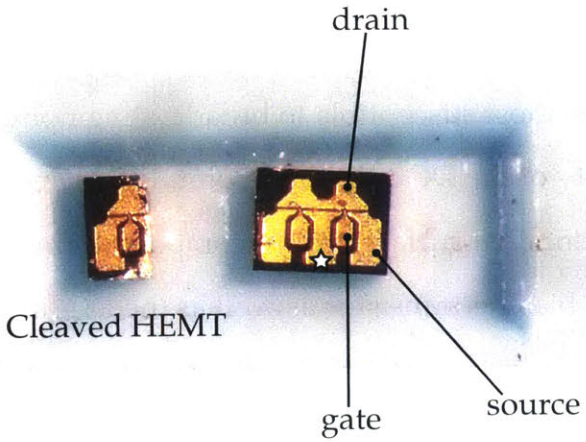

Figure B-3: **The unpackaged Fujitsu FHX35X can be cleaved in half** The HEMT on the left is a cleaved version of the full, uncleaved HEMT on the right. The gate, source, and drain are labeled on the uncleaved HEMT. The star indicates where to cleave.

The Fujitsu FHX35X can be easily cleaved with common laboratory supplies as detailed below.

1. Place an uncleaved HEMT facing upwards on a clean glass slide.

2. Place a small drop of PMMA over the HEMT so that it is completely encased.

3. Wait for the PMMA to cure in air (or on a hot plate set to $\sim$100 °C).

4. Place the glass slide beneath a long working distance microscope—preferably one designed for work with fine electronics.

5. Pace the tip of a sharp razor blade where the white star is shown in Figure B-3.

6. Pressing the razor down firmly will result in the HEMT cleanly splitting into two with a reasonably high yield. The encasing PMMA will prevent the cleaved HEMTs from flying off the glass slide.

7. With tweezers, carefully peel up the PMMA film from the glass slide and place the entire film into a beaker of acetone which will dissolve the PMMA.

8. Sonicate with both acetone and then isopropanol.

9. The cleaved HEMTs are too small to be easily removed with tweezers. After pitching the majority of the solvent, dump the remainder onto a clean fabrication wipe and allow to air dry.

10. The cleaved HEMTs can now be picked up with tweezers and stored for future use.

Bibliography

[1] H. Margenau. Van der Waals forces. *Reviews of Modern Physics*, 11:1–35, January 1939. doi: 10.1103/RevModPhys.11.1. 1.2

[2] H. Rydberg, M. Dion, N. Jacobson, E. Schröder, P. Hyldgaard, S. I. Simak, D. C. Langreth, and B. I. Lundqvist. Van der Waals density functional for layered structures. *Physical Review Letters*, 91:126402, September 2003. doi: 10.1103/PhysRevLett.91.126402. 1.2, 2-3, 2.1.1

[3] A. Y. Cho and J. R. Arthur. Molecular beam epitaxy. *Progress in Solid State Chemistry*, 10:157–191, 1975. doi: 10.1016/0079-6786(75)90005-9. 1.2

[4] R. Dingle, H. L. Störmer, A. C. Gossard, and W. Wiegmann. Electron mobilities in modulation-doped semiconductor heterojunction superlattices. *Applied Physics Letters*, 33:665–667, July 1978. doi: 10.1063/1.90457. 1.2

[5] Howard M. Smith and A. F. Turner. Vacuum deposited thin films using a ruby laser. *Applied Optics*, 4:147–148, January 1965. doi: 10.1364/AO.4.000147. 1.2

[6] D. Dijkkamp, T. Venkatesan, X. D. Wu, S. A. Shaheen, N. Jisrawi, Y. H. Min-Lee, W. L. McLean, and M. Croft. Preparation of Y–Ba–Cu oxide superconductor thin films using pulsed laser evaporation from high T_c bulk material. *Applied Physics Letters*, 51:619–621, July 1987. doi: 10.1063/1.98366. 1.2

[7] A. Ohtomo and H. Y. Hwang. A high-mobility electron gas at the $LaAlO_3/SrTiO_3$ heterointerface. *Nature*, 427:423–426, January 2004. doi: 10.1038/nature02308. 1.2

[8] A. K. Geim and I. V. Grigorieva. Van der Waals heterostructures. *Nature*, 499:419–425, July 2013. doi: 10.1038/nature12385. 1.2

[9] C. R. Dean, A. F. Young, I. Meric, C. Lee, L. Wang, S. Sorgenfrei, K. Watanabe, T. Taniguchi, P. Kim, K. L. Shepard, and J. Hone. Boron nitride substrates for high-quality graphene electronics. *Nature Nanotechnology*, 5:722–726, August 2010. doi: 10.1038/nnano.2010.172. 1.2, 6.1.1

[10] P. J. Zomer, M. H. D. Guimarães, J. C. Brant, N. Tombros, and B. J. van Wees. Fast pick up technique for high quality heterostructures of bilayer graphene and hexagonal boron nitride. *Applied Physics Letters*, 105:013101, July 2014. doi: 10.1063/1.4886096. 1.2, A.2

[11] Serge Luryi. Quantum capacitance devices. *Applied Physics Letters*, 52:501–503, November 1988. doi: 10.1063/1.99649. 1.2, 3.3.2, 4.2

[12] John Desmond Bernal. The structure of graphite. *Proceedings of the Royal Society of London. Series A, Containing Papers of a Mathematical and Physical Character*, 106: 749–773, December 1924. doi: 10.1098/rspa.1924.0101. 1.2

[13] Edward McCann and Mikito Koshino. The electronic properties of bilayer graphene. *Reports on Progress in Physics*, 76:056503, April 2013. doi: 10.1088/0034-4885/76/5/056503. 1.2, 2-7, 2.4.2

[14] J.-C. Charlier, J.-P. Michenaud, and X. Gonze. First-principles study of the electronic properties of simple hexagonal graphite. *Physical Review B*, 46:4531–4539, August 1992. doi: 10.1103/PhysRevB.46.4531. 1.2

[15] Zheng Liu, Kazu Suenaga, Peter J. F. Harris, and Sumio Iijima. Open and closed edges of graphene layers. *Physical Review Letters*, 102:015501, January 2009. doi: 10.1103/PhysRevLett.102.015501. 1.2

[16] Rafi Bistritzer and Allan H. MacDonald. Moiré bands in twisted double-layer graphene. *Proceedings of the National Academy of Sciences of the United States of America*, 108:12233–12237, July 2011. doi: 10.1073/pnas.1108174108. 1.2, 2.4.1, 2.4.2, 2.4.3, 2-15, 4.1, 4.1.1, 4.5, 4.7.2, 7

[17] Yuan Cao, Valla Fatemi, Ahmet Demir, Shiang Fang, Spencer L. Tomarken, Jason Y. Luo, Javier D. Sanchez-Yamagishi, Kenji Watanabe, Takashi Taniguchi, Efthimios Kaxiras, Ray C. Ashoori, and Pablo Jarillo-Herrero. Correlated insulator behaviour at half-filling in magic-angle graphene superlattices. *Nature*, 556:80–84, April 2018. doi: 10.1038/nature26154. 1.2, 2.4.3, 2.4.3, 4.1, 4.1.1, 4-1, 4.1.1, 4.2, 4.3.1, 4.4, 4.5, 4.7.2, 4.8, 4.9.1, A.6

[18] Yuan Cao, Valla Fatemi, Shiang Fang, Kenji Watanabe, Takashi Taniguchi, Efthimios Kaxiras, and Pablo Jarillo-Herrero. Unconventional superconductivity in magic-angle graphene superlattices. *Nature*, 556:43–50, April 2018. doi: 10.1038/nature26160. 1.2, 2.4.3, 4.1.1, 4.2, 4-3, 4.3, 4.4, 4.6, 4.9.1, A.6

[19] E. L. Wolf. *Principles of Electron Tunneling Spectroscopy*, volume 152 of *International Series of Monographs on Physics*. Oxford University Press, second edition, 2012. doi: 10.1093/acprof:oso/9780199589494.001.0001. 1.2, 5.1.1

[20] Charles Kittel. *Introduction to Solid State Physics*. John Wiley & Sons, Inc., eighth edition, 2005. ISBN 978-0-471-41526-8. 2.1, 2.1.1, 2.4.2, 2-16

[21] Hugh O. Pierson. *Handbook of Carbon, Graphite, Diamonds and Fullerenes*. William Andrew Publishing, 1993. doi: 10.1016/B978-0-8155-1339-1.50016-5. 2.1

[22] J. D. van der Waals. Die kontinuität des gasförmigen und flüssigen zustandes. *Zeitschrift für anorganische Chemie*, 20:392–392, May 1899. doi: 10.1002/zaac.620200417. 2.1.1

[23] R. Eisenschitz and F. London. Über das verhältnis der van der waalsschen kräfte zu den homöopolaren bindungskräften. *Zeitschrift für Physik*, 60:491–527, July 1930. doi: 10.1007/BF01341258. 2.1.1

[24] F. London. Zur theorie und systematik der molekularkräfte. *Zeitschrift für Physik*, 63:245–279, March 1930. doi: 10.1007/BF01421741.

[25] F. London. Über einige eigenschaften und anwendungen der molekularkräfte. *Zeitschrift für Physikalische Chemie (B)*, 11:222–251, 1930. 2.1.1

[26] Y. Baskin and L. Meyer. Lattice constants of graphite at low temperatures. *Physical Review*, 100:544, October 1955. doi: 10.1103/PhysRev.100.544. 2-3, 2.1.1

[27] K. S. Novoselov, A. K. Geim, S. V. Morozov, D. Jiang, Y. Zhang, S. V. Dubonos, I. V. Grigorieva, and A. A. Firsov. Electric field effect in atomically thin carbon films. *Science*, 306:666–669, October 2004. doi: 10.1126/science.1102896. 2.2.1

[28] P. R. Wallace. The band theory of graphite. *Physical Review*, 71:622–634, May 1947. doi: 10.1103/PhysRev.71.622. 2.2.1, 2.2.2, 2.2.3

[29] N. D. Mermin. Crystalline order in two dimensions. *Physical Review*, 176:250–254, December 1968. doi: 10.1103/PhysRev.176.250. 2.2.1

[30] Jannik C. Meyer, A. K. Geim, M. I. Katsnelson, K. S. Novoselov, T. J. Booth, and S. Roth. The structure of suspended graphene sheets. *Nature*, 446:60–63, March 2007. doi: 10.1038/nature05545. 2.2.1

[31] A. Fasolino, J. H. Los, and M. I. Katsnelson. Intrinsic ripples in graphene. *Nature Materials*, 6:858–861, September 2007. doi: 10.1038/nmat2011. 2.2.1

[32] M. O. Goerbig. Electronic properties of graphene in a strong magnetic field. *Reviews of Modern Physics*, 83:1193–1243, November 2011. doi: 10.1103/RevModPhys.83.1193. 2.2.2, 2.2.3, 2.2.3, 2.4.2, 2-16

[33] M. Mucha-Kruczyński, O. Tsyplyatyev, A. Grishin, E. McCann, Vladimir I. Fal'ko, Aaron Bostwick, and Eli Rotenberg. Characterization of graphene through anisotropy of constant-energy maps in angle-resolved photoemission. *Physical Review B*, 77:195403, May 2008. doi: 10.1103/PhysRevB.77.195403. 2-5

[34] Paul Adrien Maurice Dirac. The quantum theory of the electron. *Proceedings of the Royal Society of London. Series A, Containing Papers of a Mathematical and Physical Character*, 117:610–624, 1928. doi: 10.1098/rspa.1928.0023. 2.2.3

[35] Nguyen Hong Shon and Tsuneya Ando. Quantum transport in two-dimensional graphite system. *Journal of the Physical Society of Japan*, 67:2421–2429, January 1998. doi: 10.1143/JPSJ.67.2421. 2.2.3

[36] Kyounghwan Kim, Matthew Yankowitz, Babak Fallahazad, Sangwoo Kang, Hema C. P. Movva, Shengqiang Huang, Stefano Larentis, Chris M. Corbet, Takashi Taniguchi, Kenji Watanabe, Sanjay K. Banerjee, Brian J. LeRoy, and Emanuel Tutuc. van der Waals heterostructures with high accuracy rotational alignment. *Nano Letters*, 16:1989–1995, February 2016. doi: 10.1021/acs.nanolett.5b05263. 2.4, 4.1.1, 4.2

[37] Y. Cao, J. Y. Luo, V. Fatemi, S. Fang, J. D. Sanchez-Yamagishi, K. Watanabe, T. Taniguchi, E. Kaxiras, and P. Jarillo-Herrero. Superlattice-induced insulating states and valley-protected orbits in twisted bilayer graphene. *Physical Review Letters*, 117:116804, September 2016. doi: 10.1103/PhysRevLett.117.116804. 2.4, 4.1, 4.1.1, 4.2, 4.6, 4.9.1, A.6

[38] E. J. Mele. Commensuration and interlayer coherence in twisted bilayer graphene. *Physical Review B*, 81:161405, April 2010. doi: 10.1103/PhysRevB.81.161405. 2.4.1

[39] J. M. B. Lopes dos Santos, N. M. R. Peres, and A. H. Castro Neto. Graphene bilayer with a twist: Electronic structure. *Physical Review Letters*, 99:256802, December 2007. doi: 10.1103/PhysRevLett.99.256802. 2.4.2, 2.4.3, 2.4.3, 2-14, 2.4.3

[40] E. Suárez Morell, J. D. Correa, P. Vargas, M. Pacheco, and Z. Barticevic. Flat bands in slightly twisted bilayer graphene: Tight-binding calculations. *Physical Review B*, 82:121407, September 2010. doi: 10.1103/PhysRevB.82.121407. 2.4.2, 2.4.3, 4.1, 4.1.1, 4.5, 4.7.2

[41] J. Hass, F. Varchon, J. E. Millán-Otoya, M. Sprinkle, N. Sharma, W. A. de Heer, C. Berger, P. N. First, L. Magaud, and E. H. Conrad. Why multilayer graphene on $4h - \mathrm{SiC}(000\bar{1})$ behaves like a single sheet of graphene. *Physical Review Letters*, 100: 125504, March 2008. doi: 10.1103/PhysRevLett.100.125504. 2.4.3

[42] Sylvain Latil, Vincent Meunier, and Luc Henrard. Massless fermions in multilayer graphitic systems with misoriented layers: *Ab initio* calculations and experimental fingerprints. *Physica Review B*, 76:201402, November 2007. doi: 10.1103/PhysRevB.76.201402. 2.4.3

[43] Claire Berger, Zhimin Song, Xuebin Li, Xiaosong Wu, Nate Brown, Cécile Naud, Didier Mayou, Tianbo Li, Joanna Hass, Alexei N. Marchenkov, Edward H. Conrad, Phillip N. First, and Walt A. de Heer. Electronic confinement and coherence in patterned epitaxial graphene. *Science*, 312:1191–1196, May 2006. doi: 10.1126/science.1125925. 2.4.3

[44] G. Trambly de Laissardière, D. Mayou, and L. Magaud. Localization of dirac electrons in rotated graphene bilayers. *Nano Letters*, 10:804–808, February 2010. doi: 10.1021/nl902948m. 2.4.3, 4.1, 4.1.1, 4.5, 4.7.2

[45] Guohong Li, A. Luican, J. M. B. Lopes dos Santos, A. H. Castro Neto, A. Reina, J. Kong, and E. Y. Andrei. Observation of van Hove singularities

in twisted graphene layers. *Nature Physics*, 6:109–113, November 2010. doi: 10.1038/nphys1463. 2.4.3, 4.1.1

[46] Hoi Chun Po, Liujun Zou, Ashvin Vishwanath, and T. Senthil. Origin of mott insulating behavior and superconductivity in twisted bilayer graphene. *Physical Review X*, 8:031089, September 2018. doi: 10.1103/PhysRevX.8.031089. 2.4.3, 4.1.1

[47] Mikito Koshino, Noah F. Q. Yuan, Takashi Koretsune, Masayuki Ochi, Kazuhiko Kuroki, and Liang Fu. Maximally localized wannier orbitals and the extended hubbard model for twisted bilayer graphene. *Physical Review X*, 8:031087, September 2018. doi: 10.1103/PhysRevX.8.031087. 2.4.3

[48] D. C. Tsui, H. L. Stormer, and A. C. Gossard. Two-dimensional magnetotransport in the extreme quantum limit. *Physical Review Letter*, 48:1559–1562, May 1982. doi: 10.1103/PhysRevLett.48.1559. 2.4.4, 4.1

[49] Kirill I. Bolotin, Fereshte Ghahari, Michael D. Shulman, Horst L. Stormer, and Philip Kim. Observation of the fractional quantum Hall effect in graphene. *Nature*, 462: 196–199, November 2009. doi: 10.1038/nature08582.

[50] Xu Du, Ivan Skachko, Fabian Duerr, Adina Luican, and Eva Y. Andrei. Fractional quantum Hall effect and insulating phase of Dirac electrons in graphene. *Nature*, 462:192–195, November 2009. doi: 10.1038/nature08522. 2.4.4, 4.1

[51] S. E. Barrett, G. Dabbagh, L. N. Pfeiffer, K. W. West, and R. Tycko. Optically pumped NMR evidence for finite-size skyrmions in GaAs quantum wells near Landau level filling $\nu = 1$. *Physical Review Letters*, 74:5112–5115, June 1995. doi: 10.1103/PhysRevLett.74.5112. 2.4.4, 4.1

[52] A. F. Young, C. R. Dean, L. Wang, H. Ren, P. Cadden-Zimansky, K. Watanabe, T. Taniguchi, J. Hone, K. L. Shepard, and P. Kim. Spin and valley quantum Hall ferromagnetism in graphene. *Nature Physics*, 8:550–556, May 2012. doi: 10.1038/nphys2307. 2.4.4, 4.1, 4.6, 6.3

[53] E. Y. Andrei, G. Deville, D. C. Glattli, F. I. B. Williams, E. Paris, and B. Etienne. Observation of a magnetically induced Wigner solid. *Physical Review Letters*, 60: 2765–2768, June 1988. doi: 10.1103/PhysRevLett.60.2765. 2.4.4, 4.1

[54] V. J. Goldman, M. Santos, M. Shayegan, and J. E. Cunningham. Evidence for two-dimensional quantum Wigner crystal. *Physical Review Letters*, 65:2189–2192, October 1990. doi: 10.1103/PhysRevLett.65.2189. 2.4.4

[55] Michael Plischke and Birger Bergersen. *Equilibrium Statistical Physics*. World Scientific Publishing Co. Pte. Ltd., third edition, 2006. doi: 10.1142/5660. 3.1

[56] R. C. Ashoori, H. L. Stormer, J. S. Weiner, L. N. Pfeiffer, S. J. Pearton, K. W. Baldwin, and K. W. West. Single-electron capacitance spectroscopy of discrete quantum levels. *Physical Review Letters*, 68:3088–3091, May 1992. doi: 10.1103/PhysRevLett.68.3088. 3.4, 3.4.2, B

[57] S. Ilani, L. A. K. Donev, M. Kindermann, and P. L. McEuen. Measurement of the quantum capacitance of interacting electrons in carbon nanotubes. *Nature Physics*, 2:687–691, September 2006. doi: 10.1038/nphys412. 3.4.2

[58] Gary Alexander Steele. *Imaging Transport Resonances in the Quantum Hall Effect*. PhD thesis, Massachusetts Institute of Technology, February 2006. 3.4.3

[59] R. K. Goodall, R. J. Higgins, and J. P. Harrang. Capacitance measurements of a quantized two-dimensional electron gas in the regime of the quantum Hall effect. *Physical Review B*, 31:6597–6608, May 1985. doi: 10.1103/PhysRevB.31.6597. 3.4.3, 4.2

[60] A. F. Young, J. D. Sanchez-Yamagishi, B. Hunt, S. H. Choi, K. Watanabe, T. Taniguchi, R. C. Ashoori, and P. Jarillo-Herrero. Tunable symmetry breaking and helical edge transport in a graphene quantum spin Hall state. *Nature*, 505:528–532, January 2014. doi: 10.1038/nature12800. 3.4.3

[61] Kyounghwan Kim, Ashley DaSilva, Shengqiang Huang, Babak Fallahazad, Stefano Larentis, Takashi Taniguchi, Kenji Watanabe, Brian J. LeRoy, Allan H. MacDonald, and Emanuel Tutuc. Tunable moiré bands and strong correlations in small-twist-angle bilayer graphene. *Proceedings of the National Academy of Sciences of the United States of America*, 114:3364–3369, March 2017. doi: 10.1073/pnas.1620140114. 4.1.1, 4.6

[62] N. F. Mott. The basis of the electron theory of metals, with special reference to the transition metals. *Proceedings of the Physical Society, Section A*, 62:416–422, July 1949. doi: 10.1088/0370-1298/62/7/303. 4.1.1

[63] V. Yu. Irkhin and Yu. N. Skryabin. Dirac points, spinons, and spin liquid in twisted bilayer graphene. *Journal of Experimental and Theoretical Physics Letters*, 107:651–654, May 2018. doi: 10.1134/S0021364018100016. 4.1.1

[64] Bikash Padhi, Chandan Setty, and Philip W. Phillips. Doped twisted bilayer graphene near magic angles: Proximity to Wigner crystallization, not Mott insulation. *Nano Letters*, 18:6175–6180, September 2018. doi: 10.1021/acs.nanolett.8b02033. 4.7.1

[65] Masayuki Ochi, Mikito Koshino, and Kazuhiko Kuroki. Possible correlated insulating states in magic-angle twisted bilayer graphene under strongly competing interactions. *Physical Review B*, 98:081102, August 2018. doi: 10.1103/PhysRevB.98.081102.

[66] Alex Thomson, Shubhayu Chatterjee, Subir Sachdev, and Mathias S. Scheurer. Triangular antiferromagnetism on the honeycomb lattice of twisted bilayer graphene. *Physical Review B*, 98:075109, August 2018. doi: 10.1103/PhysRevB.98.075109.

[67] J. F. Dodaro, S. A. Kivelson, Y. Schattner, X. Q. Sun, and C. Wang. Phases of a phenomenological model of twisted bilayer graphene. *Physical Review B*, 98:075154, August 2018. doi: 10.1103/PhysRevB.98.075154.

[68] Xiao Yan Xu, K. T. Law, and Patrick A. Lee. Kekulé valence bond order in an extended hubbard model on the honeycomb lattice with possible applications to twisted bilayer graphene. *Physical Review B*, 98:121406, September 2018. doi: 10.1103/PhysRevB.98.121406.

[69] Mikito Koshino, Noah F. Q. Yuan, Takashi Koretsune, Masayuki Ochi, Kazuhiko Kuroki, and Liang Fu. Maximally localized Wannier orbitals and the extended Hubbard model for twisted bilayer graphene. *Physical Review X*, 8:031087, September 2018. doi: 10.1103/PhysRevX.8.031087.

[70] Jian Kang and Oskar Vafek. Symmetry, maximally localized Wannier states, and a low-energy model for twisted bilayer graphene narrow bands. *Physical Review X*, 8: 031088, September 2018. doi: 10.1103/PhysRevX.8.031088. 4.7.2

[71] Cheng-Cheng Liu, Li-Da Zhang, Wei-Qiang Chen, and Fan Yang. Chiral spin density wave and $d + id$ superconductivity in the magic-angle-twisted bilayer graphene. *Physical Review Letters*, 121:217001, November 2018. doi: 10.1103/PhysRevLett.121.217001.

[72] Hiroki Isobe, Noah F. Q. Yuan, and Liang Fu. Unconventional superconductivity and density waves in twisted bilayer graphene. *Physical Review X*, 8:041041, December 2018. doi: 10.1103/PhysRevX.8.041041.

[73] Grigory Tarnopolsky, Alex Jura Kruchkov, and Ashvin Vishwanath. Origin of magic angles in twisted bilayer graphene. *Physical Review Letters*, 122:106405, March 2019. doi: 10.1103/PhysRevLett.122.106405.

[74] Bikash Padhi and Philip Phillips. Pressure-induced metal-insulator transition in twisted bi-layer graphene. arXiv:1810.00884v2 [cond-mat.str-el], February 2018. 4.7.1

[75] Noah F. Q. Yuan, Hiroki Isobe, and Liang Fu. Magic of high order van Hove singularity. arXiv:1901.05432v3 [cond-mat.str-el], May 2019. 4.1.1, 4.7.2

[76] Matthew Yankowitz, Shaowen Chen, Hryhoriy Polshyn, Yuxuan Zhang, K. Watanabe, T. Taniguchi, David Graf, Andrea F. Young, and Cory R. Dean. Tuning superconductivity in twisted bilayer graphene. *Science*, 363:1059–1064, March 2019. doi: 10.1126/science.aav1910. 4.2, 4.3, 4.4, 4.6, 4.8, 7

[77] Aaron L. Sharpe, Eli J. Fox, Arthur W. Barnard, Joe Finney, Kenji Watanabe, Takashi Taniguchi, M. A. Kastner, and David Goldhaber-Gordon. Emergent ferromagnetism near three-quarters filling in twisted bilayer graphene. arXiv:1901.03520v1 [cond-mat.mes-hall], January 2019. 4.4, 7

[78] Hryhoriy Polshyn, Matthew Yankowitz, Shaowen Chen, Yuxuan Zhang, K. Watanabe, T. Taniguchi, Cory R. Dean, and Andrea F. Young. Phonon scattering dominated electron transport in twisted bilayer graphene. arXiv:1902.00763v1 [cond-mat.str-el], February 2019. 4.3, 4.4, 7

[79] Xiaobo Lu, Petr Stepanov, Wei Yang, Ming Xie, Mohammed Ali Aamir, Ipsita Das, Carles Urgell, Kenji Watanabe, Takashi Taniguchi, Guangyu Zhang, Adrian Bachtold, Allan H. MacDonald, and Dmitri K. Efetov. Superconductors, orbital magnetis, and correlated states in magic angle bilayer graphene. arXiv:1903:06513v2 [cond-mat.str-el], March 2019. 4.2, 4.3, 4.4, 4.6, 4.8

[80] Alexander Kerelsky, Leo McGilly, Dante M. Kennes, Lede Xian, Matthew Yankowitz, Shaowen Chen, K. Watanabe, T. Taniguchi, James Hone, Cory Dean, Angel Rubio, and Abhay N. Pasupathy. Magic angle spectroscopy. arXiv:1812.08776v2 [cond-mat.mes-hall], December 2018. 4.2, 4.4, 4.5, 4.8

[81] Youngjoon Choi, Jeannette Kemmer, Yang Peng, Alex Thomson, Harpreet Arora, Robert Polski, Yiran Zhang, Hechen Ren, Jason Alicea, Gil Rafael, Felix von Oppen, Kenji Watanabe, Takashi Taniguchi, and Steven Nadj-Perge. Imaging electronic correlations in twisted bilayer graphene near the magic angle. arXiv:1901.02997v1 [cond-mat.mes-hall], January 2019. 4.2, 4.4, 4.8

[82] Ya-Hui Zhang, Hoi Chun Po, and T. Senthil. Landau level degeneracy in twisted bilayer graphene: Role of symmetry breaking. arXiv:1904.10452v1 [cond-mat.str-el], April 2019. 4.6

[83] Y. Zhang, Z. Jiang, J. P. Small, M. S. Purewal, Y.-W. Tan, M. Fazlollahi, J.D. Chudow, J.A. Jaszczak, H. L. Stormer, and P. Kim. Landau-level splitting in graphene in high magnetic fields. *Physical Review Letters*, 96:136806, April 2006. doi: 10.1103/PhysRevLett.96.136806. 4.6

[84] Z. Jiang, Y. Zhang, H. L. Stormer, and P. Kim. Quantum Hall states near the charge-neutral Dirac point in graphene. *Physical Review Letters*, 99:106802, September 2007. doi: 10.1103/PhysRevLett.99.106802.

[85] Joseph G. Checkelsky, Lu Li, and N. P. Ong. Zero-energy state in graphene in a high magnetic field. *Physical Review Letters*, 100:206801, May 2008. doi: 10.1103/PhysRevLett.100.206801.

[86] Y. Zhao, P. Cadden-Zimansky, Z. Jiang, and P. Kim. Symmetry breaking in the zero-energy Landau level in bilayer graphene. *Physical Review Letters*, 104:066801, February 2010. doi: 10.1103/PhysRevLett.104.066801.

[87] B. Hunt, J. D. Sanchez-Yamagishi, A. F. Young, M. Yankowitz, B. J. LeRoy, K. Watanabe, T. Taniguchi, P. Moon, M. Koshino, P. Jarillo-Herrero, and R. C. Ashoori. Massive Dirac fermions and Hofstadter butterfly in a van der Waals heterostructure. *Science*, pages 1427–1430, June 2013. doi: 10.1126/science.1237240. 4.6

[88] Douglas R. Hofstadter. Energy levels and wave functions of Bloch electrons in rational and irrational magnetic fields. *Physical Review B*, 14:2239–2249, September 1976. doi: 10.1103/PhysRevB.14.2239. 4.6

[89] G. H. Wannier. A result not dependent on rationality for Bloch electrons in a magnetic field. *Physica Status Solidi B*, 88:757–765, August 1978. doi: 10.1002/pssb.2220880243. 4.6

[90] C. R. Dean, L. Wang, P. Maher, C. Forsythe, F. Ghahari, Y. Gao, J. Katoch, M. Ishigami, P. Moon, M. Koshino, T. Taniguchi, K. Watanabe, K. L. Shepard, J. Hone, and P. Kim. Hofstadter's butterfly and the fractal quantum Hall effect in moiré superlattices. *Nature*, 497:598–602, May 2013. doi: 10.1038/nature12186. 4.6

[91] L. A. Ponomarenko, R. V. Gorbachev, G. L. Yu, D. C. Elias, R. Jalil, A. A. Patel, A. Mishchenko, A. S. Mayorov, C. R. Woods, J. R. Wallbank, M. Mucha-Kruczynski, B. A. Piot, M. Potemski, I. V. Grigorieva, K. S. Novoselov, F. Guinea, V. I. Fal'ko, and A. K. Geim. Cloning of Dirac fermions in graphene superlattices. *Nature*, 497: 594–597, May 2013. doi: 10.1038/nature12187. 4.6

[92] M. S. Bello, E. I. Levin, B. I. Shklovskii, and A. L. Efros. Density of localized states in the surface impurity band of a metal-insulator-semiconductor structure. *Journal of Experimental and Theoretical Physics*, 80:1596–1612, April 1981. 4.7.1

[93] Bikash Padhi, Yubo Yang, David M. Ceperley, and Philip W. Phillips. (private communication), 2019. 4.7.1

[94] Ding Zhang, Xuting Huang, Werner Dietsche, Klaus von Klitzing, and Jurgen H. Smet. Signatures for Wigner crystal formation in the chemical potential of a two-dimensional electron system. *Physical Review Letters*, 113:076804, August 2014. doi: 10.1103/PhysRevLett.113.076804. 4.7.1

[95] Zhen Bi, Noah F.Q. Yuan, and Liang Fu. Designing flat band by strain. arXiv:1902.10146v1 [cond-mat.mtrl-sci], February 2019. 4.7.1

[96] Stephen Carr, Shiang Fang, Ziyan Zhu, and Efthimios Kaxiras. Minimal model for low-energy electronic states of twisted bilayer graphene. arXiv:1901.03420v4 [cond-mat.mes-hall], May 2019. 4.7.2

[97] Niels R Walet and Francisco Guinea. Lattice deformation, low energy models and flat bands in twisted graphene bilayers. arXiv:1903.00340v1 [cond-mat.str-el], March 2019. 4.7.2

[98] Procolo Lucignano, Dario Alfè, Vittorio Cataudella, Domenico Ninno, and Giovanni Cantele. Crucial role of atomic corrugation on the flat bands and energy gaps of twisted bilayer graphene at the magic angle $\theta \sim 1.08^\circ$. *Physical Review B*, 99:195419, May 2019. doi: 10.1103/PhysRevB.99.195419. 4.7.2

[99] L. Wang, I. Meric, P. Y. Huang, Q. Gao, Y. Gao, H. Tran, T. Taniguchi, K. Watanabe, L. M. Campos, D. A. Muller, J. Guo, P. Kim, J. Hone, K. L. Shepard, and C. R. Dean. One-dimensional electrical contact to a two-dimensional material. *Science*, 342:614–617, November 2013. doi: 10.1126/science.1244358. 4.9.1, A.5

[100] J. P. Eisenstein, L. N. Pfeiffer, and K. W. West. Negative compressibility of interacting two-dimensional electron and quasiparticle gases. *Physical Review Letters*, 68: 674–677, February 1992. doi: 10.1103/PhysRevLett.68.674. 4.9.5

[101] G. L. Yu, R. Jalil, Branson Belle, Alexander S. Mayorov, Peter Blake, Frederick Schedin, Sergey V. Morozov, Leonid A. Ponomarenko, F. Chiappini, S. Wiedmann, Uli Zeitler, Mikhail I. Katsnelson, A. K. Geim, Kostya S. Novoselov, and Daniel C. Elias. Interaction phenomena in graphene seen through quantum capacitance. *Proceedings of the National Academy of Sciences of the United States America*, 110:3282–3286, February 2013. doi: 10.1073/pnas.1300599110. 4.9.5

[102] Ivar Giaever. Energy gap in superconductors measured by electron tunneling. *Physical Review Letters*, 5:147–148, August 1960. doi: 10.1103/PhysRevLett.5.147. 5.1.4

[103] Ho Bun Chan. *Tunneling Spectroscopy of the Two-Dimensional Electron Gas*. PhD thesis, Massachusetts Institute of Technology, September 1999. 5.2

[104] Oliver Eugene Dial III. *Single Particle Spectrum of the Two Dimensional Electron Gas*. PhD thesis, Massachusetts Institute of Technology, June 2007. 5.2, 6.3

[105] John H. Davies. *The Physics of Low-Dimensional Semiconductors*. Cambridge University Press, 1997. doi: 10.1017/CBO9780511819070. 6.1.1

[106] Jiamin Xue, Javier Sanchez-Yamagishi, Danny Blumash, Philippe Jacquod, Aparna Deshpande, K. Watanabe, T. Taniguchi, Pablo Jarillo-Herrero, and Brian J. LeRoy. Scanning tunnelling microscopy and spectroscopy of ultra-flat graphene on hexagonal boron nitride. *Nature Materials*, 10:282–285, February 2011. doi: 10.1038/nmat2968. 6.1.1

[107] Régis Decker, Yang Wang, Victor W. Brar, William Regan, Hsin-Zon Tsai, Qiong Wu, William Gannett, Alex Zettl, and Michael F. Crommie. Local electronic properties of graphene on a BN substrate via scanning tunneling microscopy. *Nano Letters*, 11: 2291–2295, May 2011. doi: 10.1021/nl2005115. 6.1.1

[108] Gwan-Hyoung Lee, Young-Jun Yu, Changgu Lee, Cory Dean, Kenneth L. Shepard, Philip Kim, and James Hone. Electron tunneling through atomically flat and ultrathin hexagonal boron nitride. *Applied Physics Letters*, 99:243114, December 2011. doi: 10.1063/1.3662043. 6.1.1

[109] Liam Britnell, Roman V. Gorbachev, Rashid Jalil, Branson D. Belle, Fred Schedin, Mikhail I. Katsnelson, Laurence Eaves, Sergey V. Morozov, Alexander S. Mayorov, Nuno M. R. Peres, Antonio H. Castro Neto, Jon Leist, Andre K. Geim, Leonid A. Ponomarenko, and Kostya S. Novoselov. Electron tunneling through ultrathin boron nitride crystalline barriers. *Nano Letters*, 12:1707–1710, March 2012. doi: 10.1021/nl3002205. 6.1.1

[110] D. M. Hoffman, G. L. Doll, and P. C. Eklund. Optical properties of pyrolytic boron nitride in the energy range $0.05 - 10$ eV. *Physical Review B*, 30:6051–6056, November 1984. doi: 10.1103/PhysRevB.30.6051. 6.1.1

[111] X. Blase, Angel Rubio, Steven G. Louie, and Marvin L. Cohen. Quasiparticle band structure of bulk hexagonal boron nitride and related systems. *Physical Review B*, 51:6868–6875, March 1995. doi: 10.1103/PhysRevB.51.6868.

[112] Kenji Watanabe, Takashi Taniguchi, and Hisao Kanda. Direct-bandgap properties and evidence for ultraviolet lasing of hexagonal boron nitride single crystal. *Nature Materials*, 3:404–409, May 2004. doi: 10.1038/nmat1134. 6.1.1

[113] L. Britnell, R. V. Gorbachev, R. Jalil, B. D. Belle, F. Schedin, M. I. Katsnelson, L. Eaves, S. V. Morozov, N. M. R. Peres, J. Leist, A. K. Geim, K. S. Novoselov, and L. A. Ponomarenko. Field-effect tunneling transistor based on vertical graphene heterostructures. *Science*, 335:947–950, February 2012. doi: 10.1126/science.1215193. 6.1.1

[114] A. L. Efros and B. I. Shklovskii. Coulomb gap and low temperature conductivity of disordered systems. *Journal of Physics C: Solid State Physics*, 8:L49, 1975. doi: 10.1088/0022-3719/8/4/003. 6.3

[115] H. B. Chan, P. I. Glicofridis, R. C. Ashoori, and M. R. Melloch. Universal linear density of states for tunneling into the two-dimensional electron gas in a magnetic field. *Physical Review Letters*, 79:2867–2870, October 1997. doi: 10.1103/PhysRevLett.79.2867. 6.3

[116] Yuanbo Zhang, Victor W. Brar, Feng Wang, Caglar Girit, Yossi Yayon, Melissa Panlasigui, Alex Zettl, and Michael F. Crommie. Giant phonon-induced conductance in scanning tunnelling spectroscopy of gate-tunable graphene. *Nature Physics*, 4: 627–630, July 2008. doi: 10.1038/nphys1022. 6.3

[117] Cheng Shen, Na Li, Shuopei Wang, Yanchong Zhao, Jian Tang, Jieying Liu, Jinpeng Tian, Yanbang Chu, Kenji Watanabe, Takashi Taniguchi, Rong Yang, Zi Yang Meng, Dongxia Shi, and Guangyu Zhang. Observation of superconductivity with T_c onset at 12 K in electrically tunable twisted double bilayer graphene. arXiv:1903.06952v1 [cond-mat.supr-con], March 2019. 7

[118] Xiaomeng Liu, Zeyu Hao, Eslam Khalaf, Jong Yeon Lee, Kenji Watanabe, Takashi Taniguchi, Ashvin Vishwanath, and Philip Kim. Spin-polarized correlated insulator and superconductor in twisted double bilayer graphene. arXiv:1903.08130v2 [cond-mat.mes-hall], March 2019.

[119] Yuan Cao, Daniel Rodan-Legrain, Oriol Rubies-Bigorda, Jeong Min Park, Kenji Watanabe, Takashi Taniguchi, and Pablo Jarillo-Herrero. Electric field tunable correlated states and magnetic phase transitions in twisted bilayer-bilayer graphene. arXiv:1903.08596v2 [cond-mat.str-el], March 2019. 7

[120] Guorui Chen, Lili Jiang, Shuang Wu, Bosai Lyu, Hongyuan Li, Bheema Lingam Chittari, Kenji Watanabe, Takashi Taniguchi, Zhiwen Shi, Jeil Jung, Yuanbo Zhang, and Feng Wang. Evidence of a gate-tunable Mott insulator in a trilayer graphene moiré superlattice. *Nature Physics*, 15:237–241, January 2019. doi: 10.1038/s41567-018-0387-2. 7

[121] S. Y. Frank Zhao, Nicola Poccia, Margaret G. Panetta, Cyndia Yu, Jedediah W. Johnson, Hyobin Yoo, Ruidan Zhong, G. D. Gu, Kenji Watanabe, Takashi Taniguchi, Svetlana V. Postolova, Valerii M. Vinokur, and Philip Kim. Sign reversing hall effect in atomically thin high temperature superconductors. arXiv:1809.06944v2 [cond-mat.supr-con], October 2019. 7

[122] Misha Brodsky. *Charging of Small Two-Dimensional Electron Puddles*. PhD thesis, Massachusetts Institute of Technology, September 2000. B.2